CRAS 2014

Proceedings of the 4th Joint Workshop on New Technologies for Computer/Robot Assisted Surgery

October 14-16, 2014

Hotel Melià, Genoa, Italy

CRAS 2014

4th Joint Workshop on Computer/Robot Assisted Surgery

Genova, Italy October 14–16, 2014

www.cras2014.eu

Abstract

Robotic surgery is one of the most appealing fields of modern robotics. With over 2 decades history, more than 2,000 systems installed worldwide and over 200,000 interventions conducted per annum; the field of robotic surgery is considered well-established. Despite these impressive figures and increasing popularity in research labs all over the world, the list of technological advances that made it into the operating room (OR) during this last decade is fairly limited. Long expected techniques such as 3D reconstruction, motion compensation, virtual guidance, haptic feedback, under study in many labs all over the planet did not make their appearance into the market yet.

This workshop aims at bringing together researchers and clinicians involved in computer and/or robot assisted surgery to provide a clear view on the status and recent trends in this field and to propose concrete measures to achieve a critical mass in research and innovation in this field.

Horizon 2020 and MAR Special Session

The CRAS 2014 workshop will feature a half-day special session devoted to the discussion of the next EU calls, and the impact/implication of the Multi-Annual Roadmap (MAR) on the preparation of proposals and their evaluation. The focus of the session will be on healthcare robotics, which will be one of the main topics of the 2nd EU call.

The workshop occurs shortly after the publication of the outcome of the 1st ICT call in Robotics and after the completion of the Multi Annual Roadmap (MAR) developed by euRobotics aisbl to guide the proposal preparations for call 2, and the topic selection for calls 3 and 4.

Given the MAR complexity, the perceived uncertainty on how to use it, and its relation with the proposal evaluation, we have organized a special session fully devoted to this issue. Through discussion with the experts who helped writing the MAR and representatives from the Commission, we aim to clearly present how to use the MAR and its relation to the proposal evaluation criteria. Furthermore, we will discuss the outcome of the 1st call from the point of view of the Commission and of the robotics community.

In addition, a plenary talk by Geoff Pegman (euRobotics aisbl) on the 1st call outcome "from the point of view of the proposers" will compare the perception about the quality of the proposals to the actual evaluation results and the correspondence to the MAR.

Pre-commercial Procurement (PcP)

On October 16th, a plenary talk by Anne Bajart (European Commission) will discuss pre-commercial procurement (PcP). Dr. Bajart will present the new instrument and offer opportunities of networking for people interested in the idea.

Venue

The CRAS 2014 workshop will be held at the Hotel Meliá Genova.

Address: Via Corsica 4, Genova, Italy

The Meliá Genova is located in the heart of Genoa, very close to the exclusive residential neighborhood of Carignano, the Carlo Felice Theatre, Genoa Aquarium and the city's most important shops and boutiques.

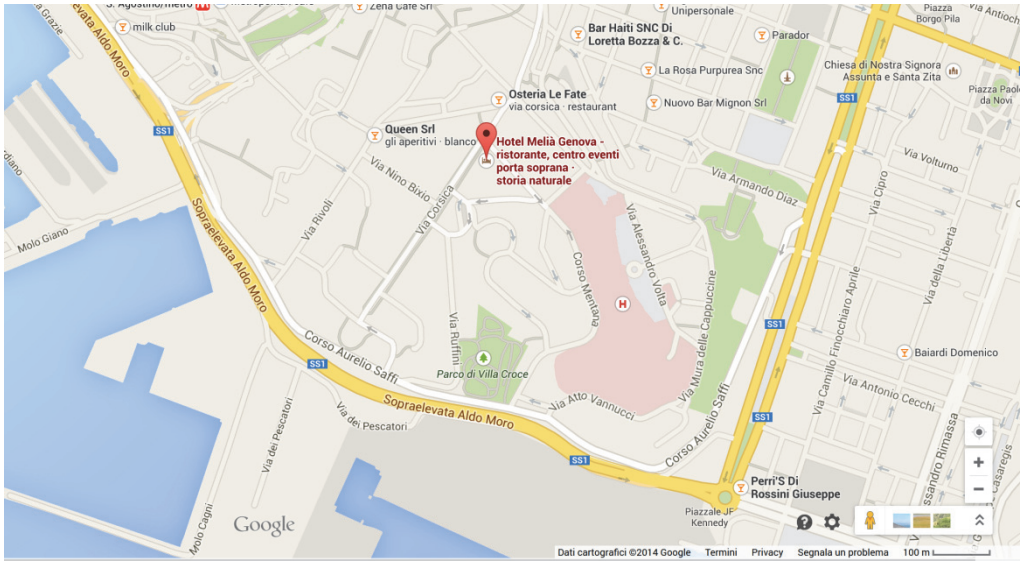

Genoa

Genoa is the capital of Liguria and the sixth largest city in Italy. It's one of Europe's largest cities on the Mediterranean Sea and the largest seaport in Italy. Genoa has been nicknamed "la Superba" due to its glorious past and impressive landmarks. Part of the city's old town is included in the World Heritage List (UNESCO). The city's rich art, music, gastronomy, architecture and history allowed it to become the 2004 European Capital of Culture. It is the birthplace of Cristoforo Colombo. Genoa is located in the Italian Riviera, near other major Italian tourist destinations such as Portofino and the Cinque Terre. It is also a short train ride away from Milan, Turin, Pisa and Florence.

(Adapted from *Wikipedia*)

Workshop Dinner

The workshop dinner will be held on October 15th at the Museo Diocesano di Genova.

Address: Via Tomaso Reggio, 20, Genoa, Italy

The Museo Diocesano is located in Genoa's historic center, near the magnificent San Lorenzo Cathedral.

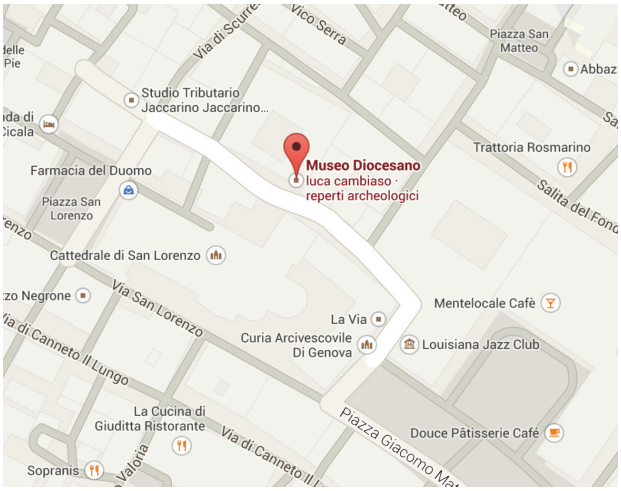

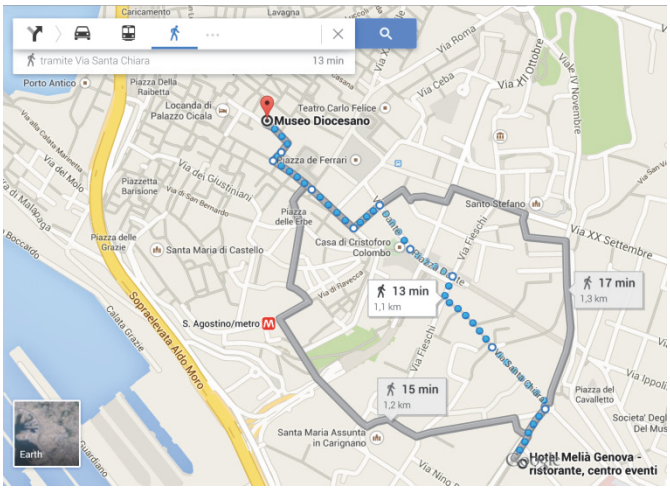

Museo Diocesano

The Diocesano museum of Genoa is housed in the cloister of San Lorenzo, the former residence of members of the Cathedral of the same name. The cloister, built in the twelfth century, is characterized by Romanesque arches resting on double columns. In the seventeenth century, two sides of the building were modified by replacing the twin columns with longer pillars adequate to handle the addition of two extra floors. The interiors are decorated with wooden floors dating from the thirteenth century, paintings from the XIV century and frescoes from the XVIII century.

Workshop Co-Chairs

Leonardo Mattos

Istituto Italiano di Tecnologia
Dept. of Advanced Robotics
Via Morego 30
16163 Genoa, Italy

Paolo Fiorini

Università di Verona
Dipartimento di Informatica
Ca' Vignal 2
Strada Le Grazie, 15
37134 Verona, Italy

Emmanuel Vander Poorten

University of Leuven
Dept. of Mechanical Engineering
Celestijnenlaan 300B
B-3001 Heverlee, Belgium

Organizing Committee

Kaspar Althoefer
(KCL)

Peter Brett
(Brunel)

Danilo Bruno
(IIT)

Marta Capiluppi
(Univ. Verona)

Brian Davies
(ICL+IIT)

Elena De Momi
(POLIMI)

Nikhil Deshpande
(IIT)

Giancarlo Ferrigno
(POLIMI)

Paolo Fiorini
(Univ. Verona)

Edward Grant
(NCSU)

Tamas Haidegger
(Obuda Univ.)

Lüder A. Kahrs
(LUH)

Leonardo Mattos
(IIT)

Arianna Menciasi
(SSSA, Pisa)

Sarthak Misra
(Univ. Twente)

George Mylonas
(ICL)

Auguste van Poelgeest
(IPA)

Philippe Poignet
(LIRRM)

E. Vander Poorten
(KU Leuven)

Domenico Prattichizzo
(Univ. Siena+IIT)

Ferdinando Rodriguez Y Baena
(ICL)

Jos Vander Sloten
(KU Leuven)

Danail Stoyanov
(UCL)

Stefan Weber
(Univ. Bern)

Helge Wurdemann
(KCL)

Program Overview

<table>
<tr><th colspan="2">Schedule</th><th>14 October</th><th colspan="2">15 October</th><th>16 October</th></tr>
<tr><td>8:45</td><td>9:00</td><td></td><td colspan="2"></td><td rowspan="3">Session 7: Continuum & Soft Robots (I)</td></tr>
<tr><td>9:00</td><td>9:30</td><td>Keynote speech by Brian Davies</td><td colspan="2">Keynote speech by Gernot Kronreif</td></tr>
<tr><td>9:30</td><td>10:00</td><td rowspan="2">Session 1: Segmentation and Registration</td><td colspan="2" rowspan="2">Session 5: Interfaces & Teleoperation</td></tr>
<tr><td>10:00</td><td>10:30</td><td>Coffee break</td></tr>
<tr><td>10:30</td><td>11:00</td><td>Coffee break</td><td colspan="2">Coffee break</td><td rowspan="2">Session 8: Continuum & Soft Robots (II)</td></tr>
<tr><td>11:00</td><td>11:30</td><td rowspan="2">Session 2: Vision, Modeling and Control</td><td colspan="2" rowspan="2">Session 6: Interfaces & Haptic Feedback</td></tr>
<tr><td>11:30</td><td>12:00</td><td>Keynote speech by Geoff Pegman</td></tr>
<tr><td>12:00</td><td>13:30</td><td rowspan="2">Lunch break</td><td colspan="2" rowspan="3">Lunch break</td><td>Lunch break</td></tr>
<tr><td>13:30</td><td>13:45</td><td rowspan="2">CRAS Evaluation & Awards</td></tr>
<tr><td>13:45</td><td>14:00</td><td rowspan="4">Session 3: Active Guidance & Assistance</td><td rowspan="9">H2020 & MAR Special Session</td></tr>
<tr><td>14:00</td><td>14:30</td><td>The MAR process and the health care domain – Christophe Leroux</td><td>Keynote speech by Anne Bajart</td></tr>
<tr><td>14:30</td><td>14:50</td><td>The Surgical sub domain – Paolo Fiorini</td><td rowspan="4">Session 9: Ontologies and Software</td></tr>
<tr><td>14:50</td><td>15:00</td><td>The Rehabilitation sub domain – Birgit Graf (remote)</td></tr>
<tr><td>15:00</td><td>15:10</td><td rowspan="2">Coffee break</td><td>Coffee break</td></tr>
<tr><td>15:10</td><td>15:30</td><td>The Assistive sub domain – Thierry Keller</td></tr>
<tr><td>15:30</td><td>15:50</td><td rowspan="4">Session 4: Novel Robotic Hardware</td><td>EU feedback about the 1st call outcome – Anne Bajart</td><td rowspan="2">Coffee break</td></tr>
<tr><td>15:50</td><td>16:00</td><td rowspan="3">Open discussions</td></tr>
<tr><td>16:00</td><td>16:20</td><td rowspan="3">Session 10: Cognitive Robotics</td></tr>
<tr><td>16:20</td><td>16:30</td></tr>
<tr><td>16:30</td><td>17:00</td><td>Keynote speech by Antonello Forgione</td></tr>
<tr><td>17:00</td><td>17:30</td><td rowspan="2"></td><td colspan="2" rowspan="2"></td><td rowspan="2"></td></tr>
<tr><td>20:00</td><td></td><td colspan="2">Conference dinner at Museo Diocesano</td></tr>
</table>

Program

Tuesday, October 14th, 2014

Schedule		14/October
9:00	**9:30**	**Keynote speech: Training for Surgeons – A niche area for robotic systems?** **Brian Davies** Chair: Leonardo Mattos
9:30	**10:30**	**Session 1: Segmentation and Registration** Chair: Su-Lin Lee
9:30	9:45	**Medical image registration in the operating room: phantom study** Bogdan Maris and Paolo Fiorini
9:45	10:00	**Simultaneous Segmentation and Registration Using a Prior Model** Ping-Lin Chang and Danail Stoyanov
10:00	10:15	**Feature points detector and descriptor for medical ultrasound data** Diego Dall'Alba and Paolo Fiorini
10:15	10:30	**Multi atlas based segmentation approach for neurosurgery planning and guidance** Paolo Zaffino, Karl Fritscher, Patrik Raudaschl, Rainer Schubert, Gregory C. Sharp, Francesco Amato and Maria Francesca Spadea
10:30	**11:00**	**Coffee break**
11:00	**12:00**	**Session 2: Vision, Modeling and Control** Chair: Nikhil Deshpande
11:00	11:15	**Hybrid electromagnet model for multiple mobile coil magnetic manipulation** Baptiste Véron, Arnaud Hubert, Joël Abadie and Nicolas Andreff
11:15	11:30	**Vessel Retargeting using Intravascular Ultrasound** Angelos Karlas and Su-Lin Lee
11:30	11:45	**Non-rigid Soft-Tissue Tracking Using Combined Feature and Intensity Information** Xiaofei Du and Danail Stoyanov
11:45	12:00	**A B-Spline Tube Model for Catheter and Guidewire Tracking** Ping-Lin Chang and Danail Stoyanov
12:00	**13:45**	**Lunch break**
13:45	**15:00**	**Session 3: Active Guidance & Assistance** Chair: Elena De Momi
13:45	14:00	**Third arm for surgeon: Embodiment and Control** Elahe Abdi, Mohamed Bouri, Etienne Burdet and Hannes Bleuler
14:00	14:15	**Proximal comanipulation of a minimally invasive surgery instrument to emulate distal forces** Cécile Poquet, Marie-Aude Vitrani and Guillaume Morel
14:15	14:30	**Virtual Assistive System for Robotic Single Incision Laparoscopic Surgery** Veronica Penza, Jesus Ortiz, Elena De Momi, Antonello Forgione and Leonardo Mattos
14:30	14.45	**Reducing Invasiveness of Robot-assisted Surgery by Semi-automatic Alignment to the Incision Point** Benoit Rosa, Emmanuel Vander Poorten, Dominiek Reynaerts and Jos Vander Sloten
14:45	15:00	**New Assistive Technologies for Laser Microsurgery** Loris Fichera, Diego Pardo, Darwin Caldwell and Leonardo Mattos
15:00	**15:30**	**Coffee break**
15:30	**16:30**	**Session 4: Novel Robotic Hardware** Chair: Auguste van Poelgeest
15:30	15:45	**FUTURA: a computer-assisted robotic platform for high-intensity focused ultrasound** Selene Tognarelli, Gastone Ciuti, Alessandro Diodato, Piero Miloro, Antonella Verbeni, Andrea Cafarelli and Arianna Menciassi
15:45	16:00	**Development of a hydraulic driven, 3-DOF, surgical instrument** Timo Cuntz and Auguste van Poelgeest
16:00	16:15	**Development of a 2-DOF force sensing needle for robotically assisted retinal vein cannulations** Andy Gijbels, Sebastiaan Colson, Dominiek Reynaerts and Emmanuel Benjamin Vander Poorten
16:15	16:30	**Neurophysiology guided single cell optical surgery** Alberto Averna, Marta Bisio, Giacomo Pruzzo, Michela Chiappalone, Paolo Bonifazi and Francesco Difato
16:30	**17:00**	**Keynote speech: No Scar Surgery – The Ultimate Step in Minimal Invasive Surgery** **Antonello Forgione** Chair: Giancarlo Ferrigno

Wednesday, October 15th, 2014

Schedule		15/October
9:00	**9:30**	**Keynote speech: Robot Systems for Image-Guided Needle-Based Procedures** **Gernot Kronreif** Chair: Edward Grant
9:30	**10:30**	**Session 5: Interfaces & Teleoperation** Chair: Benoît Herman
9:30	9:45	**Development of a modular control concept for a hydraulic 3-DOF surgical instrument** Laura Maria Comella, Andreas Rothfuss and Auguste van Poelgeest
9:45	10:00	**Advantages of mechanical back-drivability for medical applications of force control** Jerome Perret and Pierre Vercruysse
10:00	10:15	**Sensory subtraction via cutaneous feedback: a novel technique to improve the transparency of robotic surgery** Claudio Pacchierotti and Domenico Prattichizzo
10:15	10:30	**Prosthetic/assistive control via bio-signal-based HMIs: some practical experiences** Claudio Castellini and Joern Vogel
10:30	**11:00**	**Coffee break**
11:00	**12:00**	**Session 6: Interfaces & Haptic Feedback** Chair: Emmanuel Vander Poorten
11:00	11:15	**Evaluation of the effect of a robotized needle holder on ergonomics and skills** Thierry Bensignor, Brice Gayet and Guillaume Morel
11:15	11:30	**Towards Intuitive Operation of a Robotic Catheter** Alain Devreker, Sergio Portoles Diez, Andy Gijbels, Benoît Rosa, Jos Vander Sloten, Herbert De Praetere, Paul Herijgers, Emmanuel Vander Poorten and Dominiek Reynaerts
11:30	11:45	**Toward User-Friendly Robotic Assistance for Enhancing Accuracy and Safety of Reconstructive Microsurgery** Léna Vanthournhout, Benoît Herman, Jérôme Duisit, François Château, Jérôme Szewczyk, Benoît Lengelé and Benoît Raucent
11:45	12:00	**Using vibrations for haptic feedback discrimination in teleoperation** Adrian Ramos and Domenico Prattichizzo
12:00	**14:00**	**Lunch break**
14:00	**15:10**	**Horizon 2020 & MAR special session (I)**
14:00	14:30	**The MAR process and the health care domain** Christophe Leroux
14:30	14:50	**The Surgical sub domain** Paolo Fiorini
14:50	15:10	**The Rehabilitation sub domain** Birgit Graf (remote)
15:10	**15:30**	**Coffee break**
15:30	**17:30**	**Horizon 2020 & MAR special session (II)**
15:30	15:50	**The Assistive sub domain** Thierry Keller
15:50	16:20	**EU feedback about the 1st call outcome** Anne Bajart
16:20	17:30	**Open discussions**
20:00		**Conference dinner at Museo Diocesano** Address: Via Tomaso Reggio, 20, Genoa, Italy

Thursday, October 16th, 2014

Schedule		16/October
8:45	**10:00**	**Session 7: Continuum & Soft Robots (I)** Chair: Arianna Menciassi
8:45	9:00	**A new bio-inspired, antagonistically actuated and stiffness controllable manipulator** Agostino Stilli, Farahnaz Maghooa, Helge Arne Wurdemann and Kaspar Althoefer
9:00	9:15	**Biphasic Media Variable Impedance Actuation Application in Human Robotics Interaction** Bo Han, Matteo Zoppi and Rezia Molfino
9:15	9:30	**An Actuated, Flexible Endoscope for Laser Surgery inside the Larynx** Dennis Kundrat, Andreas Schoob, Lüder A. Kahrs and Tobias Ortmaier
9:30	9:45	**Modular integration of a 3 DoF F/T sensor for robotic manipulators** Emanuele Lindo Secco, Yohan Noh, Sina Sareh, Helge Wurdemann and Kaspar Althoefer
9:45	10:00	**A novel sensorized catheter for precise stenotic heart valve targeting: an application of the Medyria Trackcath Catheter Positioning System** Anita Di Iasio, Theresa Visarius, Gianluca Martena and Mauro Sette
10:00	**10:30**	**Coffee break**
10:30	**11:30**	**Session 8: Continuum & Soft Robots (II)** Chair: Kaspar Althoefer
10:30	10:45	**STIFF-FLOP surgical manipulator: design and preliminary evaluation of the multi-module design** Iris De Falco, Matteo Cianchetti and Arianna Menciassi
10:45	11:00	**Manipulability of Robotic Catheters** Phuong Toan Tran, Emmanuel Vander Poorten, Gabrijel Smoljkic, Caspar Gruijthuijsen, Paul Herijgers, Dominiek Reynaerts and Jos Vander Sloten
11:00	11:15	**Rapid Prototyping of Rod-Driven Continuum Robots for Medical Applications** Dennis Kundrat, Andreas Schoob, Lüder A. Kahrs and Tobias Ortmaier
11:15	11:30	**A new strategy to build a fully modular soft manipulator for MIS** Giada Gerboni, Tommaso Ranzani, Gastone Ciuti, Matteo Cianchetti and Arianna Menciassi
11:30	**12:00**	**Keynote speech: Feedback and Participant Response to the First Robotics PPP Call in H2020** **Geoff Pegman** Chair: Paolo Fiorini
12:00	**13:30**	**Lunch break**
13:30	**14:00**	**CRAS Evaluation & Awards** Chairs: Emmanuel Vander Poorten, Paolo Fiorini, Leonardo Mattos
14:00	**14:30**	**Keynote speech: Pre-Commercial Procurement** **Anne Bajart** Chair: Paolo Fiorini
14:30	**15:30**	**Session 9: Ontologies and Software** Chair: Tamás Haidegger
14:30	14:45	**Task Ontology Validation in Surgical Robotics** Fabrizio Boriero, Marta Capiluppi, Riccardo Muradore and Paolo Fiorini
14:45	15:00	**A New ROS Interfaced Haptic Library with an Example of Application** Emidio Olivieri and Leonardo Mattos
15:00	15:15	**Towards Open Source Surgical Robotics** Sándor Jordán, Árpád Takács, József Tar, Imre Rudas and Tamás Haidegger
15:15	15:30	**Robot visualisation concept in 3D Slicer for image-guided interventions** Sebastian Tauscher, Alexander Fuchs, Thomas Neff, Lüder Alexander Kahrs and Tobias Ortmaier
15:30	**16:00**	**Coffee break**

Thursday, October 16th, 2014

Schedule		16/October
16:00	**16:30**	**Session 10: Cognitive Robotics** Chair: Leonardo Mattos
16:00	16:15	**Towards Autonomous Robotic Catheter Navigation Using Reinforcement Learning** Abraham Temesgen Tibebu, Bingbin Yu, Yohannes Kassahun, Emmanuel Vander Poorten and Phuong Toan Tran
16:15	16:30	**Towards learning-based catheter distal section steering** Bingbin Yu, Abraham Temesgen Tibebu, Yohannes Kassahun, Felix Bernhard and Emmanuel Vander Poorten
16:30	**17:00**	**Open discussions**

Keynote speech

Tuesday, October 14th – 9:00

Training for Surgeons – A niche area for robotic systems?

Professor Brian Davies, DSc, PhD, DIC, F.I.Mech.E, FREng.

Imperial College London & Istituto Italiano di Tecnologia

Traditionally, training for surgery is undertaken using plastic phantoms and traditional tools. Apart from cadaver trials, the next time the surgeon undertakes a procedure is on you, the patient! Hence it is highly desirable to have improved systems for training surgeons that better approximate the reality of the surgical procedure. It is sometimes argued that simulation together with computer-generated images can satisfy this requirement. However, the surgeon has to use tools in order to undertake the procedure and it is essential that these be included in the enhanced training systems. This area seems to be an ideal application for CRAS. An outline of the system requirements, together with some specific examples of training systems for surgeons, will be given in the talk.

Professor Brian Davies is an Emeritus Professor of Medical Robotics at Imperial College London, where he has been since 1983, and is also a senior research investigator there. Since 2006 he has been advising on Medical Robots, particularly the μRALP project, for the Advanced Robotics Group of the Italian Institute of technology in Genoa.

He has a PhD in Medical Robotics and was awarded a DSc. in 2001 for his international contribution to Robotic and Computer Aided Surgery systems. He has over 250 refereed papers. He was made a Fellow of the Royal Academy of Engineering in 2005 and served on their focus group on medical technology. He developed the world's first special-purpose surgical robot called PROBOT, to remove quantities of prostatic tissue from a human patient in a clinical trial in April 1991. He subsequently developed the concept of Active Constraints particularly applied to orthopaedic robots and in 1999 he was a co-founder of the spin-off company ACROBOT limited, which developed robots for MIS hip and knee joint replacement. He is a founder of the new "Technologies in Medicine" section of the Royal Society of Medicine. He is on the Board of the IMechE Engineering in Medicine & Health Division. Since 2001 he has been program chair for the annual conference of the International Society for Computer Aided Orthopaedic Surgery (CAOS). Since 2000 he has chaired the Scientific Advisory Board for the Co-Me Swiss research organisation. He Participates in the EU medical robotics project ACTIVE and its predecessor ROBOCAST, and is a regular reviewer for EU FP7 projects. In July 2012 he gave the Peiyang prestigious lecture in Tianjin, China and became a visiting Professor there. In 2013-2014 he Chairs the Strategic Advisory Board for the Leeds, UK, HTC in Colorectal Cancer group and is an internal advisor on the EU "Script" project and the German funded "Cognitive Surgery" Bavarian research project.

Keynote speech

Tuesday, October 14th – 16:30

No Scar Surgery – The Ultimate Step in Minimal Invasive Surgery

Dr. Antonello Forgiione, MD PhD MBA FACS

AIMS Academy, Niguarda Cà Granda Hospital, ValueBioTech Ltd, MedTechCatalyst Association

We, human beings, don't like to undergo surgical procedures, not only for the fear and effect of the disease, but also for the expected postoperative pain, the risks and side effects of anesthesia, the recovery time needed after the operation and the permanent visible scars that will forever leave an unpleasant reminder of the experience and alter the esthetic of the person. The revolutionary concept of Natural Orifice Transluminal Endoscopic Surgery (NOTES) described by Anthony Kalloo, gastroenterologist at John Hopkins University, promised to overcome many of the historical drawbacks of the surgical approach. After a long period of testing in experimental settings the NOTES approach has now proven its feasibility and safety in preliminary clinical experience in the performance of several surgical procedures. So far, the major efforts in the field of NOTES surgery have been primarily concentrated on the use of natural orifice approaches to simply replicate traditional radical procedures whilst respecting established operative strategies. However, the NOTES approach is also stimulating the appreciation of complementary advanced technologies and new surgical concepts, that will allow us not only to perform the procedures via a minimal access, but also to minimize the extent or even the need for a surgical resection. These new concepts are represented for example by genetically driven gastrointestinal cancer treatment and manipulation of the gastrointestinal tract for the cure of metabolic disorders. Traditionally, training for surgery is undertaken using plastic phantoms and traditional tools. Apart from cadaver trials, the next time the surgeon undertakes a procedure is on you, the patient! Hence it is highly desirable to have improved systems for training surgeons that better approximate the reality of the surgical procedure. It is sometimes argued that simulation together with computer-generated images can satisfy this requirement. However, the surgeon has to use tools in order to undertake the procedure and it is essential that these be included in the enhanced training systems. This area seems to be an ideal application for CRAS. An outline of the system requirements, together with some specific examples of training systems for surgeons, will be given in the talk.

Dr. Antonello Forgione is a Digestive Surgeon with decennial experience in particular in the field of MIS, SILS, NOTES and Computer Assisted Surgery. Scientific Director of the AIMS Academy, one of the few international training center in MIS in Europe and among the few in the world, he's currently Consultant in General, Oncologic and Mininvasive Surgery in the largest public hospital in Italy, the Niguarda Cà Granda Hospital in Milan. He holds a PhD and received a Global Executive MBA from SDA Bocconi University. Dr Forgione is Founder and currently CEO of ValueBioTech Ltd, a start up company working on the development of a patented microrobotic platform for SILS and NOTES. He is also Founder and President of the MedTechCatalyst an italian based association devoted to the scouting and support of innovative projects in the biotechnology field. He is selected member of the Technology committees of the EAES and SAGES, editorial board member and reviewer of several international indexed journal. Dr Forgione is also Fellow of the American College of Surgeon.

Keynote speech

Wednesday, October 15th – 9:00

Robot Systems for Image-Guided Needle-Based Procedures

Dr. Gernot Kronreif

ACMIT - Austrian Center for Medical Innovation and Technology

Percutaneous biopsy performed under the guidance of interventional imaging has been shown to be a safe and reliable alternative to excisional surgical biopsy. Even more, the percutaneous approach in general is also a promising treatment method for tumors using needle-like ablation probes, which allow minimal invasiveness and thus reduces morbidity and the hospitalization period. The high efficacy of all these procedures, however, depends on the quality of needle placement. An accurate and fast needle insertion is important in order to maximize the biopsy result from the targeted site and minimize the invasiveness of the procedure to the patient. At times, access to a target can be technically challenging because of various factors, including limited space at the skin entry site or a difficult angulated access. Thus, a robotic-assisted needle insertion guided by imaging is of great clinical value for several reasons: (a) it will provide very stable needle guidance, even for angulated approaches, (b) it will allow access to lesions when the spatial constraints of the used imaging modality would limit the access for a biopsy needle or other interventional tools, and (c) it may further expand the time window for exploration of a lesion when using contrast agents because more time can be spent to target a lesion.

Motivated by the potential advantage of robotic systems for radio-interventional procedures, various systems have been developed or researched, from general-purpose percutaneous systems, to those specialized for prostate interventions, breast biopsy and therapy -- under the guidance of different imaging modalities such as computed tomography (CT)/fluoroscopy, ultrasound (US), or Magnet Resonance Tomography (MRT). The presentation gives an overview of the requirements for such interventional robot systems and describes some selected developments. Beside of outlining the results achieved so far, the presentation also points out some of the unsolved problems and shows some future research topics in the area of interventional robotic systems.

Gernot Kronreif received his PhD in Technical Sciences at the “Vienna University of Technology” in 1995. After five years working as research assistant at the “Institute for Handling Devices and Robotics” of the “Vienna University of Technology”, he was the head of the business unit “Advanced Service Robotics” at the “Austrian Research Centers GmbH” between 2000 and 2007 and at the “PROFACTOR GmbH” between 2007 and 2010, respectively. During these 10 years of professional work, he could initiate and conduct several national and international research projects in the area of robotics for medicine, rehabilitation and care. Since 2010 he is the Scientific Director of the “Austrian Center of Medical Innovation and Technology” (ACMIT). He is lecturer at several Universities for Applied Science and also member in various national and international scientific committees and organisations (IFAC, ISCAS, CURAC, SMIT, AMIPG, CELLI). He was member of the scientific programme committee, invited speaker, faculty member, and session chairman for various scientific conferences and symposia and has more than 130 publications in journals and scientific conferences.

Keynote speech

Thursday, October 16th – 11:30

Feedback and Participant Response to the First Robotics PPP Call in H2020

Dr. Geoff Pegman

RURobots

The talk focusses on the outcomes of the first call of the SPARC Public Private Partnership in Robotics. As well as providing data on the success rate against various criteria it will also highlight how well the call appears, at this early stage, to have met the requirements of the PPP as set out in the Strategic Research Agenda and Multi-annual Roadmap. Finally the talk will focus on upcoming calls and the process by which euRobotics members and the general robotics community can help focus these calls.

Dr. Geoff Pegman is a member of the Board of euRobotics aisbl with a special interest in representing the views of SMEs. He is also the Managing Director of R U Robots and is a Chartered Director with over 26 years' experience of the advanced robotics industry. Among his many affiliations Geoff is a visiting fellow at the Bristol Robotics Lab and is a member of the CONNECT Advisory Forum.

Keynote speech

Thursday, October 16th – 14:00

Pre-Commercial Procurement

Dr. Anne Bajart

European Commission – DG CONNECT

In 2015, pre-commercial procurement (PcP) are called in H2020 ICT-24 for demand-driven innovative robotics solutions in the healthcare sector. The goal of this workshop is to present the new instrument and offer opportunities of networking for people interested in the idea. PCP co-fund actions are H2020 funding instruments that aim to encourage public acquisition of research, development and validation of new solutions that can bring significant improvements in areas of public interest, whilst opening market opportunities for industry and researchers active in Europe. PCP helps public authorities to use research results, in order to obtain better value for money more quickly. Furthermore, PCP enables public procurers to share the risks and benefits of designing, prototyping and testing new products and services with the suppliers and other stakeholders, such as the end-users.

Dr. Anne Bajart has a PhD in Electrical Engineering. She is Research Programme Officer at the European Commission. Before working for the EC, she worked as lecturer, researcher and project manager at the University of Liège (BE), at the Ecole Polytechnique de Lausanne (CH) and at Philips Leuven (BE). Her main areas of interest today are robots, Human-Robot and Human-Computer Interaction, benchmarking and performance evaluation of systems, intelligent control of complex systems, dissemination of science, impact assessment, responsible innovation and social acceptance of technology.

Session 1

Segmentation and Registration

Chair: Dr. Su-Lin Lee, Imperial College London

Tuesday, October 14th

9:30 – 10:30

Medical image registration in the operating room: phantom study

Bogdan M. Maris
University of Verona, Italy

Paolo Fiorini
University of Verona,Italy

***Abstract*—We present here a phantom study to asses the feasibility of the medical image registration algorithms in the operating room (OR) scenario. The main issues of the registration algorithms in an OR application are, on one hand, the lack of the initial guess of the registration transformation - the images to be registered may be completely independent- and, on the other hand, the multimodality of the data. Other requirements to be addressed by the OR registration algorithms are: real-time execution and the necessity of the validation of the results. This work analyzes how, under these requirements, the current state of the art algorithms in medical image registration may be used and shows which direction should be taken when designing a OR navigation system that includes registration as a component. The classical approaches - intensity-based and landmark-based - are investigated here in an in-vitro set-up. Ultrasound (US) tracked 2D images and correspondent slices extracted from a 3D computed tomography (CT) dataset of an anatomical phantom are tested for registration. The anatomical phantom and the CT dataset are first registered in a global reference system defined by an optical tracking system. The prior constraints we have introduced for testing overcome the first issue of the initial alignment but do not suffice to obtain a further refinement of the registration results in the case of intensity-based registration. The landmark-based approach requires further constraints such as the identification of corresponding landmarks before the registration process takes place. Anyhow, this approach seems to be the only approach that have a meaning in the OR. A complete test of the state of the art algorithms in medical image registration was performed with the scope to identify which one of them is suitable for the OR scenario.**

I. Introduction

Image registration is the procedure of aligning two or more images of the same scene taken from different viewpoints, at different time, and/or by different sensors, so that corresponding features can be easily related. Image registration has application to many fields, but the one addressed here is medical imaging and medical applications with a particular regard to OR applications. In the case of an OR procedure or an image-guided system, the images to be registered are acquired in two steps: the first one takes place before the procedure and we call such dataset the *pre-operative* image, the second one occurs during the procedure and is called *intra-operative* dataset. By registering the two dataset, a spatial relationship between the anatomical structures in the two images and with the body of the patient is established.Considering the nature of the problem in medical image registration, that is the deformability of the tissue encountered in most of the medical images, except the images where the main interest is on rigid structures such as bones, most of the current registration algorithms try to find a solution that involves deformation. Then, the challenge is to find image registration techniques to be included in an image-guided system that involves structures subject to deformations.

The intensity based algorithms require three components: a distance measure, a transformation model and an optimization method. The simplest distance measure is given by the L_p-norms of the intensity differences, in case of monomodal registration. The choice of an appropriate distance measure is a harder task in the case of multi-modal imaging. The most used distance measure for multi-modal registration called *mutual information* (MI) and derived from the information theory, measures how much information two images to be registered share together and reaches its maximum when the two images are aligned. A compromise between L_2 norm and mutual information, based on normalized image intensity gradients was introduced by Haber and Modersitzki in [1]. This distance measure is based on the observation that even for images of different modalities, intensity changes appear at corresponding positions. However, the gradient also measures the strength of the change which is an unwanted information for multi-modal information, therefore the gradient is normalized by its norm. The solution of the registration process, or the registration transformation, may be generated from a physical model that constrains the registration by a smoothness term or by a parametrization of the transformation. The type of the mapping is of paramount importance for the registration, as it reflects the class of transformations that are desirable or acceptable, and therefore limits the solution to a large extent. The registration parameters estimated through the optimization step correspond to the degrees of freedom of the transformation involved. Their number varies greatly, from six in the case of global rigid transformations in the three dimensional space, to a number equal to the number of pixels/voxels of the image in the case of a dense transformation. In the following, we call the transformations constrained to belong to a certain class of functions such as rigid, linear or affine, polynomial, spline, that have a relatively low number of parameters, *parametric transformations* while the transformations given as the discretized numerical solution of the registration equation, constrained by the chosen regularizer, *non parametric transformation*. In the case of parametric transformations the models are derived from linear or nonlinear interpolation or approximation theories. When the transformation is derived from physical models, the displacement is given as the reaction of the model to a force. The force is generated by the similarity between the images. In the linear models or the *elastic body deformation* the deformation is described by the Navier-Caucy partial differential equation, while the image grid is considered as an elastic membrane. The last step of the classical approach to image registration is the optimization. The major difficulties in image registration, from

the optimization point of view, is the handling of a variety of local and even global minimum. Multilevel methods are thus essential and it is not recommended to solve a problem using one fixed level. Most of the the commonly used methods are based on the computation of the gradient: *gradient descent*, *conjugate gradient*, *quasi Newton*, *Gauss-Newton*, *stochastic gradient descent*. When using an MI-based distance measure, one must pay particular attention to the optimization schemes that require the computation of the Hessian matrix due to its high computational cost. For instance, Broyden-Fletcher-Goldfarb-Shanno (BFGS) method estimates the Hessian by an update from an initial approximation and a sequence of differences of search directions and gradients. In the case of landmark registration, the input of the algorithm is represented by two sets of landmarks. The first set of landmarks includes points belonging to the target image and the second set is composed by landmarks from the reference image. The main limitation for the extraction of landmarks from medical images is that they are not as rich in details as for instance the digital photographs. The extraction of landmarks has been studied more in the case of 2D images and less in the case of 3D images. The registration transformation can be estimated using interpolation strategies, when the correspondences between landmarks are known. The best known method that infers both the correspondences and the transformation is the iterative closest point (ICP) method. In the following we assume that the correspondences are known *a priori* and the landmark-based registration techniques we shall test are linear, polynomial and quadratic. More generally, the interpolation conditions are replaced with approximation conditions. In this case, if we want to solve the registration and find a transformation whose bending energy is minimum, we obtain the thin-plate-spline (TPS) function.

II. Experimental set-up for testing

To test some of the registration algorithms presented so far, we have used medical images obtained from a triple modality 3D abdominal phantom, developed by Computerized Imaging Reference Systems Inc (CIRS, Norwalk, VA). The model 057 interventional 3D abdominal phantom is designed to address minimally invasive procedures and to be used in different abdominal scan techniques such as CT, MRI and US, developing imaging protocol and system testing and validation. The reason for the choice of this set-up, beside the multi-modal capability, is due also to the complete control over the physical position of the scanned sections. We wanted to obtain two completely aligned 2D slices in two different modalities, therefore to create the ideal framework for the registration algorithms, considering the nature of our problem which is the registration of real-time acquired images with accurate pre-operative scans. The difficulties encountered by the registration algorithms are due on one hand to the different physical process that generates the images and, on the other hand, by the deformation of the phantom generated by the pressure of the US probe and by the different covering of the US convex probe with respect to the CT slice which is a condition often encountered in practice (see figure 1, the deformation takes place in the upper part of the US image). The phantom was equipped with 4 markers in order to register it with the CT dataset. The global coordinate system is given by an optical tracking system composed by infrared light emitting

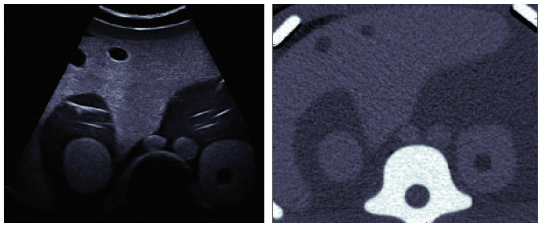

Fig. 1. An example of images used in the registration process. On the left hand side the US target image; on the right hand side the CT reference (fixed) image. Some of the structures visible in both images are: vertebra, liver and kidneys with simulated lesions, abdominal aorta, ribs.

cameras. The US images were acquired with a 2D probe equipped with markers in order to map its position to the global coordinate system. The calibration process of the US probe converts the point (u_i, v_i) in image plane coordinates (pixels) in 3D homogeneous coordinates defined with respect to the global reference system. We have used methods for multi-modal registration with transformation ranging from parametric (affine, spline) to non-parametric based on curvature or elastic. In the case of non-parametric registration the multi-level approach was necessary. The tests were performed using MATLAB environment and FAIR toolbox [2].

III. Intensity-based registration results

A. Parametric registration

We report here (figure 2) the results we have obtained using two types of parametric registration (affine and spline) and two types of distance measures (mutual information and normalized gradient field). The results obtained using MI as distance measure are not satisfactory in both affine and spline cases. The optimization process tends very quick to a local minimum, and the transformation leaves the image almost unchanged, in the case of affine transformation or applies a very small local deformation, in the case of the spline deformation. The trend of the MI measure is to quickly reach

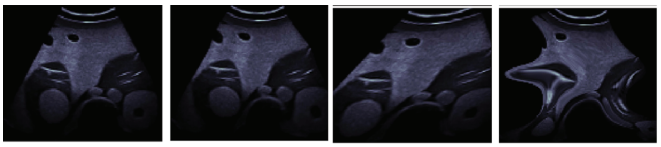

Fig. 2. The US image after the parametric multi-modal registration process. From left: affine registration using MI, spline registration using MI, affine registration using NGF, spline registration using NGF.

a stable position (figure 3) at around 66% in the affine case, and 87% in the spline case, of the of the initial value. The computation time is very long. The minimization scheme used was Gauss-Newton. The NGF measure is more efficient in terms of computation time but gives bad results in qualitative terms. Visually, figure 2 shows that in both affine and spline cases the results are meaningless and the deformation applied is arbitrary. As it can be seen in figure 3, the values of the objective function do not change over the iterations, they are indistinguishable in the graphic. In fact, they remain always very near to the initial value 1. The only advantage over the previous approach was the computation time. Also in this case we have used Gauss-Newton for the minimization.

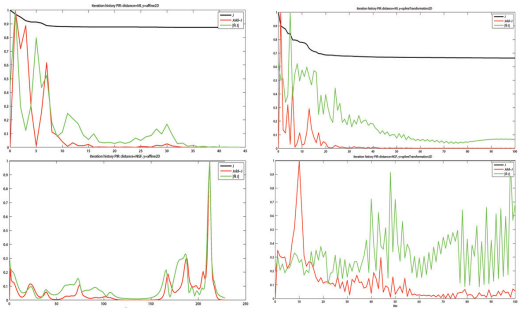

Fig. 3. Top row, left : affine registration using MI. The graphical trend of the objective function J is the black line. The green line gives the graph of $|\nabla J|$, while the red line shows the graph of the difference between the previous J value and the current value. Top row, right: spline registration using MI during. Bottom row: left - affine registration using NGF, right - spline registration using NGF.

Fig. 4. Multilevel spline registration.

B. Multilevel parametric and non parametric registration

The multilevel representation of the input data is required first of all in order to reduce the risk of being trapped by local minimum. At the same time, a solution of a coarse representation of the problem serves as a starting point for a representation with more details. Starting with a very coarse representation, the procedure is repeated on each level, until all details provided by the initial data are resolved. From an optimization point of view, the multilevel representation yield a smoother representation of the objective function. A smooth problem may be easier to resolve and, based on a good starting point, the more detailed problem can be solved quicker. The multilevel representation is also useful to reduce the computational time. The complexity of the registration algorithms increases exponentially with the dimension of the input data.

1) Parametric multilevel spline registration: Figure 4 reports the results of the multilevel spline registration. After 10 iterations on each level, the result is passed to the first iteration of the next level. The transformation also in these cases is not natural, after a strong bending obtained at the first level, the other levels tend to bend less the image. The computation time is very high and an ulterior refinement at each level through the other iterations does not improve the results as it can be seen in the figure 4. The tests using the affine transformation are not reported here but the results are similar to the non-level approach, and the transformation blocks quickly into a local minimum.

2) Non parametric multilevel registration: Figure 5 shows the results of the non-parametric elastic and curvature based multi-level registration. The algorithm starts at the coarser level using an affine transformation, then the registration at each level starts using the previous obtained result. After the initialization, there is not much interaction of the algorithm with the data, the images remain almost unchanged and the number of iterations is very low on each level. Even so, the computation time is very high.

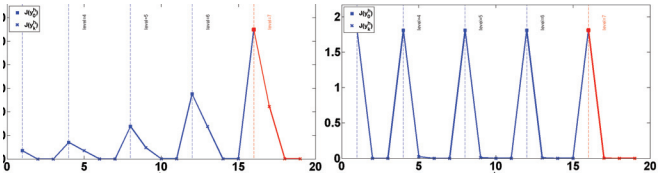

Fig. 5. Iteration history of multilevel non-parametric elastic (left) and curvature (right) registration: vertical lines separate different levels. The squares represent the initial value of MI, while the crosses show the value on each iteration.

IV. Landmark-based registration results

A. Linear registration

The linear registration in 2D involves the computation of 5 parameters, 2 for translation, 1 for rotation and 2 for scaling, therefore a minimum number of 3 landmarks is required. The solution with 3 landmarks alignes perfectly only the markers, but the overall result is not qualitatively acceptable (figure 6, top row). Increasing the number of landmarks, the registration

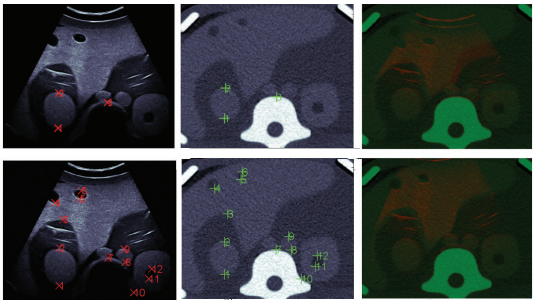

Fig. 6. Linear registration. Top row, first two images from the left: 3 selected landmarks in the target and reference image, respectively. On the right: the two images registered with the target on the red channel and the reference on the green channel. Bottom row, first two images from the left: 12 selected landmarks in the target and reference image, respectively. On the right: the two images registered.

problem becomes overdetermined and the solution is given by minimizing the sum of the distances between every pair of corresponding landmarks. Even though not all the landmarks will be aligned , the result improves a lot compared to the 3 landmarks solution (figure 6, bottom row).

B. Non-linear registration

The results of the linear registration may be improved by using a non-linear approach. The quadratic solution in 2D has a number of 12 parameters and is completely solved by 6 landmarks. In this case the error in the alignment of the landmarks is negligible because depends only on the computational precision (figure 7, row (a)). The registration result applied to the entire image, even in the 6 landmarks case, is acceptable. As in the linear case, increasing the number of landmarks, the solution is overdetermined but the overall result is better. By using the quadratic term, the alignment of 15 landmarks gives a minor error compared with the use of

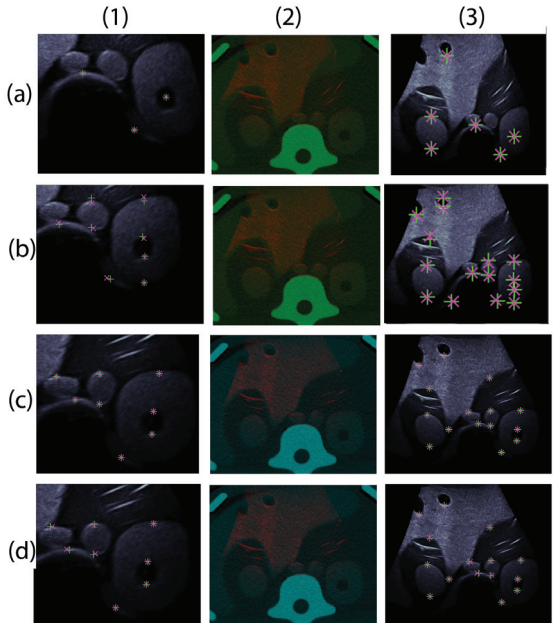

Fig. 7. Non-linear registration. Columns: (1) A close-up of the landmarks after the registration (green for the reference, red for the target); (2) The two images registered overlapped on red channel (target image) and on the green channel (reference image); (3) The target image registered. Rows: (a) Quadratic registration results with 6 landmarks; (b) Quadratic registration with 15 landmarks; (c) Spline registration with 15 landmarks and $\alpha = 0$; (d) Spline registration with 15 landmarks and $\alpha = 1000$

12 landmarks in the linear case. The polynomial solution may produce arbitrary deformations especially when the number of landmarks is low. The approach based on the thin-plate-spline (TPS) functions further refines the previous results. The spline functions may yield the perfect matching of the landmarks (interpolation) or an approximation, when the landmarks are not completely overlapped. These two conditions are realized by varying a smoothing parameter α. The solutions range from a low degree of bending when α is large to a high degree of bending in the case of small α. However, considering a number of landmarks from 6 to 15 and α ranging from 0 to 1000, this phenomenon is barely visible and the distance between the two sets of registered landmarks increases visibly only in the case of $\alpha = 1000$ (figure 7, rows (c) and (d)).

V. Discussion

Why the intensity-based medical image registration framework cannot work for OR applications? The major issues we have identified that makes this approach unfeasible in OR applications are: the distance measure MI - is very sensible at noise, incomplete data, no completely overlapping domains; the distance measure NGF - in our tests this measure has not produced the results we expected; the optimization - since the objective function is highly non convex, all the optimization methods fails in finding the global minimum or maximum; the multilevel approach - even though the multilevel approach is vital when using the non-parametric approach, in the case of multi-modal images the low level approximation of the registration transformation is not accurate at all and generates wrong results at higher levels; the computation time is very high even when only a couple of 2D images is involved.

Why the landmark-based registration works better than the intensity-based registration for an OR application? The first observation is that, in both cases, the transformations we are interested in have no physical meaning. Except in the rigid case, they are just mathematical tools that help to solve the registration. Following this observation, the intensity-based completely automatic algorithms fail and give arbitrary results if no prior information is given. In the case of landmark registration, even with a small number of landmarks and the rigid/linear constraint the results are much better. Extracting corresponding landmarks in multi-modality images excludes the computation of a multi-modal distance measure. As we have seen, the computation of MI and NGF generates misleading results and the computational time is very high, even in the 2D case. On the other hand, the landmark registration will always yield a decent result and the computation time is very low.

What are the limitations of the landmark-based registration for an OR application? Even if the registration results in the landmark case are preferable, the bottleneck of this method is not only the detection of landmarks, but also the computation of the correspondences. Having the correspondences, we can choose a mathematic model and, based on the number of landmarks, the registration is solved as some form of interpolation. This solution is simple and intuitive and it may always isolate a linear transformation, even with the TPS solution, which is an advantage since in the OR scenario a rigid motion is always required.

What is the direction for the future works? Another research area in the field of medical image processing is the segmentation, that is the extraction of contours or boundaries from the interest area. This type of processing may generate binary images, where the foreground is given by the extracted contours and the background is given by the remaining domain. The paradigm of landmark registration may be extended to this type of images but, in this case, the point to point correspondence is lost. Most of the radiologic information will disappear but, as we have seen, we don't need all the radiologic information. In fact, the radiologic information should be used only to detect the relevant features during the segmentation process. A rigid transformation should be first identified for the global alignment and, when required, a non-rigid transformation should be derived as a local refinement. This paper has not talked much about the validation of the registration algorithms. This was due to the fact that in an image-guided procedure the validation depends on the task we are addressing. For instance, in a targeted procedure for the ablation or the biopsy of a tumor, the parameter to be estimated for the validation is the overlapping volume of the tumor in the two image datasets: pre-operative and intra-operative. In a simplified scenario, when the insertion of an instrument toward a target point is required, the registration may be validated by computing the distance between the virtual point in the pre-operative image identified once the registration took place and the real position of the physical point we want to reach.

References

[1] Haber, E., Modersitzki, J.: Intensity gradient based registration and fusion of multi-modal images. In: MICCAI (2), pp. 726–733 (2006)

[2] Modersitzki, J.: FAIR: Flexible Algorithms for Image Registration. SIAM, Philadelphia (2009)

Simultaneous Segmentation and Registration Using a Prior Model

Ping-Lin Chang
Centre for Medical Image Computing
Department of Computer Science
University College London

Danail Stoyanov
Centre for Medical Image Computing
Department of Computer Science
University College London

***Abstract*—Medical image segmentation and registration are important research topics and have been studied for a long time. Unlike conventional approaches which regard the two problems independently and usually rely on image gradient, we propose a method for jointly registering a non-textured 3D model with a 2D image while segmenting it. Specifically, we use Bayesian inference to estimate the pixel-wise posterior which best fits for a prior 3D model with the 2D measurements. The approach allows the measurements not necessary to be only colour or intensity but be any kind of sensor measurement or even particularly enhanced structures. Preliminary results have shown that the probabilistic framework is very robust to noisy measurement.**

I. Introduction

Image segmentation and registration are crucial topics in medical imaging and computer assisted intervention. They are two essential processing steps towards advanced applications such as tumour localisation, augmenting reality or off-line surgical skill assessment. For example, in the training of transcatheter aortic valve implantation (TAVI), a precise segmentation for the endovascular area in the image is required in order to perform a quantitative skill assessment.

It has been found that such a segmentation task is very difficult due to the unclear image structures and dynamic image environment. Conventional gradient-based approaches such as active contour (snake) easily fails in segmenting regions without clear edges [1], [2]. Global optimisation methods which take pixel neighbourhood into account are also error-prone due to the appearance similarity. Figure 1 shows two possible training platforms used for TAVI training.

To overcome the difficulties, we can exploit a prior model for facilitating the segmentation process. This introduces a 3D to 2D image registration problem. Registration of a non-textured 3D model to an image has been very well studied with application ranging from camera tracking, augmented reality and reconstruction. Classic methods like RAPiD [3] and CONDENSATION [4] iteratively perform a search for correspondences followed by a registration step to align the model to the image. However, searching for correspondence in images with low signal-to-noise ratio such as fluoroscopy tends to fail.

A recent method PWP3D [5] uses a soft probabilistic way to register the 3D model exploiting the colour information of the foreground and background instead of strength of edge gradient. The signed distance function is used to guide the optimisation instead of correspondences. An unusually wider basin of convergence and smoothness of the objective function that it provides makes it a very appealing choice to use in the energy minimisation framework. More attractively, the use of non-parametric probability distribution allows a variety of measurements to be considered, which provides flexibility in multi-sensors setup.

In this paper, we propose a method that is based on the PWP3D framework but with extensions including robust estimation and the use of enhanced measurements. Preliminary studies have shown that a wide capture range exists when optimising with respect to the $\mathbb{SE}(3)$ model pose for the probabilistic cost function. This gives a promising direction in which given a distinguishable foreground and background measurements, the desired regions can be precisely segmented using the proposed approach. Allan et al. has successfully used the framework for surgical instrument tracking [6].

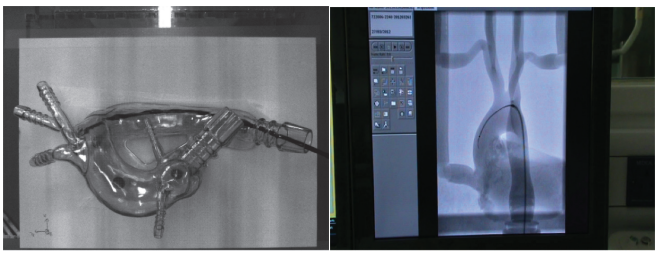

(a) (b)

Fig. 1: Simulation platforms used for TAVI skill assessment.

II. Methods

To register a non-textured prior model with a 2D image, we use a statistical model which applies a rule to express the segmented foreground and background. The main goal is to maximise its posterior which is the probability of a object contour $\mathbf{\Phi}$ given the measurement $\mathbf{\Omega}$. The $\mathbf{\Phi}$ is obtained by embedding the projection of the prior model in the 2D zero level-set (i.e., signed distance function). Assuming each pixel is independent and identically distributed (i.i.d.), the pixel-wise maximum a posteriori (MAP) estimation with respect to the $\mathbb{SE}(3)$ model pose ξ is thus

$$P(\mathbf{\Phi}|\mathbf{\Omega}) = \prod_{i=1}^{N} \Big\{ H_\varepsilon(\mathbf{\Phi}) P_f + \big(1 - H_\varepsilon(\mathbf{\Phi})\big) P_f \Big\} P(\xi) \quad (1)$$

where

$$P_f = \frac{P(\mathbf{y}_i|M_f)}{\eta_f P(\mathbf{y}_i|M_f) + \eta_b P(\mathbf{y}_i|M_b)},$$
$$P_b = \frac{P(\mathbf{y}_i|M_b)}{\eta_f P(\mathbf{y}_i|M_f) + \eta_b P(\mathbf{y}_i|M_b)},$$

$$\eta_f = \sum_{i=1}^{N} H_\varepsilon(\mathbf{\Phi}),\ \eta_b = \sum_{i=1}^{N} 1 - H_\varepsilon(\mathbf{\Phi}) \text{ and } \mathbf{\Phi} = \mathbf{\Phi}(\mathbf{x}_i).$$

over all N pixel. The pixel-wise measurement likelihood of foreground and background $P_{\{f,g\}}$ is calculated by finding the measurement value $\mathbf{y}_i$ on the pixel $\mathbf{x}_i$ in each region. The smooth heaviside function H_ε together with the level-set function $\mathbf{\Phi}$ define the weight of the P_f and P_b. The prior motion $P(\xi)$ plays a role in Kalman filtering scheme. Details for the derivation can be found in [7].

It is obvious that the maximum value of Equation (1) happens when the model is registered with a pose ξ that can best statistically express the foreground and background based on the measurement. We use Levenberg-Marquardt algorithm to optimise the non-linear function, in which the function has to be locally linearised by Taylor first-order expansion by using the Jacobian $\mathbf{J}$:

$$\mathbf{J} = \frac{\partial P(\mathbf{\Phi}|\mathbf{\Omega})}{\partial \xi} = \frac{\partial H_\varepsilon}{\partial \mathbf{\Phi}} \frac{\partial \mathbf{\Phi}}{\partial \mathbf{x}} \frac{\partial \mathbf{x}}{\partial \xi}. \quad (2)$$

III. Empirical Studies

The proposed approach is implemented in CUDA and run on the GPU in order to reach real-time performance. This means that the method can also be used for tracking a moving monocular camera in real-time.

A synthetic experiment was conducted to observe how the cost function behaves as shown in Figure 2. The pixel-wise posterior cost-function gives a very wide basin which means the registration capture range could be large. We applied Levenberg-Marquardt for optimising Eqation 1. The registration and segmentation result can be seen in Fig. 2b.

As shown in Figure 3, the classic graph-cut method fails in segmenting the entire phantom region for a real aorta image. Applying the proposed method for segmenting real images is our future work.

IV. Conclusion

We propose a method to precisely segment an object in difficult images using a prior model. For future works we will focus on using the proposed framework to register models in real fluoroscopic images with multiple sensors including electromagnetic (EM) and intravascular ultrasound (IVUS) sensor.

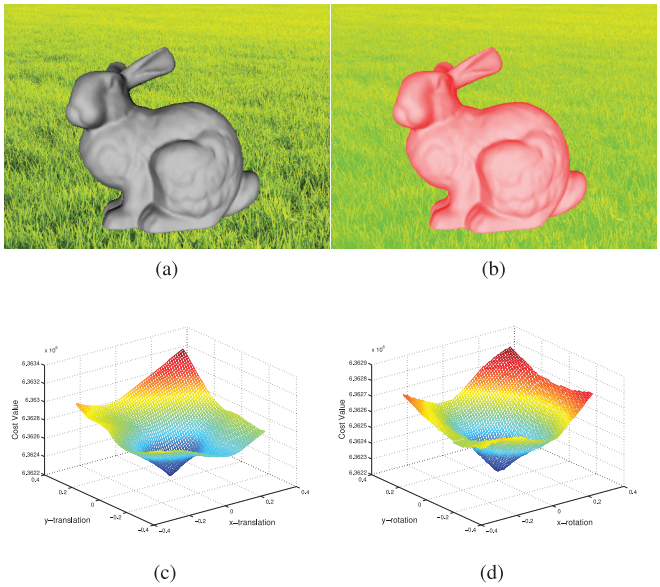

(a) (b) (c) (d)

Fig. 2: (a) The synthetic image using a non-texture Stanford bunny model and a grass image as background. (b) The segmentation result after the 3D/2D registration. By observing the $-\log\big(P(\mathbf{\Phi}|\mathbf{\Omega})\big)$ values, one can see there is a clear global minimum around the true pose (c) and (d).

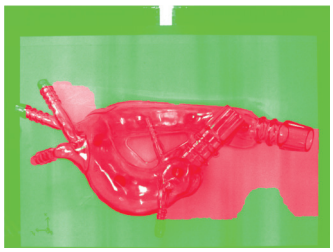

(a)

Fig. 3: The segmentation using classic graph-cut that does not give a satisfying result.

References

[1] M. Kass, A. Witkin, and D. Terzopoulos, "Snakes: Active contour models," *International Journal of Computer Vision*, vol. 1, no. 4, pp. 321–331, 1988.

[2] C. Xu and J. L. Prince, "Snakes, shapes, and gradient vector flow," *IEEE Transactions on Image Processing*, vol. 7, no. 3, pp. 359–369, 1998.

[3] C. Harris and C. Stennett, "Rapid-a video rate object tracker." in *British Machine Vision Conference*, 1990, pp. 1–6.

[4] M. Isard and A. Blake, "Condensationconditional density propagation for visual tracking," *International Journal of Computer Vision*, vol. 29, no. 1, pp. 5–28, 1998.

[5] V. A. Prisacariu and I. D. Reid, "PWP3D: Real-time segmentation and tracking of 3D objects," *International Journal of Computer Vision*, vol. 98, no. 3, pp. 335–354, 2012.

[6] M. Allan, S. Ourselin, S. Thompson, D. J. Hawkes, J. Kelly, and D. Stoyanov, "Toward detection and localization of instruments in minimally invasive surgery," *IEEE Transactions on Biomedical Engineering*, vol. 60, no. 4, pp. 1050–1058, 2013.

[7] C. Bibby and I. Reid, "Robust real-time visual tracking using pixel-wise posteriors," in *European Conference on Computer Vision*. Springer, 2008, pp. 831–844.

Feature points detector and descriptor for medical ultrasound data

Diego Dall'Alba and Paolo Fiorini
Department of Computer Science
University of Verona
Verona, Italy
diego.dallalba@univr.it

***Abstract*— Many clinical tasks are based on the detection of feature points in medical ultrasound (US) images, such as segmentation of lesion or pathological areas, estimation of organ deformation and multi-modality image registration. However obtaining reliable feature points localization is a complex task even for an expert radiologist due to the poor quality of US images. In this work, we describe a feature detector and descriptor designed for US images. The detection step is based on the phase congruency (PhC) analysis while the descriptor is based on Local Binary Pattern (LBP) operator applied to the PhC maps to improve the robustness of the proposed method. We have evaluated the proposed methods with US images subjected to synthetic transformations and comparing the results obtained with state of the art descriptors. The results of the proposed method, in terms of accuracy and precision, outperform state of the art approaches.**

Keywords*— *medical US image processing; feature detection; feature descriptor; phase congruency; local binary pattern

I. INTRODUCTION

US guided procedures are routinely performed in health facilities, starting from percutaneous interventions (e.g. biopsy) and going to computer and robotic assisted surgical procedures. As a result of physical processes responsible of image formation, the US image contrast and the resolution is lower compared to other modalities, such as magnetic resonance imaging (MRI) or Computer Tomography (CT) [1]. Furthermore, images are affected by a strong presence of non-Gaussian noise, usually referred as speckle noise, which is used in many case by clinical staff to evaluate the properties of the tissue and for the localization of structures and anatomical landmarks. Despite these difficulties, the localization of feature points in US image is an important step for different clinical tasks: tracking tissue displacement, inter-modality and multi-modality data registration [2].

Despite of the registration problems considered, point features are the input of many landmark based methods, which are usually faster and more reliable than image based registration [2]. It should be considered that correct and reliable outcome of landmark-based registration strongly depends on the correct localization of feature points and on the correct matching between points sets. Manual selection of landmarks is a time consuming and error prone process that could lead to inaccurate fusion of the data and a possible insurgence of clinical complications due to wrong assessments by the surgeon. In this scenario, automatic feature localization in the US image is a very interesting research field and some authors have applied well known methods developed for computer vision applications with encouraging results [3]. However, these methods are not designed for US data, since most of the detectors available in literature rely on image intensity and gradient maps [4]. These information are not reliable in US data, since speckle noise and image artifacts introduce significant fluctuation of the pixels values and edge localization.

In this paper, we describe a feature detector natively designed to work with US image, which considers the specific characteristic of this type of data. The detector does not rely on gradient information for the localization of salient points, instead it is based on the localization of local-maxima inside phase congruency moment maps. We are also introducing a descriptor that is based on the computation of the local binary pattern (LBP) operator over multiple scales in the region around the detected points [5].

In the next section, we describe the state of the art of feature detectors and descriptors. Next we will describe in details the proposed descriptor and detector, followed by the experimental setup description and the results. In the last part, we will discuss the test results, present our conclusions and possible future extensions of the method.

II. STATE OF THE ART

Starting from the 90's many local descriptors have been developed in the field of computer vision. One of the most successful descriptor is SIFT [6], which is based on a Gaussian scale space, where the feature points are detected as the local maxima/minima of Difference of Gaussian filters localized over multiple scales. The descriptor is based on the concatenation of local orientation histograms. SURF has been introduced as an efficient and fast alternative to SIFT and other image descriptors [7].

A pioneer approach to binary descriptor have been proposed by Calonder et al. and it is called BRIEF [8]. This descriptor is based on the local binary comparison computed on smoothed image patches. BRIEF provides a very fast processing time,

The research leading to these results has received funding from the European Union Seventh Framework Programme (FP7/2007-2013) under grant agreement no 270396 (I–SUR) and no 248960 (SAFROS).

very compact descriptor vector that speeds up also the matching step and feature matching performance comparable to other methods available, such as SIFT or SURF.

Since BRIEF only provides a method for the descriptor vector creation, many works combine this descriptor with different feature detector scheme. ORB (Oriented fast and Rotated Brief) and BRISK (Binary Robust Invariant Scalable Keypoints) combine a FAST detector [9] with BRIEF descriptor. ORB is based on an improved version of FAST able to estimate the local orientation of the point detected, then this information is used to compute the BRIEF descriptor in a rotational invariant scheme. FAST corner detector is based on binary comparisons over a circle composed of 16 sampling points to recognize interest points according to high speed and efficient testing criteria. BRISK adopts a multi-scale version of FAST and the computation of BRIEF descriptor is based on a sample point scheme derived from DAISY descriptor. FREAK extends the work of BRISK with the introduction of a binary comparison scheme inspired by the human vision system [10]. An approach that shares many details with binary descriptor is the LBP operator, used to compute binary values from a set of local comparisons between adjacent pixels [11]. LBP has been successfully applied to many different fields as local descriptor combined with a proper detector, for example combined with the SIFT detector [3].

In our work, we proposing a LPB binary descriptor combined with a phase congruency (PhC) base detector. PhC could be used as an intensity invariant feature detector, since it is based on the analysis of phase congruency of Fourier components [12]. PhC have been successfully applied in the medical context for the identification of bones fractures [13] and multi-modal image registration [4]. Once the phase congruency is computed by means of log-Gabor filters, we compute a LBP descriptor onto the local phase and local orientation maps, thus making the descriptor completely invariant to intensities changes and intrinsically invariant to image rotation. An approach similar to the one proposed in this work is described in [14], where monogenic functions are used instead of log-Gabor filter banks for the localization of feature points and uniform LBP descriptor is applied to intensity data and not to the local energy information as in our method. A local image descriptor robust to strong illumination changes is proposed in [15], where the detection is based on the response of only even component of the Gabor filter and the descriptor is based on a local statistic computed with a spatial scheme inspired by the SIFT descriptor.

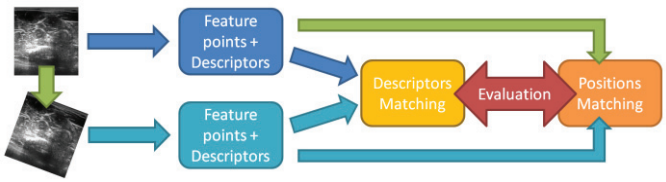

Figure 1 Scheme of the experimental evaluation procedure.

III. Method

The detector is based on the computation of PhC, according to the method proposed by Kovesi in [12]. We compute PhC based on the convolution with log-Gabor filters as proposed in the original method. All the parameters of the filter bank are selected following the guideline in [13].

We compute the map of the maximum and minimum moments for each point of the image, respectively Q and Z, and the corresponding local orientation O and the phase angles map P that maximize PhC for each point in the image.

The map Q and Z are used for the extraction of feature points by looking at the local maxima of each maps using a square window W (of dimension $w \times w$) as local search region. First, we search for local maxima in the map of the minimum moment Z, corresponding to feature with strong 2D components (spots or corners). The search is repeated over the map Q to extend the feature corresponding to edges or less localized areas. Duplicated feature points are discarded. The dimensions of the window W are twice the minimum scale used in the computation of PhC and it is the same value used for the extraction of patches centered at the detected feature points. For each feature point detected, we extract a square region W from the local orientation map O and the phase angle P independently. On these two windows, W_O and W_P respectively, we compute the uniform rotationally invariant LBP values for each point inside the window over a set of progressively decreasing dimensions of the sampling radius R but maintaining a fixed number of sampling point $N = 16$. The sampling radius used are $W/3$, $W/2$ and W.

Each pattern, computed over the entire window W, contributes to form a cumulative histogram H. The computation of the cumulative histogram is made possible by the fixed number of sampling points N, since this parameter directly affect the total number of bins in the histogram. The use on concentric sampling neighborhood has been proved effective to describe local image properties, since this scheme is used with success in recent descriptors [4].

For each window, W_O and W_P, we compute the corresponding cumulative histogram, H_O and H_P, and the concatenation of the two vectors forms the final descriptor vector D.

IV. Results

To evaluate the performance of the proposed approach, we have compared its performance with state of the art methods. In [16] a complete comparison of the available feature detector and descriptor have been performed, and SIFT and SURF prove to be an optimal choice considering the evaluation metric used.

Most of the works in literature compare the performance of the proposed method with SIFT and/or SURF, since they provide a well-known reference and enable the comparison among results obtained in different works.

Therefore we compare the performance of the proposed method with the results obtained using the SIFT and SURF

methods. We have designed an experimental setup where we consider the following synthetic in-plane transformations:

1. *Non-linear intensity shifts*: we increase or reduce the intensity of the whole image of a fixed amount s in the range ± 50, and we crop the values obtained after the transformation to the range of the original image
2. *Vertical shift*: we shift all the image rows down of a fixed amount $2 \leq v \leq 300$ and we fill the introduced gap with random generated values to avoid the detection of false feature points.
3. *Horizontal shift*: the same shifting procedure applied as in the previous transformation, but by considering a positive shift of all the columns $2 \leq h \leq 300$ of the image and by filling the gap with random generated values.
4. *In-plane rotation*: We consider an in-plane rotation of a fixed angle α in the range $\pm 90°$ around the image center.

We consider a set of K US images and for each image I_K we extract the feature point positions and relative descriptor vectors, $d(x_i, y_i),\ i \in \{0,1,\dots,F\}$, where F is the total number of detected feature points. We localize feature points and compute the descriptor with all the methods discussed: our method, SIFT and SURF. We then apply a synthetic and known transformation T to the image I_K^T and we re-apply the detector and the descriptor, obtaining a new set of vectors, referred with $d^T(x'_i, y'_i),\ i \in \{0,1,\dots,F'\}$ where (x'_i, y'_i) indicates the new position of the F' set of feature.

The known transformation T makes it possible to map the feature points extracted from original image $d(x_i, y_i)$ to the transformed locations $d(x_i^T, y_i^T)$; therefore we obtain a ground truth for the evaluation. In the ideal case of complete invariance to image transformation, our detector should be able to extract the same descriptor as in the original image in correspondence of the transformed positions, i.e. $d(x_i^T, y_i^T) = d(x_i, y_i)$. Thus, we use these mapped points as reference for computing the matching with the points extracted from the transformed image, see Fig. 1 for a schematic representation of the validation procedure.

In the experimental setup we have acquired a set of 50 US images of the left forearm of a healthy subject with a Sonix MDP device (Ultrasonix, Richmond, Canada) equipped with a linear probe (model L14-5). The depth parameter has been set to 60 mm, the frequency has been set to 5 MHz and no other parameters are changed from the standard values.

We consider each image independently and we apply all the transformations obtained by varying the parameters in the fixed range. For each pair of original and transformed images we compute the matching based only on the descriptor vectors, by using an Euclidean distance metric and a brute-forcing matching algorithm. We consider as evaluation metric the correct matching ratio (CMR), obtained as:

$$CMR = \frac{\#correct\ matching}{\#total\ detected\ feature}$$

We consider as the $\#total\ detected\ feature$ as the number of features extracted in the original image before the transformation, while we consider a $\#correct\ matching$ every time we correctly match two corresponding descriptors, $d(x'_i, y'_i)$ and $d(x_i^T, y_i^T)$.

We consider the mean CMR computed for all images and for all the transformation parameters as a measure of the accuracy of the method. The ideal descriptor invariant to all the transformations and able to handle any input image should obtain always a $CMR = 1.0$. We evaluate the precision by considering the standard deviation (STD) of the all the CMR obtained in the experiments. The optimal descriptor should obtain the smaller possible value of STD, ideally 0, that indicates matching performance independent of the input images or transformations.

V. Discussions

The results of the experiments are presented in the four plots shown in Fig. 2, one for each synthetic transformation considered. The plots represent the mean correct matching ratio as a function of the specific transformation parameter. Blue diamonds correspond to the results obtained by our proposed method, red squares correspond to SURF while green triangles correspond to SIFT. Error bars are used to visualize the STD of the CMR obtained on all the images.

Our proposed method outperforms the others in terms of both accuracy and precision for all the considered transformation type and parameter selections. We need to consider that we do not perform any pre-processing step and the matching metric considers only closest distance in the computation of the correspondence. This conditions are very challenging for SIFT and SURF descriptors, that are designed to work with low noise and high contrast images and their matching methods are based on specialized distance metric and matching strategies.

VI. Conclusion and Future works

In this work, we have introduced a feature detector and descriptor specifically designed for US data. The detector method computes the phase congruency in a US image by convolving the Fourier transform of the image with the log-Gabor wavelet over different scales and different directions. The descriptor is based on LBP operator applied to the local energy magnitude and phase angle maps extracted during the computation of phase congruency. LBP provides a compact and rotation invariant descriptor, but it is sensitive to local intensity variations. To overcome this limitation we have computed the LBP values on the local region extracted from local energy magnitude and phase angles maps, which are invariant to intensities variation, at least considering monotonic transformations. We have tested the proposed method on clinical US images, also comparing its performance in terms of accuracy and precision with the results of SIFT and SURF based methods. The results prove that the proposed method outperforms the state of the art descriptor in these very complex setups and in any condition tested but with longer

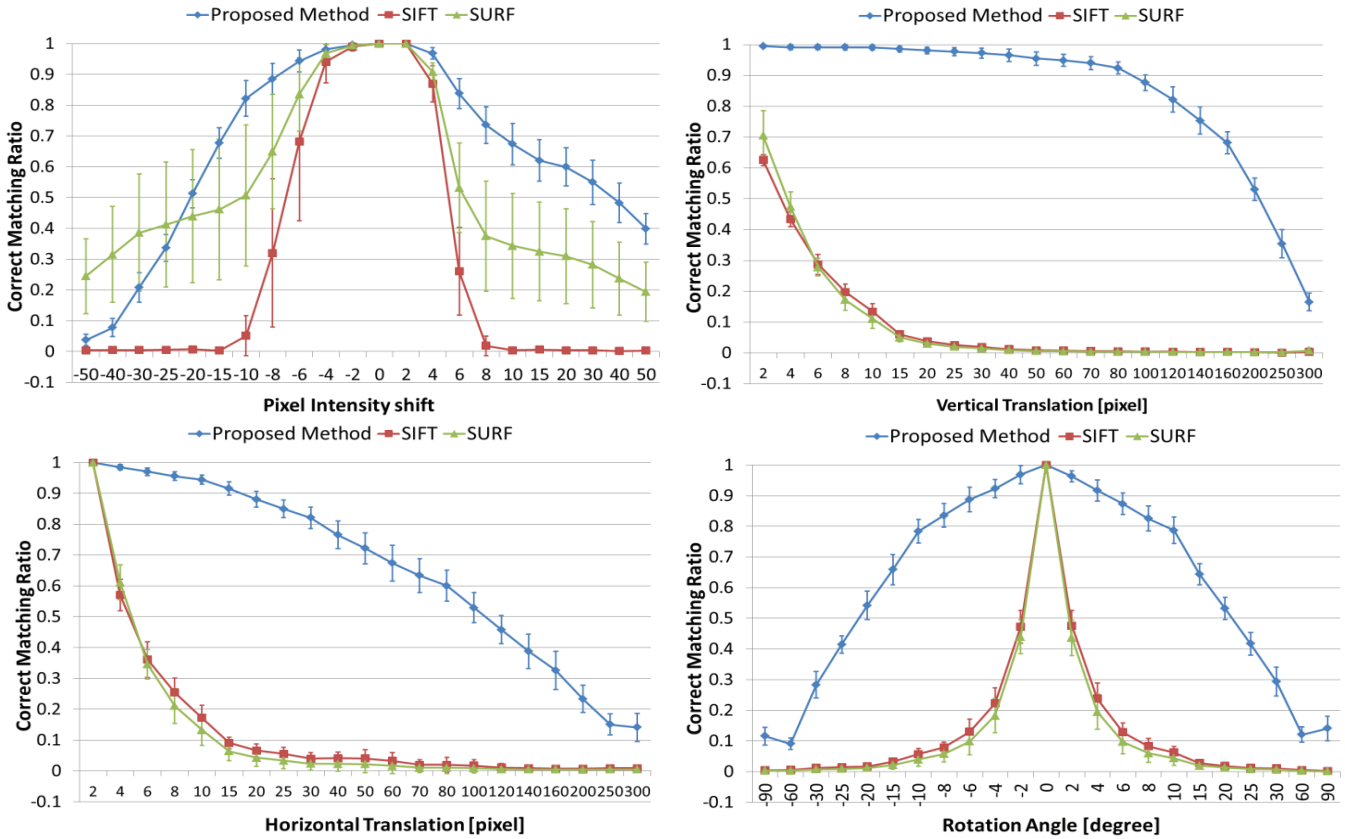

Fig. 2 Plots of the results obtained from the first experimental setup. Blue diamonds indicates the proposed method, green triangles SIFT while red squares refer to SURF. See text for more details

computation time (in the order of seconds). It should be noted that the current implementation does not provide any optimization; therefore a significant improvement in the computation time would be expected in future optimized implementations (in the order of milliseconds). In any case, this limitation is well balanced by the obtained performance, since the proposed method outperforms with great margins all the other algorithms.

Future works will focus on extending the dataset used for the experiments and improving the actual implementation in terms of execution speed by optimizing the phase congruency computation, probably with the adoption of a high performance parallel architecture, such as a graphic processing unit. A further development is to use the proposed method in combination with registration method to evaluate the applicability of this approach to the clinical problems connected to surgical navigation systems.

References

[1] I. Bankman, *Handbook of Medical Image Processing and Analysis*. Academic Press, 2008.

[2] B. Zitová and J. Flusser, "Image registration methods: a survey," *Image Vis. Comput.*, vol. 21, no. 11, pp. 977–1000, Oct. 2003.

[3] M. Heikkilä, M. Pietikäinen, and C. Schmid, "Description of Interest Regions with Center-Symmetric Local Binary Patterns," in *Computer Vision, Graphics and Image Processing*, P. K. Kalra and S. Peleg, Eds. Springer Berlin Heidelberg, 2006, pp. 58–69.

[4] T. Tuytelaars and K. Mikolajczyk, "Local Invariant Feature Detectors: A Survey," *Found Trends Comput Graph Vis*, vol. 3, no. 3, Jul. 2008.

[5] T. Ojala, M. Pietikainen, and T. Maenpaa, "Multiresolution gray-scale and rotation invariant texture classification with local binary patterns," *IEEE Trans. Pattern Anal. Mach. Intell.*, pp. 971–987, Jul. 2002.

[6] D. G. Lowe, "Distinctive Image Features from Scale-Invariant Keypoints," *Int. J. Comput. Vis.*, vol. 60, pp. 91–110, Nov. 2004.

[7] H. Bay, T. Tuytelaars, and L. V. Gool, "SURF: Speeded Up Robust Features," in *Computer Vision – ECCV 2006*, A. Leonardis, H. Bischof, and A. Pinz, Eds. Springer Berlin Heidelberg, 2006,

[8] M. Calonder, V. Lepetit, M. Özuysal, T. Trzcinski, C. Strecha, and P. Fua, *BRIEF: Computing a local binary descriptor very fast*. .

[9] E. Rosten and T. Drummond, "Fusing points and lines for high performance tracking," in *Tenth IEEE International Conference on Computer Vision, 2005. ICCV 2005*, 2005, vol. 2, pp. 1508–1515

[10] P. Vandergheynst, R. Ortiz, and A. Alahi, "FREAK: Fast Retina Keypoint," in *2013 IEEE Conference on Computer Vision and Pattern Recognition*, Los Alamitos, CA, USA, 2012, vol. 0, pp. 510–517.

[11] M. Pietikäinen, A. Hadid, G. Zhao, and T. Ahonen, "Local Binary Patterns for Still Images," in *Computer Vision Using Local Binary Patterns*, Springer London, 2011, pp. 13–47.

[12] P. Kovesi, "Phase congruency detects corners and edges," *Sch. Comput. Sci. Softw. Eng.*, 2003.

[13] I. Hacihaliloglu, R. Abugharbieh, A. J. Hodgson, and R. N. Rohling, "Automatic adaptive parameterization in local phase feature-based bone segmentation in ultrasound," *Ultrasound Med. Biol.*, vol. 37, no. 10, pp. 1689–1703, Oct. 2011.

[14] L. Zhang, D. Zhang, Z. Guo, and D. Zhang, "Monogenic-LBP: A new approach for rotation invariant texture classification," in *2010 17th IEEE International Conference on Image Processing (ICIP)*, 2010

[15] S. Zambanini and M. Kampel, "A Local Image Descriptor Robust to Illumination Changes," in *Image Analysis*, J.-K. Kämäräinen and M. Koskela, Eds. Springer Berlin Heidelberg, 2013, pp. 11–21.

[16] K. Mikolajczyk and C. Schmid, "A performance evaluation of local descriptors," *IEEE Trans. Pattern Anal. Mach. Intell.*, vol. 27, no. 10, pp. 1615–1630, Oct. 2005

Multi atlas based segmentation approach for neurosurgery planning and guidance

P. Zaffino *, K. Fritscher † ‡, P. Raudaschl †, R. Schubert †, G. C. Sharp §, F. Amato *, M. F. Spadea *

* Department of Experimental and Clinical Medicine, Magna Graecia University of Catanzaro, Italy
† Department for Biomedical Image Analysis, UMIT, Austria
‡ Medphoton, Institute for Technology Development of Radiotherapy, University Hospital for Radiotherapy and Radio Oncology Salzburg, Austria
§ Department of Radiation Oncology, Massachusetts General Hospital, Harvard Medical School, USA

Keywords: Multi atlas, brain segmentation, neurosurgery guidance

***Abstract* – Neurosurgical plannining and guidance improve treatment effects while minimizing the procedure invasiveness. In this context, the accurate identification of brain's anatomical structures is a fundamental step for succesful surgery outcome. However, manual tissue identification is a time consuming process, not compatible with the clinical routine. Moreover, it suffers from inter- and intra-subjects variability, thus making weak the entire process.**

In this work, we tested a new multi atlas based segmentation algorithm for neurosurgery applications. The algorithm is part of an open source software, Plastimatch, featuring registration and label fusion capabilities. The procedure was tested on 8 brain's structures (both left and right putamen, thalamus, hippocampus and caudate) of 20 healthy subjets. Segmentation quality was evaluated in terms of Dice Similarity Coefficient (DSC) and Hausdorff Distance (HD) between surface meshes. The ground truth was represented by manually drawn contours.

The median value of DSC was generally higher than 0.80 (with the exception of hippocampus) and HD was lower than 2 mm. The inter-quartile variability for DSC and HD ranged respectively from 0.73 to 0.95 and from 0.90 mm to 2.24 mm. In the case of hippocampus the median±quartiles for DSC and HD were 0.78±0.04 and 1.83±0.37 mm respectively. Finally, the computation time was on average 32 minutes, allowing a feasible clinical usage.

In conclusion, the proposed methodology is proved to be transferable into the clinical routine, in order to segment anatomical structures for neurosurgery planning and guidance.

INTRODUCTION

Patient specific and accurate planning is an essential step to guarantee successful neurosurgery outcome. Pre-operational information can be used to guide in real time the surgeon, in order to minimize the invasiveness of the procedure and maximize the treatment effects [1]. For this reason, the accurate identification of anatomical structures plays a fundamental role.

Manual contouring is a time consuming and operator-dependent procedure. High inter- and intra- rater variability have been reported in different applications [2, 3]. To overcome these limitations several partial and fully automatic methodologies for tissue classification have been proposed in the last years [4, 5]. The most desirable properties of this kind of procedures are simplicity, velocity, flexibility and reliability. Also, the fully automatic workflow is highly preferable to the partial one, since it minimizes the operational time.

Recently, Multi Atlas Based Segmentation (MABS) techniques have been implemented and tested to reach the mentioned aims. MABS strategies use a database of patients' images (atlases) in order to segment a new subject. Each atlas is registered on the query image and contours are warped accordingly. Eventually, using statistical approaches, the deformed labels are polished thus obtaining the final contour. In order to speed up the process, it is possible to select an optimal subset of atlases, excluding images that introduce misleading or redundant information.

In this work, we tested a new multi atlas based segmentation algorithm, Plastimatch MABS, which was recently implemented and embedded in the open source software, Plastimatch [6]. This extension exploits the image registration capabilities available in Plastimatch in order to match each atlas to the query image. Moreover, different atlas selection strategies are available, all based on image similarity estimation. We evaluated the algorithm in the framework of neurosurgical planning and guidance applications.

I. MATERIALS AND METHOD

A dataset including 20 healthy subjects was used to validate the proposed tool. For each subject, a T1-weighted magnetic resonance image of the whole head (1x1x1 mm as voxel spacing) and the manual contours of 8 brain's Volume of Interest (VOI) were available. The involved VOI were both left and right putamen, thalamus, hippocampus and caudate.

Segmentations were executed both with and without atlas-selection, to test the possibility of reducing the processing time without losing contours accuracy.

The selection of the optimal dataset was based on Normalized Mutual Information (NMI) metric [7]. For each patient, given the minimun-maximun NMI range, the acceptance value was set on a percentage threshold. Several cut-off values, ranging from 10% to 90% of the NMI range, were tested. Image background was not included in this process.

In order to maximize the statistics, a leave-one-out strategy was adopted: iteratively, a subject represented the reference volume and the remaining 19 were used as atlas. So, if no atlas selection was adopted, a total of 380 (19 x 20) cases were included in the data analysis. When atlas selection approach was used, a variable number of atlases were involved in the process.

Manual contours of the each patient were used as gold standard to validate the algorithm.

Image registration scheme consisted of a rigid alignment, followed by a deformable B-spline based stage (isotropic grid spacing equal to 10 mm, 100 iterations maximum). In order to achieve an anatomically consistent transformation, regularization strategy was also adopted [8] by setting a penalization weight for transformations that do not preserve topology. Smoothness was evaluated using the square of the vector field second derivative. Finally, a gaussian voting algorithm [9] was adopted for label fusion.

Dice Similarity coefficient (DSC) [10] was computed to quantify the morphological similarity and the overlap between two contours. DSC ranges from 0 (not overlapping structures) to 1 (perfectly identical and overlapped contours) and it was calculated using the following formula:

$$DSC = \frac{2|STRU_{auto} \cap STRU_{ref}|}{STRU_{auto} \cup STRU_{ref}} \quad (1)$$

where $STRU_{auto}$ indicates the automatic segmentation and $STRU_{ref}$ the ground truth.
To quantify the spatial mismatch between structures's surfaces, the Hausdorff distance [11] was computed between $STRU_{auto}$ and $STRU_{ref}$ at each node of their respective meshes as it follows:

$$d_p(S, S') = \max_{p \in S} d(p, S') \quad (2)$$

where d_p is the distance, evaluated at the point p, between the manual (S) and the automatic (S') contours. All the nodes belonging to reference mesh were considered and the 95th percentile of the distribution was used to quantify the spatial mismatch.

Finally, in order to assess whether or not statistical differences exists between no selection and atlas selection segmentation, Wilcoxon matched paired test was ran on DSC and distance couples. The same statistical test was executed to check the hypothesis that no difference exists between segmenting structures in the right and left lobe.

A GNU/Linux workstation equipped with an Intel Xeon CPU 2.5 GHz and 8 GB of RAM was used for the tests.

II. Results

The average time to run a full segmentation (8 structures) using the whole atlas database (19 subjects) was equal to 44 minutes. In figure 1 and in figure 2 are depicted respectively an example of 3D and of 2D segmentation.

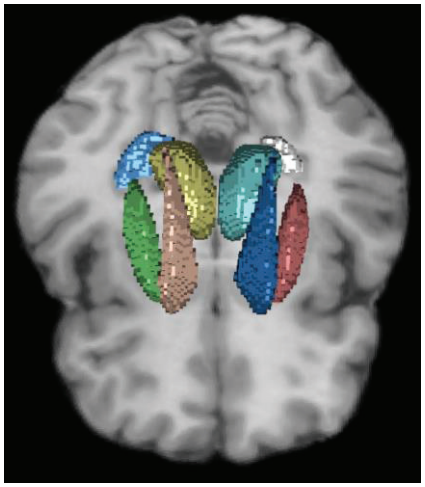

Figure 1: 3D segmentation example

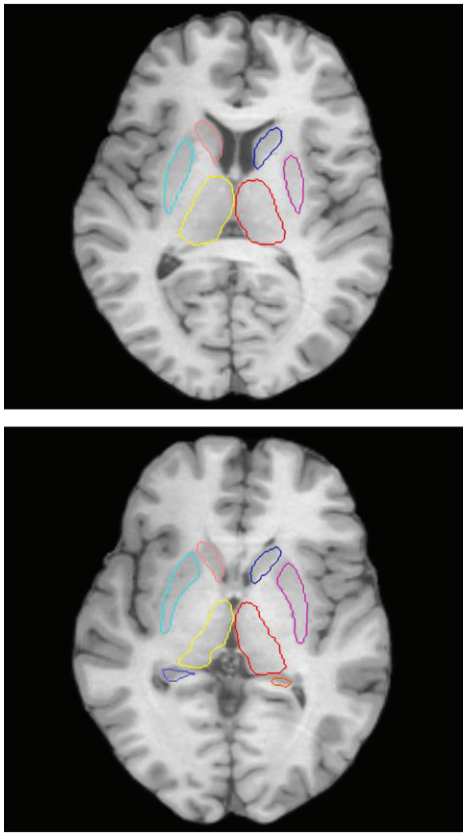

Figure 2: 2D segmentation example

For each structure DSCs and distances are respectively shown in figure 3 and in figure 4. Thalamus was the best automatically contoured structure, resulting in the highest DSC median value (0.936 left, 0.938 right) and lowest variability (0.013 left, 0.007 right). On the other hand, the worst result was obtained for hippocampus (0.784 ± 0.039 left DSC, 0.778 ± 0.042 right DSC). Distance confirmed this finding (1.00 ± 0.207 mm and 1.00 ± 0.093 mm respectively for left and right thalamus, 1.825 ± 0.368 mm and 1.825 ± 0.281 mm for left and right hippocampus)

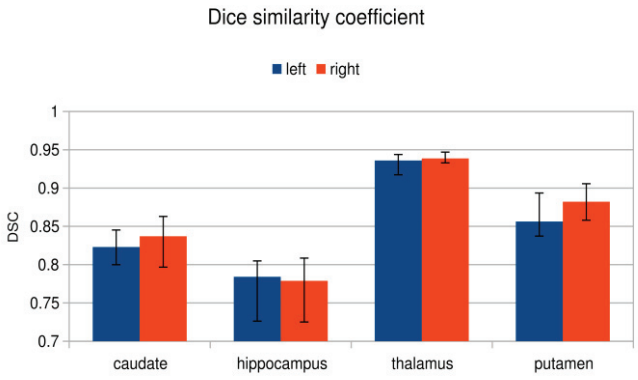

Figure 3: DSC results (median, 25th and 75th percentiles)

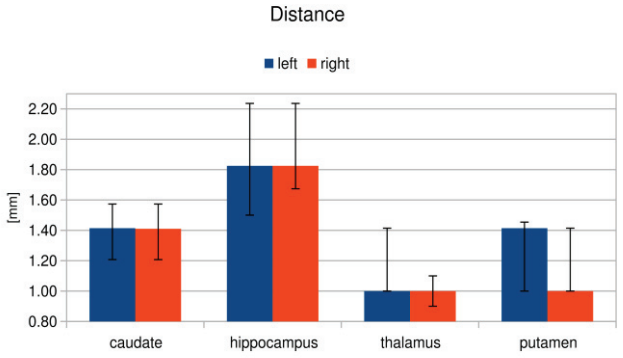

Figure 4: Distance results (median, 25th and 75th percentiles)

Atlas selection with a percentage threshold equal to 50% makes possible to reduce the computational time to an average value equal to 32 minutes without loss in segmentation accuracy (Wilcoxon p-value > 0.15).

No statistical differences in segmentation accuracy were found between equal structures located in the left and in the right side of the brain.

III. Discussion and Conclusion

In this work we described and tested Plastimatch MABS, a novel tool for automatic medical image segmentation. In particular, we evaluated the capability of the algorithm for neurosurgical planning and guidance applications.

In addition to the core features included in the classical implementation of MABS (registration and label fusion), Plastimatch MABS offers also atlas selection capabilities and high flexible voting algorithm. Each step of the workflow is highly adjustable. The parameters used in this work for registration and voting were carefully optimized for brain segmentation, as well as the strategy for atlas selection. The obtained results show good segmentations quality while the computational time allows a practical clinical usage. DSC was always greater than 0.80, except for left/right hippocampus. Distance between meshes was evaluated in the worst case, since 95th percentile was presented. Despite that, the spatial mismatch was lower than 2 mm, highlighting the accuracy of the obtained contours and in accordance with DSC result.

In addition, vector field regularization guarantees that transformations preserve the anatomical coherence, enhancing the reliability of the output contours.

By comparing the algorithm to the current state of the art, in some case we obtained more accurate segmentation [12]; in other situations, a slightly lower precision was compensated by faster processing time [13].

As in each atlas based procedure, the composition of the image database is a crucial aspect for the good performance of the algorithm. It is recommendable to have a large group of cases, representing different patients' morphologies, and select only the atlases that provide worthwhile information for the specific segmentation process. This task is accomplished by the atlas selection step that chooses the most similar atlases to the subject. As we proved in a previous work [14], NMI based selection with a percentage threshold equal to 50% allows to save time without lose segmentation quality. In case of atlas selection the number of included atlases dropped, on average from 19 to 13, speeding up the process of the 30%. Lower cut-off values gave the same results in longer time (more atlases used) while higher values quickly provided worst segmentations (fewer atlases included).

Future efforts will be focused on testing the algorithm by using other structures and improving the atlas selection algorithm. Our idea is to further refine the selection by investigating feature based selection [15].

In conclusion, we proved that Plastimatch MABS can be profitably used to segment anatomical structures for neurosurgery planning and guidance.

References

[1] R. R. Shamir, I. Tamir, E. Dabool, L. Joskowicz and Y. Shoshan.
"A method for planning safe trajectories in image-guided keyhole neurosurgery". Medical Image Computing and Computer-Assisted Intervention–MICCAI 2010, pp. 457-464.

[2] M. Filippi, M. A. Horsfield, M. Rovaris, T. Yousry, M. A. Rocca, C. Baratti et al. "Intraobserver and interobserver variability in schemes for estimating volume of brain lesions on

MR images in multiple sclerosis". American journal of neuroradiology, vol. 19, no. 2, pp. 239-244, 1998.

[3] M. Rovaris, M. Filippi, G. Calori, M. Rodegher, A. Campi, B. Colombo, and G. Comi. "Intra-observer reproducibility in measuring new putative MR markers of demyelination and axonal loss in multiple sclerosis: a comparison with conventional T2-weighted images". Journal of neurology, vol. 244, no. 4, pp. 266-270, 1997.

[4] B. Fischl, A. van der Kouwe, C. Destrieux, E. Halgren, F. Ségonne, D. H. Salat et al. "Automatically parcellating the human cerebral cortex". Cerebral cortex, vol. 14, no. 1, pp. 11-22, 2004.

[5] F. Klauschen, A. Goldman, V. Barra, A. Meyer-Lindenberg and A. Lundervold. "Evaluation of automated brain MR image segmentation and volumetry methods". Human brain mapping, vol. 30, no. 4, pp. 1310-1327, 2009.

[6] J. Shackleford, N. Shusharina, J. Verberg, G. Warmerdam, B. Winey, M. Neuner et al. "Plastimatch 1.6 – design, architecture, and future directions". Proceeding of MICCAI 2012.

[7] C. Studholme, D. L. G. Hill, and D. J. Hawkes, "An overlap invariant entropy measure of 3D medical image alignment". Pattern Recognit., vol. 32, no. 1, pp. 71–86, 1999.

[8] J. A. Shackleford, Q. Yang, A. M. Lourenço, N. Shusharina, N. Kandasamy and G. C. Sharp. "Analytic regularization of uniform cubic b-spline deformation fields". In Medical Image Computing and Computer-Assisted Intervention–MICCAI 2012, pp. 122-129.

[9] M. Sabuncu, B. Yeo, K. Van Leemput, B. Fischl and P. Golland. "A generative model for image segmentation based on label fusion" Medical Imaging, IEEE Transactions, vol 29, no. 10, pp. 1714 –1729, 2010.

[10] L. R. Dice. "Measures of the Amount of Ecologic Association Between Species" Ecology, vol. 26, no. 3, pp. 297–302, 1945.

[11] N. Aspert, D. Santa-Cruz and T. Ebrahimi. "MESH: measuring errors between surfaces using the hausdorff distance". Multimedia and Expo, 2002, ICME '02. Proceedings. 2002 IEEE International Conference, vol. 1, 2002, pp. 705 - 708.

[12] A. R. Khan, M. K. Chung and M. F. Beg. "Robust atlas-based brain segmentation using multi-structure confidence-weighted registration". Medical Image Computing and Computer-Assisted Intervention–MICCAI 2009, pp. 549-557.

[13] P. Aljabar, R. A. Heckemann, A. Hammers, J. V. Hajnal and D. Rueckert. "Multi-atlas based segmentation of brain images: atlas selection and its effect on accuracy". Neuroimage, vol. 46, no. 3, pp. 726-738, 2009.

[14] P. Zaffino, K. Fritscher, M. Peroni, M. F. Spadea, R. Schubert and G. C. Sharp. "Atlas selection strategies for multi atlas based segmentation algorithm for head and neck radiotherapy". Radioth Oncol, vol. 111 supplement 1, pp. 81-82, 2013.

[15] G. Sanroma, G. Wu, Y. Gao and D. Shen. "Learning to Rank Atlases for Multiple-Atlas Segmentation". IEEE transactions on medical imaging, 2014.

Session 2

Vision, Modeling and Control

Chair: Dr. Nikhil Deshpande, Istituto Italiano di Tecnologia

Tuesday, October 14th

11:00 – 12:00

Hybrid electromagnet model for multiple mobile coil magnetic manipulation

Baptiste Véron, Arnaud Hubert, Joël Abadie and Nicolas Andreff
FEMTO-ST Institute - UMR CNRS 6174
AS2M department (Automatic control and Micro-Mechatronic Systems)
24 rue Alain Savary, 25000 Besancon (FRANCE).
Email: firstname.name@femto-st.fr

***Abstract*—In gastroenterology, endoscopic capsules have demonstrated their usefulness for diagnosis in the small bowel. However, they also show limitations due to the impossibility to control their progress in the small bowel. Magnetic actuation is often considered to control these capsules, but current systems are very bulky and some have stability concerns. To improve the manipulability of the capsule and to reduce the size of the magnetic system, it is interesting to consider a system composed of mobile electromagnets having a ferromagnetic core. These electromagnets allow to create large efforts at lower currents, but produce a magnetic field highly non-linear. This paper proposes a hybrid model (analytical adjusted on measures) to compute the magnetic field created by the electromagnets, and discusses the usefulness of this model.**

I. INTRODUCTION

There exist several paths towards small bowel exploration. The double-balloon enteroscopy allows the visualization of some parts of the small bowel (up to the beginning of the ileum) in real time, but not the whole small bowel. The capsule endoscope is a swallowable capsule embedding a camera which allows to take pictures all along the gastrointestinal tract, but has the major drawback of only moving thanks to peristalsis.

To cope with this lack of means for small bowel diagnosis several studies tried to enhance the capabilities of the capsule endoscopes, especially to actuate the capsule and allow the control of its position. Magnetic steering is quite appropriate for that, because magnetism is a contactless effect for which body tissues are transparent. Some studies have already been led on that topic using external permanent magnets (EPM) moving around the patient to steer the capsule embedding a small permanent magnet [1]. With the same objective, the Niobe II system from Stereotaxis has also been used [2]. These approaches showed critical limitations. The impossibility of turning off the magnetic field leads to a lack of stability, and the use of an industrial robot to move the EPM, can be dangerous for the patient and the medical staff. Other studies have led to the use of static electromagnets placed around the patient similarly to an MRI system [3]. These systems are extremely bulky, they do not let the staff access to the patient, and they use a large amount of energy.

Thus, these two approches can be combined to study a light weight system composed of several mobile electromagnets. This kind of system presents many advantages, as shown in [4]. It allows full dexterity with a shorter distance between the electromagnet and the manipulated object, what reduces the heat and the energy consumption. More, it allows to easily design redundant systems to enhance the manipulability of the magnetic object and the stability. Furthermore, the bulkiness of such a system is even more reduced by the use of electromagnets composed of a winding and a ferromagnetic core. These electromagnets permit to get large effort at lower currents, but the magnetic field created is highly non-linear, what makes its precise real-time computation difficult. To overcome this, an analytical model is proposed, and its usability is discussed.

II. ELECTROMAGNETIC MODELING

The magnetic efforts are computed via the magnetic field $\boldsymbol{B}$ produced by a magnetic source :

$$\begin{aligned} \boldsymbol{F_m} &= V \cdot \boldsymbol{\nabla}\left(\boldsymbol{M} \cdot \boldsymbol{B}(\boldsymbol{P})\right) \\ \boldsymbol{C_m} &= V \cdot \boldsymbol{M} \wedge \boldsymbol{B}(\boldsymbol{P}) \end{aligned}$$

where V is the volume of the permanent magnet, $\boldsymbol{\nabla}$ is the gradient operator and $\wedge$ is the cross-product.

For electromagnets, three methods are commonly used to compute this magnetic field. The first method is to measure and to map the magnetic field over the whole workspace. The accuracy of this method relies on the precision and the number of measures. Its implementation is long and requires a large amount of memory to store the measures.

The second method, usually used for the design, consists in finite element modeling. This method is based on a mesh of the space, thus, it requires long computation time and a large amount of memory to store the data.

The third method is to use the well known dipole approximation :

$$\boldsymbol{B} = \frac{\mu_0}{4}\frac{I\,a^2}{r^3}\begin{pmatrix} 2\cos\theta \\ \sin\theta \\ 0 \end{pmatrix} \tag{1}$$

where μ_0 is the magnetic permeability of free space, a is the radius of a loop, I the current flowing in this turn, and (r, θ, φ) are the spherical coordinates where $\boldsymbol{B}$ is computed.

This analytical formula is only valid on some parts of the space around the electromagnet (for $r \gg a$) and does not take the ferromagnetic core into account. This greatly limits its use.

None of the existing models for computing $\boldsymbol{B}$ (mapping, finite elements, dipole approximation) satisfy the contradictory requirements of accuracy and real-time computation.

Actually, $\boldsymbol{B}$ is the curl of the vector potential $\boldsymbol{A}$: $\boldsymbol{B} = \boldsymbol{\nabla} \wedge \boldsymbol{A}$. In spherical coordinates, $\boldsymbol{A} = (A_r \ A_\theta \ A_\varphi)^T$ of one current loop has only one component :

$$A_\varphi = \frac{\mu_0}{4\pi} \frac{4Ia}{\sqrt{a^2 + r^2 + 2ar\sin\theta}} \left(\frac{(2-k^2)K(k) - 2E(k)}{k^2} \right) \quad (2)$$

where $K(k)$ and $E(k)$ are respectively the complete elliptic integrals of first and second order, for which k is defined as :

$$k^2 = \frac{4ar\sin\theta}{a^2 + r^2 + 2ar\sin\theta}$$

This allows to compute the magnetic field created by the winding by summing the contribution of each turn. To be taken into account, the ferromagnetic core is considered as a magnetic dipole located at the center of the coil, its magnetization depending on the current flowing in the coil. Thus, we propose to model the field generated by the coil and the core as a linear combination of (2) and the dipole approximation (1) :

$$\boldsymbol{B} = G_1 \cdot \sum_{a_{min}}^{a_{max}} \sum_{-L/2}^{L/2} \boldsymbol{\nabla} \wedge \boldsymbol{A} + G_2 \cdot \frac{\mu_0}{4} \frac{I\,a^2}{r^3} \begin{pmatrix} 2\cos\theta \\ \sin\theta \\ 0 \end{pmatrix} \quad (3)$$

where G_1 and G_2 are introduced to adjust the relative contribution of the winding and the core. These gains depend on parameters such as the core material, its temperature, etc.

The gains are identified by magnetic measures and robust linear regression, what makes (3) a hybrid model. TABLE I shows the relevance of this model compared to the others. Because it is analytical, it does not require memory for data storage, and it alows real-time computation. More, has a good accuracy, and it is setted up quickly, with few measures to identify the gains.

	Measures	Finite element	Dipole approximation	Hybrid model
Memory used	↑↑	↑	↓↓	↓↓
Real-time	↓↓	↑↑	↓↓	↓
Set up time	↑↑	↑	↓↓	↓
Accuracy	↑↑	↑↑	↓↓	↑

TABLE I. ELECTROMAGNET MODELING METHODS

III. USABILITY OF THE MODEL TO CONTROL A SYSTEM

The first way to use (3) is to compute the efforts produced by an electromagnet at a given point, for a given current. Thereby, it is easy to verify wether a system is able to produce the expected forces over the whole workspace. For instance, a system consisting of three electromagnets rotating about a vertical axis (Fig. 1) was simulated and shown to be capable of producing an effort of $0.3N$, needed to drive a capsule in the small bowel [5], throughout its workspace with a current not exceeding $2A$ in each coil.

The second way to use (3) relies on its analytical nature, and invert it to compute the current and the position of each electromagnet to achieve a given effort. This allows to implement the control system. The system in Fig. 1 permits the manipulation of a capsule in the plane (3 DOF) and has 6 inputs (3 currents and 3 orientations). This redundant system

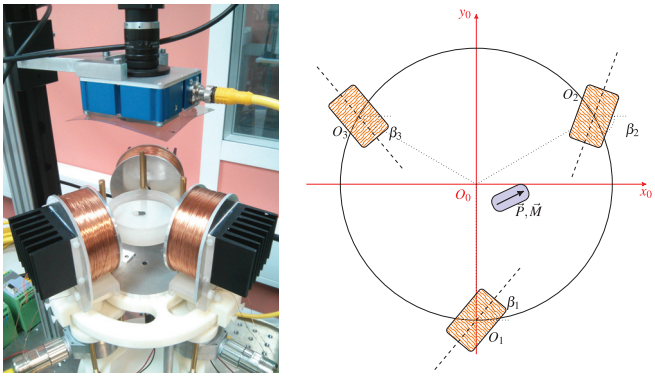

(a) (b)

Fig. 1. (a) System studied, and (b) diagram of this system (top-view).

allows to develop commands to optimize the manipulation of the capsule while optimally positioning the coils to achieve the efforts needed. This control method has been tested in simulations [6], and is now being implemented on a prototype.

An example of results obtained with such a simulation is shown on Fig. 2 and Fig. 3. In this simulation, the expected trajectory is perfectly realized with an error in position less than a tenth of a millimeter (Fig. 3(a)), and an error in orientation less than one tenth of a degree (Fig. 3(b)). Note that these simulation results were obtained by including disturbances on the detection of the capsule, the positions of the coils, and the currents in the coils.

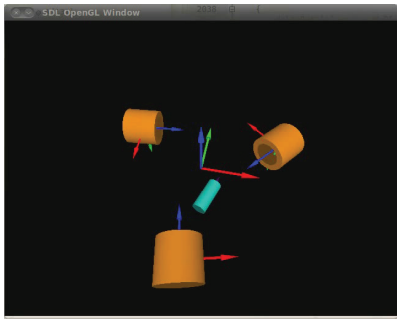

(a) Simulator.

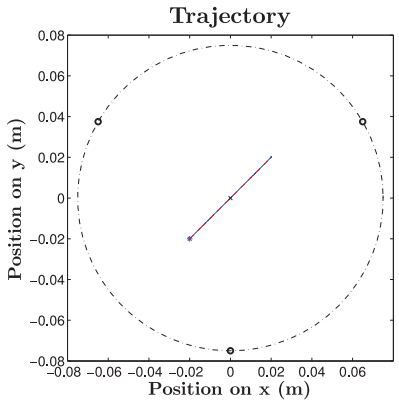

(b) Trajectory.

Fig. 2. Simulation of the system studied on a planned trajectory.

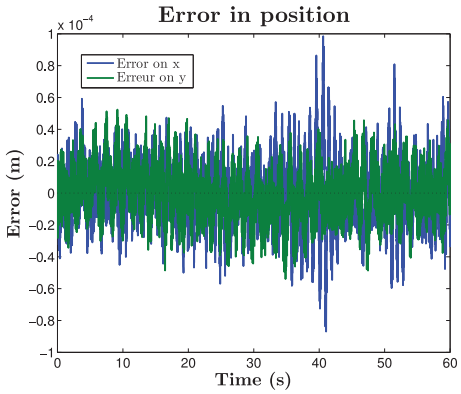

(a) Error in position.

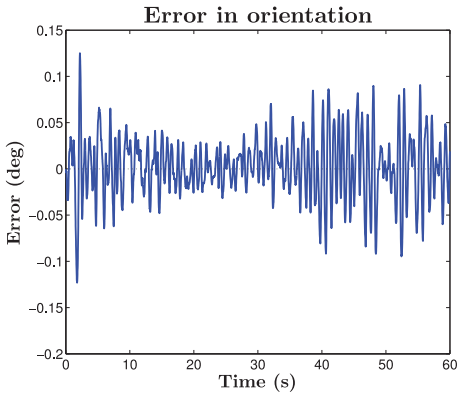

(b) Error in orientation.

Fig. 3. Errors on the position and orientation of the capsule obtained along the trajectory Fig. 2.

Furthermore, this method can be extended to more complex systems. One can imagine a system such as that shown in Fig. 4. Its configuration can be adapted to the part of the body wherein the object is manipulated, to realize the best control.

Fig. 4. Artistic view of a reconfigurable system with mobile electromagnets.

IV. Usability of the Model for Design Optimisation

From another point of view, this model can also be used to optimize the design of a system. Thanks to their high precision, finite element models are usually used for this purpose, but these calculations are time consuming, requiring to select a limited number of parameters for the optimization.

Model (3) allows faster computation while maintaining good accuracy. For example, for a single electromagnet the finite element model is extremely simple since it is reduced to an axisymmetric simulation. In this case, model (3) needs 80% less computation time. In 3D systems, computation time exponentially increases in finite element simulations. This highlights the usefulness of an analytical model for optimization of complex systems.

V. Conclusion

We have shown the importance of efforts for non-contact manipulation. Better control of these efforts ensures the manipulability of the object, which benefits both the patient whose safety is ensured, and the medician for whom the manipulation of the capsule is simplified, more reliable, and more accurate.

Electromagnets make sense when it comes to producing magnetic efforts by taking into account access to the patient by medical staff. Indeed, the system must be lightweight and not bulky, while enabling to produce efforts powerful enough to overcome any blocquage of the object (for endoscopic capsule, the passage of a sphincter for instance). The hybrid model developed here allows easy calculation of the magnetic efforts in real time, as well as the control system composed of such electromagnets. This promotes the automation of some procedures, such as navigation in the stomach before a physician performs the passing of the pylorus.

We also showed that this model allows to optimize the design of the system, ensuring that all the movements of the capsule are possible at any point of the workspace.

References

[1] G. Ciuti, P. Valdastri, A. Menciassi, and P. Dario, "Robotic magnetic steering and locomotion of capsule endoscope for diagnostic and surgical endolumial procedures," *Robotica*, vol. 28, no. 2, pp. 199–207, 2010.

[2] F. Carpi and C. Pappone, "Magnetic maneuvering of endoscopic capsules by means of a robotic navigation system," *Biomedical Engineering, IEEE Transactions on*, vol. 56, no. 5, pp. 1482–1490, May 2009.

[3] J.-F. Rey, H. Ogata, N. Hosoe, K. Ohtsuka, N. Ogata, K. Ikeda, H. Aihara, I. Pangtay, T. Hibi, S.-E. Kudo, and H. Tajiri, "Blinded nonrandomized comparative study of gastric examination with a magnetically guided capsule endoscope and standard videoendoscope," *Gastrointestinal endoscopy*, vol. 75, no. 2, pp. 373–381, 2012. [Online]. Available: http://www.sciencedirect.com/science/article/pii/S0016510711022188

[4] B. Véron, A. Hubert, J. Abadie, N. Andreff, and P. Renaud, "Advocacy for multi mobile coil magnetic manipulation in active digestiveendoscopy." in *Workshop on Magnetically Actuated Multiscale Medical Robots, International Conference on Intelligent Robots and Systems.*, 2012.

[5] X. Wang, M. Meng, and Y. Chan, "Physiological factors of the small intestine in design of active capsule endoscopy," in *Engineering in Medicine and Biology Society, 2005. IEEE-EMBS 2005. 27th Annual International Conference of the*. IEEE, 2006, pp. 2942–2945.

[6] B. Véron, A. Hubert, J. Abadie, and N. Andreff, "Geometric analysis of the singularities of a magnetic manipulation system with several mobile coils," in *Intelligent Robots and Systems (IROS), 2013 IEEE/RSJ International Conference on*. IEEE, 2013, pp. 4996–5001.

Vessel Retargeting using Intravascular Ultrasound

Angelos Karlas
The Hamlyn Centre for Robotic Surgery
Imperial College London
London, UK
a.karlas13@imperial.ac.uk

Su-Lin Lee
The Hamlyn Centre for Robotic Surgery
Imperial College London
London, UK
su-lin.lee@imperial.ac.uk

***Abstract*—Cardiovascular diseases remain one of the main causes of morbidity and mortality in the developed world. Atherosclerosis, a multifactorial disease of the vascular wall, holds by far the first place among their aetiologies. The gold standard method for setting the diagnoses and guiding any required endovascular interventions is X-ray angiography. However, this technique provides only a planar lumenogram of the vessel under investigation and additional error-prone tracking equipment (e.g., electromagnetic-based) would be required in order to achieve navigational precision. A complementary imaging technique, intravascular ultrasound, can provide additional information since it creates a cross-sectional full-range view of the artery. This study proposes a novel method of navigation during blood vessel catheterisation that relies exclusively on intravascular ultrasound data and a preoperative 3D imaging scan. The disengagement of such a system from X-ray angiography and external tracking devices constitutes the primary innovation of our project.**

Keywords—intravascular ultrasound; endovascular navigation; image guided intervention; catheterisation.

I. INTRODUCTION

Cardiovascular diseases (CVDs) constitute the most significant group of health problems in the world. Despite the considerable improvements in the fields of prevention and diagnosis, ischemic heart disease and stroke remain the number-one causes of disability (disability-adjusted life year, DALY measure [1]) or death (~50% of NCD deaths [2]) worldwide. Atherosclerosis, a complex pathological entity, is the main cause of CVDs [3]. It is characterised by the degrading deposit of heterogeneous plaques (atheromata) inside the arterial wall, resulting in localised architectural disorganisation, hemodynamic disturbances and acute clinical events.

The heterogeneity and complexity of CVDs are reflected in the variety of therapeutic schemes followed during their management. These may be conservative, interventional, surgical, or even combinations of them, while no one offers a definite and complete solution to a certain clinical case. Endovascular procedures form a set of popular interventional strategies, since >1 million cardiac catheterisation procedures are performed annually in the USA [4]. These techniques are usually associated with remarkable technical and clinical outcomes [5] and high safety levels [6]. However, there are still various complications, ranging from minor (e.g. hematoma, allergic reaction, arrhythmia etc) to major (e.g. perforation, stroke, dissection etc). In order to achieve high technical success rates and avoid complications an operator has to be precise. Procedural precision is nonnegotiable even for the most trivial lesions in terms of clinical phenotype.

Traditional clinical navigation systems are based on real-time X-ray imaging of the intralumenal blood pool via appropriate contrast agent injections. This provides clinician with planar projections of all detectable structures at any scanning direction but lacks direct three dimensional data. A major problem is that angiography uses ionising radiation (X-rays) and contrast agents which can lead to complications (e.g. allergic reactions, kidney failure etc). The images produced also illustrate a detailed description of the lumenal network but provide no clear and direct information about the vascular wall (except for the case of severe calcifications). Considering that atherosclerosis is intrawall, the accurate imaging of the vascular full diameter (lumen and wall) is a critical need.

Intravascular ultrasound (IVUS) is an invasive imaging modality that allows for the collection of full-range cross-sectional images along a vessel of interest. Its frequency-varying technical features (spatial [7] and contrast resolution [8] and tissue penetration depth [9], [10]) makes it ideal for a wide range of vascular structures. IVUS reveals significant features facilitating the quantitative and qualitative assessment of vessel anatomy [11]. The potential discrimination of three arterial wall layers (intima, media and adventitia) further enriches the tomographic lumen-wall visualisation. Accurate lumen and atheroma measurements may be performed and combined with tissue characterisation data in order to detect specific lesions and useful landmarks. The use of IVUS is associated with improved procedural success rates [12], optimised technical outcomes and reduced complications [13]. Despite its various advantages, IVUS is not very popular in everyday clinical practice (1/5 cases of intermediate coronary stenosis) [14]. One limiting factor is the current guidance of IVUS catheters, which is based on X-ray fluoroscopy; the planar projections prevent the accurate re-localisation of the IVUS catheter within the vasculature. The use of electromagnetic (EM) tracking devices may be used here but they are bulky, with relatively limited spatial range and susceptibility to exogenous EM interference [15].

In this study, we propose a novel endovascular navigation system using IVUS as its main component. The proposed implementation does not make any use of X-ray fluoroscopic data or catheter-tracking devices. The method aligns a stack of images acquired via an IVUS pullback within the vessel of

interest and registers them to a 3D vessel centreline obtained from a preoperative scan. This then provides clinicians with a map of the vessel and allows them to return to points of interest (retarget) with further IVUS images.

Revisiting an area along a vessel is a common action during an operation. Even an experienced interventionalist may need to exchange multiple wires or alter the followed strategy in order to achieve the desired support, pass through the lesion and deploy an endoprothesis. These manipulations are of great clinical importance since they may extent the procedural time (irradiation dose and contrast agent volume increase). Our system tackles this technical issue. Here, we present preliminary results of the system on a phantom setup.

II. Methods

The proposed system relies on an intraoperative IVUS pullback sequence and a preoperative CT scan of the patient's vessel. The first was used in order to create a longitudinal landmark map of the vessel while the second served as a 3D descriptor of the vascular volume. After detecting the landmark (branches, stenoses or aneurysmatic dilations) positions along the image stack, IVUS slices were fused with the CT-derived mesh model. This process resulted in a geometrically correct ultrasound-generated model of the vascular structure. Finally, this model can be used as a reference in order to extract navigation-related information. This will allow the clinician to retarget a specific point of interest during a procedure. The full system workflow can be seen in Fig.1.

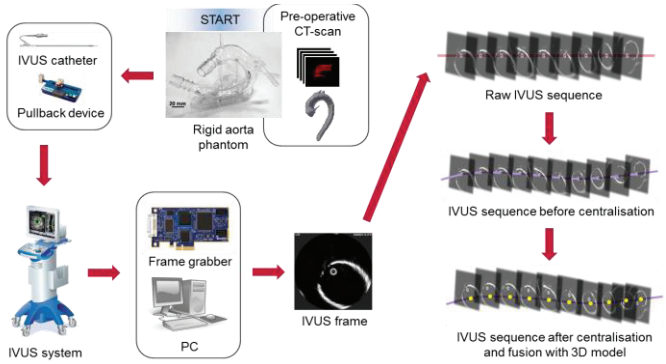

Fig.1. Full system workflow.

A. Data acquisition

For the purposes of this study, a Volcano© Visions® PV 8.2 Phased-Array Intravascular Ultrasound Imaging Catheter was used with a Volcano s5^{TM} imaging system (Volcano, San Diego, CA, USA). Firstly, the catheter was inserted in the vessel up to a predefined point. Subsequently, the catheter was smoothly withdrawn while trying to adapt to the longitudinal morphological changes of the vessel by applying rotational manipulations manually (pullback scan). Alternatively, a pullback device could be used in order to maintain a constant catheter velocity of 0.5 or 1.0 mm/sec; however, this offers only one degree of freedom which could complicate the route of the catheter's tip. Pullback scans were obtained both manually and using the pullback device of a rigid phantom of the aorta (Materialise, Leuven, Belgium) filled with warm water. A CT scan was also obtained of the phantom in a GE Innova 4100 interventional imaging system.

B. IVUS image processing

A pre-processing sequence (ROI definition, polar transform, catheter artefact removal, Cartesian retransform, local median filtering, global speckle reducing bilateral filtering [16], and contrast enhancement) was first performed on the images prior to segmentation. In this study, the absence of peripheral tissues and blood flow, as well as the structural homogeneity of the phantom vascular wall, allowed the application of a global thresholding strategy using the Otsu's method. This is a simple, fast and unsupervised two-class classifier based exclusively on lower order statistics [17]. The thresholded images were then further processed via hole-filling in order to remove textural imperfections. To remove residual noise, outlier removal based on known anatomical geometrical constraints was applied.

C. Landmark detection

Morphological landmarks are structures which: 1) can adequately describe a specific shape, 2) are present in all shapes of the same class and 3) can be easily detected [18], [19]. In our case these landmarks not only have to be effective descriptors of the vascular structure but also have to be of anatomical and clinical significance. Thus, we have first limited our landmarks search to:

- branches,
- aneurysms, and
- stenoses.

To this end, each previously processed image was used as input to an ellipse fitting algorithm [20]. Its output consisted of two elliptical curves fitted to the points of the inner and outer wall boundaries. The longitudinal fluctuations of the absolute and relative lengths of their axes can be used as indicators of a landmark presence. Their absolute lengths defined the size of the area covered by the ellipse, while their relative lengths (their fraction) formed an index of the shape of it, as this reflected the eccentricity level of the calculated ellipse.

Within this framework, it was meaningful to assume that an aneurysmatic "imprint" (without wall thinning or thickening) is characterised by a smooth crescendo-decrescendo pattern of the inner ellipses axes lengths (major and minor) while maintaining their ratio and leading to a relatively stable ellipse eccentricity index. Moreover, an atheromatic stenosis (negative concentric remodeling) can be described by a decrease-increase profile along the vessel, regarding the absolute axes lengths, in combination with invariable eccentricity. Last but not least, a branch presence was clearly reflected on a localised increase in the eccentricity index. The method also allowed for the empirical detection of a wide range of special cases (e.g. aneurysmatic dilation along with atheroma).

D. Automatic3D IVUS image registration

After segmenting the vessel of interest from the CT scan, a 3D mesh was produced which is subsequently used as a skeleton to be mapped to the corresponding IVUS image sequence. As a first step, the segmented IVUS images are transformed in order to achieve the alignment of the lumen centre to the central pixel of each image slice. This rigid transformation requires both the central point of the blood-pool area and the 3D central axis of the vessel mesh. The first was achieved through the previously described ellipse fitting technique on the pixels of the inner wall surface (endothelium). The central axis of the 3D mesh was calculated by applying a mesh thinning algorithm, *thinvox* [21], [22], part of the popular voxeliser *binvox* [23], [24].

The vessel central axis must be identified by finding and deleting any voxels belonging to skeleton branches. Considering that the centroid of a cubic voxel could be an effective descriptor of its position, this correspondence was used. Two neighbouring voxels can only be connected: 1) via a common side (four common vertices), 2) via a common edge (two common vertices) and 3) via a single common vertex. Using this information, the pathway among the given centroid set that best describes the vessel central axis was searched for.

At first, a full list of neighbours for every single voxel was created. This was based on the observation that the centroid distance between two adjacent voxels can only be equal to one of three permitted values: S, $S\sqrt{2}$ and $S\sqrt{3}$, where S is the voxel side length. Thus, a point can be characterized as "endpoint" if it has only one neighbour and "branchpoint" if it has more than three neighbours. As a next step, k-means clustering was used to partition the detected branchpoints into an optimal number of clusters, given that every junction may include multiple branchpoints. This allowed for the selection of one branch point per junction and resulted in a set of known "anchoring points" which belong to the desired central path and are either end- or branchpoints. Sorting these points along the path was critical to the success of the method. For this reason, geometrical criteria in 3D space were used to produce a list of nodes that started with an endpoint, "encapsulated" a sorted set of branch points and finished with another endpoint. Finally, a Dijkstra-based [25] directed path-search algorithm was applied in order to successively navigate from one anchoring point to the next until reaching the final endpoint. The total output path was considered to be the central axis of the vascular mesh.

After smoothing the path via a spline curve the corresponding IVUS slice patches were registered to the positions of the detected end- and branchpoints and interpolate in-between them. In this preliminary study IVUS slices were initially oriented perfectly perpendicular to the central axis.

III. Results

Fig.2 shows the results of the image processing steps following the definition of the region of interest. The output image is also centralised.

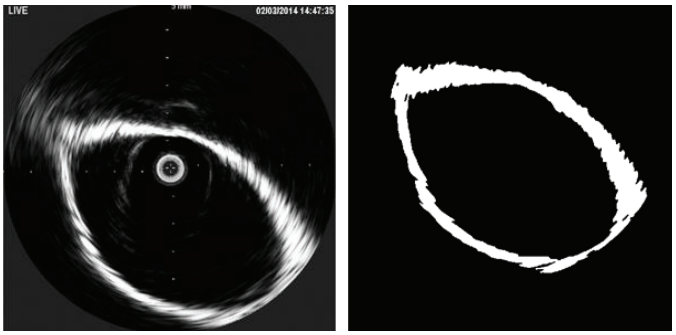

Fig.2. Image processing output. (*left: initial ROI, right: final image after processing and centre alignment).*

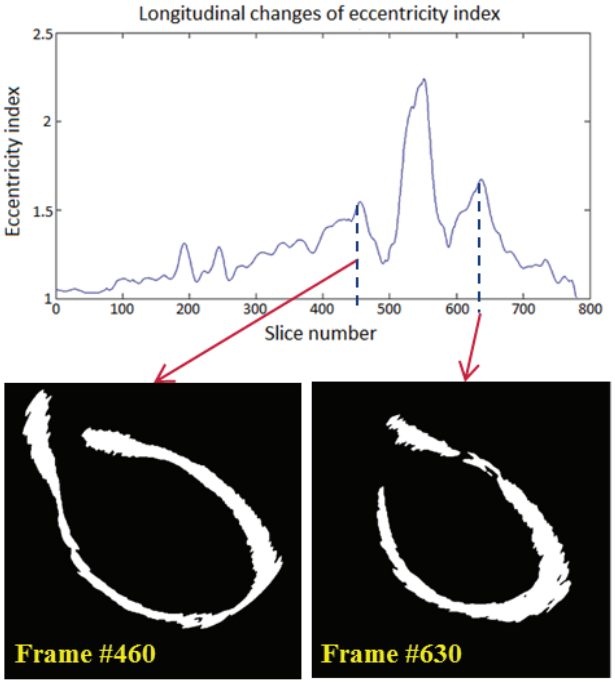

Fig.3. Longitudinal profile of eccentricity index and branch landmark detection along the catheter pullback sequence. *(Thresholded IVUS images: left-first branch of an aorta phantom, right-third branch of the same phantom).*

Fig.3 illustrates the preliminary results of the landmark detection process. The plot shows the eccentricity index (major axis/minor axis) of the inner fitted ellipse along the image stack (x-axis: number of slices). As expected, the protruding peaks correspond to positions of branches. Finally, in Fig.4 we present the output of the 3D modelling step.

IV. Discussion and Conclusion

The current preliminary system is off-line but the creation of an integrated system for endovascular navigation based exclusively on real-time IVUS image data is clearly feasible. Regarding the landmark detection step, in this preliminary implementation we allow the visual detection of each landmark by the clinician via an interactive graphical user interface. In the near future, we intend to implement a fully automatic way of landmark detection (e.g. by using the continuous wavelet transform). Furthermore, the initial results correspond to a rigid

aorta phantom where the second branch is not distinct enough. Thus, Fig.3 demonstrates a worst case scenario where a branch is misdetected either due to smooth bifurcation angle or a catheter jump during scanning.

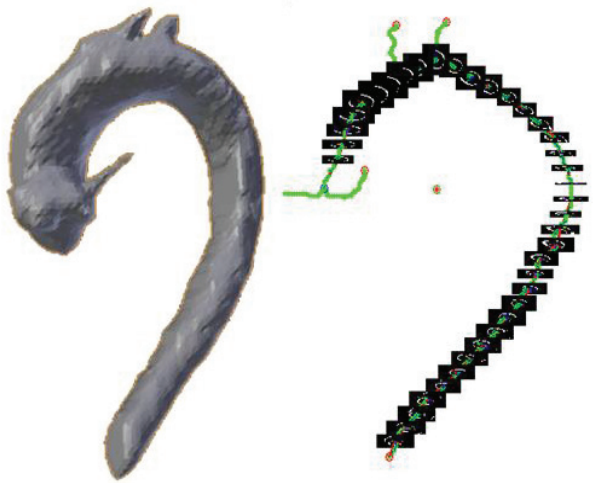

Fig.4. CT-scan derived phantom model *(left)* and preliminary fusion of the calculated vessel axis with collected IVUS data *(right)*. The red skeleton points on the right part represent automatically detected endpoints.

Currently, our initial results lack of valuable information on the catheter's tip orientation, usually provided by a 6-DOF EM tracking system. We propose a method based on the changes of the wall thickness along eight different directions of an image plane (0^o, 45^o, 90^o, 135^o, 180^o, 225^o, 270^o, and 315^o). This technique assumes that the vessel has a constant wall thickness at every point. Although it shows considerable limitations this method seems to be a logical first step towards finding an effective solution to the problem.

To conclude, we present an initial endovascular navigation system based solely on intraoperative IVUS images and a preoperative scan. This removes the need of ionizing radiation through traditional X-ray fluoroscopy and the use of nephrotoxic contrast agent to visualize the vessels. The proposed system provides clinicians with a 3D map of the vessels and allows them to retarget regions of interest. Our future work will focus on catheter tip orientation and validation with user studies.

References

[1] WHO, "The global burden of disease: 2004 update," 2008. [Online]. Available: http://www.who.int/healthinfo/global_burden_disease/2004_report_update/en/. [Accessed: 07-Aug-2014].

[2] A. Alwan, D. MacLean, and L. Riley, "Monitoring and surveillance of chronic non-communicable diseases: progress and capacity in high-burden countries," *Lancet*, 2010.

[3] J. Frostegård, "Immunity, atherosclerosis and cardiovascular disease.," *BMC Med.*, vol. 11, no. 1, p. 117, Jan. 2013.

[4] M. J. Hall, C. J. DeFrances, S. N. Williams, A. Golosinskiy, and A. Schwartzman, "National Hospital Discharge Survey: 2007 summary.," *Natl. Health Stat. Report.*, no. 29, pp. 1–20, 24, Oct. 2010.

[5] V. G. Patel, K. M. Brayton, A. Tamayo, O. Mogabgab, T. T. Michael, N. Lo, M. Alomar, D. Shorrock, D. Cipher, S. Abdullah, S. Banerjee, and E. S. Brilakis, "Angiographic success and procedural complications in patients undergoing percutaneous coronary chronic total occlusion interventions: a weighted meta-analysis of 18,061 patients from 65 studies.," *JACC. Cardiovasc. Interv.*, vol. 6, no. 2, pp. 128–36, Feb. 2013.

[6] T. Slagboom, F. Kiemeneij, G. J. Laarman, and R. van der Wieken, "Outpatient coronary angioplasty: feasible and safe.," *Catheter. Cardiovasc. Interv.*, vol. 64, no. 4, pp. 421–7, Apr. 2005.

[7] S. E. Nissen and P. Yock, "Intravascular ultrasound: novel pathophysiological insights and current clinical applications.," *Circulation*, vol. 103, no. 4, pp. 604–16, Jan. 2001.

[8] Mintz GS., *Intracoronary Ultrasound*. Taylor & Francis, 2005.

[9] N. Bom, A. F. W. van der Steen, and C. T. Lancee, "History and Principles," in *Vascular Ultrasound*, Y. Saijo and A. F. W. van der Steen, Eds. Tokyo: Springer-Verlag, 2003.

[10] N. Bom, C. T. Lancee, W. J. Gussenhoven, and W. Li et al., "Basic principles of intravascular ultrasound imaging," in *Intravascular Ultrasound Imaging*, J. M. Tobis and P. Yock, Eds. New York: Churchill Livingston Medical Publishers, 1992.

[11] G. S. Mintz, S. E. Nissen, W. D. Anderson, S. R. Bailey, R. Erbel, P. J. Fitzgerald, F. J. Pinto, K. Rosenfield, R. J. Siegel, E. M. Tuzcu, and P. G. Yock, "American College of Cardiology Clinical Expert Consensus Document on Standards for Acquisition, Measurement and Reporting of Intravascular Ultrasound Studies (IVUS). A report of the American College of Cardiology Task Force on Clinical Expert Consensus Do," *J. Am. Coll. Cardiol.*, vol. 37, no. 5, pp. 1478–92, Apr. 2001.

[12] Y. Takahashi, H. Okazaki, and K. Mizuno, "Transvenous IVUS-guided percutaneous coronary intervention for chronic total occlusion: a novel strategy.," *J. Invasive Cardiol.*, vol. 25, no. 7, pp. E143–6, Jul. 2013.

[13] H.-J. Yoon and S.-H. Hur, "Optimization of stent deployment by intravascular ultrasound.," *Korean J. Intern. Med.*, vol. 27, no. 1, pp. 30–8, Mar. 2012.

[14] P. B. Dattilo, A. Prasad, E. Honeycutt, T. Y. Wang, and J. C. Messenger, "Contemporary patterns of fractional flow reserve and intravascular ultrasound use among patients undergoing percutaneous coronary intervention in the United States: insights from the National Cardiovascular Data Registry.," *J. Am. Coll. Cardiol.*, vol. 60, no. 22, pp. 2337–9, Dec. 2012.

[15] B. J. Wood, H. Zhang, A. Durrani, N. Glossop, S. Ranjan, D. Lindisch, E. Levy, F. Banovac, J. Borgert, S. Krueger, J. Kruecker, A. Viswanathan, and K. Cleary, "Navigation with electromagnetic tracking for interventional radiology procedures: a feasibility study.," *J. Vasc. Interv. Radiol.*, vol. 16, no. 4, pp. 493–505, Apr. 2005.

[16] S. Balocco, C. Gatta, O. Pujol, J. Mauri, and P. Radeva, "SRBF: Speckle reducing bilateral filtering.," *Ultrasound Med. Biol.*, vol. 36, no. 8, pp. 1353–63, Aug. 2010.

[17] N. Otsu, "A Threshold Selection Method from Gray-Level Histograms," *IEEE Trans. Syst. Man. Cybern.*, vol. 9, no. 1, pp. 62–66, 1979.

[18] F. Bookstein, *Morphometric tools for landmark data: geometry and biology*. Cambridge University Press, 1991.

[19] S. Palaniswamy, N. A. Thacker, and C. P. Klingenberg, "Automatic identification of landmarks in digital images," *IET Comput. Vis.*, vol. 4, no. 4, p. 247, Dec. 2010.

[20] A. Fitzgibbon, M. Pilu, and R. Fisher, "Direct least square fitting of ellipses," *Pattern Anal. Mach. Intell. IEEE Trans.*, vol. 21, no. 5, pp. 476–480, 1999.

[21] K. Palágyi and A. Kuba, "Directional 3D Thinning Using 8 Subiterations," pp. 325–336, Mar. 1999.

[22] P. Min, "Thinvox. 3D Voxel Model Thinning." [Online]. Available: http://www.cs.princeton.edu/~min/thinvox/. [Accessed: 08-Sep-2014].

[23] F. S. Nooruddin and G. Turk, "Simplification and repair of polygonal models using volumetric techniques," *IEEE Trans. Vis. Comput. Graph.*, vol. 9, no. 2, pp. 191–205, Apr. 2003.

[24] P. Min, "Binvox. 3D Mesh Voxeliser." [Online]. Available: http://www.cs.princeton.edu/~min/binvox/. [Accessed: 08-Sep-2014].

[25] E. Dijkstra, "A note on two problems in connexion with graphs," *Numer. Math.*, vol. 1, no. 1, pp. 269–271, 1959.

Non-rigid Soft-Tissue Tracking Using Combined Feature and Intensity Information

Xiaofei Du
Center for Medical Image Computing
Department of Computer Science
University College London

Danail Stoyanov
Center for Medical Image Computing
Department of Computer Science
University College London

***Abstract*—During robotic-assisted MIS procedures, tissue deformation estimation plays a critical role in improving surgeon's operating capabilities in a highly dynamic environment. Traditional methods like feature-based methods or intensity-based methods have their limitations when dealing with soft-tissue or complex deformations. In our study, we used a triangular geometric mesh model and presented a hybrid method which combined the advantages of both feature and intensity information. Synthetic and *in vivo* experiment results showed that the hybrid tracking method is more robust and has improved the capability of correct convergence as a larger displacement of intra-frame occurs.**

I. Introduction

During robotic-assisted MIS procedures, tissue deformation estimation plays a critical role in improving surgeon's operating capabilities in a highly dynamic environment. Various methods for recovering tissue deformation have been widely studied, and traditional methods like feature-based methods [1], [2] or intensity-based methods [3], [4] have their limitations when dealing with soft-tissue or complex deformations. In our study, we used triangular geometric mesh model and combined the advantages of both feature and appearance information to track the tissue surface.

II. Methods

A. Triangular geometric mesh model

The non-rigid surface M to be tracked is modelled as a 2D triangular geometric mesh as shown in Fig. 1. Each triangle vertex $v = [v_x, v_y]$ is part of a state vector S, which controls the shape and motion of M. As Eq. (1) shows, any point p within M can be located via S by using its barycentric coordinates $B = (B_1, B_2, B_3)$ and the vertices of the triangle it lies within $V = (v_1, v_2, v_3)$.

$$T_S(p) = \begin{bmatrix} B_1 & B_2 & B_3 \end{bmatrix} \begin{bmatrix} v_{1x} & v_{1y} \\ v_{2x} & v_{2y} \\ v_{3x} & v_{3y} \end{bmatrix} \tag{1}$$

Based on the above triangular mesh model, we present the approach to non-rigid surface tracking in details.

B. Feature-based tracking

We used the Shi-Tomasi corner detector and Lucas-Kanade-Tomasi feature tracker to get the feature correspondences. To estimate the deformation of M given a set of feature correspondences, we minimize an energy function subject to S in Eq. (2)

$$\varepsilon(S) = \lambda \varepsilon_R(S) + \varepsilon_F(S) \tag{2}$$

where regularization energy ε_R is defined as proposed in [2] to preserve the regularity of the mesh, λ controls the regularization influence, and feature correspondence energy ε_F is defined as proposed in [5]

$$\varepsilon_F(S) = \sum_{c \in F} \rho(\|c_t - W_S(c_{t-1})\|, r)) \tag{3}$$

where ρ is the robust estimator, it uses a coarse-to-fine scheme to deal with the outliers. The energy function in Eq. (2) can be formulated into an unconstrained quadratic optimization problem, and then be solved by modified finite Newton method.

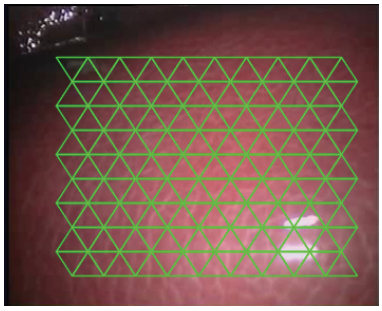

Fig. 1. Triangular geometric mesh model

C. Deformable Lucas-Kanade method

The above feature-based tracking has limitations like the sparse motion field and the reliance on salient image texture. So we add the mesh refinement step, we changed the widely-used Lucas-Kanade method [3] into deformable variation. The energy function subject to S in Eq. (4)

$$\varepsilon(S) = \eta \varepsilon_R(S) + \varepsilon_T(S) \tag{4}$$

Where ε_R represents the regularization energy, ε_T is intensity-based measure and η controls the regularization influence. To reduce the computational cost, here we use the inverse compositional variation of the algorithm.

$$\varepsilon_T(S) = \sum_p \left[T(W(p; \Delta S) - I(W(p; S))\right]^2 \tag{5}$$

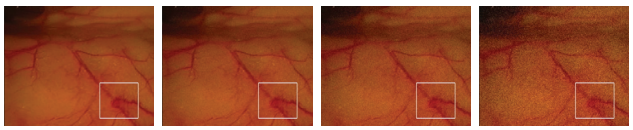

(a) (b) (c) (d)

Fig. 2. Template images with and without noise for synthetic data experiments (white box represents the tracking region): (a) noise=0%; (b) noise=5%; (c) noise=10%; (d) noise=20%

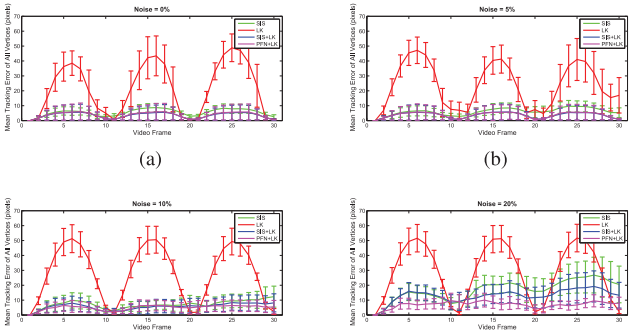

(a) (b) (c) (d)

Fig. 3. Comparison of tracking errors of the synthetic image sequence: (a) noise=0%; (b) noise=5%; (c) noise=10%; (d) noise=20%

$$W(p;S) = \begin{bmatrix} 1 & 0 & \sum_{i=1}^{3} B_i v_{ix} \\ 0 & 1 & \sum_{i=1}^{3} B_i v_{iy} \end{bmatrix} \tag{6}$$

The Lucas-Kanade method is based on the assumption that the displacement of intra-frame is small, so we use the feature tracking mesh as initial result to lead the algorithm to correct convergence.

III. Experiments and Initial Results

A. Synthetic data experiments

We generated synthetic image sequence and added different level of noise as shown in Fig. 2. The same region of interest was tracked with four different methods, including the state-of-the-art feature-based semi-implicit snake (SIS) method [2], Lucas-Kanade (LK) method and two hybrid methods. Following our idea, we combined SIS method with LK method (SIS+LK), and the other one is our proposed hybrid PFN+LK method. Then we computed the tracking error of vertex location in each frame using the ground truth.

Fig. 3 showed the tracking results, LK method fails because the displacement between frames in the synthetic sequence is too large. SIS method works better but as the noise level increased, the tracking error become larger. Among the four, the performance of the two hybrid methods are better, and even when the noise level is up to 20%, the tracking error of our proposed PFN+LK method still can maintain at an acceptable level.

B. In vivo data experiments

For evaluating the potential clinical value, experiments on recorded *in vivo* image sequence at 25 fps using DaVinci robotic platform have been conducted. We chose two sequences and manually tracked the movement of one point in each sequence, then using the results as the ground truth (GT).

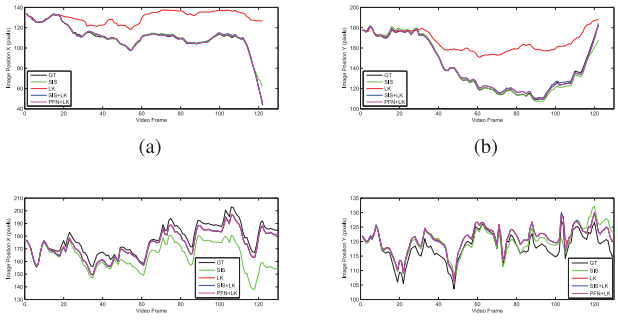

(a) (b) (c) (d)

Fig. 4. Trajectories of the tracked points along x and y axis: (a) Trajectory along x axis of point #1 from the first sequence; (b) Trajectory along y axis of point #1 from the first sequence; (c) Trajectory along x axis of point #2 from the second sequence; (d) Trajectory along y axis of point #2 from the second sequence

The bar chart on Fig. 4 shows the trajectories of the two points. For point #1, LK method lost tracking quite quickly; SIS method performed relatively well; the hybrid methods accurately tracked the points. In regards to point #2, SIS method drifted away gradually; LK method and the hybrid methods tracked the points fairly accurate. So compared to the methods which only depend on the feature or the intensity information, the hybrid methods are more robust. As for the computation speed, PFN method requires around half the iterations of SIS method, which makes it more efficient.

IV. Conclusion

In our study, we presented a hybrid tracking method which combined feature and intensity information for estimating the soft-tissue deformation. The experiment results indicate it improves the capability of correct convergence as a larger displacement of intra-frame occurs. Besides the proposed algorithm is very fast and therefore suitable for real-time application.

References

[1] D. Stoyanov, A. Rayshubskiy, and E. Hillman, "Robust registration of multispectral images of the cortical surface in neurosurgery," in *Biomedical Imaging (ISBI), 2012 9th IEEE International Symposium on*. IEEE, 2012, pp. 1643–1646.

[2] J. Pilet, V. Lepetit, and P. Fua, "Fast non-rigid surface detection, registration and realistic augmentation," *International Journal of Computer Vision*, vol. 76, no. 2, pp. 109–122, 2008.

[3] S. Baker and I. Matthews, "Lucas-kanade 20 years on: A unifying framework," *International journal of computer vision*, vol. 56, no. 3, pp. 221–255, 2004.

[4] D. Stoyanov, A. Darzi, and G. Z. Yang, "A practical approach towards accurate dense 3d depth recovery for robotic laparoscopic surgery," *Computer Aided Surgery*, vol. 10, no. 4, pp. 199–208, 2005.

[5] J. Zhu, M. R. Lyu, and T. S. Huang, "A fast 2d shape recovery approach by fusing features and appearance," *Pattern Analysis and Machine Intelligence, IEEE Transactions on*, vol. 31, no. 7, pp. 1210–1224, 2009.

A B-spline Tube Model for Catheter and Guidewire Tracking

Ping-Lin Chang*, Alexander Rolls†, Celia V Riga†, Colin D Bicknell†, and Danail Stoyanov*
*Centre for Medical Image Computing, Department of Computer Science, University College London
†Division of Surgery, Department of Surgery and Cancer, Imperial College London

***Abstract*—Catheter and guidewire tracking is an extremely difficult task due to their thin appearance, the low frame-rate and the low signal-to-noise ratio of fluoroscopy, and the presence of several similar objects in the images. To reduce the complexity of such tracking problem, we propose a deformable B-spline tube model for model-based tracking algorithms. The proposed model can precisely represent the shape of catheter and guidewire. By using the proposed model, a catheter or guidewire can be tracked using a region-based probabilistic framework which does not rely on intensity gradients and allows the use of various measurements. Preliminary results have shown that the proposed tube model can successfully fit the catheter and guidewire.**

I. Introduction

In computer assisted intervention, catheter and guidewire are two medical devices used for balloon inflation in transcatheter aortic valve implantation (TAVI). Robust catheter and guidewire tracking is essential for many applications in image guided interventions, such as real-time assessment of catheter and guidewire position and shape, visibility enhancement, and registration between 2D and 3D imaging modalities. Images that required the tracking can be various, depending on what task is performed. Some exemplar catheter and guidewire images are shown in Figure 1.

Tracking for either catheter or guidewire body is an extremely difficult task especially in real fluoroscopy. First, catheter and guidewire are thin so in the low signal-to-noise ratio fluoroscopic image, such weak and thin wire structures is barely seen. Second, catheter and guidewire exhibit large variations in their appearances, shapes and motions. The shape deformation is mainly due to a patients breathing and cardiac motions. Third, there are many other wire-like structures, such as guiding catheters and ribs. Some of the structures are close to the catheter and guidewire, which could significantly distract a tracking algorithm. A robust and flexible tracking algorithm that can deal with such dynamic environment is thus on demand.

Due to the specific characteristics of the catheter and guidewire, conventional tracking methods would encounter troubles and consequently fail, especially for the tracking algorithm based on intensity gradients [1]. Barbu et al. presented a learning-based detection method to perform tracking-by-detection scheme for guidewire localisation [2]. Since the detection has to be done in each individual frame, the kind of method is generally slow. Heibel et al. used a discrete optimisation scheme based on iterative graph-cuts for fitting a B-spline curve to guidewires [3]. Beart et al. also modelled the guidewire by using B-spline and used coherence-enhanced structures for the curve optimisation [4].

The pervious works all used B-spline for modelling the catheter and guidewire shape. To the best of our knowledge, there is yet no work using a tube structure for the representation. In this paper we propose a B-spline tube model which can precisely represent the shape of the catheter and guidewire. The tube model provides a strong regularisation during optimisation, which can significantly help avoid undesired local optimum. In addition, using a prior shape together with a probabilistic framework enables us to exploit various measurements instead of only intensity [5].

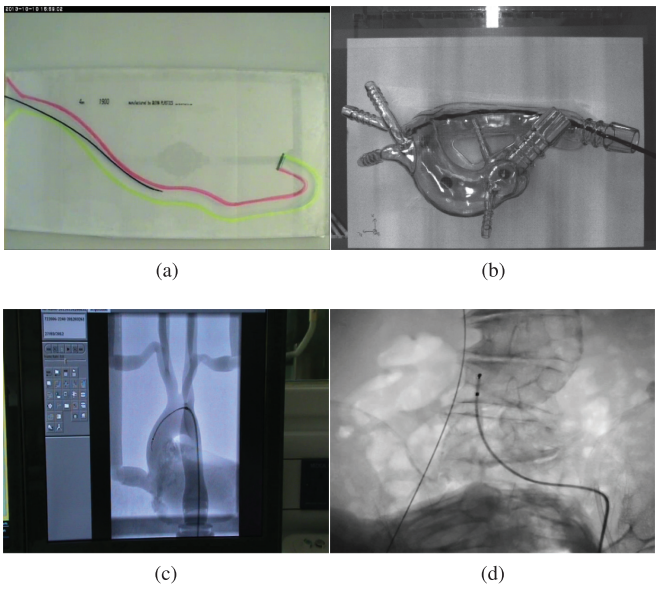

(a) (b) (c) (d)

Fig. 1: (a) TAVI training using a 2D mock-up mode. (b) A 3D mock-up model. (c) A simulation platform [6]. (d) Real fluoroscopic image.

II. Methods

A cubic B-spline is used for modelling the tube shape of guidewire and catheter. Since the thickness of a catheter and a guidewire can be different, it is important to introduce one more parameter for representing the tube radius. Figure 2 shows the concept of the proposed tube model.

A. Analytical B-spline tube model

A cubic B-spline is a class C^2 continuously differentiable function in which the curve point b is defined by the linear

combination of the set of control points $\mathbf{C}_i$ with a cubic polynomial $\mathbf{k}(t)$. That is

$$b(t) = \mathbf{k}(t)\mathbf{B}\begin{bmatrix}\mathbf{C}_{i-1}\\ \mathbf{C}_i\\ \mathbf{C}_{i+1}\\ \mathbf{C}_{i+2}\end{bmatrix}, \quad \mathbf{k}(t) = \begin{bmatrix} t^3 & t^2 & t & 1 \end{bmatrix},$$

and

$$\mathbf{B} = \frac{1}{6}\begin{bmatrix} -1 & 3 & -3 & 1\\ 3 & -6 & 3 & 0\\ -3 & 0 & 3 & 0\\ 1 & 4 & 1 & 0 \end{bmatrix}$$

The sampling parameter $t \in [0, 1]$ and the knots are found at $t = 0$. The tube contour can be further derived by

$$c(t) = r\left(\frac{\partial b}{\partial t}\right)^{\perp}, \tag{1}$$

where the r defines the tube radius and $(\cdot)^{\perp}$ is an operator for normalising a vector and converting it to its corresponding orthogonal vector.

B. Optimisation

The tracking problem is essentially modelled with a probabilistic framework in which the measurement probability distributions of foreground and background are optimised using Bayesian inference for pixel-wise posterior estimation [5]. In addition, the analytical B-spline tube model enables us to exploit the efficient Jacobian-based non-linear optimiser such as gradient descent, Gauss-Newton or Levenberg-Marquardt.

Most of previous works fit the cubic B-spline by driving the control points [2]–[4], [7]. However, since the tracking algorithm is region-based, the motion of control points cannot exactly represent the local deformation of the tube contour as they could be far away from the tube region (see Figure 2). We thus adopt a knot-driven optimisation scheme in which the update is directly applied on the region around the knots instead.

III. Preliminary Results

To validate the proposed approach, Figure 3 shows the fitting results that even when the catheter and guidewire are barely to seen, the tube model together with the probabilistic framework can successfully fit the objects. In the experiment, in addition to the image intensity, a vessel-enhanced image is also employed as a measurement [8].

IV. Conclusion

In this paper we proposed a B-spline tube model for fitting the catheter and guidewire shape. The model is further used for tracking the catheter and guidewire using a region-based probabilistic framework. Preliminary results have shown the proposed tube model is promising in robust tracking in difficult images.

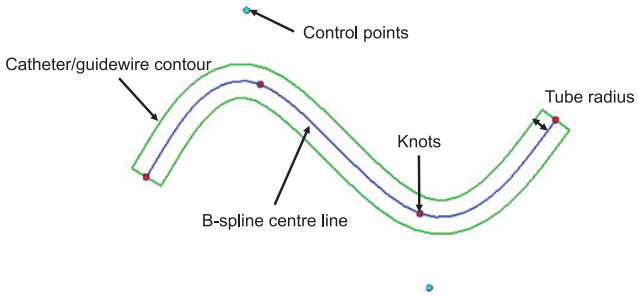

Fig. 2: The proposed B-spline tube model.

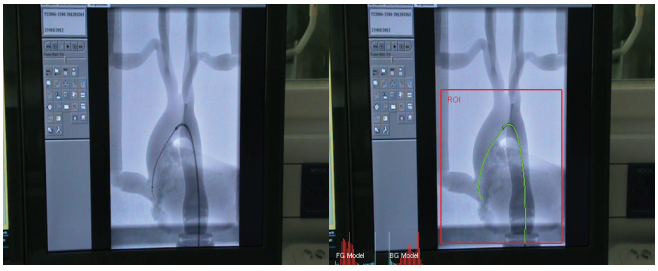

(a) (b)

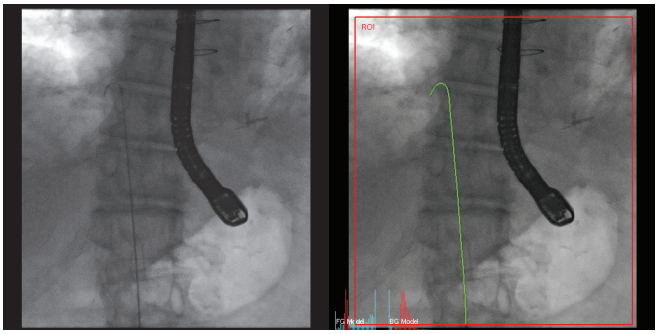

(c) (d)

Fig. 3: The results (c) and (d) of fitting the proposed tube model using the region-based probabilistic framework in difficult images (a) and (b). The green B-spline tube models are fitted with measurements using image intensity (red histogram) and Frangi filtering magnitude (cyan histogram) inside the ROIs. The histograms show that the foreground and background statistical model indeed has distinctive probability distribution. The figure is best viewed on screen with colour and zoom-in.

References

[1] M. Kass, A. Witkin, and D. Terzopoulos, "Snakes: Active contour models," *International Journal of Computer Vision*, vol. 1, no. 4, pp. 321–331, 1988.

[2] A. Barbu, V. Athitsos, B. Georgescu, S. Boehm, P. Durlak, and D. Comaniciu, "Hierarchical learning of curves application to guidewire localization in fluoroscopy," in *IEEE Conference on Computer Vision and Pattern Recognition*, 2007, pp. 1–8.

[3] H. Heibel, B. Glocker, M. Groher, M. Pfister, and N. Navab, "Interventional tool tracking using discrete optimization," *IEEE Transactions on Medical Imaging*, vol. 32, no. 3, pp. 544–555, 2013.

[4] S. A. Baert, M. A. Viergever, and W. J. Niessen, "Guide-wire tracking during endovascular interventions," *IEEE Transactions on Medical Imaging*, vol. 22, no. 8, pp. 965–972, 2003.

[5] C. Bibby and I. Reid, “Robust real-time visual tracking using pixel-wise posteriors,” in *European Conference on Computer Vision*, 2008, pp. 831–844.

[6] A. Rolls, C. Riga, C. Bicknell, D. Stoyanov, C. Shah, I. Van Herzeele, M. Hamady, and N. Cheshire, “A pilot study of video-motion analysis in endovascular surgery: development of real-time discriminatory skill metrics,” *European Journal of Vascular and Endovascular Surgery*, vol. 45, no. 5, pp. 509–515, 2013.

[7] P. Wang, T. Chen, Y. Zhu, W. Zhang, S. K. Zhou, and D. Comaniciu, “Robust guidewire tracking in fluoroscopy,” in *IEEE Conference on Computer Vision and Pattern Recognition (CVPR)*, 2009, pp. 691–698.

[8] A. F. Frangi, W. J. Niessen, K. L. Vincken, and M. A. Viergever, “Multiscale vessel enhancement filtering,” in *Medical Image Computing and Computer-Assisted Intervention (MICCAI)*, 1998, pp. 130–137.

Session 3

Active Guidance & Assistance

Chair: Dr. Elena De Momi, Politecnico di Milano

Tuesday, October 14th

13:45 – 15:00

Third arm for surgeon: Embodiment and Control

Elahe Abdi,
Robotics Lab LSRO
EPFL Lausanne
Switzerland

Mohamed Bouri
Robotics Lab LSRO
EPFL Lausanne
Switzerland

Etienne Burdet
Dept of Bioengineering
Imperial College of
Science Techn. & Medic.
London, UK

Hannes Bleuler
Robotics Lab LSRO
EPFL Lausanne
Switzerland

***Abstract*—The need of teamwork can be the source of error in different types of surgery. A third robotic arm under the surgeon's full control may improve his/her dexterity. This paper introduces two different experimental setups to study the possibility of having such an arm and the appropriate control strategy. The process of embodiment of the third arm and the learning curve of the subjects are also investigated.**

Keywords— Third arm, telemanipulator, embodiment, virtual reality, haptics, robotic surgery

I. Introduction

The idea of supernumerary limbs which can improve the power and dexterity of the user has been present in science-fiction movies and stories for a long time. A supernumerary arm may especially be useful for surgeons who should perform tiresome, repeated and long lasting tasks during the surgery. In the majority of cases they need one or more assistants to hold the surgical instruments, hand them the required tools and assist in performing the tasks that are not possible to be done single handed. This issue is more obvious in some special kinds of surgery such as laparoscopic surgery and microsurgery. Previous studies [1] have shown that communication and information flow between the surgeon and the surgical staff has an important role in team performance and a mistake may affect the patient safety. The need of teamwork can be the source of error especially if the assistant is novice or unfamiliar with the surgeon [2]. Novice assistants often have difficulty in positioning the camera appropriately in the 3D space, are confused with the fulcrum effect and suffer from fatigue [3]. In addition, elimination of physiological tremor - critical in microsurgery - is one of the main advantages of using a robotic arm [4].

Previous studies on embodiment and human's sense of ownership shows that our perception of peripersonal space is plastic and can be modified easily. The rubber hand illusion experiment [5] and other studies ([6],[7]) prove the possibility of having sense of ownership towards an artificial or even a virtual limb either in place of our own limbs or as an additional limb.

Such neuro-scientific studies along with the mentioned difficulties in the operational room suggest the idea of a surgeon with a third robotic arm. Such an arm may improve the autonomy and dexterity of the surgeon and make him more independent. This study thus investigates the possibility of having a third arm under natural, intuitive control of the operator's sensori-motor system. The control strategy, the appropriate level of complexity of the tasks and the necessary conditions for developing a sense of ownership towards the third arm are studied.

In the present work, we propose to use a foot as a master-input for the hand. In a first experimental setup, only two degrees of freedom (the (x,y)-coordinates of the foot position on the floor) are used as input variables.The foot is used as an interface for a variety of complex actions, such as driving a car, piloting an airplane, playing an organ or even painting and writing by amputees. Very fine motor control can be reached in such cases. In this study, we aim at investigating the possibilities of using the foot in the context of embodiment of a surgery telemanipulator.

II. Experimental Studies

Currently experiments are performed in virtual reality. Two different experimental setups are used for studying the possibility of performing tasks with three hands.

In the first setup there is only visual feedback and not force feedback. Three hands appear on the screen two of which correspond to the two real hands of the user. The third hand is controlled by the foot. The movements of the two hands and the foot are tracked by two Kinect® cameras. Thanks to a software development kit from the 3Gear company, some hand gestures and finger movements are also tracked. Since each PC can support only one tracking server, the system works in a network of two PCs.

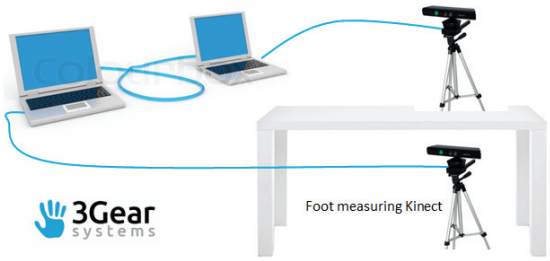

Figure 1 Setup for third arm experiment without force feedback.

The experimental paradigm consists of three games which are played in increasing order of difficulty. In every game the user has to use the three virtual hands to succeed. The first game studies the possibility of controlling the third hand by the foot. Three rectangles appear on the screen which the subject has to touch as fast as possible with the three hands.

The second game examines whether the three hands can be moved independently in different directions. The subject should move three objects in the direction of the arrows that appear on the screen. In the third game the user has to do a more complicated task. Three objects fall from top of the screen to the bottom and the objective is to catch them before reaching the ground. They fall faster as the player progresses in the game.

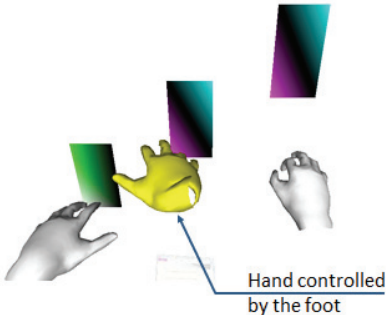

Figure 2 A screen shot of the first game without force feedback.

The second experimental setup includes both visual and force feedback. Here, three virtual spherical tools represent the two hands and the foot. Two Falcon haptic devices are used in this experiment to provide the haptic feedback. A 2D footmouse (without force feedback) tracks the foot movements. The open source CHAI 3D libraries are used for developing the virtual interface. The task is to pick up a cube with two or three spherical tools. It is obvious that holding a cube with only two spheres (two points of contact) and limited dry friction can be quite hard and requires attention and dexterity. However, doing the same task with three spherical tools is easier as the third tool improves the stability of the grip. Although the footmouse delivers no force feedback, the exerted force by the foot can be sensed indirectly through the handles at the hand feeding back the reaction forces on the cube.

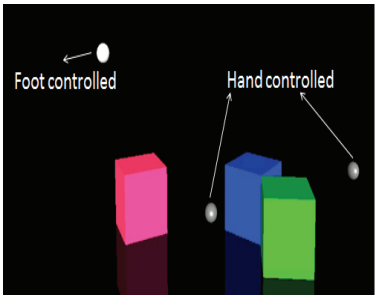

Figure 3 Top: Setup for third arm experiment with force feedback, Bottom: Screen shot of the experiment.

We are also moving towards developing a dedicated 4 DOF interface for the foot with several degrees of freedom.

III. Results

The first experimental setup (without force feedback) has already been tested with thirteen subjects. All the subjects played the three games in the same chronology from the easiest to the hardest. Each game was played at least twice. They filled a questionnaire after each game and a set of comparative questions at the end of the whole experiment. Time needed to complete each task and the number of successes and failures were recorded in each game. Results showed that it is possible to control the third arm by foot and the embodiment works naturally. Also the performance improved significantly with a few minutes of practice.

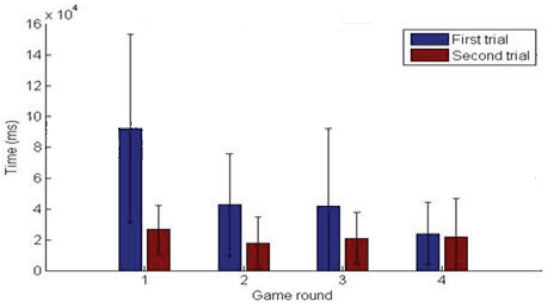

Figure 5 Average performance of all subjects in two trials of third game

Answers to the questionnaires indicated that subjects develop a sense of ownership towards the third arm as they played more. Also participants stated that in general the experiment had not been tiring for them either mentally or physically. Comparative questionnaires showed that the third game enhanced the sense of ownership towards the third arm and was more helpful in mastering the simultaneous control of three hands. This may be because of the more interactive nature of the third game. Also subjects gained some experience in the past two games and this practice might have helped them in the third game.

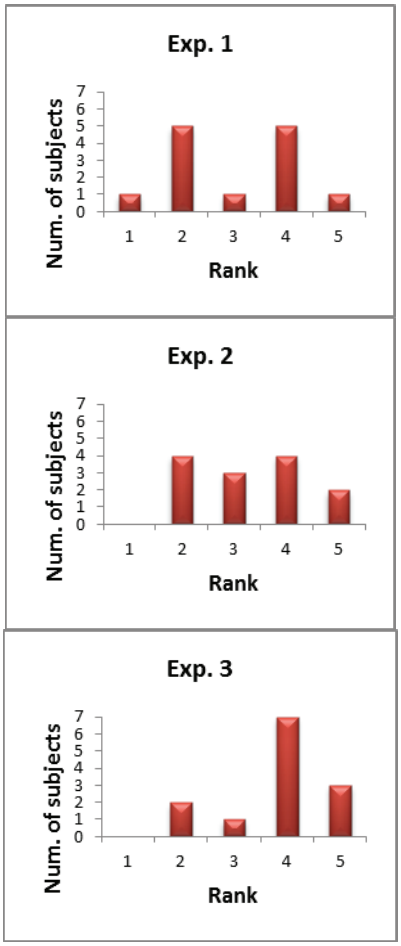

Figure 6 Questionnaire results: I felt as if the virtual third hand was my own. (1: Disagree, 5: Agree)

The second experimental setup is going to be used for future tests.

IV. Conclusion

The need of teamwork in the operational room may be the source of error and inefficiency. Providing the surgeon with a third robotic arm may improve his/her independency and dexterity. Therefore the feasibility of controlling a third arm in a natural and intuitive manner (embodiment) is investigated. Results indicate the possibility of performing tasks with three hands, one of them controlled by the foot. Surgeons already use the foot for simple tasks in conventional and robotic surgery, we are interested in the possibilities of much more complex manipulations. Questionnaire results clearly indicate the influence of practice and the development of a sense of ownership towards the third arm. This study is just the beginning of a larger project aiming at greater manipulation dexterity by merging recent advances in cognitive neuro-sciences and robotics.

We propose to introduce the name “cognetics” for this new research activity at the intersection of cognitive neurosciences and robotics.

References

[1] Lingard, L., et al., Team communications in the operating room: Talk patterns, sites of tension, and implications for novices. Academic Medicine, 2002. **77**(3): p. 232-237.

[2] Nurok, M., T.M. Sundt, and A. Frankel, Teamwork and Communication in the Operating Room: Relationship to Discrete Outcomes and Research Challenges. Anesthesiology Clinics, 2011. **29**(1): p. 1-11.

[3] Dong-Soo Kwon, S.-Y.K.a.J.K., Intelligent Laparoscopic Assistant Robot through Surgery Task Model: How to Give Intelligence to Medical Robots.

[4] Gudeloglu, A., J.V. Brahmbhatt, and S.J. Parekattil, Robotic-assisted microsurgery for an elective microsurgical practice. Seminars in plastic surgery, 2014. **28**(1): p. 11-9.

[5] Botvinick, M. and J. Cohen, Rubber hands 'feel' touch that eyes see. Nature, 1998. **391**(6669): p. 756-756.

[6] Sengul, A.v.E., M.; Rognini, G.; Aspell, J. E.; Bleuler, H.; Blanke, O., Extending the Body to Virtual Tools Using a Robotic Surgical Interface: Evidence from the Crossmodal Congruency Task. Plos One, 2012. **7**(12).

[7] Shokur, S.I., Peter; Lebedev, A. Mikhail; Bleuler, Hannes; Nicolelis, Miguel, Social interaction probed by reaching to face images: Rhesus monkeys consider a textured monkey avatar as a conspecific, in socity for Neuroscience. 2011: Washington DC, USA.

Proximal comanipulation of a minimally invasive surgery instrument to emulate distal forces

Cécile Poquet, Marie-Aude Vitrani, Guillaume Morel

I. Introduction

Virtual fixtures are geometrical constraints actively imposed by a robot to its end-effector [1], [2]. They have been conceived in the context of telemanipulation, where they were applied to a motorized master arm. In this case, they constitute an additional haptic feedback provided to the user, thus easing the slave telemanipulator control. In the present paper, virtual fixtures are considered in the context of *comanipulation*.

Comanipulation is a paradigm in which a robot and a subject simultaneously hold a tool and perform a task. A comanipulator is often used to apply virtual fixtures. A first approach consists in imposing a given geometrical equality constrain to the tool. For example the robot can impose that a given point T of the tool remains still, while the tool orientation around T is freely set by the user. In a second approach, virtual fixtures can be conceived as inequality constraints, thus separating the space into free regions and forbidden regions.

The concepts of comanipulation and virtual fixtures have received an increasing interest in the particular context of surgical robotics. Application examples of comanipulation in the domain of surgical robotics concern eye surgery [3] and orthopedic surgery [4].

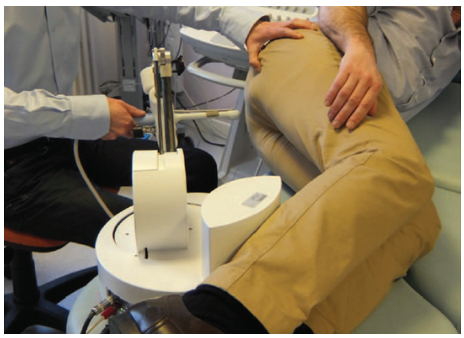

Figure 1. Comanipulating an instrument through a fulcrum: the 6 DOFs robot Apollo assists a urologist who manipulates an endorectal ultrasound probe to perform prostate biopsies, [5]

In this paper we focus on applying comanipulation and virtual fixtures in the context of so-called *key hole surgery*, as illustrated in Fig. 1. With this clinical practice, instruments are introduced into the patient's body through natural orifices or small incisions. As a result, the instrument possesses only 4 Degrees of Freedom (DOFs): three independent rotations around the incision point and one translation along the instrument longitudinal axis.

Little literature is available of force control through a fulcrum. Most of it proposes to integrate a force sensor at the distal end of the instrument and to implement a distal force closed loop controller. In the context of comanipulation, the question of force control is not limited to the distal interaction. Rather, it is required to deal with simultaneous distal (instrument-organs) and proximal (instrument-surgeon-robot) interactions, while minimizing the forces applied to the fulcrum. To our knowledge, there is no literature dealing with the control of the wrench applied by a robot to the handle of an instrument in order to produce virtual fixture to its distal end, the instrument being comanipulated through a fulcrum. Such a configuration illustrated in Fig. 1, for two different applications: prostate biopsies and endoscopic surgery.

II. Two possible control strategies

A. Problem formulation

Our aim in this paper is to evaluate how to generate distal virtual fixtures for a minimally invasive instrument comanipulated at its proximal end.

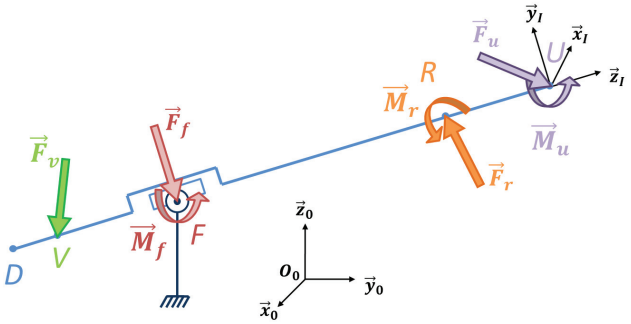

Figure 2. The robot shall apply a wrench $\{\mathscr{W}_r\}$ at point R in such a way that a user, applying a wrench $\{\mathscr{W}_u\}$ at point U feels that a force $\vec{f}_v$ was applied at point V. Meanwhile, an interaction with the entry point generates a wrench $\{\mathscr{W}_f\}$ at fulcrum F.

As depicted in Fig. 2, the instrument is modeled as a straight line joining the proximal (user) end U to the distal end D. A frame $\mathscr{F}_I = (U, \vec{x}_I, \vec{y}_I, \vec{z}_I)$, with $\vec{z}_I = (1/\|\overrightarrow{DU}\|)\overrightarrow{DU}$ is attached

Authors are with (1) Sorbonne Universités UPMC Univ. Paris 06, UMR 7222, ISIR, Paris, France, (2) INSERM, U1150, Agathe-ISIR, F-75005, Paris France, (3) CNRS, UMR 7222, ISIR, F-75005, Paris, France. Email: {poquet, vitrani, morel}@isir.upmc.fr.

This work was partly supported by the project PROSBOT funded by ANR, TECSAN 2011 program, under reference ANR-11-TECS-0017 and by french state funds managed by the ANR within the Investissements d'Avenir programme (Labex CAMI) under reference ANR-11-LABX-0004.

to the instrument. Three wrenches are applied to the instrument during a comanipulated experiment.

Firstly, the user applies a wrench denoted:

$$\{\mathscr{W}_u\} = \begin{Bmatrix} \vec{F}_u \\ \vec{M}_u \end{Bmatrix}_U , \quad (1)$$

where $\vec{F}_u$ is a vector force and $\vec{M}_u$ is a vector moment applied at proximal point U.

Secondly, the instrument interacts with the patient; the corresponding wrench, expressed at the insertion point (fulcrum F) is noted:

$$\{\mathscr{W}_f\} = \begin{Bmatrix} \vec{F}_f \\ \vec{M}_f \end{Bmatrix}_F , \quad (2)$$

where $\vec{F}_f$ is a vector force and $\vec{M}_f$ is a vector moment applied at the insertion point F.

The third wrench applied to the instrument is produced by the comanipulator. In this paper, the robot is supposed to be able to apply a controlled wrench:

$$\{\mathscr{W}_r\} = \begin{Bmatrix} \vec{F}_r \\ \vec{M}_r \end{Bmatrix}_R , \quad (3)$$

where $\vec{F}_r$ is a vector force and $\vec{M}_r$ is a vector moment applied at a given proximal point R.

The robot shall be programmed to apply virtual fixtures, *i.e.* to emulate a force $\vec{F}_v$ produced by a virtual object. In a conventional configuration, this vector force $\vec{F}_v$ should be applied at a distal point V, inside the patient, which location is also provided by the virtual fixture generator. However, in the configuration of minimally invasive surgery,the robot shall apply a wrench $\{\mathscr{W}_r\}$ at a proximal point W in such a way that the user feels that the virtual wrench $\{\mathscr{W}_v\}$:

$$\{\mathscr{W}_v\} = \begin{Bmatrix} \vec{F}_v \\ \vec{0} \end{Bmatrix}_V \quad (4)$$

has been distally applied.

It is important to notice that, from a mechanical point of view, the solution to this problem is not unique due to the presence of internal forces. We have explored two possible strategies, described hereafter.

B. Exact Wrench Computation (EWC)

An immediate way to proceed is to apply with the robot a wrench $\{\mathscr{W}_r\}$ that is equal to the wrench $\{\mathscr{W}_v\}$. This corresponds to the conventional wrench moment displacement formula:

$$\{\mathscr{W}_r\} = \begin{Bmatrix} \vec{F}_v \\ \vec{0} \end{Bmatrix}_V = \begin{Bmatrix} \vec{F}_v \\ \overrightarrow{RV} \times \vec{F}_v \end{Bmatrix}_R = \begin{Bmatrix} \vec{F}_v \\ -l_V \vec{z}_I \times \vec{F}_v \end{Bmatrix}_R \quad (5)$$

where $l_V > 0$ is defined by $l_V \vec{z}_I = \overrightarrow{VR}$.

C. Lever Model Computation (LMC)

Another possible approach consists of using the lever principle, *i.e.* balancing the distal pure force $\vec{F}_v$ with a proximal pure force $\vec{F}_r$. With this approach, the robot is controlled to apply a wrench with a null moment at point R ($\vec{M}_r = \vec{0}$). It shall balance the pure force $\vec{F}_v$ applied at point V, given the particular kinematic constraint imposed by the fulcrum.

Denoting:

$$\{\mathscr{W}_v\} = \begin{Bmatrix} F_{vx}\vec{x}_I + F_{vy}\vec{y}_I + F_{vz}\vec{z}_I \\ \vec{0} \end{Bmatrix}_V , \quad (6)$$

it is straightforward to show that the equivalent lever force applied by the robot writes:

$$\{\mathscr{W}_r\} = \begin{Bmatrix} \vec{F}_r = -\alpha F_{vx}\vec{x}_I - \alpha F_{vy}\vec{y}_I + F_{vz}\vec{z}_I \\ \vec{M}_r = \vec{0} \end{Bmatrix}_R , \quad (7)$$

where $\alpha = \frac{l_V - l_F}{l_F} > 0$ while $l_F > 0$ is defined by: $l_F \vec{z}_I = \overrightarrow{FR}$.

D. Discussion

Two ways of computing $\{\mathscr{W}_r\}$ from a given $\vec{F}_v$ virtually applied at point V are given by Eqs. (5) and (7). In theory, they are mechanically equivalent. From a perceptual point of view, the user may not feel any difference although the values of the force/moment components drastically differ: force components along $\vec{x}_I$ and $\vec{y}_I$ have opposite signs in both Equations while the moment components in Eq. (5) are zeroed in Eq. (7). However, this may result in differences in terms of forces applied at the fulcrum (internal forces). This was investigated through experiments.

III. Experiments

Experiments have been conducted in order to compare the efficiency of the two proposed approaches.

A. Experimental set-up

The comanipulator used for the experiments is a 6 active DOFs haptic device (model: Virtuose 6D - provider: Haption). Its kinematics comprises 3 first pivot joints that position a point R and a 3 joint wrist realzing a ball joint around R. Depending on the strategy to be experimented, the wrist joints will be actuated or not.It allows controlling $\{\mathscr{W}_r\}$ in open loop with a rather high precision.

A rod with a handle is connected to the robot end-effector in order to emulate a surgical tool. To emulate the patient, a dedicated apparatus has been designed and fabricated. It presents flexibility (to simulate realistic conditions) and is equipped with a force sensor measuring $\{\mathscr{W}_f\}$.

As we want to assess the efficiency of the virtual fixtures for the two proposed control laws, the space that is behind the drum is hidden by a screen. Therefore, the users cannot directly visualize the probe tip position.

Three types of virtual fixtures have been implemented for the experiments.

- Repulsive spherical region
- Repulsive plane
- Attractive line

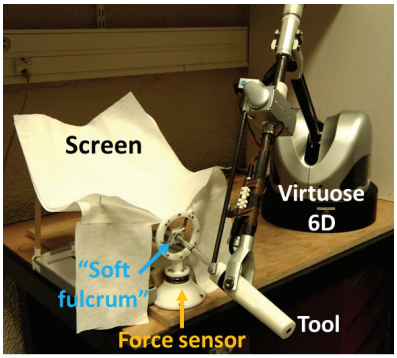

Figure 3. Experimental set-up.

B. Experimental protocol

Fourteen naive subjects have been enrolled in the study, aged 13 to 60. They had to perform 3 different exercises:

1) a Ball Sorting Out (BSO) exercise during which 4 virtual spheres with different sizes were simulated by the robot while the subjects were asked to blindly palpate them and to sort them out from the smallest one to the largest one.
2) a Plane Sorting Out (PSO) exercise during which 4 planes with identical geometry but different stiffnesses were simulated by the robot while the subjects were asked to blindly palpate them and to sort them out from the softest one to the hardest one.
3) a Line Following (LF) exercise during which they were asked to draw a straight line with the instrument tip "following the robot indication".

The general context of the study (key hole surgery) was explained to the subjects, with particular emphasis on the prostate biopsy procedure. This was aimed at making them aware that during the exercises, forces applied at the fulcrum should be minimized. Subjects were explicitly asked to pay attention to this objective during all the exercises. They had to perform each exercise twice: one trial for each controller, chosen in a random order for the three exercise, thus avoiding an influence of the learning effect on the statistical results. However, the subjects were not aware that two different controllers are being used. They were simply asked to repeat twice each exercise.

Ball sorting out (BSO) In this exercise, the subject had to put four virtual balls (randomly labeled 1, 2, 3 and 4) in order, from the smallest to the largest. These balls all had the same stiffness $K = 200 N/m$ while their radius were log-distributed: $R = \{1.5, 2.4, 3.75, 6\}\, cm$. There was only one virtual ball at a time in the workspace. The balls were directly facing the entry point. Whatever the ball size, its most proximal point was always at the same location, in such a way that the user could not distinguish balls from their locations.

The balls were presented to the subject in a random order, then the subjects were allowed to switch to a previously presented ball, as many times as they want. Once they tought they had sorted out the balls, they stopped the exercise and named the ball from the smallest to the largest.

Plane sorting out (PSO). This exercise was very similar to the previous one, except that the subjects had to order four virtual elastic planes (all located at the same place) according to their stiffness, which values are log-distributed: $K = \{200, 340, 580, 1000\}\, N/m$. Note that although palpating only one point of the plane could be enough for a subject to infer the stiffness, all the subjects decided to palpate the plane at several locations. The exercise stopped when the subjects named the plane from the softest to the stiffest.

Line following (LF). In this exercise, an initial configuration was given to the tool by the operator. The subject had then to make the tip of the tool go back and forth (3 times) on a straight line at his/her own pace. The line was horizontal but not otherwise aligned with the drum. To allow the subject for identifying the maximum and minimum penetration depth, marks were made on the tool.

C. Indicators

In order to assess the differences between EWC and LMC, several physical variables are recorded during the experiments. Among them, those that are representative of the gesture quality (forces at the fulcrum, positioning precision, movements smoothness) and the perception quality (duration and adequacy of the sorting out exercises) are used as perfromance indicators. Namely, the selected indicators are, for all the exercises:

- the task completion time t_{total}, which is the time needed by the subject to perform the exercise.
- the Spectral Arc Length SAL of the trajectories of point R as defined in [6]. SAL is the opposite of the length along the spectral curve of a movement. Not only is it an image of the complexity of the movement Fourier magnitude spectrum, but it is also dimensionless and independent of the movement magnitude and duration. Its value is negative; the closer it is to zero, the simpler the movement Fourier spectrum is and thus the smoother the movement is.
- the maximal force F_{max} applied by the tool on the fulcrum.
- the mean force F_{mean} applied by the tool on the fulcrum.

In addition, for LF exercise two precision indicators are used:

- the largest distance d_{max} from the probe tip E to the virtual line.
- the mean distance d_{mean} from the probe tip T to the virtual line.

IV. Results

Table I presents the accuracy of the subjects for the sorting out exercises: an answer is considered correct when the subject names the balls/planes in the right order and there is one inversion when the subject switches two consecutive objects.

The mean value (across subjects) for the numerical indicators are given in Fig. 4.

	BSO		PSO	
	EWC	LMC	EWC	LMC
Correct answers	7	9	6	10
Answers with one inversion	1	2	3	2
Answers with more inversions	4	1	3	0

Table I
ACCURACY OF THE SUBJECTS FOR THE SORTING OUT EXERCISES

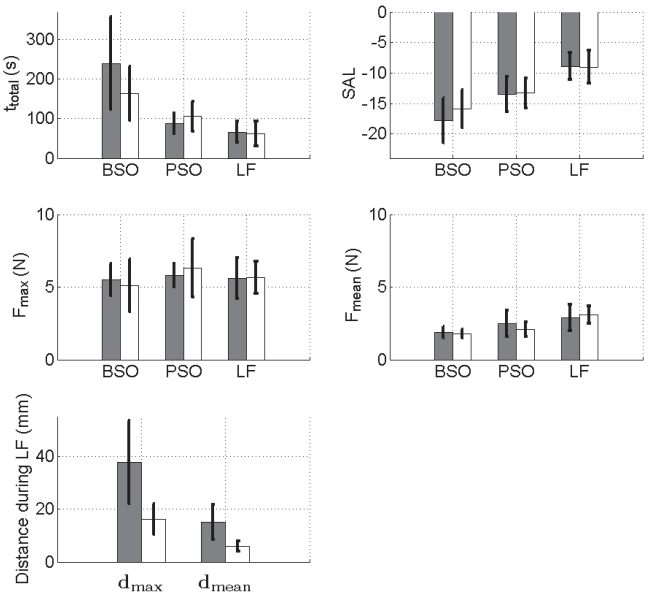

Figure 4. Value of the different indicators for each concerned exercise (gray: LMC control law; white: EWC control law; black bars: standard deviation).

A Student t-test was performed for each indicator and eligible exercise in order to quantitatively assess the comparative performances of EWC and LMC control laws. The p-values are presented in table II. Note that in general, in the literature of human motion analysis, a difference between observed mean values is said to be statistically significant when the p-value is smaller than 0.05.

	BSO	PSO	LF
t_{total}	0.064	0.199	0.692
SAL	0.189	0.851	0.912
F_{max}	0.337	0.558	0.960
F_{mean}	0.818	0.243	0.639
d_{max}	N/A	N/A	0.0001
d_{mean}	N/A	N/A	0.00007

Table II
RESULTS OF THE STUDENT T-TEST PERFORMED ON THE VARIOUS INDICATORS AND DIFFERENT EXERCISES.

V. DISCUSSION

After the exercises were completed, subjects were asked whether they felt a difference between the two repetitions of each exercise. The answers we got fall in three categories:

- one subject felt more comfortable with the LMC command but wasn't able to explain what was different from the EWC command;
- two subjects felt that the EWC command provided "more help" than the LMC command for the LF exercise, but they were not able to differentiate both commands in BSO and PSO exercises;
- ten subjects didn't realize that there was a difference between two repetitions of a given exercise.

This tends to indicate that both control laws are equivalently perceived by the subjects. Again, recall that signs of the forces have opposite signs along the lateral directions.

The p-values associated to t_{total}, *SAL*, F_{max} and F_{mean} are above 0.05 for each exercise. It means that passing from one command to the other does not have a statistically significant impact on these indicators. Most importantly, the control law was not found to influence the way the subject leans on the insertion point when performing a given task. He controls the force applied to point F in a comparable way under both studied conditions.

On the other hand, the p-values for d_{max} and d_{mean} during LF exercise are 0.0001 and 0.00007, respectively: the precision of the line following task statistically meaningfully depends on the command: the subjects follow the line with the tool tip more closely under EWC command than under LMC command. Table I shows that subjects gave better answers with the LMC command than with the EWC answers. This indicates that LMC command eases the size and stiffness discrimination.

From these observations, it is hypothesized that subjects are capable of handling the two subtasks (distal virtual contacts and fulcrum force minimization) independently. Depending on the robot controller, they clearly must apply a wrench that is different in order to minimize the fulcrum forces, which they can handle without changing their ability to interpret complimentary wrenches in terms of a distal force.

This observation has a major impact on the design of a co-manipulator for applying virtual fixtures when comanipulating through a fulcrum. Indeed, LMC control may be applied with a robot that possesses only 3 actuated DOFs and a 3 passive DOF wrist realizing a ball joint at point R.

REFERENCES

[1] J. Abbott, P. Marayong, and A. Okamura, "Haptic virtual fixtures for robot-assisted manipulation," *Robotics Research, Springer Tracts in Advanced Robotics*, vol. 28, pp. 49–64, 2007.

[2] S. Bowyer, B. Davies, and F. Rodriguez Y Baena, "Active constraints/virtual fixtures: A survey," *IEEE Transactions on Robotics*, vol. 30, pp. 138–157, 2014.

[3] B. Mitchell, J. Koo, M. Iordachita, P. Kazanzides, A. Kapoor, J. Handa, G. Hager, and R. Taylor, "Development and application of a new steady-hand manipulator for retinal surgery," in *Proc. of the 2010 IEEE Int. Conf. on Robotics and Automation (ICRA'10)*, may. 2007, pp. 623–629.

[4] M. Jakopec, F. Rodriguez y Baena, S. J. Harris, P. Gomes, J. Cobb, and B. Davies, "The hands-on orthopaedic robot "acrobot": Early clinical trials of total knee replacement surgery," *Robotics and Automation, IEEE Transactions on*, vol. 19, no. 5, pp. 902–911, 2003.

[5] C. Poquet, P. Mozer, G. Morel, and M.-A. Vitrani, "A novel comanipulation device for assisting needle placement in ultrasound guided prostate biopsies," in *IEEE/RSJ International Conference on Intelligent Robots and Systems, 2013.*, Nov. 2013, pp. 4084–4091.

[6] S. Balasubramanian, A. Melendez-Calderon, and E. Burdet, "A robuste and sensitive metric for quantifying movement smoothness," *IEEE Transactions on Biomedical Engineering*, vol. 59, no. 8, pp. 2126–2136, 2012.

Virtual Assistive System for Robotic Single Incision Laparoscopic Surgery

Veronica Penza[*†], **Jesús Ortiz**[*], **Elena De Momi**[†], **Antonello Forgione**[‡§¶], **Leonardo Mattos**[*]
[*]Department of Advanced Robotics, Istituto Italiano di Tecnologia, via Morego, 30, 16163 Genova
[†]NearLab, Department of Electronics Information and Bioengineering, Politecnico di Milano, Milano, Italy
[‡]ValueBiotech srl, Milano, Italy
[§]AIMS Academy, Milano, Italy
[¶]Ospedale Niguarda Ca' Granda, Milano, Italy

***Abstract*—Single Incision Laparoscopic Surgery (SILS) reduces the trauma of large wounds decreasing the post-operative infections, but introduces technical difficulties for the surgeon, who has to deal with at least three instruments in a single incision. These drawbacks can be overcome with the introduction of robotic arms inside the abdominal cavity, but still remain difficulties in the vision of the surgical field.**

This work is aimed at developing a system to improve the information required by the surgeon and enhance the vision during a robotic SILS. In the pre-operative phase, the segmentation and surface rendering of organs allow the surgeon to plan the surgery. During the intra-operative phase, the run-time information (tools and endoscope pose) and the pre-operative information (3D models of organs) are combined in a virtual environment. A point-based rigid registration of the virtual abdomen on the real patient creates a connection between reality and virtuality. The camera-image plane calibration allows to know at run-time the pose of the endoscopic view.

The results show how using a small set of 4 points (the minimal number of points that would be used in a real procedure) for the camera-image plane calibration and for the registration between real and virtual model of the abdomen, is enough to provide a calibration/registration accuracy within the requirements.

I. Introduction

In open surgery of the abdominal areas, the resulting wound carries the risk of infection or dehiscence and can contribute to post-operative chest infection, ileus and immobility. Minimally Invasive Surgery (MIS) can improve the physiological and immune responses associated with open surgery, reducing the trauma to a minimum [1][2]. Single Incision Laparoscopic Surgery (SILS) has been advocated as the next step towards even less invasive surgery. However, SILS introduces some limitations: the surgeon's maneuverability is reduced due to the clustering of instruments in a single access port, which increases instrument collisions. Also the surgeon has to cross the instruments during the operation to achieve triangulation for tissue retraction. Moreover, the freedom of movement of the endoscopic cameras inside the patient's body is extremely restricted due to the single port access to the inside of the patient, decreasing the number of perspectives. Thus, structures of interest, as blood vessels or cancer areas, cannot be seen from different points of view, compromising the accuracy and safety of the surgery. The operative view is also restricted and the tactile sensing reduced, resulting in a long learning curve and increased operative times [3].

These drawbacks have motivated the recent development of advanced robotic systems for SILS [3]. Robotic-assistant may be able to restore the intuitive perception of the operation field to the surgeon. The commercial systems Da Vinci® and Amadeus® have been modified with a set up for SILS. And projects like SPRINT [4] are based on the concept of single port surgery. The main difficulties for the surgeon remain the loss of depth perception, in case of monocular endoscopic camera, and the restricted field of view of the endoscopic camera (usually 70° instead of 120° of the human eyes) [5]. Another issue to be considered in single port robotic surgery is the fact that the robot could be completely inside the abdomen. In vivo devices need automatic tracking and localization systems in order to know exactly their position and to better use the potentials of the surgical tools that are completely hidden to the eyes of the surgeons.

These disadvantages can be reduced by computer technologies by enhancing the view of the surgical field [6]. Information related to the pre-operative analysis of the disease and to the planning of the surgery can be fused with the intra-operative visualization of the surgical field. This gives the surgeon all the necessary information to perform an accurate intervention. An Augmented Reality (AR) or Augmented Virtuality (AV) system allows to reduce the previously cited drawbacks and provide a more comfortable and efficient environment for the surgeon [7]. Motivated by the increasing amount of imaging data, which makes the analysis of 2D imagery obsolete, current researchers investigate efficient 3D volume rendering techniques for presenting CT or MRI data. There are multiple software packages allowing the segmentation of organs in CT/MR images and 3D modeling and visualization of patient anatomy. In [8] the authors developed an augmented reality computer guiding system combining the pre-operative 3D modeling with the intra-operative information provided by endoscopic cameras.

In this paper we propose a novel architecture for robotic SILS which easily allows the extraction of the a 3D model of the patient from a CT scan, acquired during the pre-operative planning, and the use of it during the intra-operative phase. This architecture allows the guidance of the surgical intervention improving the operative vision and the safety of the system. In this work we present a pipeline for the extraction

of the surface rendering of abdominal organs, and the development and evaluation of the intra-operative assistive system. In a first implementation, the system accuracy required by our team of surgeons has to be inferior to $10mm$, considering the motion of the organs due to heart beating and breathing. Future development has to take into account this important issue.

II. System Description

The following subsections describe the proposed virtual assistive system. In the pre-operative phase a pipeline developed in 3DSlicer [9] allows to create a virtual model of the specific patient. While in the intra-operative phase, the coexistence of virtual and real surgical environment enhances the information required by the surgeon.

A. Pre-operative Pipeline

Providing a 3D visualization of the pre-operative patient data is the first step to develop an enhanced vision system. It helps the surgeon to view the entire model of the abdomen and to identify and highlight important structures, such as main vessels or cancer areas. The extraction of such information is fundamental during the surgery. The main targets, suggested by surgeons with experience in abdominal surgery, are: liver, kidneys, spleen, gallbladder, aorta and main veins. A standardization of a workflow for segmentation and surface rendering of anatomical structures from pre-operative abdominal CT-scan was designed and developed, using already implemented modules of the open-source software 3DSlicer. The segmentation of the organs is initialized by drawing a seed on CT slices. An active contour model then evolves to segment the organ in the sagittal, coronal and axial planes [10]. The 3D surface model is computed through a marching cubes algorithm, using triangle reduction and triangle smoothing algorithms [11]. This process can be realized by a trained technician using only a few mouse clicks. An example of the different capabilities of this module is shown in Figure 1.

B. Intra-operative Virtual Environment

During the intra-operative phase, in our setup, the surgeon is performing the operation through a small incision using a robot. The arms of the robot are completely inside the abdomen and are controlled by the surgeon from a remote console. The surgeon lacks of direct visual feedback since he cannot view directly the robot arms. The feedback of the surgeon is provided only by the stereo cameras mounted on the robot. However, the field of view of the stereo-cameras is restricted with respect to the field of view of the human eyes, and the cameras show only a small portion of the surgical scene. This is not enough in case of robotic single port surgery, since single port robotic procedure requires to view the pose of the robot and of the tools with respect to the organs in order to perform surgery safely. Usually AR is proposed in order to superimpose pre-operative information on the real images, adding knowledge related to the pathology of the patient. This technique is used only in specific particular moments during the surgical procedure, because the physician

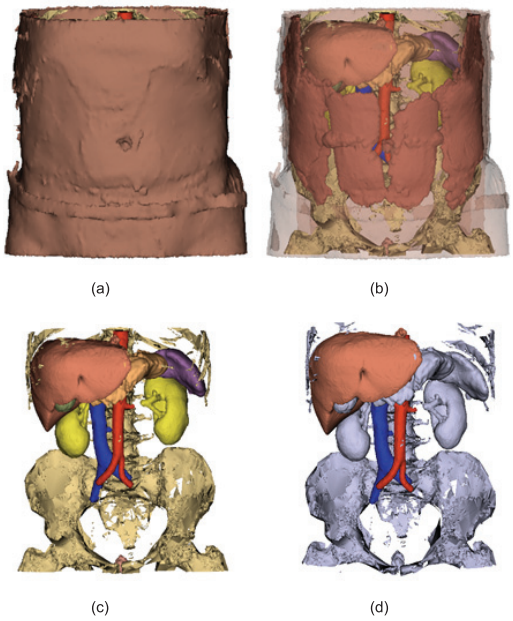

Fig. 1. Sample views of 3DSlicer showing different representations of a man abdominal model extracted from a CT scan. a) This image shows the model of the skin. b) The software allows to put the skin in transparency to visualise the internal structures. c) Representation of the internal structures with a color labeling code. d) It is also possible to highlight target structures (vein, aorta and liver).

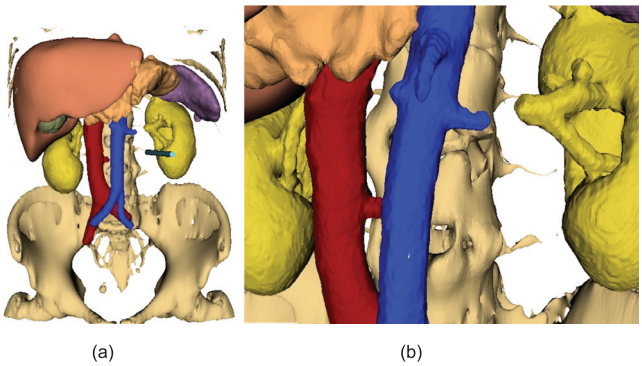

Fig. 2. This figure represents the virtual environment viewed by the surgeon during the surgical operation. a) The view of the entire abdomen makes possible to visualise at run-time the motion of the surgical tools inside a virtual abdomen patient-specific. b) The virtual camera image plane shows the structures visualized by the camera form the same point of view in the virtual environment.

prefers to work without superimposition for a long time. In our system we propose the coexistence of virtual and real environment representing the surgical scene during the entire surgery, instead of AR. It consists of two main views, showed in Figure 2:

- **view of the entire abdomen**: In this view, the reconstructed 3D patient abdomen anatomy is displayed to the surgeon intra-operatively. The system allows to add or remove structures; to rotate and translate the model in

order to view the structure of interest from different points of view; and to change the transparency of the organs to see the internal vessels or cancer areas. Moreover, the virtual robot and its camera can be added to the reconstructed patient model. If the real pose of the robot is known, the virtual model of the robot can be mapped to the real one. The surgeon views in the virtual environment the same elements of the reality navigating in the patient abdomen following its real motion.

- **view of the virtual camera**: Alongside the view of the entire abdomen, the image plane of a virtual camera is used to mimic the point of view of the real camera. In this work, we simulate the camera attached to the robot with a simple webcam, that is tracked by an optical tracker. In order to know the position of the real image plane, a *camera-image plane calibration* is computed. First, a planar chessboard is used to compute the intrinsic parameters of the camera. On the same chessboard, four points are identified both by the camera, using image processing, and by a pointer tracked by the optical tracker. Using the positions of the same corners in the reference frame $\{ImagePlane\}$ and $\{Tracker\}$ it is possible to compute the transformation $T^{ImagePlane}_{Tracker}$. But $T^{ImagePlane}_{Camera}$ still has to be known. Knowing the position of the camera in $\{Tracker\}$, the transformation $T^{ImagePlane}_{Camera}$ is computed, as shown in Equation 1. Figure 4 explains the relation between the different reference frames. In order to have correspondence between the real and virtual model, a *virtual-real 3D/3D registration* is computed. It consists in the rigid point based registration [12] of the virtual model on the real abdomen of the patient. The same fiducial landmarks are selected on the virtual model, positioning virtual fiducial points and on the real patient pointing the same landmarks with a tracked pointer, as shown in Figure 3. Using three or more points the transformation between the two model is computed and the virtual model is re-oriented. In the evaluation of the virtual assistive system we simulate a patient using a simple chessboard and we decided to use a minimum number of points in order to simulate as much as possible the real procedure executed by the surgeon during the surgery. In the real scenario, the surgeon would choose external anatomical landmarks easily identifiable.

$$T^{ImagePlane}_{Camera} = (T^{Camera}_{Tracker})^{-1} * T^{ImagePlane}_{Tracker} \quad (1)$$

III. Evaluation

The evaluation of the system is done by testing the *virtual-real 3D/3D registration* and the *camera-image plane calibration*. These procedures affect the accuracy of the guiding system.

Regarding the registration between the real and the virtual model, a virtual and real planar chessboard is used to evaluate the registration error. 12 corners are selected in $\{RealWorld\}$ using a pointer tracked by the optical tracker

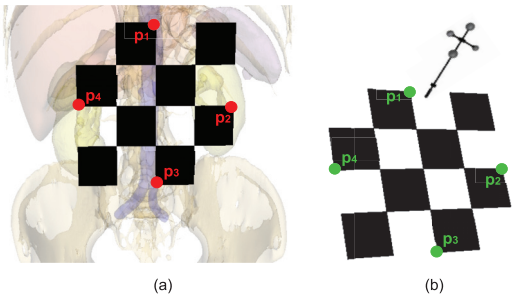

Fig. 3. a) This figure shows the virtual model of the chessboard used for the simulation of the registration process. In 3DSlicer the surgeon selects the fiducial landmarks, in this case four corners. b) The same fiducial landmarks are pointed on the real model with a pointer tracked by the Optical Tracker.

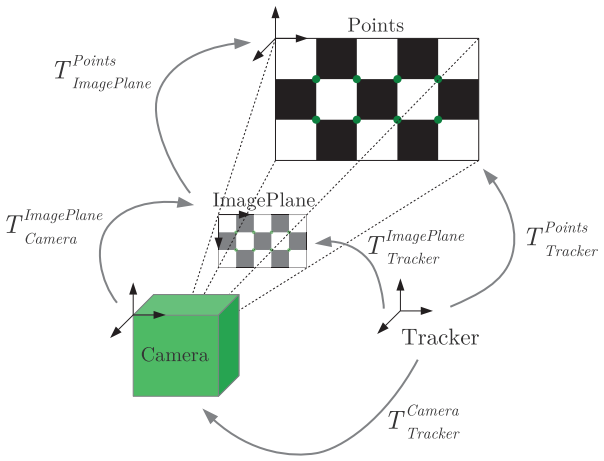

Fig. 4. Relation between the different reference frames used during the camera-image plane calibration.

and in $\{VirtualWorld\}$, adding points on the chessboard in the virtual environment. The $T^{VirtualWorld}_{RealWorld}$ is used to re-project the 12 points selected from $\{RealWorld\}$ to $\{VirtualWorld\}$. The registration error is calculated with the Root Mean Square Error (RMSE) of the point distances, as shown in Equation 2.

$$RMSE = \sqrt{\frac{\sum_{n=1}^{12}(p_x^2 + p_y^2 + p_z^2)}{n}} \quad (2)$$

In Table I we can see the results of the registration procedure, which was executed 10 times. The mean of the registration error was $4.13mm$.

TABLE I
Experimental measurements of the registration error

Trial	1	2	3	4	5
RMSE (mm)	3.65	4.15	4.29	4.39	4.12
Trial	6	7	8	9	10
RMSE (mm)	3.65	3.40	4.17	4.22	3.79

The same evaluation was performed to test the *camera-image plane calibration*. 8 points were selected in $\{ImagePlane\}$ using image processing function for the corners detection and in $\{Tracker\}$ using a tracked pointer. Table II shows the calibration error in 10 trials. The median value of the error was $1.72mm$.

TABLE II
EXPERIMENTAL MEASUREMENTS OF THE CAMERA-IMAGEPLANE CALIBRATION ERROR

Trial	1	2	3	4	5
RMSE (mm)	2.25	2.32	2.03	1.09	1.07
Trial	6	7	8	9	10
RMSE (mm)	1.58	1.90	1.84	1.61	1.43

Note that the registration and calibration errors are affected by several factors: the accuracy of the optical tracker, the accuracy of the pointer, the human error in the positioning of the pointer and the precision of the recognition of the chessboard corners. The optical tracker used for the experiments was an Optitrack Motion Capture System (NatualPoint). In our setup, it was composed by four cameras, covering a volume of around $1m^3$. The obtained mean error of system calibration was $0.2mm$.

The position of the tip of the pointer was computed using the pivoting method. In this method the tip of the pointer is maintained in a fixed position, while the pointer is rotated along two perpendicular axes. Consequently, the position of the tip of the pointer is calculated as the center of the sphere described by the markers. The maximum residual error of this procedure was $0.59mm$.

IV. DISCUSSION AND CONCLUSION

The system presented in this paper is aimed at enhancing the information that the surgeon receives during robotic SILS. Using the pre-operative pipeline, the surgeon can extract 3D surface models from CT scans of the patient with a few mouse clicks. During the surgery, semi-automatic point-based registration of the virtual abdomen on the real patient creates a connection between reality and virtuality. The virtual environment, composed of the view of the entire abdomen and the view of the image plane of the virtual camera, makes possible to visualize at run-time the motion of the robot and of the surgical tools inside a virtual abdomen specific for each patient. The possibility to change the transparency of the skin allows the surgeon to plan the entry point, adjusting the access region with respect to the target to reach. Moreover, the virtual camera image plane shows the structures visualized by the camera from the same point of view in the virtual environment. Adding or removing organs in the virtual patient enables the visualization of the hidden structures using transparencies and to zoom out if the surgeon desires to view a wider field of view.

The results obtained form the *virtual-real 3D/3D registration* and the *camera-image plane calibration* are within the specification requirements of the surgeon (accuracy below $10mm$). Regarding the *virtual-real 3D/3D registration* results, it has to be considered that we used only four points for the registration of the models, in order to simulate as much as possible the real procedure executed by the surgeon during the surgery. In a real scenario, the number of available reference points would be very limited, so the system was tested under that assumption. However, there are several sources that influence the accuracy of the registration, such as the inherent error of the Optical Tracker and the tool calibration, which can be improved in future developments.

V. FUTURE WORKS

The presence of a virtual environment representing the reality during the surgical operation is an additional tool, which could improve the safety of the robotic surgery. Future tests will be aimed to evaluate the usability of the virtual environment.

Considering the drawbacks of organs motion due to breathing, blood circulation, and surgical tool interaction, a future goal is to track abdominal structures and to adjust at run-time the registration of the virtual model. The final system will consist also in a 3D reconstruction of the surgical field using stereo cameras and in the definition of dynamic active constraints, which will adapt in real-time to compensate for tissue motions and deformations.

REFERENCES

[1] J. E. Varela, S. E. Wilson, and N. T. Nguyen, "Laparoscopic surgery significantly reduces surgical-site infections compared with open surgery," *Surgical endoscopy*, vol. 24, no. 2, pp. 270–276, 2010.

[2] R. H. Taylor and D. Stoianovici, "Medical robotics in computer-integrated surgery," *Robotics and Automation, IEEE Transactions on*, vol. 19, no. 5, pp. 765–781, 2003.

[3] G. Taylor, J. Barrie, A. Hood, P. Culmer, A. Neville, and D. Jayne, "Surgical innovations: Addressing the technology gaps in minimally invasive surgery," *Trends in Anaesthesia and Critical Care*, vol. 3, no. 2, pp. 56–61, 2013.

[4] M. Piccigallo, U. Scarfogliero, C. Quaglia, G. Petroni, P. Valdastri, A. Menciassi, and P. Dario, "Design of a novel bimanual robotic system for single-port laparoscopy," *Mechatronics, IEEE/ASME Transactions on*, vol. 15, no. 6, pp. 871–878, 2010.

[5] M. Baumhauer, M. Feuerstein, H.-P. Meinzer, and J. Rassweiler, "Navigation in endoscopic soft tissue surgery: perspectives and limitations," *Journal of Endourology*, vol. 22, no. 4, pp. 751–766, 2008.

[6] S. Nicolau, L. Soler, D. Mutter, and J. Marescaux, "Augmented reality in laparoscopic surgical oncology," *Surgical oncology*, vol. 20, no. 3, pp. 189–201, 2011.

[7] S. Nicolau, L. Goffin, and L. Soler, "A low cost and accurate guidance system for laparoscopic surgery: Validation on an abdominal phantom," in *Proceedings of the ACM symposium on Virtual reality software and technology*. ACM, 2005, pp. 124–133.

[8] C. Bichlmeier, S. M. Heining, M. Feuerstein, and N. Navab, "The virtual mirror: a new interaction paradigm for augmented reality environments," *Medical Imaging, IEEE Transactions on*, vol. 28, no. 9, pp. 1498–1510, 2009.

[9] S. Pieper, M. Halle, and R. Kikinis, "3d slicer," in *Biomedical Imaging: Nano to Macro, 2004. IEEE International Symposium on*. IEEE, 2004, pp. 632–635.

[10] Y. Gao, A. Tannenbaum, and R. Kikinis, "Simultaneous multi-object segmentation using local robust statistics and contour interaction," in *Medical Computer Vision. Recognition Techniques and Applications in Medical Imaging*. Springer, 2011, pp. 195–203.

[11] J. Rossignac and P. Borrel, *Multi-resolution 3D approximations for rendering complex scenes*. Springer, 1993.

[12] B. K. Horn, "Closed-form solution of absolute orientation using unit quaternions," *JOSA A*, vol. 4, no. 4, pp. 629–642, 1987.

Reducing Invasiveness of Robot-assisted Surgery by Semi-automatic Alignment to the Incision Point

Benoît Rosa, Emmanuel Vander Poorten, Bertram Van Soom, Dominiek Reynaerts and Jos Vander Sloten
KU Leuven, Department of Mechanical Engineering, 3000 Leuven, Belgium
Email: firstname.name -at- kuleuven.be

***Abstract*—Interest for robotic assisted minimally invasive surgery (MIS) is rising, both in the technical and clinical communities. Since in MIS all instruments enter the body through small incisions in the skin that are placed carefully at pre-planned and well-defined locations, MIS robots should respect these incisions during the operation. Virtually every MIS robot is therefore foreseen of some means, be it mechanic or software-based, to pivot the instruments it is handling about a fixed point in space also referred to as Remote Center of Motion (RCM). The quality of such means is however only as good as the quality of the knowledge of the location of the incision and the accuracy at which the robot can be programmed to align its RCM with the incision point.**

In previous work the authors proposed a method and algorithm that allows to estimate the location of an optimal pivot point (OPP) at the incision. Here the authors address the second part of the problem, namely the alignment of a surgical robot with the OPP. The proposed method consists of first identifying the OPP and then tracking the robot's RCM in 3D in order to guide the user towards the OPP using simple buttons attached on the robot itself. Preliminary experiments carried out showed that it is possible and easy to align the remote center of motion of a robot using the proposed method. Guidance allows a higher positioning precision compared to manual positioning. Future work will be directed towards a thorough validation using a realistic force-sensitive mockup and comparison with manual and visual methods used in current practice.

I. Introduction

In minimally invasive surgery (MIS), surgeons typically insert a camera and small instruments (diameter 3 to 12 mm) inside the body of the patient through a trocar in order to perform a surgical act. This type of surgery induces low recovery time and morbidity rate, which is beneficial to the patient. However, the surgeon's performance is impeded by several factors, among which the limited vision, uneasy hand-eye coordination, lack of haptic feedback, etc. On top of those, the keyhole at the incision point restricts the degrees of freedom of the instruments to only four.

In order to improve this situation, robotic devices have been designed to help the surgeon. One important requirement is to limit the stress on the body wall by respecting the mechanical constraints imposed at the incision. Therefore, several approaches have been adopted. Passive pivoting approaches make use of a two degrees of freedom passive joint at the end of the robot [1, 2]. This approach ensures that the instrument freely rotates and aligns with the trocar point. However, the uncertainty on the exact location of the insertion point make the control in Cartesian space imprecise [3]. Software approaches make use of a redundant robotic arm and appropriate control software that ensures that the instrument passes through the trocar point at all times [4]. Finally, mechanical approaches use constrained kinematic structures to force the instrument to rotate around the incision point, either using a local approach (LCM) [5] or a remote center of motion (RCM) [6, 7, 8].

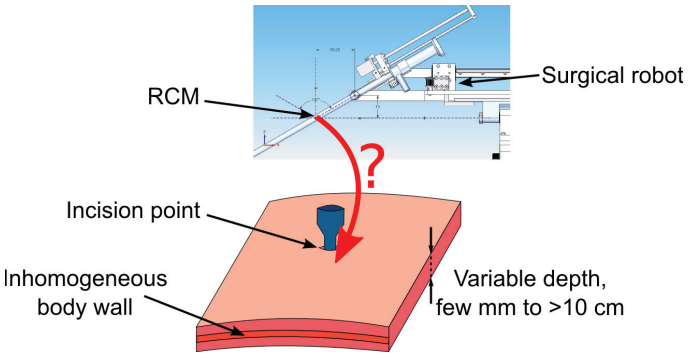

Figure 1. Alignment of a robot with the incision

All those methods have in common that their functionality depends on a good alignment of the robot's center-of-motion with the incision point. However, few efforts have been made so far in order to 1) determine the location of an optimal pivot point at the incision and 2) align the robot with that point. The challenges are illustrated on Fig. 1. Simply aligning the robot's RCM with the incision point at the outer surface is not an option as its optimal position is often significantly lower than the incision point due to the thickness of the body wall. The tissue thickness can range from a few to more than 80 millimetres depending on the location of the incision and the patient's morphology [9, 10]. In the case of the da Vinci robot (Intuitive Surgical, USA), dedicated cannulas with markers are employed to visually align the remote center of motion (RCM) of the robot with respect to the inner part of the body wall [11]. This approach is simple and practical but there is no guarantee that the robot's RCM will be placed properly. Moreover, it is difficult to extend that type of RCM placement to future operations such as single-incision surgery, since it needs direct camera vision of the trocar inside the body cavity and the camera would be, in the latter case, inside the trocar.

The few studies that did look at estimation of the incision's point location either focused only on passive pivoting robots [3, 12], requiring special instrumentation, or on previously acquired or manually input information: instrument tracking prior to detection in [13], black instrument on white background in [14], manual input in [15, 16]. Recently, the authors presented a convenient, cheap and reliable method

that allows to estimate the location of an optimal pivot point (OPP) at the incision [17]. In this paper, a method is proposed for aligning the RCM of a surgical robot with the OPP. Section II briefly presents the method for estimating the OPP and the robot alignment procedures. Section III discusses the experiments and results. Finally, section IV concludes the article.

II. Methods

This section briefly reviews the method for estimation of OPP and introduces an intuitive approach to guide the surgeon in aligning the robot's motion center with the OPP.

A. Estimation of the OPP

The proposed method to estimate the OPP is depicted on Fig. 3. It is a fast, low-cost approach that allows to estimate the position of the OPP in 3D within a few seconds. Similarly to methods used with passive pivoting robots [3, 12, 13], it is based on the assumption that an instrument gently moved inside the trocar (i.e. no torque imposed at the handling point) will rotate around the OPP, i.e. the point that minimizes the interaction forces with the patient. Therefore, the surgeon is asked to move an instrument of his choice in the trocar for a few seconds, applying as low torque as possible on the handle.

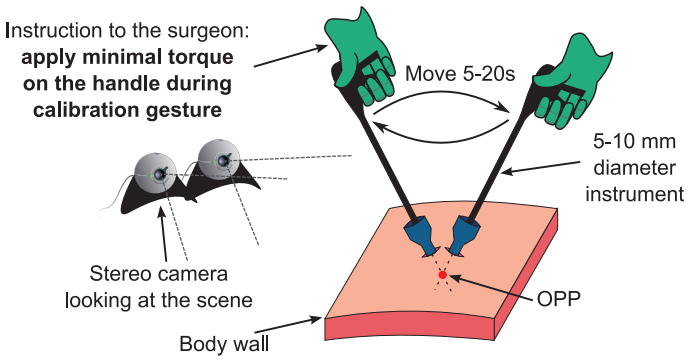

Figure 2. General workflow for estimating the OPP

Images are used for estimating the OPP. Contrarily to previously published works that used the endoscopic images, two external cameras that look at the scene from a distance (30 cm to a few meters) are used. This allows to avoid the problem of endoscopic camera calibration (external cameras can easily be pre-calibrated for their intrinsic and extrinsic parameters provided that they are rigidly fixed together). Moreover, those cameras can be placed anywhere in the operating room, for instance on the endoscopic tower, provided that they look at the scene.

Once the surgeon made the calibration gesture, a dedicated RANSAC-based algorithm is used to extract the OPP. This algorithm allows to differentiate the instrument lines (modelled as moving inside a cone whose apex is the OPP) from background and other lines. The algorithm is described in greater details in [17]. Validations using dedicated rigid and flexible mockups mimicking the abdominal wall showed that the method is robust and reliable: the 3D location of the OPP is estimated in the frame of the cameras with an average error of less than a few millimeters. Moreover, the algorithm is robust to different lighting and background conditions.

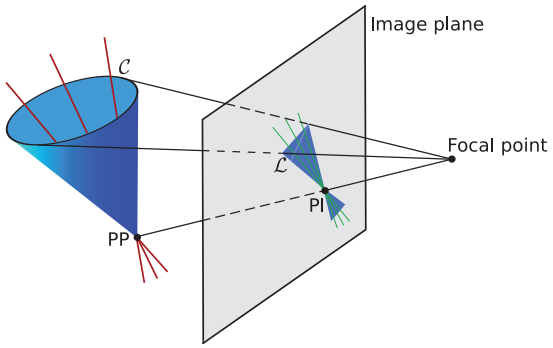

Figure 3. Lines of the instrument during the calibration gesture (inside the cone C) project into a set of lines L in the image plane of each camera (one represented here)

B. Estimation of the position of the robots RCM

Without loss of generality, the focus here is on RCM mechanisms since the robot that is available for experimental validation makes use of that technology. Once the calibration gesture has been performed and the OPP is estimated, the robot can be positioned in order to minimize interaction forces at the trocar. However, since the OPP estimation is an image-based method, the OPP location is known in the camera frame F_C. Therefore, it is necessary to express the RCM position in the same frame F_C. This can be done, for instance, by tracking salient features on the robot and knowing their position with respect to its RCM by registering them with the CAD model of the robot.

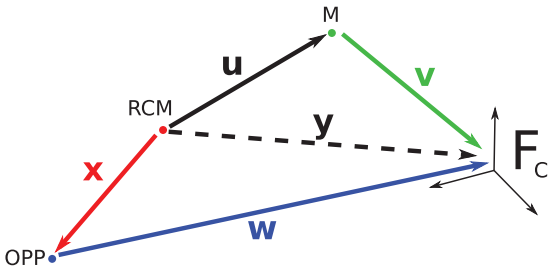

Figure 4. Relation between the different points in the system. F_C is the stereo camera frame in which the OPP position is estimated, M is the marker that is used. All vectors are 3D vectors.

For practical purposes, a simpler approach is used here. A fiducial marker is placed at a fixed position on the robot in order to be tracked by the cameras. The ArUco library is used, since it provides highly reliable and fast tracking [18]. The center of the marker is extracted in real-time, and its 3D position in F_C is estimated using the pre-calibrated intrinsic and extrinsic parameters of the cameras.

The problem is illustrated in Fig. 4. One wants to estimate the value of $\mathbf{x}$ in the frame F_C, knowing $\mathbf{v}$ from the marker tracking and $\mathbf{w}$ from the OPP algorithm. The relation is then $\mathbf{x} = \mathbf{u} + \mathbf{v} - \mathbf{w}$. In order to estimate the value of $\mathbf{u}$ the OPP algorithm is used. By making the robot, holding an endoscope, moving around its RCM for a few seconds, the position $\mathbf{y}$ of the RCM in F_C can be estimated. Because the marker M is at a fixed place on the robot, the vector $\mathbf{u}$ does not change in time and is therefore calibrated as $\mathbf{u} = \mathbf{y} - \mathbf{v}$. In practice,

this experiment is run several times and the average position of the RCM is used in order to increase the precision.

C. Robotic guidance for RCM alignment

Once the position of the OPP and the robots RCM are known in the same frame, guidance can be provided to the user in order to align them. In order to let the surgeon maintain maximal control over the procedure, and for safety reasons, the robot is not allowed to move independently. Rather, we propose to use buttons on the robot that move the RCM in the Cartesian space. Guidance is provided to the user in two ways. First, the distance between the OPP and the RCM is output on a screen. Second, the user can only move *towards* the OPP, i.e. pushing a button that would result in moving the RCM farther away from the OPP will not move the robot.

III. Experimental validation

A. Experimental setup and protocol

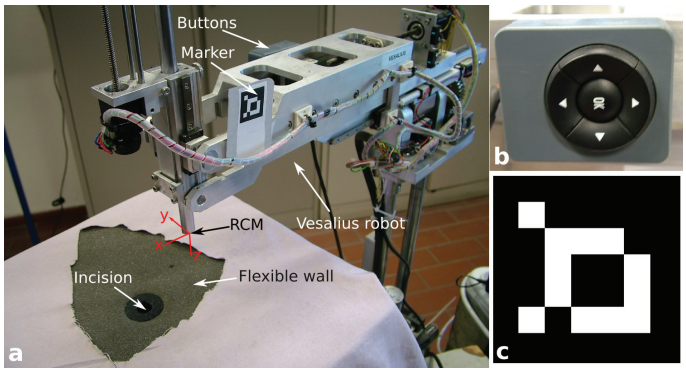

Figure 5. Experimental setup. a: overview of the robot and setup; b: buttons to align the RCM; c: marker used for tracking of the RCM

The experimental setup is depicted on Fig. 5. The robot that is used is the VESALIUS robot that has been developed within the KU Leuven and that is based on the Adjustable Remote Center of Motion mechanism [8]. Note that the current embodiment of the RCM adjustment mechanism only allows to move it in 2 DOF, namely in the x and z directions (see Fig. 5). Therefore, the four buttons (Fig. 5b) can be directly mapped to the directions in which the user moves the RCM. The alignment of the RCM in the y direction is manually made before the experiments.

Two RCM alignment modes are tested during the experiments. In the *manual mode*, the user can directly control the position of the RCM using the buttons, without any restriction but also without any guidance. Note that during the alignment phase, the robot is positioned such as the tip of the held endoscope coincides with the position of the RCM (see Fig. 5) As such, it provides a visual indication of the RCM position in space. In the *semi-automatic mode*, the user must first perform the calibration gesture in order to estimate the OPP position and then is guided for alignment as described in subsection II-C.

For experiments in both the manual mode and the semi-automatic mode the OPP was estimated by making the calibration gesture in order to get a reference point. The thickness of the flexible wall (4cm) was known to the user and the robot was placed in a position where the tip of the instrument is at the RCM (see Fig. 5) in order to be able to estimate the correct position of the RCM visually for manual alignment. For each experiment, the positioning error between the OPP and the RCM was recorded when the user was satisfied by the result.

B. Results

An expert carried out 7 manual alignments and 5 guided alignments of the RCM of the robot. The results are gathered in table I. e_x and e_z are the projections of the error vector in the **x** and **z** directions (see Fig. 5).

Manual mode			
	e_x	e_z	e
Average	4.5	2.1	5.2
Std. dev.	0.5	2.1	1.1

Semi-automatic mode			
	e_x	e_z	e
Average	0.2	0.9	1.1
Std. dev.	0.5	0.8	0.6

Table I. Positioning errors during the experiments. All values are in mm

One can see that the average error is much smaller in the semi-automatic mode than in the manual mode. This tends to show that the guidance provided in the semi-automatic mode is effective in reducing the positioning error made by the user. However, statistical significance could not be achieved because the number of experiments was not large enough.

The user subjectively preferred the semi-automatic mode over the manual mode because the feedback of the robot gave confidence during the positioning task. From the fact that the situation was simplified during the experiments (2 dof alignment, known body wall thickness, homogeneous body wall) one can conclude that this guidance will most probably become even more useful and appreciated in a real surgical situation. There was no significant difference in time between the experiments.

IV. Conclusion

This paper presents a method for semi-automatically aligning a surgical robot at the optimal pivot point in the incision, in order to minimize the forces applied on the patient. The proposed method makes use of the OPP estimation algorithm that has been previously published by the authors in order to estimate that point.

Experiments carried out with a surgical robot making use of a mechanical remote center of motion suggest that this method is reliable and intuitive, and allows to position the RCM of a robot with higher precision than in a manual way. The authors want to stree the point that the method is nevertheless not reduced to remote center of motion-type of surgical robots.

Further work will be directed towards the estimation of the forces applied to a realistically simulated body wall. A thorough comparison with all kinds of visual and manual alignment approaches used in current practice is also considered.

References

[1] M. Oddsdottir and G. Birgisson. Aesop: A voice-controlled camera holder. *Primer of Robotic & Telerobotic Surgery*, pages 35–41, 2004.

[2] B. Herman, B. Dehez, K. T. Duy, B. Raucent, E. Dombre, and S. Krut. Design and preliminary in vivo validation of a robotic laparoscope holder for minimally invasive surgery. *The International Journal of Medical Robotics and Computer Assisted Surgery*, 5(3):319–326, 2009.

[3] T. Ortmaier and G. Hirzinger. Cartesian control issues for minimally invasive robot surgery. In *Intelligent Robots and Systems, 2000.(IROS 2000). Proceedings. 2000 IEEE/RSJ International Conference on*, volume 1, pages 565–571. IEEE, 2000.

[4] H. Mayer, I. Nagy, and A. Knoll. Kinematics and modelling of a system for robotic surgery. In *On Advances in Robot Kinematics*, pages 181–190. Springer, 2004.

[5] S. Voros, G.-P. Haber, J.-F. Menudet, J.-A. Long, and P. Cinquin. Viky robotic scope holder: initial clinical experience and preliminary results using instrument tracking. *Mechatronics, IEEE/ASME Transactions on*, 15 (6):879–886, 2010.

[6] R. H. Taylor, J. Funda, B. Eldridge, S. Gomory, K. Gruben, D. LaRose, M. Talamini, L. Kavoussi, and J. Anderson. A telerobotic assistant for laparoscopic surgery. *Engineering in Medicine and Biology Magazine, IEEE*, 14(3):279–288, 1995.

[7] M. Schurr, A. Arezzo, B. Neisius, H. Rininsland, H.-U. Hilzinger, J. Dorn, K. Roth, and G. Buess. Trocar and instrument positioning system TISKA. *Surgical endoscopy*, 13(5):528–531, 1999.

[8] H.-W. Tang, H. Van Brussel, J. Peirs, and T. Janssens. Remote centre of motion positioner, nov 2010. WO Patent 2,010,130,817.

[9] C. Song, A. Alijani, T. Frank, G. Hanna, and A. Cuschieri. Mechanical properties of the human abdominal wall measured in vivo during insufflation for laparoscopic surgery. *Surgical Endoscopy And Other Interventional Techniques*, 20(6):987–990, 2006.

[10] M. R. Kwaan, A. M. Sirany, D. A. Rothenberger, and R. D. Madoff. Abdominal wall thickness: is it associated with superficial and deep incisional surgical site infection after colorectal surgery? *Surg Infect (Larchmt)*, 14(4): 363–368, Aug 2013.

[11] Intuitive Surgical. da Vinci prostatectomy procedure guide. PN 871403 Rev. A 4/06.

[12] A. Krupa, J. Gangloff, C. Doignon, M. F. de Mathelin, G. Morel, J. Leroy, L. Soler, and J. Marescaux. Autonomous 3-d positioning of surgical instruments in robotized laparoscopic surgery using visual servoing. *Robotics and Automation, IEEE Transactions on*, 19(5): 842–853, 2003.

[13] C. Doignon, P. Graebling, and M. de Mathelin. Real-time segmentation of surgical instruments inside the abdominal cavity using a joint hue saturation color feature. *Real-Time Imaging*, 11(5):429–442, 2005.

[14] J. Wilson, T.-C. Tsao, J. Hubschman, and S. Schwartz. Evaluating remote centers of motion for minimally invasive surgical robots by computer vision. In *Advanced Intelligent Mechatronics (AIM), 2010 IEEE/ASME International Conference on*, pages 1413–1418, 2010.

[15] S. Voros, J.-A. Long, and P. Cinquin. Automatic detection of instruments in laparoscopic images: A first step towards high-level command of robotic endoscopic holders. *The International Journal of Robotics Research*, 26(11-12):1173–1190, 2007.

[16] R. Wolf, J. Duchateau, P. Cinquin, and S. Voros. 3d tracking of laparoscopic instruments using statistical and geometric modeling. In *Medical Image Computing and Computer-Assisted Intervention–MICCAI 2011*, pages 203–210. Springer, 2011.

[17] B. Rosa, C. Gruijthuijsen, B. Van Cleynenbreugel, J. Vander Sloten, D. Reynaerts, and E. Vander Poorten. Estimation of optimal pivot point for remote center of motion alignment in surgery. *International Journal of Computer Assisted Radiology and Surgery*, 2014. In Press, DOI 10.1007/s11548-014-1071-3.

[18] S. Garrido-Jurado, R. Munoz-Salinas, F. Madrid-Cuevas, and M. Maran-Jimenez. Automatic generation and detection of highly reliable fiducial markers under occlusion. *Pattern Recognition*, 47(6):2280 – 2292, 2014.

New Assistive Technologies for Laser Microsurgery

Loris Fichera, Diego Pardo, Darwin G. Caldwell, Leonardo S. Mattos
Department of Advanced Robotics
Istituto Italiano di Tecnologia
16163 Genova, Italy
email: loris.fichera@iit.it

***Abstract*—This paper describes the implementation of two assistive technologies for laser microsurgery into an experimental surgical platform. These technologies enable the monitoring of the state of tissue during the execution of laser resections. Specifically, the focus of these technologies is on the estimation of the laser cutting depth and the thermal state of tissue during laser irradiation. The estimations rely on mathematical models capable of mapping the applied laser energy to the resulting effects on tissue. These models have been integrated to an experimental surgical setup, thereby allowing the implementation of prototypes of the proposed technologies.**

I. Introduction

Transoral Laser Microsurgery (TLM) denotes a set of surgical techniques aiming at the treatment of laryngeal cancer. These procedures consist of inserting a laryngoscope into the oral cavity down to the larynx, thereby allowing tumor visualization. The tumoral mass is resected with a laser, the carbon dioxide (CO_2) laser is commonly employed for this task [1]. Clinicians visually determine the amount of tissue that should be removed to ensure the complete eradication of the tumor (Fig. 1). Radical organ resection is commonly considered a last resort for the treatment of late stage cancers [1], [2]. Where applicable, organ preservation strategies are employed. These include limiting the amount of healthy tissue that is removed during the intervention, as well as minimizing the thermal damage inflicted by the laser on surrounding structures. The execution of accurate resections with minimal collateral damage requires precise control of the effects of the laser on tissue.

Technologies commercially available for TLM do not include any support for sensing the state of the tissue during the intervention. The quality of resections relies entirely on the dexterity and experience of clinicians. Extensive training is required to develop an effective laser cutting technique. This includes the acquisition of a basic knowledge of the physical principles behind laser ablation of tissue; the ability to manipulate the laser dosimetry parameters and its exposure time in order to obtain adequate cutting [1], [2]. Laser parameters used in clinical practice include power, energy delivery mode, pulse duration, incision scanning frequency and exposure time. At present times, no standard recipe exists to determine the parameters and the exposure required to obtain an optimal incision. Physicians use different settings, depending on their skills, experience and preferred technique [1].

Based on the limitations above, we recently proposed the concept of two assistive technologies for laser microsurgery [3]. These technologies enable the on-line monitoring of the laser incision process [4], providing visual information

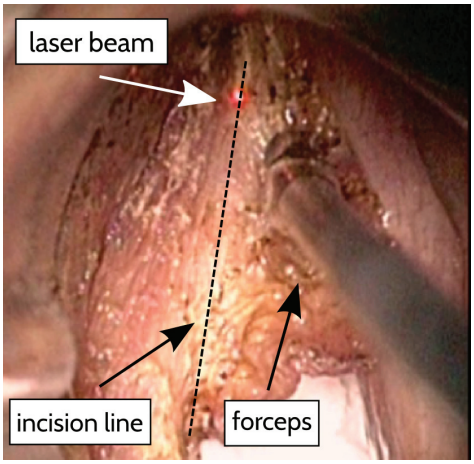

Fig. 1. Transoral Laser Microresection of a Squamous Cell Carcinoma affecting the left vocal fold. The tumor is resected through several laser passes along an incision line. Forceps are used to apply traction on the tissue while the incision is performed.

that supports the decision making process of the surgeon. Specifically, these technologies produce estimations of (i) the laser cutting depth and (ii) the variation of tissue temperature produced by laser irradiation. Extending the work presented in [3], prototypes of these technologies have been implemented. Here, we describe the implementation of these prototypes into an experimental system for TLM.

II. Methods

Finding effective techniques to monitor the state of tissue during laser treatment is an active area of research. Different approaches have been proposed to estimate the temperature of tissue [5] and the depth of laser incisions [6], [7]. However, none of these approaches can be straightforward employed during Transoral Laser Microsurgery (TLM). Some of them require the introduction of invasive sensing devices in direct contact with the surgical site. This is impractical in a TLM setup due to space constraints: the small size of the larynx does not offer enough volume for the introduction of additional equipment. Non-invasive techniques are available, still these may require the introduction of substantial changes to the medical protocol, e.g. the use of MRI-compatible equipment.

As an alternative to previously proposed approaches, we implemented online monitoring of tissue using a virtual sensing approach [8]; i.e. we used mathematical models that map the application of laser inputs to the resulting effects on tissue (incision depth and temperature variation). It was shown that

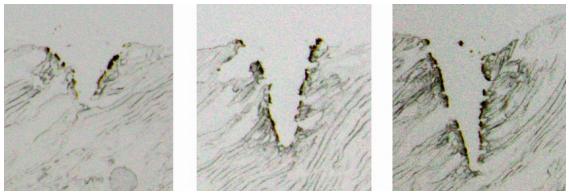

Fig. 2. Incision profiles produced with increasing exposures times (2.5, 3.5 and 4.5 s) and constant power density, scanning frequency and length. In order to get a complete exposure of the crater profile, targets were sectioned into thin slices (30 μm) with a cryostat microtome.

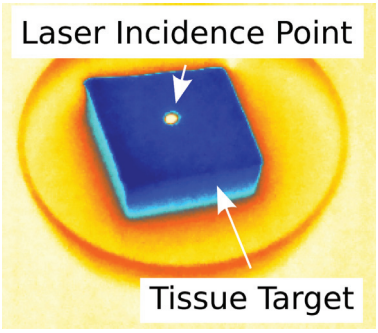

Fig. 3. Raw thermal image of a tissue target during laser irradiation. Brighter colours represent higher values of temperature.

machine learning methods can be used to generate models compatible with the set of laser inputs typically used during surgery [9], [10]. Data needed for the learning task was collected during controlled laser experiments.

A. *Model of Laser Cutting Depth*

This model takes as input the laser parameters and the exposure time an produces an on-line estimation of cutting depth. The model is based on statistical regression analysis, i.e. is generated using data captured during real laser incisions. Data used to produce this model was collected during experiments involving laser incision of ex-vivo soft tissue (chicken breast). Laser trials for different values of exposure time have been performed; the resulting depth of incision was measured with a microscope (Fig. 2).

B. *Model of Tissue Temperature*

This model estimates the superficial temperature of tissue during laser ablation. The estimation is based on the laser parameters as well as the total exposure time. The model is created through non-linear regression analysis of experimental data. Controlled laser experiments have been performed to gather data for the approximation task. During these experiments, we recorded the superficial temperature of tissue using a thermal camera (Fig. 3).

III. Technology Implementation

This section describes the implementation of the technologies to monitor the laser incision depth and the temperature of tissue. These technologies have been integrated in the µRALP platform, an experimental surgical system being developed for transoral laser microsurgery [11]. The system features an endoscopic device [12] which is inserted into the larynx and delivers the laser beam to the surgical site. A computerized surgeon-machine interface [13] allows to control the system. This system is shown in Fig. 4. A graphics tablet is used for laser aiming; three-dimensional visualization of the surgical site is offered by a binocular Head Mounted Display.

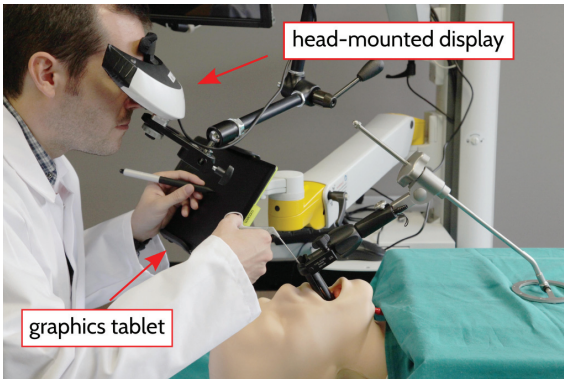

Fig. 4. Here, the surgeons use a recently developed user interface [13], which allows them to visualize the surgical site through a head-mounted display (HUD), while controlling the position of the laser beam using a virtual scalpel (stylus and graphics tablet).

The integration of the models described in section II was accomplished at a software level. The Microralp system adopts a distributed software architecture: different subsystems are managed by distinct software modules, each instantiated as a separate Operating System (OS) process. These processes interact through a message passing scheme. The Robot Operating System (ROS) is used as communication middleware. The inclusion of a new module in the system requires the specification of its interface, i.e. the information it exchanges with other processed of the system.

The models are encapsulated into shared libraries (.so) and instantiated by a software module called the Cognitive Supervisor (CS). This module is responsible for feeding the models with the required input and for distributing their output to other software components. The interconnection of this module in the Microralp software architecture is shown in Fig. 5. The CS is enabled by the laser activation signal emitted by the laser controller (ROS Actionlib). During the application of laser power on tissue, the supervisor module produces two distinct messages; these contain estimations of the current depth of incision and tissue temperature. This information is made available to the user interface through publication on specific ROS topics. To produce the estimations mentioned above, the CS needs to know the laser dosimetry parameters in use (laser power, scanning frequency, delivery mode). These parameters are set by the user through the system interface and made available under the form of ROS parameters.

The surgeon interface has been customized in order to display the information produced by the CS. An example is shown in Fig. 6. A widget was added to the surgical viewer, which shows the progression of the incision depth. This information is represented both numerically (in millimetres) and graphically through the use of a coloured bar gauge.

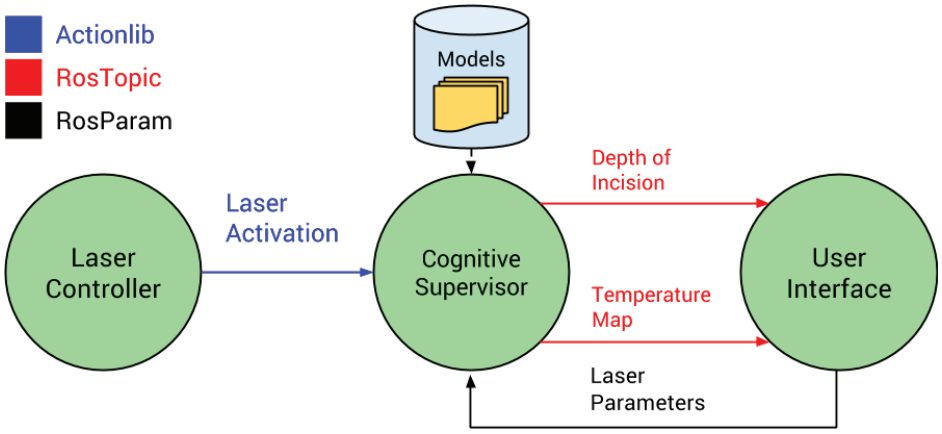

Fig. 5. Coordination of the software processes involved in the on-line estimation of laser cutting depth/thermal state of tissue. The estimations are calculated by the Cognitive Supervisor (CS), based on mathematical models that are loaded from file. The laser parameters required to calculate the estimations are received from the User Interface. The CS is synchronized with the activation signal produced by the Laser Controller. When the laser is activated, the CS delivers the output of the models to the User Interface, by means of a continuous flow of messages.

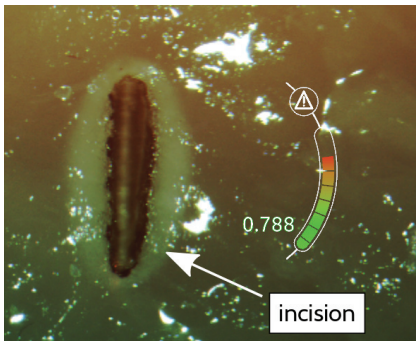

Fig. 6. On-line estimation of cutting depth. A number indicates the depth of incision in millimetres. The same information is represented visually by means of a coloured bar gauge. The top limit of the gauge represents a safety threshold which triggers a warning signal when a certain incision depth is exceeded. The value of the threshold can be configured in the software.

IV. Conclusion

This abstract has presented the development of novel assistive technologies for transoral laser microsurgery. These technologies aim to enhance to perception of the clinicians about the state of the tissue during the intervention. At the present time, no other assistive system exists that allows clinicians to monitor the effects of laser radiation on tissue during the execution of resections. Providing clinicians with such facilities will enable a better control of the laser incision depth, while maximizing the preservation of healthy tissues. This will create unprecedented levels of surgical precision, quality and safety.

The implementation of these technologies in an experimental surgical platform was described. Future efforts will be oriented towards the evaluation of this technologies in a clinical environment.

Acknowledgment

The research leading to these results has received funding from the European Union Seventh Framework Programme FP7/2007-2013 – Challenge 2 – Cognitive Systems, Interaction, Robotics – under grant agreement μRALP N°288233.

References

[1] M. Rubinstein and W. Armstrong, "Transoral laser microsurgery for laryngeal cancer: A primer and review of laser dosimetry," *Lasers in Medical Science*, vol. 26, no. 1, pp. 113–124, 2011.

[2] W. Steiner and P. Ambrosch, *Endoscopic laser surgery of the upper aerodigestive tract: with special emphasis on cancer surgery*. Thieme, 2000.

[3] L. Fichera, D. Pardo, and L. S. Mattos, "Supervisory system for robot assisted laser phonomicrosurgery," in *Proceedings of the 35th International Conference of the IEEE Engineering in Medicine and Biology Society (EMBC)*, 2013.

[4] ——, "Artificial cognitive supervision during robot-assisted laser surgery," in *3rd Joint Workshop on New Technologies for Computer/Robot Assisted Surgery, Verona*, 2013.

[5] P. Saccomandi, E. Schena, and S. Silvestri, "Techniques for temperature monitoring during laser-induced thermotherapy: An overview." *International Journal of Hyperthermia*, vol. 29, no. 7, pp. 609–619, 2013.

[6] B. Y. Leung, P. J. Webster, J. M. Fraser, and V. X. Yang, "Real-time guidance of thermal and ultrashort pulsed laser ablation in hard tissue using inline coherent imaging," *Lasers in Surgery and Medicine*, vol. 44, no. 3, pp. 249–256, 2012.

[7] E. Bay, X. L. Den-Ben, G. A. Pang, A. Douplik, and D. Razansky, "Real-time monitoring of incision profile during laser surgery using shock wave detection," *Journal of Biophotonics*, 2013.

[8] L. Fichera, D. Pardo, and L. S. Mattos, "Virtual supervision for a virtual scalpel," in *Proceedings of the 1st Russian-German Conference on Biomedical Engineering, Hanover*, 2013.

[9] D. Pardo, L. Fichera, D. G. Caldwell, and L. S. Mattos, "Thermal supervision during robotic laser microsurgery," in *IEEE International Conference on Biomedical Robotics and Biomechatronics (BIOROB)*, 2014.

[10] L. Fichera, D. Pardo, N. Deshpande, and L. S. Mattos, "On-line estimation of ablation depth during co2-laser exposure," in *Workshop on Cognitive Surgical Robotics, IEEE/RSJ International Conference on Intelligent Robots and Systems (IROS 2013)*, 2013.

[11] The microralp project. [Online]. Available: http://www.microralp.eu

[12] D. Kundrat, A. Schoob, B. Munske, and T. Ortmaier, "Towards and endoscopic device for laser-assisted phonomicrosurgery," in *Proceedings of the Hamlyn Symposium on Medical Robotics*, 2013.

[13] L. S. Mattos, N. Deshpande, G. Barresi, L. Guastini, and G. Peretti, "A novel computerized surgeon-machine interface for robot-assisted laser phonomicrosurgery," *The Laryngoscope*, 2014.

Session 4

Novel Robotic Hardware

Chair: Dr. Auguste van Poelgeest, Fraunhofer PAMB

Tuesday, October 14th

15:30 – 16:30

FUTURA: a computer-assisted robotic platform for high-intensity focused ultrasound

Selene Tognarelli, Gastone Ciuti*, Alessandro Diodato, Piero Miloro, Antonella Verbeni, Andrea Cafarelli, Arianna Menciassi
The BioRobotics Institute, Scuola Superiore Sant'Anna (SSSA), Pontedera (PI), Italy
*corresponding author: g.ciuti@sssup.it

***Abstract*—FUTURA (Focused Ultrasound Therapy Using Robotic Approaches) is a European 7th research framework project aiming at creating an innovative robotic platform for non-invasive interventions. Focused Ultrasound Surgery (FUS) is the ideal benchmark for robotic surgery. Merging surgical robotics together with non-invasive ultrasound monitoring and therapy has the ambitious goal to improve precision and accuracy of the intervention, thus enabling a large use of this therapeutic strategy for the treatment of different pathologies. Aim of this work is to present the concept and project objectives to the Robotics Community.**

Keywords— Focused Ultrasound Surgery; Computer-assisted robotic platform;US-imaging.

I. INTRODUCTION

In the last century, medicine showed considerable advancements in terms of new technologies, devices and diagnostic/therapeutic strategies leading to a significant reduction of invasiveness and an improvement of surgical outcomes. Advanced technical capabilities have been reached mostly by Information and Communication Technologies (ICT technologies), which dramatically grow up the medical field. In particular, applications of robotics in surgery and in therapy delivery have several advantages, including augmented task precision, dexterity, and repeatability [1], extending the ability of surgeons to plan and carry out surgical interventions more accurately and less invasively. Robots assist surgeons in treating patients by moving surgical instruments, but these motions are even controlled by the surgeon in different ways [2]: i) pre-programmed, semi-autonomous motion, ii) teleoperation or iii) hands-on compliant control. In a pre-programmed robot, the movement of a tool is earlier specified by the surgeon. The da Vinci robot (http://www.intuitivesurgical.com) is the paradigmatic example of telesurgery system where the surgeon specifies the desired motions directly through a dedicated human machine interface. Finally, in a hands-on compliant control the surgeon grasps directly the surgical tool supported also by the robot's end-effector. However, real translation of robots into the operating room is still far from being achieved, especially considering that requirements for integration are completely different than those for industry applications, where robots are predominant [3]. Moreover, from a technical viewpoint, encumbrance and rigidity of tools, as well as the lack of haptic feedback, remain major limitations of these systems [4, 5].

From a clinical viewpoint, the ideal and paradigmatic example of Minimally Invasive Surgery (MIS) is whenever the therapy can be completely non-invasive, such as, for example, in Focused Ultrasound Surgery (FUS), also referred as High Intensity Focused Ultrasound (HIFU). FUS involves the transmission of acoustic energy through the body from an external source: being the transducer focused, large levels of energy can be deposited in very small spots, thus causing tissue necrosis, while preserving healthy tissues outside the target area. FUS has been used extensively in the treatment of uterine fibroids (in excess of 10.000 patients worldwide) as well as being shown to be an effective treatment for painful bone metastases. Early studies on its use for the treatment of breast cancer, prostate cancer, and pancreatic cancer have demonstrated very encouraging results that support further research. It will also be possible to treat kidney and liver tumours soon as new developments to solve the problem of respiratory motion are implemented (www.fusfoundation.org). However, this technique suffers from some drawbacks, such as limited precision, repeatability and highly operator-dependence [6] which narrow the applicability to non-moving and non-essential organs, mainly under guidance of Magnetic Resonance (MR). These limitations are mainly due to the low frame rate of MR Imaging (MRI), in particular as regards thermal mapping sequences, which are fundamental for monitoring the therapy. This frame rate (i.e. in the order of 1 Hz) is not compatible with motion compensation of physiological movements (mainly breathing). Furthermore, the specificity of the current devices (i.e., one FUS instrument for one or few pathologies) makes market penetration slow and difficult. Finally, HIFU therapy is still strongly operator-dependant, and the flow of information to the operator is incomplete. A robotic-assisted approach may offer the chance to overcome these limitations, improving robustness, accuracy, repeatability and safety of the therapy [7]. Moreover, robotics enables a large use of FUS for the treatment of different pathologies accessible to a high number of patients and virtually performed in many healthcare centers without requesting extremely expensive and dedicated instrumentations (such as the MRI).

In this framework, a European 7th research framework project stemmed from the idea to develop an autonomous, multi-functional and multi-robotic assisted surgical platform able to perform non-invasive FUS therapies applied to deformable tissues. FUTURA (Focused Ultrasound Therapy Using Robotic Approaches) project (www.futuraproject.eu) proposes a robotic approach for FUS therapy. The robotic platform is expected to operate into the surgical room, which appears as an unstructured and extremely critical environment; perception capabilities and understanding will be augmented by merging external sensors and internal control strategies. Robot co-

operation, robot collaboration, and robot interaction, both with medical doctors and patients, represent the core of the project. FUTURA will address all these issues by integrating cognitive processes in the operational workflow, all blended with state-of-the-art, flexible and safe instruments and techniques for therapy planning, delivery and monitoring.

Aim of this work is to present the FUTURA concept, the project objectives and the status of the activity to the Robotics Community, for encouraging an active discussion about this topic of surgical robotics.

II. FUTURA PLATFORM OVERVIEW

As already mentioned, FUTURA proposes an autonomous, multifunctional and multi-robotic robotic-assisted surgical platform able to perform non-invasive FUS therapies applied to deformable tissues. The expected contribution is to advance robustness, accuracy, precision and reliability of the therapy, as well as, to improve safety and acceptability of multifunctional robotic platforms in the surgical room. Four specific objectives are addressed in FUTURA: i) merging surgical robotics, non-invasive ultrasound therapy and machine learning for medical imaging, ii) developing a multifunctional robotic surgical platform able to perform different tasks and which possesses cognitive capabilities such as collision avoidance and obstacle perception, iii) improving planning and monitoring of ultrasound therapy, and iv) improving therapy delivery.

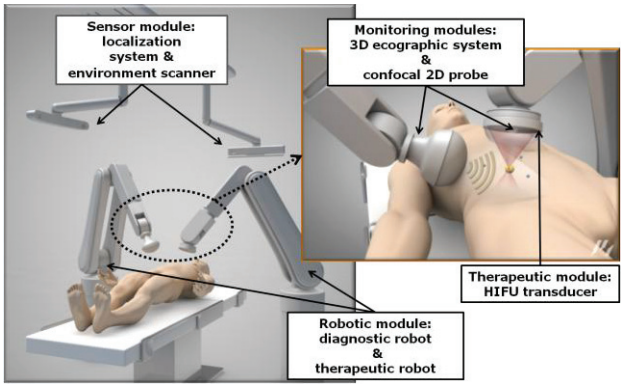

Figure 1: FUTURA platform.

In order to reach this broad and ambitious goal, the FUTURA platform consists of a dedicated robotic platform, monitoring and delivery systems, internal and external sensors both for platform registration (including robotic platform, surgical room and medical instruments), robot-patient interactions monitoring and environment control. Entering in the details of the project, the essential modules of the platform are the following: i) two serial manipulators able to match technical and medical specifications in terms of workspace, payload, speed and reaction time, software accessibility and communication interfaces; ii) therapeutic module composed of a dedicated HIFU transducer for delivering therapy; iii) monitoring module composed of two different UltraSonography (US) probes, one to monitor the advancement of the therapy (2D imaging US probe confocal to the HIFU transducer mounted on one robotic manipulator) and the other to guarantee a continuous adjustment of robots position (3D imaging US probe mounted on the second robotic arm manipulator); iv) sensor module: proprioceptive and exteroceptive sensors for dedicated control strategies implementation. These sensors will be also exploited for platform registration, monitoring robot-patient interactions and environment. Furthermore, a software framework will allow the exchange of information and the synchronization between various modules. The main components of FUTURA are sketched in Figure 1.

A. *FUTURA platform workflow*

The workflow of the FUS image-guided procedure (both from a therapeutic and from a monitoring viewpoint) is presented in Figure 2, by highlighting how the interventional tasks and the control activities are shared between the doctor and the autonomous robotic platform.

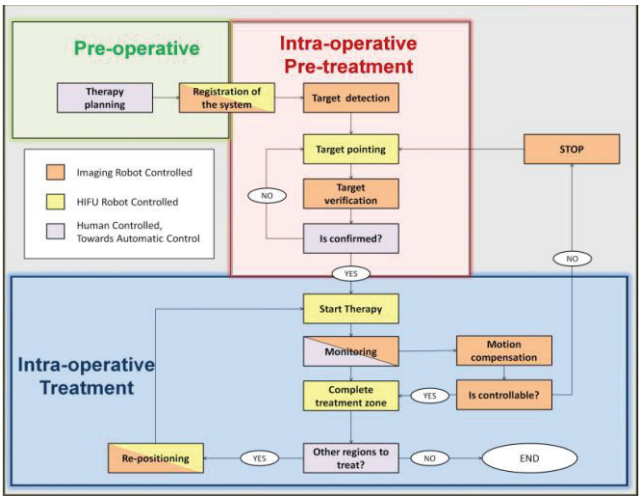

Figure 2: Workflow of the FUTURA platform.

The first phase of the interventional procedure is the pre-operative phase and is related to the planning of the therapy. During this step, pre-operative imaging (i.e. MRI and/or Computed Tomography (CT)) is exploited to define motion pathways for the robot-patient registration and for robotic treatment. Using these images, a high precision robot positioning strategy will be implemented. Furthermore, pre-operative imaging is used for defining the optimal ultrasonic window, thus to avoid dangerous interaction of the ultrasound waves in the human body (*e.g.*, with bones, air filled intestine, pleura, or large blood vessels and nerves) while delivering the therapy.

Once the overall system is accurately calibrated in the operating scenario, the intra-operative phase can start and the robotic manipulators are correctly positioned thanks to a US-based scanning procedure of the target area; it is mandatory for registration purposes with the patient preoperative model. The procedure is accomplished with the diagnostic robot on the patient just before the treatment beginning.

Intraoperatively, on-line adjustment of HIFU transducer installed on the therapeutic robot will be achieved using image-based methodologies, to allow locking on the target and to treat the complete targeted volume based on the preoperative planning. It is worth mentioning that, if the organ motion cannot be tracked, the procedure must be stopped and the robotic platform re-positioned to correctly address the target. Loss of tracking will also lead to a failsafe mode to avoid inadvertent damages on other organs or important adjacent structures. In

addition, the coupling between skin and probe will be continuously monitored and, if coupling becomes incomplete, sonication will be interrupted to avoid skin burn.

During the therapeutic phase, the known spatial configuration of both imaging probes will allow to display a composite and co-registered image set. The display will also show - as an overlay possibly on previously acquired 3D CT or MRI images used in the treatment planning phase - the parts of the target volume that have been already treated and the remaining ablation steps to achieve complete necrosis of the tumour. Once the target tumour is completely ablated, if there are no other regions to treat, the therapy can finish. The control architecture of the FUTURA platform will be designed in a multi-module configuration in order to easily integrate the single functional operations and strategies, which will be implemented by the several partners of the project in the control core of the platform. In particular, Robot Operating System software (ROS - Willow Garage, Stanford Artificial Intelligence Laboratory) will be used as the platform framework. If no critical event occurs, the control logic core will manage all the information collected by the different nodes in a bidirectional manner in order to define the on-line execution of the procedure stage-by-stage. When relevant/critical events are detected in the environment or if patient status changes abruptly, adequate strategies may be adopted directly by the software nodes endowed with cognitive analysis systems.

B. *FUTURA Robotic module and Control*

As previously reported, the FUTURA robotic module will be composed by two robotic manipulators: one supporting and moving the HIFU transducer with a confocal US imaging probe, and the second one holding and moving the 3D imaging US probe for treatment monitoring. Among different models of robots and with the support of dynamic simulations in order to evaluate the effectiveness and reliability of the robotic manipulator to perform the specified medical tasks in terms of workspace, movements trajectories and required end-tools configurations, 6 degrees-of freedom ABB IRB 120 anthropomorphic industrial robotic arms were selected as candidate for the FUTURA platform (http://www.abb.com/). The two robotic manipulators will be provided with two force/torque sensors, one on each robot. In particular an ATI mini45 force/torque sensors (ATI Industrial Automation, NC, USA) will be installed and interfaced to the manipulators in order to control the forces and torques acting on the patient along the procedure (thus maintaining an appropriate contact force with the patient, directly or through a US coupling interface). The force/torque sensor installed on the diagnostic/tracking robot will be also exploited for implementing a shared control on the robotic arm in order to perform, by directly interacting with the robot, the initial US-based scanning procedure of the target area for registration purposes with the preoperative model. The control of the manipulators, implemented in ROS, consists of the bidirectional exchange of specific data structures with the ABB controller, under the supervision of the logic core of the FUTURA software framework.

C. *FUTURA Monitoring module*

The FUTURA monitoring system is composed mainly of two different US probes embedded in the platform in order to monitor the advancement of the therapy and ensure continuous adjustment of the robots' positions. More in detail, one 2D imaging probe will be mounted confocally within the HIFU transducer in order to have a direct feedback on the target-focal region; it will be exploited to monitor the treatment and to ensure that the acoustic beam path remains adequate for all the procedure lifetime. A second 3D imaging probe will be positioned independently via the second robot arm in such a way to provide a tridimensional, wide-range and high frame rate overall vision of the therapeutic Region of Interest (RoI) and to assess the lesion size and location. This probe will also be used to track the organ motion and to direct the HIFU transducer robotic arm to follow the target. Tridimensional, wide-range and high frame rate overall vision of the RoI is critical for the on-line monitoring of the therapy and for the self-adjustment of the procedure. Images from the coaxial US probe and from the 3D imaging US probe will be processed and will return information on target position and therapy advancement, *e.g.* through sono-elastography obtained by the 2D imaging coaxial US probe. This information will be continuously converted by the custom-made algorithms into inputs for the robotic platform, mainly in terms of position and orientation of the manipulators' end-effectors. The therapy advancement will be further monitored by contrast enhanced ultrasound imaging and the imaging data will be upgraded accordingly.

D. *FUTURA Therapeutic module*

The design specifications for the therapy delivery system (HIFU module) consider a phased array configuration as the proper solution, in order to reach electronically various depths in the body, by deflecting the focal spot toward or away from the transducer. Design constraints consider: i) to enable treatment of target organs of various sizes, at different depth and locations in the body, ii) to be light enough so as not to put too much load on the robotic arm, iii) to enable high ablation rate for reducing the overall treatment time, iv) to be flexible in term of operating mode for the HIFU transducer (*i.e.*, continuous or pulsed sonications, different frequencies, etc.) and v) to be rugged because the transducer is exposed and in contact with the patient, interfaced through an acoustic coupling. The acoustic coupling between the transducer and the patient body will be provided by a flexible membrane fixed to the front of the transducer and filled with circulating degassed water. The use of a feedback controlled, multi degrees of freedom robotic arm for the positioning of the HIFU transducer allows treatment of large tumors by scanning the target volume with the focused ultrasound beam (tumour painting).

E. *FUTURA Sensor module and safety strategies*

The operating room is an unstructured and crowded environment; furthermore the human presence and interaction with robotic manipulators require a high awareness in order to avoid any possible collision and perceiving obstacles. Integration of external sensors and internal control strategies will represent one of the main topics of FUTURA.

Intra-operative multi-modal control and safety strategies will be implemented to improve precision, accuracy and safety

of the therapeutic procedure, thus ensuring redundant information to the platform control core for the assessment and confirmation of the target position, and consequently for the correctness of the therapy delivery. Final targeting accuracy, which depends from all the modules features of the FUTURA pipeline, will be guaranteed within the HIFU focal spot volumetric dimensions, i.e. a cigar shape of about 5mm in maximum diameter and 10mm in length.

Proper planning/simulation software will be implemented to allow a re-planning of the trajectory for collision avoidance and obstacle perception purposes; appropriate algorithms will manage any difference with the planned scenario, adding online correction to the robot motion in order to react to moving or unplanned obstacles and to adjust the treatment path based on image guidance and information from external sensors. In particular, a precise calibration procedure of the overall system for defining the position and orientation of each component in the operating theatre is required. Each component of the robotic platform (*e.g.*, the two robotic manipulators with the 3D imaging monitoring probe and the HIFU transducer with the confocal probe, and the surgical table) has to be appropriately localized within the operating room. The registration procedure, thanks to an optical tracker (*i.e.*, NDI Polaris Spectra, Ontario, Canada), will be accomplished with a hand-eye calibration approach in an iterative form with calibration algorithms, as already presented by Dornaika et al. [8] and Strobl et al. [9]. An accuracy lower than about 1mm in position and 0.5° in orientation has been obtained through the metric introduce in Strobl et al. [9]. Moreover, the data from the integrated optical sensors will be included and processed in the on-line procedure for assessing position and orientation error of the end-tools and constraining the platform to be re-registered during the procedure itself. 3D environment reconstruction will be essential for the implementation of the obstacles perception and avoidance strategies. The knowledge of the 3D structures of the operating theatre will avoid the collision of the manipulators against unplanned obstacles, such as the medical staff. In this framework an IR-based reconstruction system, *e.g.* the Microsoft Kinect depth space sensor, will be included in the platform, registered, and exploited to determine the position and distances between the robotic arm and an external objects or people in order to avoid any possible collision.

III. Conclusions

The main research efforts in therapeutic field are dedicated to reduction of invasiveness of surgical interventions and personalized medicine. The ideal and paradigmatic example of MIS is whenever the therapy can be completely non-invasive, such as, for example, in FUS. We strongly believe that robotics is the way to improve the robustness, precision, repeatability and reproducibility of FUS, which is used currently in the treatment of uterine fibroids as well as for painful bone metastases (www.fusfundation.org). Based on this consideration, the aim of FUTURA is to develop an autonomous and human-supervised robotic platform to perform a completely non-invasive therapy by means of FUS applied to deformable tissues. The robustness, safety, and accuracy of FUS procedures will be enhanced by exploiting robotic assistance, through closed-loop control – by means of real-time therapy monitoring and self-learning procedures – thanks to specifically developed algorithms. Furthermore, an additional expected outcome of the FUTURA project is improving safety and acceptability of multifunctional robotic platforms into the surgical theatre, with the final goal to allow a FUS widespread diffusion into routine clinical applications. The WHO organization estimates that in Europe of 2020 there will be an increase of 24% in the annual incidence of males suffering from cancer from 1.5 million cases in 2002 to 1.864 million cases and a 15% increase in the annual incidence of females suffering from cancer from 1.321 million to 1.521 million, driven primarily by the aging of the population. FUS has the potential to reduce the number of physician/hospital visits, treatment sessions, thus significantly reduce the burden to the healthcare system. Furthermore, the good understanding of biological effects of FUS, reflected on an economic progress: the global market of Ultrasound ablators is expected to grow with a compound annual growth rate of 13.1% to reach the level of 1,759 million USD by 2016 (from "Ablation Technology Market", Markets and Markets, 2012). Finally, surgical robot device markets amounted to $2.4 billion only in 2011 and are anticipated to reach $8.5 billion by 2018 (from WinterGreen Research, Inc., 2012).

Acknowledgments

The research leading to these results has received funding from the European Community's Seventh Framework Programme (FP7/2007-2013) under grant agreement 611963 (FUTURA Project). The authors wish to thank the FUTURA consortium (www.futuraproject.eu/beneficiaries).

References

[1] P. Dario. B. Hannaford. A. Menciassi. Smart surgical tools and augmenting devices. (2003) *Robotics and Automation. IEEE Transactions on.* 19(5): 782-792.

[2] R.H. Taylor. and D. Stoianovici. Medical robotics in computer-integrated surgery. (2003) *IEEE Transactions on Robotics and Automation* 19(5): 765-781.

[3] H. Ren. and M. Q. H. Meng. Investigation of the Essentials for Integrating Off-The-Shelf Industrial Robotics in Precise Computer-Assisted Surgery. (2011) *Journal of Mechanics in Medicine and Biology* 11(5): 1113-1123.

[4] A. M. Okamura Methods for haptic feedback in teleoperated robot-assisted surgery. (2004) *Industrial Robot: An International Journal* 31(6): 499-508.

[5] A. Marbán. A. Casals. J. Fernandez. J. Amat. Haptic Feedback in Surgical Robotics: Still a Challenge. ROBOT2013: First Iberian Robotics Conference 2014. Springer.

[6] J.-F. Aubry. K. B. Pauly. et al.. The road to clinical use of high-intensity focused ultrasound for liver cancer: technical and clinical consensus. (2013) *Journal of Therapeutic Ultrasound*. 1(1): 13.

[7] B. Siciliano, O. Khatib, Springer handbook of robotics, Springer (2008).

[8] K.H Strobl and H. Gerd. Optimal hand-eye calibration. Intelligent Robots and Systems. (2006) *IEEE/RSJ International Conference on. IEEE*.

[9] F. Dornaika and H. Radu. Simultaneous robot-world and hand-eye calibration. (1998) *Robotics and Automation. IEEE Transactions on*. 14(4): 617-622.

Development of a hydraulic driven, 3-DOF, surgical instrument

Timo Cuntz
Medical Assistance Systems
Fraunhofer PAMB
Mannheim, Germany
Timo.Cuntz@ipa.Fraunhofer.de

Auguste van Poeelgest
Control Systems in Medical Engineering
Fraunhofer PAMB
Mannheim, Germany
Auguste.van.Poelgeest@ipa.fraunhofer.de

***Abstract*—As the use of minimal invasive surgery techniques has increased steadily, the development of new tools for these procedures has stagnated. Indeed a new generation of surgical instruments, with tips that have multiple degrees of freedom, has been developed. However they are facing so many technical problems, that none have been able to establish themselves in the medical market. To overcome the problems these instruments are facing, a micro hydraulic power transmission system has been developed. With these driving units it was possible to design an instrument for minimal invasive surgery with a tip which is movable in 3 degrees of freedom (DOF) and being light in weight, small in size and powerful in movements and gripping.**

Keywords— MIS-Systems, articulating instrument, NOTES, man-machine-interface, micro actuators, hydraulic actuators

I. Introduction

Surgical techniques for minimally invasive surgery have seen major developments over the last two decades. However, the tools and instruments for laparoscopic surgery have not kept up with this progress. The equipment setup in this domain has remained largely unchanged since the days in which this surgical method was being introduced. Besides some exceptions, the instrumentation consists of rigid rod-like graspers and scissors. Nonetheless, minimally invasive procedures have continued to evolve and new operation modes have been developed such as Single Port and NOTES surgery. These procedures aim to reduce complications related to port placement, but they make high demands on the instrumentation setup [1].

Innovative, novel instruments have been developed such as articulating and flexible shaft instruments. However, none of them have been successfully applied due to several weaknesses: limited force transmission, lack of powerful grasp, and complicated handling of the multiple DOFs. Due to limited force transmission, impossibility of robust grasping and complicated handling, these mechanical multi degree-of-freedom (DOF) instruments have never really found their application [2].

By integrating drives in the instrument's handle to actuate the tip's DOFs it was possible to overcome some of the disadvantages described above. Yet it created new problems due to the weight of the motors. Hence this solution failed before it could become widespread. This is supported by the fact that one of these systems has already been withdrawn from the market [3].

II. Methods

To determine the specifications of a handheld surgical instrument with multiple degrees of freedom at the tip, requirement analyses have been conducted (see Table 1).

Table 1: List of requirements for instruments for minimal invasive surgery

	Nr.	Requirements	Description /Quantification
		Claim (C), Request(R)	
	1	Size/Geometry	
C	1.1	Diameter shaft	<10mm
R			<5mm
C	1.2	Diameter actuator	<8mm
R			<3mm
C	1.3	Travel of actuator	3mm
R			10mm
C	1.4	Fixed length of the tip of a flexible instrument	<40mm
	2	Kinematics	
C	2.1	Actuation of gripper	Gripping or bracing
R			Gripping and bracing
	2.2	Maximum time to open and close	0,5 sec
C			
R	2.3	Bendable instrument tip	
R	2.4	Turnable instrument tip	
	3	Forces	
C	3.1	Min. closing force of branch	>35N
C	3.2	Min. bracing force of branch	>20N
C	3.3	Force applicable by hand	<50 N
C	3.4	Clamping force constant	>10 sec.
	4	Energy	
R	4.1	Flexible energy transmission between hand piece and end effector	
R	4.3	Bending radius connection tube	<20mm
	5	Materials	
F	5.1	Hydraulic fluid	Biocompatible, sterilizable
F	5.2	Building materials	Biocompatible, sterilizable
	6	Safety	
C	6.1	Leakage	Very low leakage
C	6.2	Working temperature	0°C -50°C
	6.3	Temperature while transport or storage	- 20°C - 80°C
R			
	7	Maintenance	
C	7.1	Possible to clean, disinfect, sterilize,	

Together with the problems existing instruments are facing, this breakdown has shown that it is impossible to develop mechanically driven instruments that fit the specifications. The main reason being the combination of holding the instrument, moving and applying force on the instrument's tip for multi degrees of freedom.

To solve this, mechanical decoupling of the movements and forces applied by the doctor to the user interface and the movements and forces working on the instrument's tip is necessary. This decoupling necessitates built-in drives in the instrument [4]. Hence possible drive solutions have been explored. As result, actuation with micro hydraulic systems was the only solution to fulfill the requirements listed above.

Subsequently the usability of hydraulic systems for medical applications was verified. Therefore potential hydraulic fluids compatible with use in medical devices have been examined. Then the feasibility of sterilizing hydraulic systems filled with these fluids was investigated [5].

III. Results

Having proven the feasibility of hydraulics to drive surgical instruments, the next logical step was to develop instruments with such actuators. For example a hydraulic driven, flexible instrument with a tip diameter of 2.7mm, that is shown in Figure 1 [4].

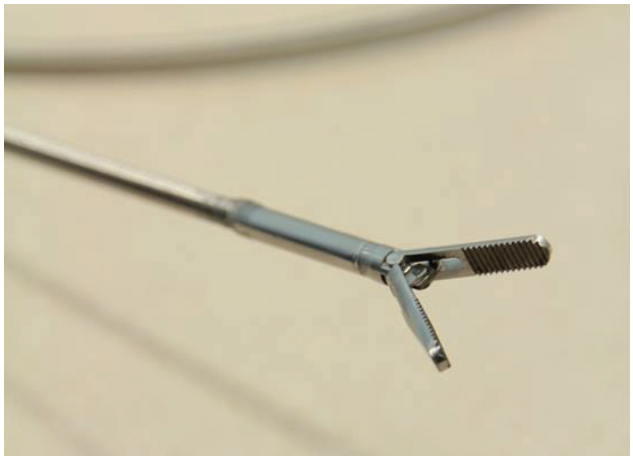

Figure 1: Grasper of a hydraulic driven 2.7mm Ø Instrument [5]

This instrument is small enough to be inserted in a 3.1mm working channel of a flexible endoscope (see Figure 2), while enabling gripping forces of more than 50N.

Figure 2: hydraulic driven 2.7mm Ø instrument used in a 3.1mm Ø working channel of a flexible endoscope

With the knowledge gained from designing this gripping instrument powered by micro hydraulic drives, it was possible to develop the surgical instrument tip with 3 hydraulically actuated DOF shown in Figure 3.

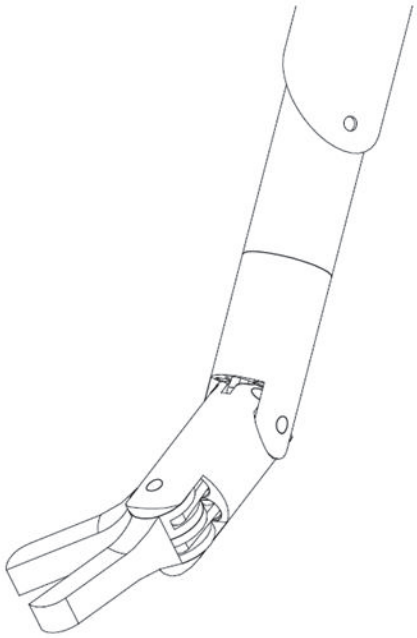

Figure 3: 3 DOF instrument tip, actuated by 6 hydraulic cylinders

The movements of the tip are powered by 6 integrated micro hydraulic cylinders with a piston diameter of 2.45mm. Being designed for a maximum working pressure of 200 bar they can produce an actuator force of 94N each. Sealed with

micro O-rings which are lubricated with medical white oil their average internal friction can be kept below 2N, about 2% of the total actuator force. All the actuators and mechanical parts can be integrated in a cylindrical shape of 8 mm in diameter.

The single cylinders are powered by hydraulic syringe pumps each cylinder connected with an own pump over a closed circuit. For filling and bleeding out of the air the circuit can be opened with valves. More detailed information about the control principle and relating data are given in [6].

To operate and hold an instrument equipped with this tip, a custom handle was developed. This novel human-machine-interface enables the control of 3 DOF with forefinger and thumb while being supported by the remaining three fingers (see figure 4).

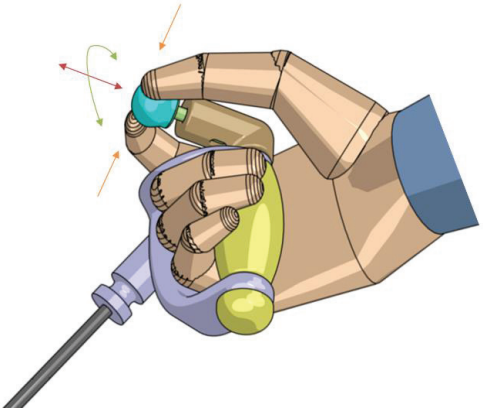

Figure 4: Concept of a new interface for multi DOF instruments

IV. Discussion

It was feasible to develop solutions making hydraulics suitable for use in medical devices. Potential hydraulic fluids meeting with the requirements in medical applications were found. It was also shown that sterilizing the hydraulic systems is not an issue as the complete system filled with hydraulic fluid can be sterilized in the autoclave. The developed cylinders were miniaturized down to outer diameters below 3mm including housing. Such dimensions allowed for flexible shaft instruments suitable to fit through the working channels of flexible endoscopes.

The main advantages of hydraulic systems are exhibited when they power instruments with multiple DOFs at the tip (shown in Figure 5).

Figure 5: New hand held multi DOF instrument for MIC

As even small hydraulic cylinders with diameters of 2.5mm can produce forces up to 100N, it is possible to place the actuation of the tips DOF directly in the tip.

As the hydraulic power can be transmitted through thin tubes, the power units to produce the hydraulic pressure can be placed beside the operating table. So it is possible to build powerful surgical instruments not exceeding the weight of those being actuated by hand.

V. Conclusion

A hydraulically actuated surgical instrument with a multiple DOF tip was designed. As these systems can be built as lightweight, powerful and small assemblies, they have the potential to overcome the majority of problems that similar mechanically or electrically powered instruments face.

References

[1] R. Autorino, R. J. Stein, E. Lima, R. Damiano, R. Khanna, G.-P. Haber, M. a White, and J. H. Kaouk, “Current status and future perspectives in laparoendoscopic single-site and natural orifice transluminal endoscopic urological surgery,” International journal of urology : official journal of the Japanese Urological Association, vol. 17, no. 5, pp. 410–31, May 2010.

[2] P. Dasgupta, J. Fitzpatrick, R. Kirby, and I. S. Gill, “New Technologies in Urology”. Springer, 2010.

[3] Terumo, “Announcement on homepage”, 2014.[Online] Available: http://www.kymerax.com/

[4] Cuntz T., James G., Valkov V., Sanagoo A., Kaltenbacher D., “Next generation surgical instruments powered by hydraulics”, Biomedizinische Technik/Biomedical Engineering, 09/2013

[5] Cuntz T., “Untersuchungen zur Eignung mikrohydraulischer Antriebe für die minimal invasive Chirurgie”, in press

[6] Comella L., Rothfuss A., Van Poelgeest A., “Development of a modular control concept for a hydraulic 3-DOF surgical instrument”, CRAS, Oct. 2014

Design and manufacturing of a 2-DOF force sensing needle for retinal surgery

A. Gijbels, S. Colson, D. Reynaerts and
E. B. Vander Poorten
Department of Mechanical Engineering
University of Leuven
Leuven, Belgium

P. Stalmans
University Hospital Leuven
Leuven, Belgium

***Abstract*—Retinal Vein Occlusion is a common retinal vascular disorder which can cause severe loss of vision. Retinal vein cannulation is a promising treatment, but given the scale and the fragility of retinal veins on one side and the surgeon's limited positioning precision and force perception on the other side, it is considered too risky to perform this procedure manually. The authors previously reported on the development of both a robotic comanipulation and telemanipulation system which have been shown to augment the surgeon's positioning precision. This paper reports on the development of a force-sensing needle instrument with 0.5mN resolution to tackle the problem of limited force perception during retinal vein cannulations.**

I. Introduction

Retinal surgery is considered as an extremely challenging type of surgery because of the scale and the fragility of the retinal anatomy. For some diseases, such as Retinal Vein Occlusion (RVO), the most promising procedure is even too difficult and risky to perform, forcing the surgeons to rely on less effective procedures. RVO is an eye condition which affects an estimated 16.4 million people worldwide [1]. It is the second most common retinal vascular disorder after diabetic retinal disease. The disease occurs when a clot is formed in a retinal vein (Fig. 1). This causes the patient to slowly lose his/her sight. Today, there is no proven effective treatment clinically available for this disease [2]. A promising treatment is retinal vein cannulation (Fig. 1). During this procedure, the surgeon's objective is to inject an adequate dose of t-PA, a clot-dissolving agent, directly into the occluded retinal vein. A surgical microscope is placed above the patient's eye in order to have visual feedback on the surgical scene. Several research groups previously reported on successful cannulations in animal and human models [3,4]. However, due to safety issues, the procedure is not performed clinically today. The needle must be inserted into a fragile vein with a diameter of only 400µm or smaller [5] and kept there for several minutes before the fluid is fully injected. The limited positioning precision and force perception of the surgeon make it extremely difficult to correctly insert and keep the needle inside the vein without damaging it. Surgeons suffer from physiological tremor. Riviere et al. [6] reported on tremor rms amplitudes of 182µm. Gupta et al. [7] showed that 75% of the interaction forces between the instrument and the retina are lower than 7.5mN. The surgeon can only feel these forces in 19% of the cases. This demonstrates that micro surgeons solely rely on visual feedback for these tasks.

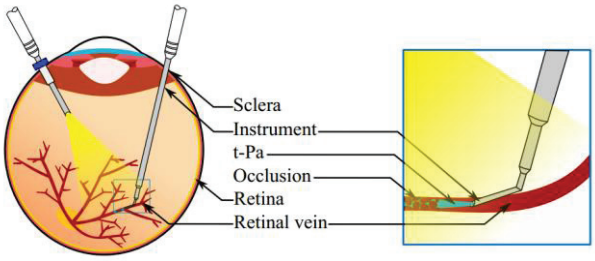

Fig. 1. Retinal Vein Cannulation: a hollow needle is guided through the sclera and used to inject a clot-dissolving agent into an occluded vein which is causing RVO.

II. Robotically Assisted Retinal Surgery

A fair number of robotic systems for retinal surgery have been reported in literature [8-14]. The authors previously reported on the development of a robotic comanipulation system [15] and a telemanipulation system [16] for retinal surgery (Fig. 2). Using either of these systems was shown to significantly increase the positioning precision during a positioning task in an eye simulator [17]. The aim of this work is to develop a force-sensing needle instrument to deal with the problem of limited force perception during a retinal vein cannulation.

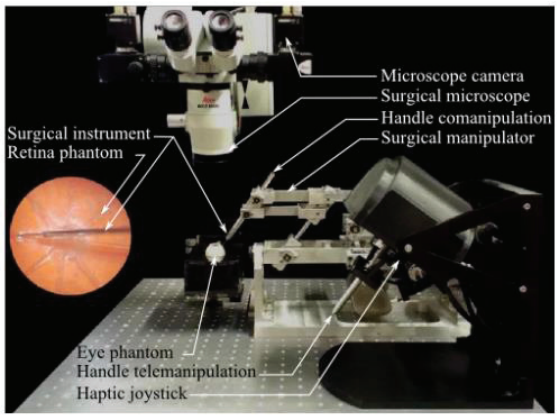

Fig. 2. Overview on the developed robotic systems.

III. FORCE SENSING TOOLS FOR RETINAL SURGERY

Ergeneman et al. [18] investigated vessel puncture forces during in vivo cannulations in vessels of a fertilized chicken egg CAM membrane. Force magnitudes between 2mN and 15mN are reported for the targeted vessel diameters (100µm-400µm). Given these imperceptible force levels, there is a high risk of a double penetration of the occluded vein when trying to perform a retinal cannulation (Fig. 3(a)). With a force-sensing needle in place, the moment of the first puncture could be registered. Event-based force feedback on the comanipulation or telemanipulation device and/or auditory feedback can be implemented to prevent the surgeon from making a double penetration.

A force-sensitive cannulation needle has not been developed earlier, mainly because of manufacturing problems. First, it is extremely difficult to produce a needle with a tip diameter small enough to cannulate most of the retinal veins. Second, the force sensor should be integrated into the portion of the needle which is inside the eye during the cannulation. This is because for a handle-mounted force sensor it would be practically impossible to distinguish the force at the tip of the needle from the contact force at the sclera. Latter force is typically an order of magnitude higher [19]. Iordachita et al. previously reported on the development of pick instrument for retinal peeling which consists of a 3-DOF force sensor integrated into the shaft of the instrument [20]. It uses a flexure and four Fiber Bragg Gratings (FBGs) in order to measure force with a resolution of 0.25mN. FBGs are small (80µm-200µm diameter), extremely precise, stable, easy to sterilize and immune to electrical noise. This work reports on the development of a 2-DOF force sensing cannulation needle using a similar technique.

IV. DEVELOPMENT OF A 2-DOF FORCE SENSING NEEDLE

A. Main design specifications

Since the targeted veins have a diameter of 100µm-400µm, a maximum allowable needle tip diameter of 80µm is considered. Retinal surgeons suggested preparing needles of which the tip is bended 45° with respect to the tool shaft (Fig. 3(b)). When a straight needle is used the vein walls are pushed against each other during the insertion such that a double penetration is almost inevitable (Fig. 3(a)). Since it takes around 2mN to insert the needle into the vein a measurement accuracy and precision of 0.2mN are considered to be sufficient.

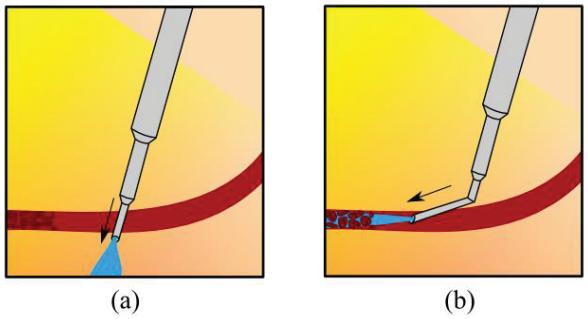

Fig. 3. (a) The use of a straight needle easily results in a double penetration of the occluded vein. (b) The risk of double penetration can significantly be lowered by using a bended needle.

B. Design

While the tool tip should be as thin as 80µm having a rigid instrument is desirable for easy handling and in order to obtain a good positioning precision. Therefore the needle is split into multiple stainless steel tubes (Fig. 4(a)). The tool shaft is a 4cm long tube and has an outer diameter of 550µm. These dimensions are comparable to those of the tool shaft of conventional instruments. The needle tip is 3mm long and has an outer and inner diameter of 80µm and 35µm respectively. Further, it consists of a 15° bevel to simplify the insertion process. Both tubes are connected via an intermediate tube which has a bending angle of 45°. To measure the interaction forces at the tip three FBGs are integrated into the tool shaft. The tool shaft directly acts as the flexure of the force sensor resulting in a 0.5mN resolution for lateral forces.

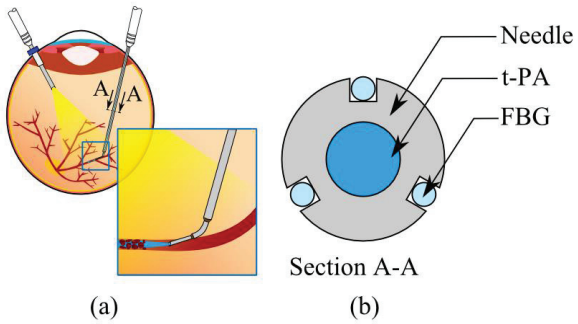

Fig. 4. (a) The developed instrument is a bended needle which is an assembly of three stainless steel tubes. (b) Crossectional view A-A of the needle displayed in (a). Three FBGs are integrated into the tool shaft to measure the lateral forces while eliminating the effect of temperature on the readings.

Direct measurement of axial forces is not possible because of the high axial stiffness of the shaft. However, as previously mentioned this is not considered to be a problem for two reasons. Firstly, the needle is bended thus that the force that acts on the needle during a cannulation is not merely an axial force but also consists of measurable lateral force components. Secondly, it is the event of a penetration that should be registered instead of the actual level of force acting on the needle tip. Theoretically two FBGs are sufficient to measure the lateral forces. However, a third FBG is used to

differentially measure the lateral forces such that the effect of temperature on the readings can be eliminated. Lastly, although not the case in this work, it is worth mentioning that if also geometrical information is used, more in particular the knowledge about the relative position and orientation of instrument and vessel e.g. obtained through image processing, it becomes possible to have a more accurate estimate of the actual amplitude of the cannulation.

C. Production

Commercially available straight drawn tubes are used to manufacture the needle. The outer tip diameter of 80µm is reached by reducing the diameter of a 120µm-tube using a µEDM-machine. The grooves are made inside the tool shaft by using a disc saw. The FBGs have an outer diameter of 80µm and are manufactured by the company FBGS Belgium. A Micron Optics SM-130 interrogator is used to send light into the fibers and to read out the reflected spectrum in order to derive the strains in the shaft. It is both time consuming and expensive to make a needle shaft with integrated FBGs. Since the needle tip is fragile and thus easy to break during experiments, thirty needle inserts which consist of the two smallest tubes have been manufactured (Fig. 5). These inserts can be glued into the tool shaft. When an insert breaks it can easily be replaced such that the tool shaft can be reused. Fig. 6(a) depicts a detail of the needle tip. Fig 6(b) depicts a detail of one of the shaft grooves with a FBG glued inside.

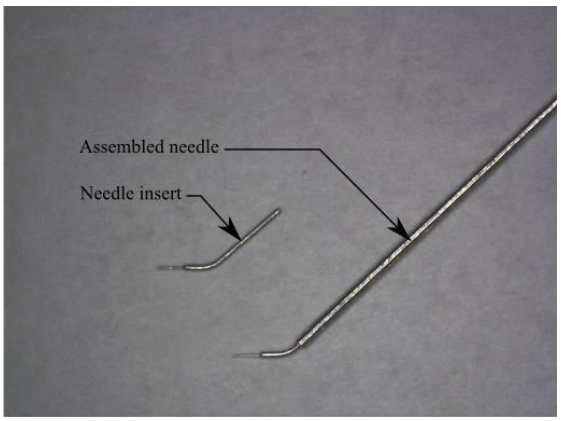

Fig. 5. View upon assembled force-sensing needle and a needle insert

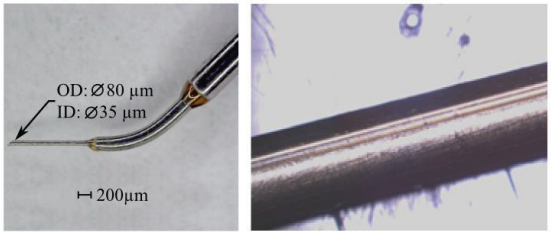

Fig. 6. (a) Detail of the needle insert. (b) FBG glued inside a groove in the tool shaft.

D. Preliminary tests results

After the sensor was calibrated, the resolution and range of the sensor were measured by putting different test weights at the needle tip while the needle shaft was kept horizontal. Fig. 7 shows that the sensor is able to distinguish forces from 0.5mN upto 5mN. Next the temperature stability of the sensor was measured by exposing the instrument to a temperature rise of 15°C by putting it into hot water. Fig. 8 shows the apparent lateral force measured. The time constant for stabilization of the sensor readout is 2,5s. This is acceptable since a temperature shock of 15° only takes place when entering the eye while it takes more than 2,5s to carefully approach the retina once inside the eye. Thus, at the moment of puncture the effect of the temperature shock on the force readings will be eliminated.

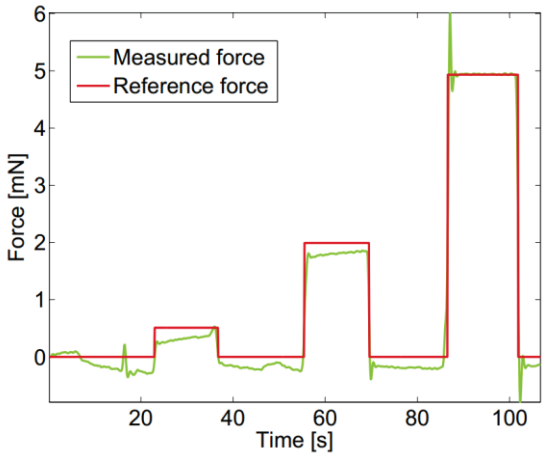

Fig. 7. Lateral force measurement when applying different test weights on the needle tip.

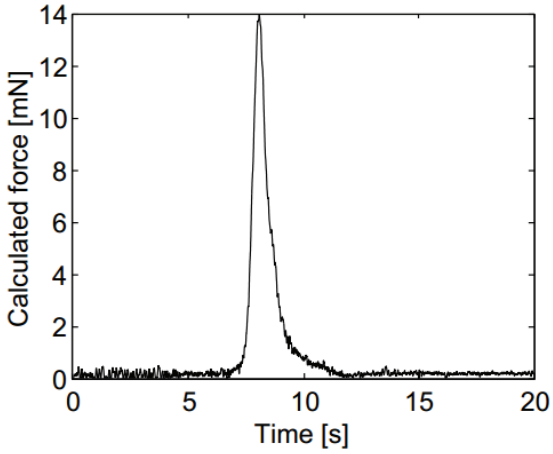

Fig. 8. Apparent lateral force measured during a temperature shock of 15°C.

V. Conclusion and Future Work

This work reported on the development of a force-sensing needle instrument to assist surgeons during a retinal vein cannulation. The needle is foreseen of a three FBGs which are integrated into an assembly of three stainless steel tubes. Preliminary experiments show that the sensor has a resolution

of 0.5mN and that the sensor can compensate for changes in temperature in a reasonable amount of time. In the near future, the force measurement will be used to allow a robotic system to detect the moment of vein penetration in order to keep the surgeon from both making a double penetration. This could be done e.g. by using event- based force feedback and/or auditory feedback.

ACKNOWLEDGMENT

This work was supported by an FP7-People Marie Curie Reintegration Grant, PIRG03-2008-231045 and by a PhD grant from the Institute for the Promotion of Innovation through Science and Technology in Flanders (I.W.T.-Vlaanderen), 101445.

REFERENCES

[1] R. Sophie, "The prevalence of retinal vein occlusion: Pooled data from population studies from the united states, europe, asia, and australia," Ophthalmology, vol. 117, pp. 313– 319, 2010.

[2] B. Nilufer and B. Cosar, "Surgical treatment of central retinal vein occlusion," Acta Ophthalmologica, vol. 86, pp. 245–252, 2008.I.S.

[3] J. Weiss and L. Bynoe, "Injection of tissue plasminogen activator into a branch retinal vein in eyes with central retinal vein occlusion," Ophthalmology, vol. 108-12, pp. 2249–2257, 2001.

[4] L. A. Bynoe, R. K. Hutchins, H. S. Lazarus, and M. A. Friedberg, "Retinal endovascular surgery for central retinal vein occlusion: Initial experience of four surgeons," Retina, vol. 25, pp. 625–32, 2005.

[5] F. Skovborg, V. Nielsen, E. Lauritzen, and O. Hartkopp, "Diameters of the retinal vessels in diabetic and normal subjects," Diabetes, vol. 18(5), pp. 292–298, 1969.

[6] C. N. Riviere and P. S. Jensen, "A study of instrument motion in retinal microsurgery," in Conf. IEEE Eng. Med. Biol. Soc, pp. 59–60, 2000.

[7] P. Gupta, P. Jensen, and E. Juan, "Surgical forces and tactile perception during retinal microsurgery," Proc. of the Second Int. Conf. on Medical Image Computing and Computer Assisted Intervention (MICCAI), pp. 1218–1225, 1999.

[8] S. Yang, R. A. MacLachlan, and C. N. Riviere, "Design and analysis of 6 dof handheld micromanipulator," Proc. IEEE Int. Conf. on Robotics and Automation (ICRA)., pp. 1946 – 1951, 2012.

[9] A. Uneri, M. Balicki, J. Handa, P. Gehlbach, R. Taylor, and I. Iordachita, "New steady-hand eye robot with microforce sensing for vitreoretinal surgery research," Int. Conf. on Biomedical Robotics and Biomechatronics, pp. 814–819, 2010.

[10] S. Charles, H. Das, T. Ohm, C. Boswell, G. Rodriguez, R. Steele, and D. Istrate, "Dexterity-enhanced telerobotic microsurgery," Proc. of the IEEE Int. Conf on Advanced Robotics, pp. 5–10, 1997.

[11] W. Wei, R. Goldman, N. Simaan, H. Fine, and S. Chang, "Design and theoretical evaluation of micro-surgical manipulators for orbital manipulation and intraocular dexterity," ICRA, pp. 3389–3395, 2007.

[12] A. Guerrouad and P. Vidal, "Smos: Stereotaxical microtelemanipulator for ocular surgery.," Medicine and Biology Society, pp. 879–880, 1989.

[13] H. Meenink, R. Hendrix, P. Rosielle, M. Steinbuch, and M. de Smet, "A master-slave robot for vitreo-retinal eye surgery," Proc. of the 10th Int. Conf. of European Society for Precision Engineering and Nanotechnology, 2010.

[14] M. Nasseri, M. Eder, S. Nair, E. Dean, M. Maier, D. Zapp, C. Lohmann, and A. Knoll, "The introduction of a new robot for assistance in ophthalmic surgery," 35th Annual Int. Conf. of the IEEE Engineering in Medicine and Biology Soc. (EMBC'13), 2013.

[15] A. Gijbels, N. Wouters, P. Stalmans, H. Van Brussel, D. Reynaerts, and E.B. Vander Poorten, "Design and realisation of a novel robotic manipulator for retinal surgery," Proc. IEEE Int. Conf. on Intelligent Robots and Systems, 2013.

[16] A. Gijbels., E.B. Vander Poorten, P. Stalmans, H. Van Brussel, and D. Reynaerts, "Design of a teleoperated robotic system for retinal surgery," Proc. IEEE Int. Conf. on Robotics and Automation, 2014.

[17] A. Gijbels., E.B. Vander Poorten, B. Gorissen, A. Devreker, P. Stalmans and D. Reynaerts, "Experimental Validation of a Robotic Comanipulation and Telemanipulation System for Retinal Surgery," Proc. IEEE RAS & EMBS Int. Conf. on Biomedical Robotics and Biomechatronics, 2014.

[18] O. Ergeneman, J. Pokki, V. Pocepcova, H. Hall, J. Abott and B.J. Nelson, " Characterization of puncture forces for Retinal Vein Cannulation", Journal of Medical Devices, 2011, vol.5, pp. 1-6

[19] A. S. Jagtap and C. N. Riviere, "Applied force during vitreoretinal microsurgery with handheld instruments," Proc. IEEE Eng. Med. Biol. Soc., 2004, vol. 4, no. 1, pp. 2771–2773

[20] X. He, J. Handa, P. Gehlbach, R. Taylor and I. Iordachita, "A submillimetric 3-DOF force sensing instrument with integrated fiber bragg grating for tetinal microsurgery," IEEE Transactions on Biomedical Engineering, vol. 61, no. 2, 2014, pp. 522-534

Neurophysiology guided single cell optical surgery

Averna A.[1], Bisio M.[1], Pruzzo G.[1], Chiappalone M.[1], Bonifazi P.[2], Difato F.[1]
l- Department of Neuroscience and Brain Technologies, Istituto Italiano di Tecnologia, Genova, Italy
2- School of Physics and Astronomy, Tel Aviv University, Tel Aviv, Israel
Corresponding author mail: Francesco.difato@iit.it

***Abstract*—Surgical protocols require unbiased localization of the pathological tissue, and precise removal or manipulation of the individuated target. In the last decades, optical methods achieved sub-cellular resolution to stimulate and monitor the physiological response of living samples, up to in-vivo applications exploiting genetically encoded optical probes. Furthermore, laser ablation systems are recognized as the more precise surgical tools. Therefore, optical approaches are emerging as powerful tools integrated in robotic-surgery systems. In the present work, we report an in-vitro model of neurophysiology guided laser surgery based on functional calcium imaging. The established experimental protocol achieved neurophysiology guided single-cell surgery precision and low-invasive single-cell optical stimulation not requiring genetically-encoded opsins.**

***Keywords*—Neurophysiology; Laser surgery; calcium imaging; single-cell optical surgery; single-cell optical stimulation.**

I. INTRODUCTION

Tissue removal or implantation of prosthetic devices requires high surgical skills, in order to recover pathological conditions currently untreatable, such as cancer tissues, or rehabilitation of damaged tissues [1]. In the first case, distinct tools are currently tested and developed to achieve precision down to single-cell resolution, in order to minimize collateral effects of surgical procedures [2]. In the latter case, intraoperative surgery demand integration of monitoring systems and actuating tools to on-line monitor the effectiveness of tissue manipulation, either to insert a prosthetic device in the right position within a tissue, or to selectively affect cellular assemblies modulating their physiological activity [3].

Development of innovative neuro-prostheses represent an emerging field in Neuroscience, combining high resolution physiological recording, computational decoding of recorded activity, and delivery of encoded stimulation signals [4]. Nowadays, brain machine interfaces (BMIs) are mainly based on acquisition and processing of electrical signals. However, the recent introduction of genetically encoded fluorescent ion indicators, and light-sensitive ion channels pave the way for the development of opto-BMIs, based on optical signals and thus achieving sub-cellular resolution. Although, the sub-cellular optical resolution to stimulate or monitor neurophysiological activity of opto-BMIs is incomparable to other methods, their uses are currently limited to research applications, because genetic alteration in humans are difficult or not possible yet [5].

In the present work, we report an in-vitro model of optical surgery guided by fluorescence calcium imaging. We show how accurate control of laser energy delivery, combined with optical monitoring of neurophysiological activity allows targeting and dissecting a sub-cellular compartment, leaving the surrounding cells unaffected. Moreover, we show that calibrated delivery of laser pulses could provide alternative method to optically stimulate single neurons without the need of cellular genetic-manipulation. Although, the reported laser surgery protocol is applied in an in-vitro model, it allows understanding the potential impact of single-cell optical surgery to alter the local activity of neural circuits while restraining unwanted damage of surrounding neural subpopulations.

II. MATERIAL AND METHODS

A. Optical setup

The entire optical system was described in a previous work [6]. Briefly, the laser dissection source is a pulsed sub-nanosecond UV Nd:YAG laser at 355 nm (PNV-001525-040, PowerChip nano-Pulse UV laser – Teem Photonics),), whose output is modulated with the aid of an acousto-optical modulator (MQ110-A3-UV, 355 nm fused silica, AA-Opto-electronic) driven by a custom low impedance linear driver. The laser dissector has been integrated in a modified upright microscope (BX51 – Olympus) equipped with a 20x, 0.5 NA water dipping objective. A custom-made software interface based on LabVIEW (National Instruments) controlled, the UV laser intensity, pulse repetition rate, and the number of pulses delivered to the sample. Synchronization signals between devices were sent through a D/A board (PCI-6529, 24 bit, 4 channels, 204.8 kSamples/second, National Instruments), in order to synchronize CCD image acquisition (Andor DU-897D-C00), sample positioning trough motorized stage (assembled 3-axis linear stages, M-126.CG1, Physics-Instruments), and the trigger of UV laser pulses.

B. Analysis of network spontaneous activity

Custom software running in MATLAB (The Mathworks, Natick, USA) [7] was used for the automatic identification of the cells loaded with the calcium indicator, for the extraction of their fluorescence signals. The functional connectivity map of the network was reconstructed trough a pair-wise correlation

analysis of the onset time series extracted from the calcium imaging data, before and after single-cell laser ablation.

C. Neuronal culture preparation

All the experimental protocols were approved by the Italian Ministry of Health. Primary cultures were obtained from embryos of pregnant rat at embryonic day 18 (Sprague–Dawley derived by Charles River in 1955, IGS). Specifically, we used a cellular solution at the concentration of 1500 cells/µl and we placed 1 ml of cellular suspension on the culture support (Petri dishes). So, the final nominal density resulted to be around 3000 cells/mm^2. Fluorescence calcium imaging was performed with Fluo-4AM dye (Invitrogen) loaded cells (5 mM for 10 min), starting from at 21 days in vitro.

III. Results

Accurate calibration of needed laser power to produce local material ablation is usually based on analysis of structural changes. However, such calibration give a good estimate of ablated volume, but it could not correspond to the effective damaged region when laser dissection is applied on living sample, where the link between structure and function is highly correlated. In Fig. 1, we illustrate an example of laser ablation within a neural network. We deliver about 50 pulses (the laser spot is shown at 20 second in Fig.1) with energy of 200 nJ per pulse, and a repetition rate of 100 Hz. After the delivery of optical pulses, we observed a propagation of calcium wave within the network extending far from the ablation site. Such calcium wave is due to the leaking of extracellular solution in the ablated and neighboring cells, thus producing strong calcium mediated electrophysiological signal propagating within the network.

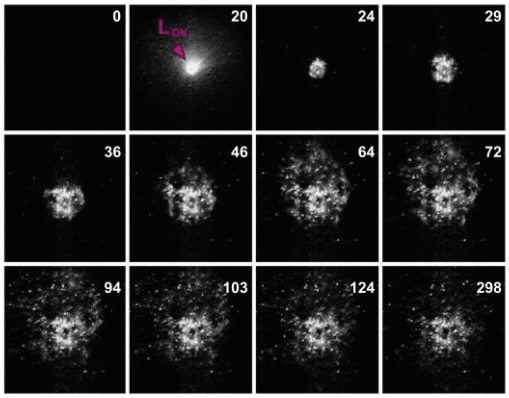

Fig. 1. Fluorescence images of a homogenous neural network. The intensity proportional to the fluctuation of calcium signal (F-F_0, with F_0 equal to the first frame) is reported in the different consecutive panels. The violet arrow depicted with L_{on} indicates the position of the UV laser focus spot. The average power delivered at the sample is 20 µW. We delivered 50 UV light pulse, at pulse-repetition rate of 100 Hz. The shock calcium wave spreads in all directions through the whole homogeneous culture. The cells directly affected by the UV laser presented saturated calcium signal, even after calcium wave propagation. Numbers indicate seconds. The field of view is 200 x 200 µm. Time lapse calcium imaging was acquired at 10 Hz. The shock wave spreads in all directions through the whole homogeneous culture.

After few minutes the calcium wave disappears, many cells recover their initial value of fluorescence signal. However, cells around the ablation site present high level of calcium signal. These cells suffered a huge amount of calcium influx from the extracellular solution, and therefore their functionality could be hampered. Therefore, the damaged region during laser dissection could extend furthermore the ablation site (see last panel in fig. 1).

A. Single-cell laser ablation

Calcium imaging does not only provide the fluctuation of intracellular calcium concentration correlated with the electrophysiological activity of the network; the basal level of fluorescence signal furnishes a direct map of the network topography with sub-cellular resolution. Therefore, accurate targeting of ablation site is achievable within the network. We combine such high resolution map, with an accurate control of optical pulses energy, and number of pulses delivered to sample, in order to obtain a confined ablation site with single-cell precision [8].

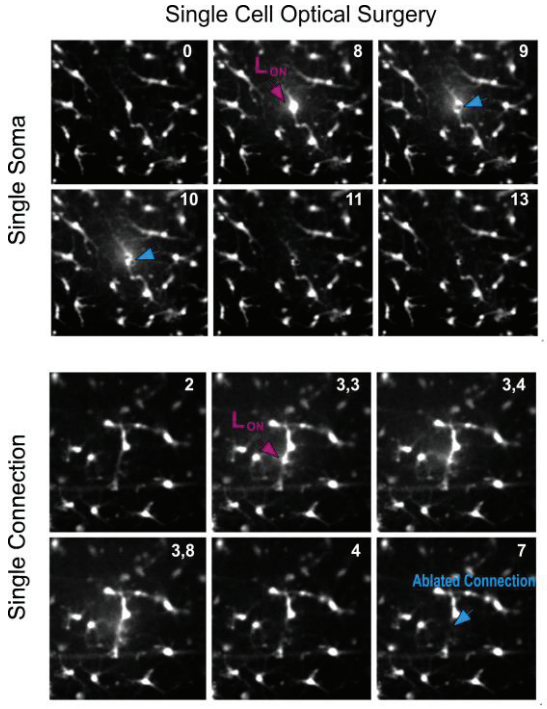

Fig. 2. Fluorescence images of a homogeneous neural network. In the upper panel the optical surgery of a single cell soma trough micro-bublle cavitation (indicated with cyan arrows) is shown. The violet arrow represents the laser spot position and start of optical pulses delivery. In the lower panel, we show ablation of single neuronal connection. The field of view on both panel is 250 x 250 µm. Time lapse calcium imaging was acquired at 10 Hz. Numbers indicate seconds.

In fig. 2, we report two example of single cell optical surgery. In the upper panel, we show the ablation of a single cell soma trough laser induced micro-bubble cavitation. We deliver about 70 pulses (the laser spot is indicated in fig. 2 with a violet arrow depicted with L_{on}) with energy of 25 nJ per pulse, and a repetition rate of 100 Hz. In the lower panel, we show

ablation of a single neuronal connection within the neural network. In this case, we delivered 60 pulses, with a slightly lower energy per pulse (22 nJ). In both cases, the neighboring cells are unaffected.

.

B. Neurophysiology guided single-cell surgery

Once achieved single cell resolution, either in monitoring and manipulating single neuronal units in a neural network, we tried to target such high resolution optical surgery trough functional neurophysiological measurements. Therefore, we acquired spontaneous activity of a subpopulation of neural network by fluorescence calcium imaging, and we analyze the functional connectivity within the network before perform laser surgery.

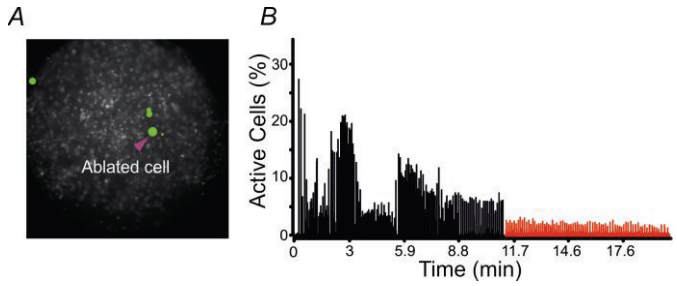

Fig. 3. A) Field of view (0.8x0.8 µm) showing a subpopulation of cells loaded with the calcium indicator Fluo4. The five green spots correspond to the cells with the higher direct functional connectivity (see section "Materials and Methods"), while the arrow indicates the ablated cell (i.e. the one with the highest functional connectivity). B) In black, the graph reports the percentage of cells activated within each time frame before the laser ablation. In red, it reports the percentage soon after the laser ablation (about 5 minutes after cell ablation). Time lapse calcium imaging was acquired at 57 Hz

Fig. 3A shows the fluorescent image of a specific field of view of a neuronal subpopulation presenting sustained calcium dynamics within the network. In the selected field of view (fig3A), we detected 532 cells. After the analysis of network spontaneous activity, we identified five cells with the higher direct functional connectivity (see section "Materials and Methods"). They have been marked with five green disks (see fig. 3), of which the dimension is correlated to the degree of cell connectivity. In order to test single cell laser surgery efficiency, we decide to ablate the cell with the higher functional connectivity (indicated by violet arrow), and to monitor the network spontaneous activity after the surgical procedure. Fig. 3B reports the percentage of neurons activated per time, during a 20 minutes recording of spontaneous activity covering the time before and after the single cell ablation (in black before, in red after). It is worth notice that, after performing laser ablation, the percentage of active cells during spontaneous activity decreases. An average value has been computed within a time window of about 6 minutes right before and after the laser ablation: before laser ablation about 33% of cells within the field of view where involved in the spontaneous activity of the network; after ablation the number of cells reduced to 27%. Considering that we dissect one cell out of a total number of about 500 cells, we observed a decrease of about 20% of the number of cells involved in the spontaneous activity of the neuronal subpopulation.

C. Single-cell laser stimulation

The results presented in fig. 3 suggested us that efficient modulation of network dynamics could be achieved even by manipulating a single neuronal units. Therefore, we tested if the laser surgery system could be calibrated to perform no-invasive single cell optical manipulation.

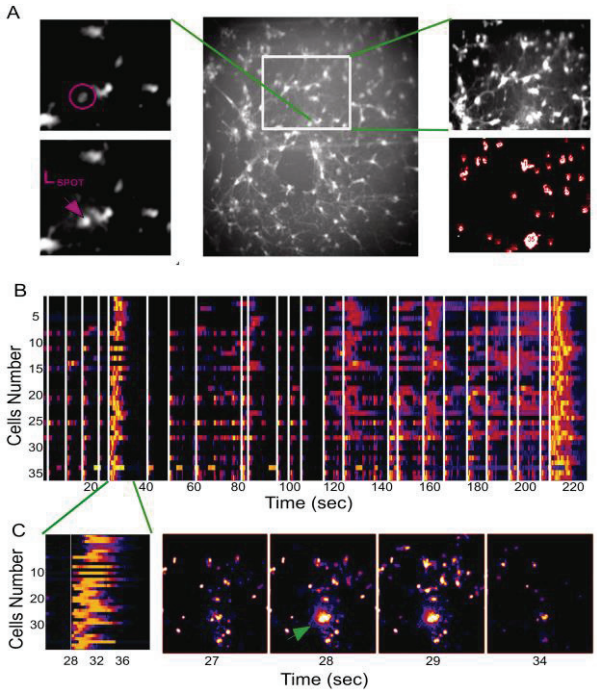

Fig. 4. A) Field of view (0.7x0.8 µm) showing a subpopulation of cells loaded with the calcium indicator Fluo4. On the left, we show the stimulated cell (highlighted by violet circle) and the position of the laser spot on it. On the right side, we report the subpopulation of neuron surrounding the stimulated cell, and the corresponding segmented image used to recognize the cell bodies. B) Raster plot of calcium fluctuation in cell bodies illustrate on the right side of panel A (white lines represent the time of laser stimulation). C) A zoom of the raster plot in B, and the field of view (200x230 µm) around the stimulated cell showing the calcium fluctuation during a single laser stimulus event. Green arrow indicates the position and onset of laser stimulus. Time lapse calcium imaging was acquired at 10 Hz. Numbers indicate seconds.

With this aim we used optical pulses with lower energy (7 nJ) and higher repetition rate (300 Hz), to fine tune the total energy delivered to the cell, and the time of pulses delivery, to achieve reversible cell membrane optoporation [9]. In such a way, during membrane optoporation influx of extracellular solution (with higher calcium concentration respect to intracellular solution) could produce an instantaneous calcium wave inside the single cell, mimicking a direct stimulation of the cell itself. Fig. 4 shows a field of view of the neural network. On the left side of panel A, we illustrate the cell we choose to stimulate, and the laser spot on it. On the right side of panel A, we show a neuronal subpopulation around the stimulated cell, and the corresponding segmented image used to recognize the cell bodies. In panel B, we report the raster plot of calcium fluctuation in the recognized cell bodies, during repetitive single-cell laser stimulation (white lines in the raster plot represent the times of laser stimulation). We

perform 29 times laser stimulation on the same cell on a time window of about 5 minutes (we delivered between 150 and 300 pulses per stimulus). In panel C, we can observe how during laser stimulation the surrounding cells present increased signal, and how after laser stimulation the cell recover to a low level of calcium signal. Moreover, we can observe how the cells, included the stimulated one (cell number 35), maintain their activity during the whole time of recordings (see raster plot in fig.4B), suggesting us that we achieved physiological calcium increase within the stimulated cell to perform non-invasive and reversible activity modulation of a neuronal subpopulation.

Conclusion

The presented results highlight how laser surgery could achieve single-cell resolution. Considering the incomparable precision of a laser ablation system, its tight fit with high resolution imaging allows precise and repeatable targeting of single cells units within a population [10]. Moreover, when the imaging provides also a functional correlate to the structure of the sample, laser surgery could achieve extreme high efficiency with respect to the area of intervention. Indeed, we could obtain a 20% network activity silencing trough ablation of only one highly connected neuron, in a population composed of 500 units. As a further achievement, we show how optical approaches could represent an alternative way to apply local neuronal stimulation without requiring genetic modification of the cells. Several technical challenges have to be yet overcome to apply the presented model in-vivo, in order to perform surgery on single-cell scale, and to provide a tool for low invasive intervention, avoiding abrupt tissue removal affecting both healthy and pathological tissue [3]. Currently, clinical application of laser surgery are mainly based on continuous wave (i. e. CO_2 lasers) or nanosecond pulsed lasers. Those instruments produce tissue ablation through linear absorption of light, inducing thermal photodamage [11]. However, precise confinement of the ablation volume through thermal affect is not achievable [12]. Moreover, infrared light (IR) has inherent physical limits in producing small focal volume compared to shorter wavelength of light. A big effort is spent to adopt the new generation of IR-femtosecond or UV-picosecond pulsed laser sources in clinical applications. These lasers provide non-thermal regime of tissue ablation based on non-linear absorption of light, achieving incomparable surgical precision, which is no more diffraction limited [13], and thus exploitable to perform single cell surgery.

The main technical challenge for clinical applications of these systems is the controlled deliver of high peak intensity pulses on the bulk tissue. Optical fibers still present problems regarding non linear effect in the fiber itself, such as the pulse broadening due to group velocity dispersion (GVD), and self-phase modulation (SPM). Hollow core fibers and pulse pre-chirping approaches are investigated as possible technical solutions [12][14]. Moreover, significant advantage could be achieved through development of robotic systems controlling mechanical and electronic devices to perform automated surgical procedure and calibrated delivery of optical pulses [15]. Considering the high cost, maintenance and complexity of a system based on femtosecond laser, optical layout based on UVA laser, as the setup presented in this work, are currently investigated as a powerful, compact and cost effective alternative [16].

Acknowledgments

This work was supported by grants from the European Union's Seventh Framework Programme (ICT-FET FP7/2007-2013, FET Young Explorers scheme) under grant agreement n° 284772 BRAIN BOW (www.brainbowproject.eu).

References

[1] M. A. Nicolelis, "Brain-machine interfaces to restore motor function and probe neural circuits," Nat. Rev. Neurosci. **4**, 417-422 (2003).

[2] L. S. Mattos and D. G. Caldwell, "Safe teleoperation based on flexible intraoperative planning for robot-assisted laser microsurgery," Conf. Proc. IEEE Eng Med. Biol. Soc **2012**, 174-178 (2012).

[3] G. M. van Dam, G. Themelis, L. M. Crane, N. J. Harlaar, R. G. Pleijhuis, W. Kelder, A. Sarantopoulos, J. S. de Jong, H. J. Arts, A. G. van der Zee, J. Bart, P. S. Low, and V. Ntziachristos, "Intraoperative tumor-specific fluorescence imaging in ovarian cancer by folate receptor-alpha targeting: first in-human results," Nat. Med. **17**, 1315-1319 (2011).

[4] P. Bonifazi, F. Difato, P. Massobrio, G. L. Breschi, V. Pasquale, T. e. Levi, M. Goldin, Y. Bornat, M. Tedesco, M. Bisio, S. Kanner, R. Galron, J. Tessadori, S. Taverna, and M. Chiappalone, "In vitro large-scale experimental and theoretical studies for the realization of bi-directional brain-prostheses," **7**, (2013).

[5] F. A. Wininger, J. L. Schei, and D. M. Rector, "Complete optical neurophysiology: toward optical stimulation and recording of neural tissue," Appl. Opt **48**, D218-D224 (2009).

[6] F. Difato, L. Schibalsky, F. Benfenati, and A. Blau, "Integration of optical manipulation and electrophysiological tools to modulate and record activity in neuronal networks" **5**, 191-216 (2011).

[7] P. Bonifazi, M. Goldin, M. A. Picardo, I. Jorquera, A. Cattani, G. Bianconi, A. Represa, Y. Ben-Ari, and R. Cossart, "GABAergic hub neurons orchestrate synchrony in developing hippocampal networks," Science **326**, 1419-1424 (2009).

[8] F. Difato, M. Dal Maschio, E. Marconi, G. Ronzitti, A. Maccione, T. Fellin, L. Berdondini, E. Chieregatti, F. Benfenati, and A. Blau, "Combined optical tweezers and laser dissector for controlled ablation of functional connections in neural networks," **16**, (2011).

[9] A. P. Rudhall, M. Antkowiak, X. Tsampoula, M. Mazilu, N. K. Metzger, F. Gunn-Moore, and K. Dholakia, "Exploring the ultrashort pulse laser parameter space for membrane permeabilisation in mammalian cells," Sci. Rep. **2**, 858 (2012).

[10] M. B. Zeigler and D. T. Chiu, "Single-cell nanosurgery" Methods Mol. Biol. **991**, 139-148 (2013).

[11] C. L. Hoy, O. Ferhanoglu, M. Yildirim, K. H. Kim, S. S. Karajanagi, K. M. C. Chan, J. B. Kobler, S. M. Zeitels, A. Ben-Yakar, "Clinical ultrafast laser surgery: Recent advances and future directions." IEEE J. Sel. Topics in Quantum Elect. 20, 2 (2014).

[12] W. S Grundfest, I. F. Litvack, T. Goldenberg, T. Sherman, L. Morgenstern, R. Carroll, M. Fishbein, J. Forrester, J. Margitan, S. McDermid, T. J. Pacala, D. M. Rider, J. B. Laudenslager, " Pulsed ultraviolet lasers and the potential for safe laser angioplasty" The American Journal of Surgery **150**, 2, 220-226 (1985).

[13] M. W. Berns, J. Aist, J. Edwards, K. Strahs, J. Girton, P. McNeill, J. B. Rattner, M. Kitzes, M. Hammer-Wilson, L. H. Liaw, A. Siemens, M. Koonce, S. Peterson, S. Brenner, J. Burt, R. Walter, P. J. Bryant, D. van Dyk, J. Coulombe, T. Cahill, G. S. Berns, "Laser microsurgery in cell and developmental biology." Science 213.4507 (1981): 505-513.

[14] A. Ben-Yakar and C. Hoy, "Targeting single cells with a laser microscalpel" SPIE (2008).

[15] T. Juhasz, G. Djotyan, F. H. Loesel, R. M. Kurtz, C. Horvath, J. F. Bille and G. Mourou. "Applications of femtosecond lasers in corneal surgery." LASER PHYSICS-LAWRENCE-, 10(2), 495-500 (2000).

[16] A. Vogel, N. Linz, S. Freidank, J. Noack and G. Paltauf. "Femtosecond and Nanosecond Laser-Induced Nanoeffects for Cell Surgery and Modifications of Glass." In Conference on Lasers and Electro-Optics (p. CMHH1). Optical Society of America (2008).

Session 5

Interfaces & Teleoperation

Chair: Dr. Benoît Herman, Université Catholique de Louvain

Wednesday, October 15th

9:30 – 10:30

Development of a modular control concept for a hydraulic 3-DOF surgical instrument

Laura Maria Comella, Andreas Rothfuss and Auguste van Poelgeest
Project Group for Automation in Medicine and Biotechnology
Fraunhofer IPA, Mannheim, Germany
Email: Laura.Maria.Comella@ipa.fhg.de

***Abstract*—Novel technologies play an increasingly important role in the advancement of modern medicine. For example the tools for minimally invasive surgery have seen various groundbreaking developments in recent years, like actuated and bendable tip instruments. One of the last and for the future most promising developments for laparoscopic instruments, presented in [1], [2], uses hydraulic actuation. This paper presents the theoretical basis for the control of this novel hydraulically actuated laparoscopic instrument with 3 degrees of freedom. The focus of this work is the inverse kinematic model of the instrument itself and a discussion of the external drives.**

I. Introduction

The role of laparoscopy has an increasingly relevant place in modern medicine. The reasons for its success are the advantages for the patients, such as reduced haemorrhaging and smaller incisions, which in turn reduce pain and shorten recovery time [3], [4]. Although the technique benefits patients, it causes difficulties and actuation limitations to the surgeon, such as reduced workspace and loss of dexterity.
In order to overcome the limits implied by this surgical method, technologies have been developed to aid the surgeon [5], such as increased degrees of freedom of the tip and automatic actuated laparoscopic instruments.
The current state of the art for laparoscopic instruments is represented by [6]–[8]. Instruments with mechanical power transmission, powered and controlled either manually or electromechanically. Fraunhofer PAMB, instead, proposes in [1], [2] a new approach: laparoscopic instruments powered by hydraulics. This technology has the advantage that the actuators have a higher force and power density than most of the others [9] and because of this, they can be small enough to be located directly on the tip. The instruments developed with this technology are small and light because the drives can be located remotely. Moreover, sensors to measure actuator parameters do not contribute to the instrument's weight, as they can be located anywhere in the hydraulic circuit. In this paper the chosen drives and their configuration will be discussed together with the instrument's inverse kinematic. These are the first steps toward a control solution, which in contrast with the state of the art, is independent from the kind of handheld interface. The state of the art instruments show this dependency because of the direct connection between joints and handhald device movements. The goal is, instead, the realization of a modular system composed by: any handheld interface, which defines the tip position and a control software, which processes the input data and calculates the joints position.

II. Solution

The new concept severs the direct link between the handheld interface and the instrument's DOFs. The sensor inputs measured at the interface are not the input signals to the instrument's actuators. Instead, these are interpreted as a relative measurement of displacement from instrument's current position. To implement this, a position control system was developed where the controller gets the new desired tool tip position, its inverse kinematic equations calculate the corresponding actuator extensions which are then sent as a command to the actuator drives. This new control concept has beed developed for a new generation of hydraulically powered surgical instrument [1], [2], designed by Fraunhofer PAMB and shown in (Fig.1). The instrument's tip consists of three segments connected via two cylindrical joints which are offset by 90 degrees about their longitudinal axis. The joints are connected in a serial chain and each joint is actuated by an internal mechanism consisting of two antagonistic linear hydraulic actuators.

Fig. 1. CAD drawing of the hydraulic instrument developed at Fraunhofer PAMB, for which our control software has been developed. It consists of a 3-DOF actuator at the instrument's tip and a hand held grip, which interprets the surgeon movement via a sensors interface.

Given the mechanical design of the instrument, a relationship needs to be established between the actuator extensions, hence the joint rotations, and finally the tool tip position. The equations will be derived by applying inverse kinematic theory for both mechanisms: the serial chain and the internal mechanisms. The relationship between tool tip position and joint rotations can be established by applying the inverse serial kinematic method of Denavit Hartemberg. The relationship between the joint rotations and the actuator extensions can be determined applying a geometrical method. The details of the derivations are described in the following paragraphs.
In order to find the relationship between tool tip position and

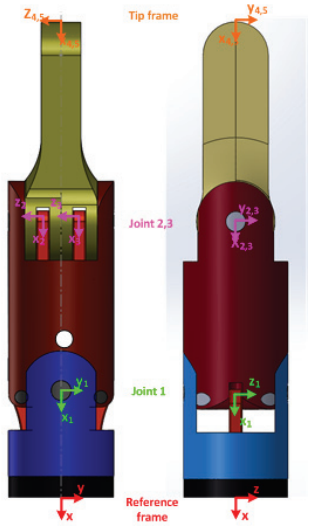

Fig. 2. Image showing the instrument's tip from two sides: a frontal face and a view of the instrument rotated of 90 degrees. The frames position and orientation, placed on the joints according to the Denavit Hartemberg convention, are also defined.

TABLE I. DENAVIT HARTEMBERG PARAMENTERS DEFINED FOR FINDING THE RELATIONSHIP BETWEEN INSTRUMENT TOOL TIP POSITION AND JOINT ROTATION

joint	theta	d	a	alpha
1	0	0	a	0
2	theta1	0	b	90
3	theta2	0	c	0

joint rotations, reference frames of the mechanism's joints were affixed according to the Denavit-Hartemberg convention, [10, chap.3], as shown in Fig. 2. Next, the Denavit-Hartenberg parameters were defined as shown in Table I.
where:
a is the distance between z_i and z_{i+1} measured along x_i;
α is the angle from z_i to z_{i+1} around x_i;
d is the distance between x_{i-1} and x_i measured along z_i;
θ is the angle from x_{i-1} to x_i around z_i;
Using these parameters it is then possible to define the homogeneous transformation matrix ${}^0_3\mathrm{T}$.

$$ {}^0_3\mathrm{T} = {}^0_1\mathrm{A} \times {}^1_2\mathrm{A} \times {}^2_3\mathrm{A} = \tag{1} $$

$$ = \begin{pmatrix} c\theta_1 c\theta_2 & c\theta_1 s\theta_1 & s\theta_1 & -c \times c\theta_2 c\theta_1 - b \times c\theta_1 - a \\ s\theta_1 c\theta_2 & -s\theta_2 s\theta_1 & -c\theta_1 & -c \times c\theta_2 s\theta_1 - b \times s\theta_1 \\ s\theta_2 & c\theta_2 & 0 & -cs\theta_2 \\ 0 & 0 & 0 & 1 \end{pmatrix} $$

where:

$$ {}^0_1\mathrm{A} = \begin{pmatrix} 1 & 0 & 0 & a \\ 0 & 1 & 0 & 0 \\ 0 & 0 & 1 & 0 \\ 0 & 0 & 0 & 1 \end{pmatrix} \tag{2} $$

$$ {}^1_2\mathrm{A} = \begin{pmatrix} \cos\theta_1 & 0 & \sin\theta_1 & b\cos\theta_1 \\ \sin\theta_1 & 0 & -\cos\theta_1 & -b\sin\theta_1 \\ 0 & 1 & 0 & 0 \\ 0 & 0 & 0 & 1 \end{pmatrix} \tag{3} $$

$$ {}^2_3\mathrm{A} = \begin{pmatrix} \cos\theta_2 & -\sin\theta_2 & 0 & -c\cos\theta_2 \\ \sin\theta_2 & \cos\theta_2 & 0 & -c\sin\theta_2 \\ 0 & 0 & 1 & 0 \\ 0 & 0 & 0 & 1 \end{pmatrix} \tag{4} $$

The last column of the matrix (1) represents the vector that links the tip reference frame and the origin. Its components are defined as:

$$ \begin{cases} p_x = -c\cos\theta_2\cos\theta_1 - b\cos\theta_1 - a \\ p_y = -c\cos\theta_2\sin\theta_1 - b\sin\theta_1 \\ p_z = -c\sin\theta_2 \end{cases} \tag{5} $$

where:
a is the distance between reference frame and join 1;
b is the distance between joint 1 and joint 2;
c is the distance between joint 2 and the tip frame;
p_x, p_y and p_z are the pliers jaw number one desired position in the reference coordinate system;
θ_1 and θ_2 are the angles that determine the joints rotation. Hence from equation (5) it is possible to deduce the relationship between end-effector jaw position and joints rotations:

$$ \theta_1 = \arcsin\left(-\frac{p_y}{c\cos\theta_2}\right) \tag{6} $$

$$ \theta_2 = \arcsin\left(-\frac{p_z}{c\cos\theta_2 + b}\right) \tag{7} $$

With the relationship between tool tip position and joint rotation defined, a relationship can be established between the joint rotation and actuator extensions from the inverse kinematics of the internal mechanism. A schematic of this mechanism is shown in Fig. 3.

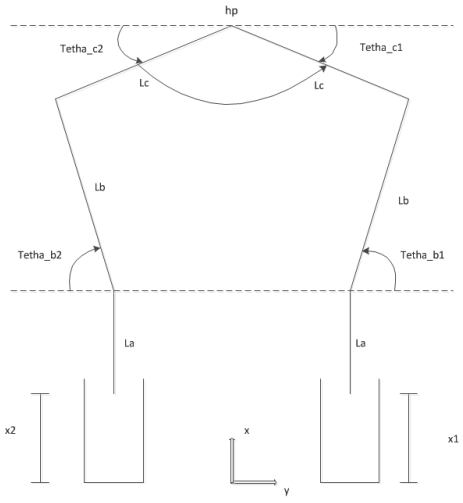

Fig. 3. Schematic diagram showing the parallel kinematic mechanism

Being: h_p the x coordinate of the joint; L_a, L_b and L_c the segments dimension of the parallel kinematic; θ_{b1} and θ_{b2} the angle between the first and the second segment of the two branches of the mechanism; θ_{c1} and θ_{c2} the angle between the third segment of the two mechanism branches and an horizontal line; x_1 and x_2 the distance between piston and cylinder base
A geometrical method is used to establish the following

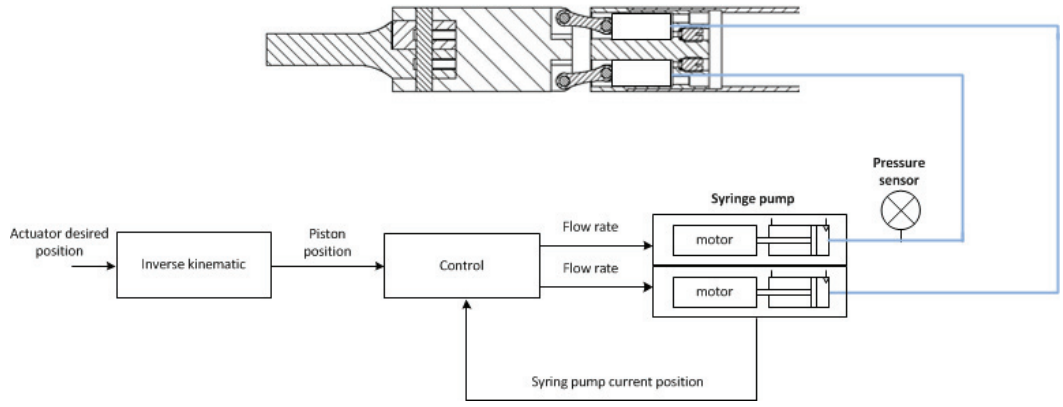

Fig. 4. Schematic of the overall control concept and data flow between user, control software and instrument.

kinematic relationships:

$$\theta_{b1} = \arccos[\frac{1}{L_b}(L_c \cos\theta_{c1} - L_d)] \tag{8}$$

$$x_1 = h_p - L_a - L_b \sin[\arccos(\frac{L_c}{L_b}\cos\theta_{c1} - \frac{L_d}{L_b})] - L_c \sin\theta_{c1} \tag{9}$$

$$\theta_{b2} = \arccos[\frac{1}{L_b}(L_c \cos\theta_{c2} - L_d)] \tag{10}$$

$$x_2 = h_p - L_a - L_b \sin[\arccos(\frac{L_c}{L_b}\cos\theta_{c2} - \frac{L_d}{L_b})] + L_c \sin\theta_{c2} \tag{11}$$

$$\theta_{c2} + \phi - \theta_{c1} = \pi \tag{12}$$

The identities resulting from the serial and internal mechanisms are linked by the following geometrical relationship:

$$\theta_{c1} = C_\theta + \theta_1 \tag{13}$$

Where C_θ is a constant angle due to the parallel kinematic structure: C_θ is the value of θ_{c1} when $x_1 = x_2$. (13) defines that a rotation of the joint corresponds to an equal change of θ_{c1} from its equilibrium position.
It can be concluded that once the end-effector position (p_x, p_y and p_z) is defined, θ_1 and θ_2 can be calculated from (6) and (7). Knowing θ_1, the orientation of joint 1, it is possible to calculate θ_{c1} from (13) and then θ_{c2} from (12). Than θ_{c2} can be substitute in (9) and (11), obtaining x_1 and x_2, the pistons extension. This process can subsequently be repeated for joint 2 by substituting θ_2 in the inverse kinematic formulas of the internal mechanism. For θ_3, the rotation of joint 3, the whole procedure must be started from (5), substituting θ_2 with θ_3 and changing the coordinate of jaw number one with the one of jaw number two.
To control the actuator extension, every cylinder in the instrument is connected to a syringe pump, as shown in Fig. 4. This hardware configuration is free from non-linearity associated with the use of valves in hydraulic circuits. Moreover with a position measurement in every pump syringe, it will be possible a future development of a closed-loop control system. The complete control concept is summarized in Fig. 4. The inverse kinematics module receives the desired tool tip position, calculates the actuator extensions for every joint and sends a command to each syringe. The syringe pump displacement translates directly to an actuator extension with a known transmission ratio.

III. Conclusion

A new control concept for a new hydraulically actuated instrument has been developed together with the mathematical description of its inverse kinematic.
The pressure supply configuration with 6 syringe pumps driving 6 hydraulic cylinders has the advantages of a direct transmission of the pump displacement to the hydraulic actuator extension as well as enabling a straightforward implementation of closed-loop control. However, it may not be optimal in terms of size and cost. Hence a future work could focus on developing alternative pressure supply methods which can match the current system's performance.

References

[1] T. Cuntz, G. James, V. Valkov, A. Sanagoo, and D. Kaltenbacher, "Next generation surgical instruments powered by hydraulics," *Biomedical Engineering/Biomedizinische Technik*, 2013.

[2] *Proc. CRAS 2014, WS on Computer/Robot Assisted Surgery*, 2014.

[3] T. Carus, *Operationsatlas Laparoskopische Chirurgie*. Springer, 2010.

[4] P. Dasgupta, J. Fitzpatrick, I. S. Gill, and R. Kirby, *New Technologies in Urology*. Springer, 2010, vol. 7.

[5] D.-I. R. Kramme and D.-V.-W. H. Kramme, "Die rolle der technik in der medizin und ihre gesundheitspolitische bedeutung," in *Medizintechnik*. Springer, 2011, pp. 3–6.

[6] tuebingen scientific. (2013) r2 drive. [Online]. Available: http://www.tuebingen-scientific.com/deutsch/staendige-navigatioin/resource-center/

[7] A. Hackethal, M. Koppan, K. Eskef, and H.-R. Tinneberg, "Handheld articulating laparoscopic instruments driven by robotic technology. first clinical experience in gynecological surgery," *Gynecological Surgery*, vol. 9, no. 2, pp. 203–206, 2012.

[8] endo control. (2013) jaimy. [Online]. Available: http://www.endocontrol-medical.com/jaimy.php

[9] M. De Volder, "Pneumatic and hydraulic microactuators: a new approach for achieving high force and power densities at microscale," *status: published*, 2007.

[10] J. J. Craig, *Introduction to Robotics*, P. E. international, Ed.

Advantages of mechanical backdrivability for medical applications of force control

Jérôme Perret
Haption GmbH
Aachen, Germany
jerome.perret@haption.com

Pierre Vercruysse
Haption S.A.
Laval, France
pierre.vercruysse@haption.com

***Abstract*—When contemplating the introduction of robotic equipment into the operating room, one is faced with regulation constraints dealing with safety, redundancy, and dependability. One key issue is the ability to control the forces applied by the robot, or in other words, its back-drivability. In this position paper, we will explain why mechanical back-drivability has many advantages with respect to its opposite, instrumented back-drivability. We then give an example of a design carried out for a research projects in the medical domain.**

Keywords—haptics; force control; safety

I. INTRODUCTION

A robot in an operating room is both an asset and a risk. One approach for increasing the former and limiting the latter consists in implementing functionalities for controlling the forces applied by the machine. Here, "controlling" means altogether the ability to apply a given force with high precision, to ensure that it will never go over a set limit, and to measure its value for purposes of traceability. While the measurement and limitation can be done on any kind of machine with simple force sensors, the "application" part is much more difficult.

Basically, there are two main approaches for controlling the force applied by a robot on its environment (here, the "environment" encompasses other devices in the operating room, but also the medical personnel and the patient). The first approach, often referred to as "instrumented compliance", consists in adding force sensors and implementing a feedback loop in the control software. The main advantage is that it can be applied on virtually any existing robot, with a low impact on its design. In the second approach, called "mechanical back-drivability", the mechanical structure of the robot is designed in such a way that the force applied on the environment reflects directly the motor torques.

The purpose of this position paper is to describe how back-drivability can be achieved, and explain its benefits for medical applications.

II. MECHANICAL BACK-DRIVABILITY

For a mechanism, backdrivability means that a force applied at the end-effector will be reflected on the motors. The canonical example of a non-backdrivable system is the "worm drive": if a torque is applied on the worm wheel, it is not transmitted to the worm itself. On the opposite, the "rack and pinion" used in automobile steering wheels is backdrivable, thus enabling the driver to feel the adherence of the tires on the road.

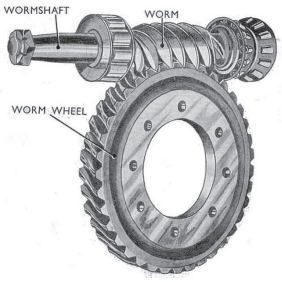

Fig. 1. Worm gear (public domain)

The best backdrivability is achieved when the motors are used in "direct-drive", meaning that the motor shaft is fixed directly on the robot segment without any transmission system. However, except for some hydraulic actuators, available motors are not strong enough for direct-drive mounting, and need some sort of mechanical amplification. And most transmission mechanisms are backdrivable, up to a point. For example, in the case of gearboxes, which are essential components of most robotic systems, the backdrivability decreases with the speed ratio, due to internal friction; in practice, a speed ratio of 15:1, which gives a torque amplification of 1:15, is unusable for efficient force control.

The backdrivable transmission mechanism which is most used in robotics is the "capstan drive". It is similar to a simple parallel gear train, but the gears are replaced by pulleys and the teeth by a cable. The advantage of the capstan drive is that it has almost no friction and no backlash. Provided a cable with good properties can be found, it can provide speed ratios down to 30:1 with very good backdrivability.

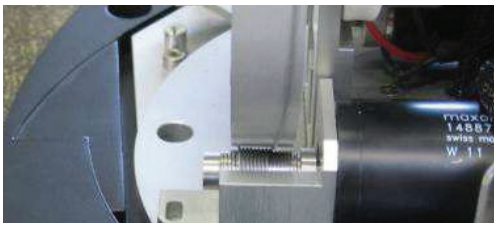

Fig. 2. Capstan drive of the haptic device Virtuose 6D (Haption)

Other mechanisms based on cables have been used in the past, which provide even lower speed ratios, like the "block-and-tackle" implemented in the MA23 robot of CEA/La Calhène [1]. But while very efficient in terms of force transmission, such systems are bulky, fragile and difficult to maintain. A recent evolution, implemented in the haptic device MAT 6D, uses a ballscrew inside the cable loop with a patented fixation for reduced friction [2, 3].

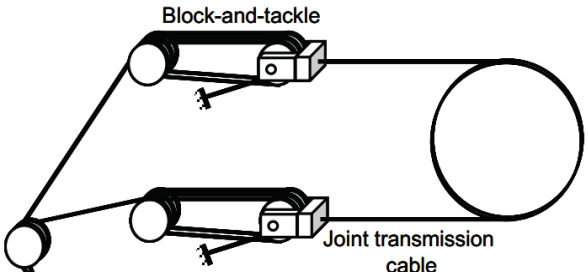

Fig. 3. Block-and-tackle of MA23 (courtesy of CEA LIST)

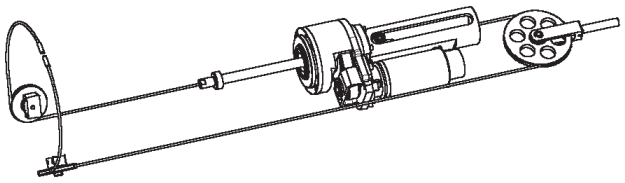

Fig. 4. Cable loop of the MAT 6D (Haption)

III. DISCUSSION

As explained above, backdrivability means that the transfer function from the motor torques to the external forces is reversible. In other words, the external force can be calculated based on the motor torques, and controlled without any other measuring device. Of course, that demonstration applies only if the robot electronics is able to control the motor torques.

Any machine used inside an operating room needs to fulfill strict safety constraints, as expressed i.e. in the international standard ISO 13485. In particular, a risk analysis has to be carried out in the early phases of the design, and suitable measures have to be taken for controlling the risks. As a consequence, it is impossible that a robot could be certified for such an environment if it were not equipped with a monitoring of the power fed into its motors. In short, the ability to control the motor torques seems to be a logical consequence of the risk analysis.

In this context, mechanical backdrivability provides a lot of benefits:

- Force control can be achieved without any additional sensor
- System complexity is reduced, compared to instrumented compliance
- Dependability is increased due to the reduced number of failure modes
- Force control is available for the whole mechanism, not only the end-effector
- In case of a major breakdown, the robot can be removed/pushed away by the personnel, even if powered down
- Since there are no active components near the end-effector, the system is easier to sterilize
- The absence of force sensors near the end-effector lowers the electromagnetic susceptibility

In order to make full use of those benefits, the transmission system must be chosen with great care. Indeed, the risk reduction brought by the absence of force sensors could easily be negated by the introduction of a fragile transmission cable. Another potential drawback is the reduction of the overall stiffness, especially when using heavy tools against hard tissue (e.g. in orthopedic surgery).

Compared to a classical robot with gears, a back-drivable system is characterized by lower reduction ratios, lower friction, and lower inertia. As a consequence, the maximum achievable control stiffness is also much lower [5]. However, the stiffness can be increased significantly by using a very high position resolution on the motors and a fast update rate on the control loop. Other approaches have been proposed for increasing the time-domain passivity, by adding controllable damping [6].

In spite of the absence of force sensors, the approach of mechanical backdrivability does not result in a lower cost. Indeed, the mechanical transmission system is usually more complex than simple gearboxes. In addition, if a high overall stiffness is required, then it is necessary to adopt high-resolution position sensors and a fast computing unit.

IV. EXAMPLE

The purpose of the research project SURGICOBOT was to provide future surgeons with a robotic assistant to make spinal release surgery quick and secure. One of the key objectives was the design of a "cobot" (collaborative robot) able to hold the milling tool together with the surgeon, which guarantees that the tool tip cannot penetrate a virtual tube built around the spinal cord.

The project partners decided to use a robot structure with a very close similarity to Haption's haptic device Virtuose 6D, which is highly backdrivable, and complement it with a wrist giving a virtual rotation point around the tool tip. The global system was tested and validated by surgeons on representative sawbones [4].

Fig. 5. The haptic device Virtuose 6D (Haption)

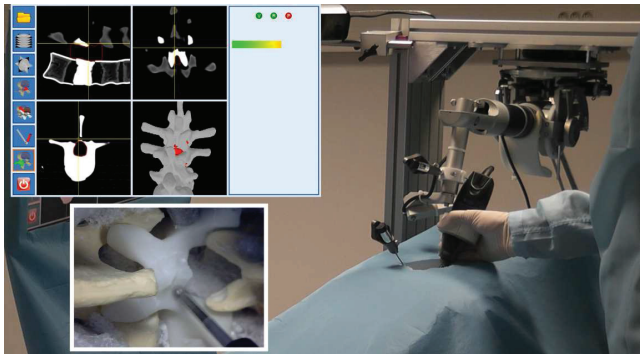

Fig. 6. Prototype of the SURGICOBOT (courtesy of CEA LIST)

V. Acknowledgments

The project SURGICOBOT was supported by the French National Research Agency ANR under the TECSAN framework.

References

[1] J. Vertut, and al., Bilateral Servo Manipulator MA23 in Direct Mode and Via Optimized Computer Control, 2nd Remotely Manned Syst. Technology Conference, 1975

[2] Garrec P. Design of an anthropomorphic upper limb exoskeleton actuated by ball-screws and cables. , National Conference on Mechanics of Solids, CNMS – XXXIII, Bucharest, 10-12 September 2009.

[3] P. Garrec, J.P. Friconneau, F. Louveau, Virtuose 6D: A new force-control master arm using innovative ball-screw actuators, in Proceedings of ISIR 35th International Symposium in Robotics, Paris, March 2004.

[4] A. Riwan, B. Giudicelli, F. Taha, J.-Y. Lazennec, A. Sabhani, P. Kilian, Z. Jabbour, J. VanRhijn, F. Louveau, G. Morel, V. Françoise, D. Armand, S. Lavallée, Surgicobot project: Robotic assistant for spine surgery, IRBM Volume 32, Issue 2, April 2011, Pages 130–134.

[5] B. Hannaford and J. Ryu. Time-Domain Passivity Control of Haptic Interfaces. IEEE Transactions on Robotics and Automation, 18(1):1–10, 2002

[6] C. Gosline, A. H. and Hayward, V. 2007. Time-Domain Passivity Control of Haptic Interfaces with Tunable Damping Hardware. Proc. World Haptics 2007 (Second Joint Eurohaptics Conference And Symposium On Haptic Interfaces For Virtual Environment And Teleoperator Systems), pp. 164-169

Sensory subtraction via cutaneous feedback: a novel technique to improve the transparency of robotic surgery

Claudio Pacchierotti and Domenico Prattichizzo

***Abstract*— In this paper we present a novel technique to force feedback in robot-assisted surgery. It consists of substituting haptic force, composed by kinesthetic and cutaneous components, with cutaneous stimuli only. The force generated can be thus thought as a subtraction between the complete haptic interaction, cutaneous and kinesthetic, and the kinesthetic part of it. For this reason, we refer to this approach as *sensory subtraction* and not sensory substitution. Sensory subtraction, first introduced in [1], aims at improving the performance of conventional force feedback techniques in teleoperation while guaranteeing the same stability properties. In this work we recall the idea of sensory subtraction in teleoperation, together with its evaluation in two paradigmatic surgical teleoperation scenarios.**

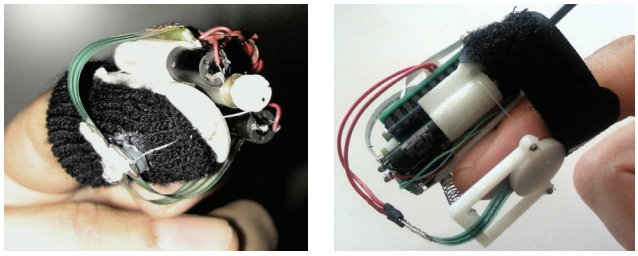

(a) Chinello *et al.* in [17]. (b) Pacchierotti *et al.* in [18].

Fig. 1: Two of the custom cutaneous devices employed in sensory subtraction.

I. INTRODUCTION

Achieving a good illusion of telepresence in robotic teleoperation is a matter of technology. If the teleoperator transmits sufficient information to the user, displayed in a sufficiently articulated way, the illusion of telepresence can be compelling [2], [3]. The primary tool to achieve this objective is providing a *transparent* implementation of the teleoperation system. Transparency can be defined as the correspondence between the master and slave positions and forces [4], or as the match between the impedance of the environment and the one perceived by the operator [5]. A compelling illusion of telepresence can be achieved through different types of information, which flow from the remote scenario to the human operator. Haptic force feedback is one piece of this information flow and it has been proved to play an important role in enhancing teleoperation performance in terms of task completion time [6], [7], [8], accuracy [7], [1], peak [9], [10], and mean exerted force [10], [8].

However, employing haptic force feedback may affect the *stability* of teleoperation systems. For this reason, researchers have proposed a great variety of stability bilateral controllers [11], [12] and it has always been a big challenge to find a good trade-off between stability and transparency. In this respect, passivity [13] has been exploited as the main tool for providing a sufficient condition for stable teleoperation in several controller design approaches, such as Time Domain Passivity Control [14], Energy Bounding Algorithm [15] and Passive Set Position Modulation [16]. However, control techniques guarantee the stability of the system at the price of a temporary loss of transparency, which could lead to degraded performance.

Another interesting approach to provide information about forces exerted at the slave side consists in completely avoiding the usage of actuators on the master device, and then providing alternative forms of feedback using *sensory substitution* techniques. In this case, since no kinesthetic force is fed back to the operator, the haptic loop becomes intrinsically stable and no bilateral controller is thus needed [1]. Force feedback is then substituted with other forms of stimuli, such as vibrotactile [19], auditory, and/or visual feedback [20]. However, these stimuli are clearly very different from the ones being substituted (e.g. a beep sound instead of force feedback) and they thus show worse performance than that achieved employing unaltered haptic force feedback.

In this paper we present a novel approach to force feedback in robotic teleoperation. It consists of substituting haptic force feedback, composed by kinesthetic and cutaneous components, with cutaneous feedback only, provided by custom cutaneous devices. It aims at outperforming conventional sensory substitution techniques while guaranteeing the same stability properties. Cutaneous stimuli does not in fact affect the stability of the system, since the contact force is applied directly to the user's skin and does not affect the position of the master device end-effector, thus opening the haptic loop [1], [21]. However, with respect to popular sensory substitution techniques, the stimuli provided are much more similar to the one being substituted [1], [18]. Moreover, cutaneous feedback will be exerted exactly where it is expected to be (e.g., the fingertips), providing the operator with a direct and co-located perception of the contact force.

The research leading to these results has received funding from the European Union Seventh Framework Programme FP7/2007-2013 under grant agreement n° 270460 of the project "ACTIVE - Active Constraints Technologies for Ill-defined or Volatile Environments" and under grant agreement n° 601165 of the project "WEARHAP - WEARable HAPtics for humans and robots".

C. Pacchierotti and D. Prattichizzo are with the Dept. of Information Engineering and Mathematics, University of Siena, Via Roma 56, 53100 Siena, Italy and with the Dept. of Advanced Robotics, Istituto Italiano di Tecnologia, via Morego 30, 16163 Genova, Italy. pacchierotti,prattichizzo@dii.unisi.it

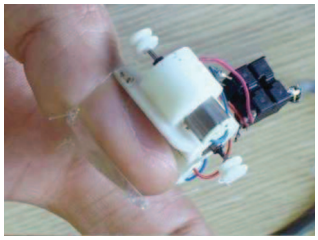

(a) Cutaneous device

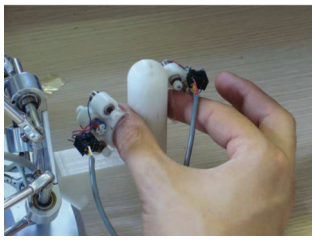

(b) Handle of the Omega 3

Fig. 2: Experimental setup of [1]. Users had to wear four cutaneous devices, one on the thumb and one on the index finger of each hand.

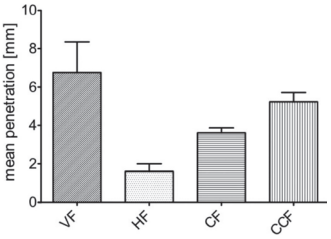

(a) Average penetration

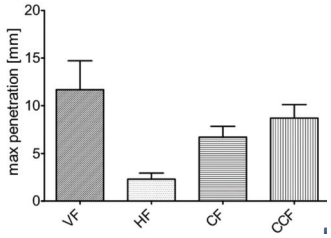

(b) Maximum penetration

Fig. 3: Experiment of sensory subtraction in [1]. Average and maximum penetration beyond the stiff constraint (mean and std), for the visual (VF), haptic (HF) and cutaneous feedback conditions (CF, CCF). A null value of this metric indicated the best accuracy in reaching the target depth. The sensory subtraction approach is employed in condition CF.

On the other hand, with the aim of improving transparency, this approach can be also combined with popular control techniques able to provide kinesthesia while guaranteeing stability. As the control algorithm detects a violation of its stability conditions, and the kinesthetic device is thus unable to provide the required feedback, the cutaneous devices convey a suitable amount of force, thus (partially) recovering transparency. For instance, we can provide as much kinesthetic force as the stability controller permits and then provide the rest via cutaneous feedback [21].

Sensory subtraction is thus similar to sensory substitution, since we *substitute* haptic force with cutaneous stimuli. However, since haptic force provided by popular grounded haptic interface is composed by kinesthetic and cutaneous components [18], we like to refer to this technique as *sensory subtraction*: kinesthetic force can be considered as *subtracted* from the complete haptic interaction, thus resulting in cutaneous force only. This idea was first introduced by Prattichizzo *et al.* in [1] and then further validated in different teleoperation scenarios [8], [21], [22], [23], [24]. In this work we are going to present the sensory subtraction idea and provide a comprehensive view of the scenarios where it has been employed, focusing on its application in the field of robot-assisted surgery.

II. SENSORY SUBTRACTION: THE CUTANEOUS AND KINESTHETIC COMPONENTS

Most of the well-known haptic devices for single-point contact interaction, such as the Omega (Force Dimension, Switzerland) or the Phantom (Sensable group, USA), provide kinesthetic force feedback to the users [25]. However, these devices *also* provide cutaneous stimuli to the fingertips if we assume that the interaction with the remote environment is mediated by a stylus, a ball, or any other tool mounted on the haptic interface [1], [18]. Cutaneous stimuli are sensed by pressure receptors in the skin and they are useful to recognize the local properties of objects such as shape, edges, embossings and recessed features. This is possible, principally, thanks to a direct measure of intensity and direction of contact forces and to the encoding of the force spatial distribution over the fingertip [26], [27]. On the other hand, kinesthetic feedback provides humans with information about the position and velocity of neighboring body parts, as well as the applied force and torque, mainly by means of receptors in the skin, muscles and joints [28], [25].

Sensory subtraction consists in substituting this haptic force with cutaneous stimuli only, provided by custom cutaneous devices. The first device developed for this purpose was the 3-DoF wearable cutaneous interface presented in [17] and shown in Fig. 1a. It consists of two main parts: the first one is placed on the dorsal side of the finger and supports three small electrical motors; the other one is a mobile platform in contact with the volar skin surface of the fingertip. These two parts are connected by three cables. The motors, by controlling the length of the cables, are able to move the platform towards the user's fingertip. As a result, a force is generated, simulating the contact of the fingertip with an arbitrary surface. Three force sensors are placed near to the platform vertices, in contact with the finger, so that they measured the three components of the cutaneous force applied to the fingertip. A second device was presented in [18]. It is similar to the one mentioned above but showed higher accuracy. It consists again of two platforms connected by three cables. Three small electrical motors, equipped with position encoders, control the length of the cables, thus being able to move the platform towards the fingertip. One force sensor is placed at the platform's centre, in contact with the finger, so that it can measure the component of the cutaneous force perpendicular to the volar skin surface of the fingertip (see Fig. 1b). Employing a cutaneous device instead of a grounded haptic interface to provide force feedback makes the idea of sensory subtraction possible: we disregard haptic force feedback in favour of cutaneous stimuli only.

More information about the role of kinesthetic and cutaneous sensory channels in sensory subtraction can be found in [18]. Features and limitations of this kind of cutaneous devices are discussed in [17].

III. SENSORY SUBTRACTION IN MEDICAL TELEOPERATION

The idea of sensory subtraction has been effectively employed in many teleoperation scenarios, achieving high performance while guaranteeing stability. Prattichizzo *et al.* [1] used it in a teleoperated needle insertion task along one direction. They used four cutaneous devices, similar to the one presented in [17] (see Fig. 2a), and a commercial haptic

device. The operator wore two devices on one hand, one on the thumb and one on the index finger, and grabbed the handle of the grounded interface as shown in Fig. 2b. Two additional cutaneous devices were worn on the thumb and index finger of the contralateral hand. The haptic device was an Omega 3 by Force Dimension, to which three clamps were applied to reduce the degrees of freedom from three to one. Moreover, a plastic handle was attached to its end-effector to allow the operator to easily grab the device with two fingers. During the experiments the hardware was operated in two different conditions. In the first one the force feedback was provided by the Omega, while the wearable devices were switched off. In the second condition the sensory subtraction technique was implemented. The Omega 3 was used only to track the motion of the hand and did not apply any active force to the operator. At the same time, the cutaneous devices were used to reproduce the cutaneous sensation associated to the manipulation task being simulated. Moreover, to investigate the role of feedback localization with respect to the hand involved in the task, either the devices on the active hand or those worn on the contralateral hand were alternatively activated.

The task consisted in inserting a simulated needle into a soft tissue and stopping the motion as soon as a stiff constraint was perceived. A video of the experiment can be found at http://goo.gl/hfy24. The average penetration inside the constraint provided a measure of accuracy in reaching the target depth. Prattichizzo *et al.* compared task performance while providing (1) complete haptic feedback through the Omega 3 (HF), (2) cutaneous feedback through the cutaneous devices, applied to the hand holding the handle (CF), (3) cutaneous feedback through the cutaneous devices, applied to the contralateral handle (CCF), and (4) visual feedback in substitution of force feedback through a horizontal bar (VF), which is a popular sensory substitution technique [20].

Results reported in [1] are shown in Fig. 3. Figures 3a and 3b report, respectively, the average and maximum penetrations beyond the stiff constraint for each feedback condition. A null value of these metrics indicate no overshoot in reaching the target depth and, therefore, maximum accuracy. Results show that the sensory subtraction condition (CF) outperformed visual substitution of force feedback, but it performed worse than complete haptic feedback. This behaviour was, however, largely expected, since cutaneous force is just a subset of the complete haptic feedback provided by grounded interfaces. However, Prattichizzo *et al.* tested the idea only for a simple one degree-of-freedom (DoF) task.

For this reason, Meli *et al.* [23] decided to evaluate the sensory subtraction idea in a more challenging teleoperation scenario, considering a 7-DoF bimanual teleoperation task similar to the Peg Board experiment of the da Vinci Skills Simulator. Fig. 4 shows the experimental setup. The master system was composed of two Omega 7 haptic interfaces and four cutaneous devices. The cutaneous devices are similar to the ones presented in Sec. II and were worn as shown in Fig. 4b, i.e. on the thumb and index finger of both hands.

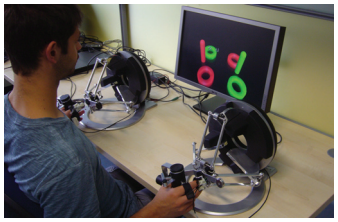

(a) General overview of the setup.

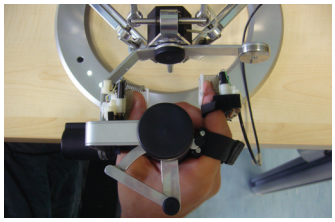

(b) Detail of one hand.

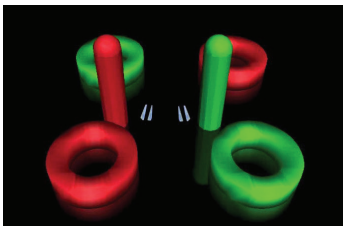

(c) Virtual environment.

Fig. 4: Experimental setup. Users had to wear four cutaneous devices, one on the thumb and one on the index finger of both hands, and teleoperate two pairs of surgical pliers using a couple of Omega 7 haptic interfaces.

The slave system was composed of two virtual surgical pliers, directly controlled by the master interfaces. The pliers accurately resembled fingers' motion on the Omega devices. Users were able to move and rotate the pliers in the 3-D space and control their gripping force. The virtual environment consisted of four rings, two green and two red, and two pegs, one green and one red (see Fig. 4c). The rings weighed 30 g and had a minor radius of 3 cm, a major radius of 5 cm, and a height of 1 cm. The pegs were fixed to the ground and had a base diameter of 4 cm and a height of 10 cm. A spring $k_0 = 40$ N/m was used to model the contact force between the proxies and the objects, according to the god-object model [29]. The virtual environment was built using CHAI 3D, an open-source set of C++ libraries for computer haptics and interactive real-time simulation. The task consisted of lifting, one by one, the rings from the ground with one pair of pliers, handing them to the other pair and inserting them into the peg of the corresponding color. An insertion was considered valid only when the ring was inserted in the correct peg. The task started when the user grasped a ring for the very first time and ended when all the rings were inserted into the pegs. A video of the experiment can be download at http://goo.gl/Wc6WYB. Meli *et al.* compared task performance while providing (1) complete haptic feedback through the two Omega 7 (H), (2) cutaneous feedback through the cutaneous devices (C), (3) visual feedback in substitution of force feedback, provided by changing color brightness of the ring being grasped (V), and (4) auditory feedback in substitution of force feedback, provided by changing the repetition frequency of a stereo beep tone (A). The time needed to complete the task and the forces generated by the contact between the pliers and the rings provided a measure of performance.

Results reported in [23] are shown in Fig. 5. Fig. 5a shows the average task completion time, while Fig. 5b shows the

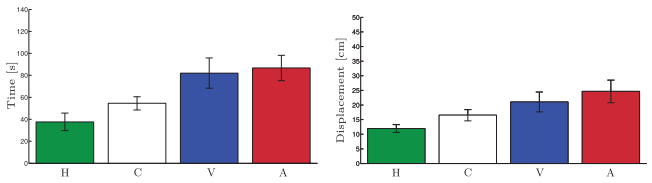

(a) Completion time (b) Rings' displacement

Fig. 5: 7-DoF bimanual peg board experiment. Completion time and contact forces for the haptic (H), cutaneous (C), visual (V) and auditive (A) conditions. Lower values of this metrics indicate higher performances in completing the given peg board task.

average grip forces generated between the two pairs of pliers and the rings along the direction of actuation of the Omega's gripper, i.e. the one perpendicular to the object surface. Sensory subtraction led to improved performance with respect to providing no force feedback at all and with respect to the considered sensory substitution techniques. However, as in the experiment presented in [1], cutaneous feedback showed worse performance with respect to providing complete haptic force feedback.

IV. CONCLUSIONS

This work presents the idea of sensory subtraction, a novel approach to force feedback in bilateral teleoperation systems. It consists of substituting haptic feedback with cutaneous feedback. We call this approach *sensory subtraction*, in contrast to *sensory substitution*, as it subtracts the kinesthetic part from the complete haptic interaction to leave only the cutaneous cues. Sensory subtraction was first introduced in [1] and later evaluated in several different scenarios [8], [21], [22], [23], [24]. The main advantage of this approach is that it makes the teleoperation system intrinsically stable. However, it still performs worse than providing complete haptic feedback through grounded haptic interfaces. For this reason, we are now developing new approaches to combine the idea of sensory subtraction with common force reflection techniques, in order to provide additional kinesthetic force and enhance transparency [21].

REFERENCES

[1] D. Prattichizzo, C. Pacchierotti, and G. Rosati, "Cutaneous force feedback as a sensory subtraction technique in haptics," *IEEE Transactions on Haptics*, vol. 5, no. 4, pp. 289–300, 2012.

[2] T. B. Sheridan, "Teleoperation, telerobotics and telepresence: A progress report," *Control Engineering Practice*, vol. 3, no. 2, pp. 205–214, 1995.

[3] J. V. Draper, D. B. Kaber, and J. M. Usher, "Telepresence," *Human Factors: The Journal of the Human Factors and Ergonomics Society*, vol. 40, no. 3, pp. 354–375, 1998.

[4] K. Hashtrudi-Zaad and S. E. Salcudean, "Transparency in time-delayed systems and the effect of local force feedback for transparent teleoperation," *IEEE Transactions on Robotics and Automation*, vol. 18, no. 1, pp. 108–114, 2002.

[5] D. A. Lawrence, "Stability and transparency in bilateral teleoperation," *IEEE Transactions on Robotics and Automation*, vol. 9, no. 5, pp. 624–637, 1993.

[6] M. J. Massimino and T. B. Sheridan, "Teleoperator performance with varying force and visual feedback," *Human Factors: The Journal of the Human Factors and Ergonomics Society*, vol. 36, no. 1, pp. 145–157, 1994.

[7] L. Moody, C. Baber, T. N. Arvanitis, *et al.*, "Objective surgical performance evaluation based on haptic feedback," *Studies in health technology and informatics*, pp. 304–310, 2002.

[8] C. Pacchierotti, F. Chinello, M. Malvezzi, L. Meli, and D. Prattichizzo, "Two finger grasping simulation with cutaneous and kinesthetic force feedback," in *Haptics: Perception, Devices, Mobility, and Communication. Eurohaptics*, pp. 373–382, 2012.

[9] B. Hannaford, "Task-level testing of the JPL-OMV smart end effector," in *Proc. of the Workshop on Space Telerobotics*, vol. 2, 1987.

[10] C. R. Wagner, N. Stylopoulos, and R. D. Howe, "The role of force feedback in surgery: analysis of blunt dissection," in *Proc. of 10th Symposium on Haptic Interfaces for Virtual Environment and Teleoperator Systems*, pp. 68–74, 2002.

[11] S. Salcudean, "Control for teleoperation and haptic interfaces," *Control problems in robotics and automation*, pp. 51–66, 1998.

[12] M. Franken, S. Stramigioli, S. Misra, C. Secchi, and A. Macchelli, "Bilateral telemanipulation with time delays: a two-layer approach combining passivity and transparency," *IEEE Transactions on Robotics*, vol. 27, no. 4, pp. 741–756, 2011.

[13] A. J. van der Schaft, *L2-gain and passivity techniques in nonlinear control*. Springer Verlag, 2000.

[14] J. Ryu, D. Kwon, and B. Hannaford, "Stable teleoperation with time-domain passivity control," *IEEE Transactions on Robotics and Automation*, vol. 20, no. 2, pp. 365–373, 2004.

[15] J. P. Kim and J. Ryu, "Robustly stable haptic interaction control using an energy-bounding algorithm," *The International Journal of Robotics Research*, vol. 29, no. 6, pp. 666–679, 2010.

[16] D. Lee and K. Huang, "Passive-set-position-modulation framework for interactive robotic systems," *IEEE Transactions on Robotics*, vol. 26, no. 2, pp. 354–369, 2010.

[17] D. Prattichizzo, F. Chinello, C. Pacchierotti, and M. Malvezzi, "Towards wearability in fingertip haptics: a 3-DoF wearable device for cutaneous force feedback," vol. 6, pp. 506–516, 2013.

[18] C. Pacchierotti, A. Tirmizi, and D. Prattichizzo, "Improving transparency in teleoperation by means of cutaneous tactile force feedback," *ACM Transactions on Applied Perception*, vol. 11, no. 1, pp. 4–4, 2014.

[19] R. E. Schoonmaker and C. G. L. Cao, "Vibrotactile force feedback system for minimally invasive surgical procedures," in *Proc. of IEEE International Conference on Systems, Man and Cybernetics*, vol. 3, pp. 2464–2469, 2006.

[20] M. Kitagawa, D. Dokko, A. M. Okamura, and D. D. Yuh, "Effect of sensory substitution on suture-manipulation forces for robotic surgical systems," *Journal of Thoracic and Cardiovascular Surgery*, vol. 129, no. 1, pp. 151–158, 2005.

[21] C. Pacchierotti, A. Tirmizi, G. Bianchini, and D. Prattichizzo, "Improving transparency in passive teleoperation by combining cutaneous and kinesthetic force feedback," in *Proc. IEEE/RSJ Int. Conf. Intelligent Robots and Systems*, (Tokyo, Japan), pp. 4958–4963, 2013.

[22] C. Pacchierotti, F. Chinello, and D. Prattichizzo, "Cutaneous device for teleoperated needle insertion," in *Proc. IEEE Int. Conf. on Biomedical Robotics and Biomechatronics*, pp. 32–37, 2012.

[23] L. Meli, C. Pacchierotti, and D. Prattichizzo, "Sensory subtraction in robot-assisted surgery: fingertip skin deformation feedback to ensure safety and improve transparency in bimanual haptic interaction," *IEEE Transactions on Biomedical Engineering*, vol. 61, no. 4, pp. 1318–1327, 2014.

[24] L. Meli, S. Scheggi, C. Pacchierotti, and D. Prattichizzo, "Wearable haptics and hand tracking via an rgb-d camera for immersive tactile experiences," in *Proc. ACM Special Interest Group on Computer Graphics and Interactive Techniques Conference (SIGGRAPH)*, 2014.

[25] V. Hayward, O. R. Astley, M. Cruz-Hernandez, D. Grant, and G. Robles-De-La-Torre, "Haptic interfaces and devices," *Sensor Review*, vol. 24, no. 1, pp. 16–29, 2004.

[26] I. Birznieks, P. Jenmalm, A. W. Goodwin, and R. S. Johansson, "Encoding of direction of fingertip forces by human tactile afferents," *The Journal of Neuroscience*, vol. 21, no. 20, pp. 8222–8237, 2001.

[27] K. O. Johnson, "The roles and functions of cutaneous mechanoreceptors," *Current opinion in neurobiology*, vol. 11, no. 4, pp. 455–461, 2001.

[28] B. B. Edin and N. Johansson, "Skin strain patterns provide kinaesthetic information to the human central nervous system.," *The Journal of physiology*, vol. 487, no. Pt 1, pp. 243–251, 1995.

[29] C. B. Zilles and J. K. Salisbury, "A constraint-based god-object method for haptic display," in *Proc. of IEEE/RSJ International Conference on Intelligent Robots and Systems*, vol. 3, pp. 146–151, 1995.

Prosthetic/assistive control via bio-signal-based HMIs: some practical experiences

Claudio Castellini and Jörn Vogel

Robotics and Mechatronics Center
German Aerospace Center (DLR)
Oberpfaffenhofen, Germany
{claudio.castellini, joern.vogel}@dlr.de

Abstract

One of today's main challenges in the rehab robotics community consists of enabling a disabled properly control the robotic device at hand. This entails adapting the machine to the patient's signals in order to provide an immersive experience and restore the function of the missing/impaired limb as accurately as possible. It's a formidable challenge: signals recorded from the human body are complex and subject to change in time, and still they must be reliably associated to the patient's intent so that the control is natural. The take-home lesson we have learned so far at the DLR, after four years of development of such HMIs, is almost obvious: the human subject must be put in the loop from the beginning, and remain there all the time. In particular, a reliable form of control can be achieved only if reciprocal learning can happen: the machine must adapt to the subject, the subject must learn how to use the machine. This short paper is a summary of some of our experiences.

1 Introduction

The ever-improving human-friendliness of robotic systems has recently opened up a new realm of human-robot interaction applications. In particular, the use of robot manipulators as personal assistants for the disabled is nowadays realistic and affordable. The as-yet low availability of such systems suggests however that more research on the brain- or body-computer interface is still required. In the context of arm/wrist/hand prosthetics for instance, it is well-known [11, 13] that poor control by the human subject is one of the main reasons for a surprisingly high rate of rejection of the prostheses — this, notwithstanding the blazing progress achieved in the past decades by mechanical hands, arms and manipulators. Clearly, what is missing is a generally accepted Human-Machine Interface (HMI), flexible enough to adapt to each and every patient, *and* to enable the patient himself *learn* how to use the system, creating a virtuous loop of *reciprocal learning*.

The signals used to interpret the subject's intent range from neuron discharges, directly gathered from the brain cortex, to surface electromyography (sEMG), non-invasively recorded from a stump or remaining limb, through implanted EMG, peripheral nerve interfaces, ultrasound imaging and tactile sensing. The signal of choice depends of course on the impairment of the subject; but in general, the communities' feeling is that (a) new kinds of signals are required, to be integrated in a unitary system, (b) concrete measures of success are required, i.e., the systems must be tested in the clinics, on patients, engaged in daily-life activity [7]. Measuring the root-mean-squared error in an offline lab experiment is no longer enough! ([17] is a remarkable outcry, corroborating this claim.)

The rest of the paper focusses on the experiences we have gathered in the past four years at the DLR, with the aim of providing *practically usable* HMIs. We first introduce (Section 2) the signals we have been concerned with and the methods used to convert them into control signals for rehabilitation and/or prosthetic and assistive devices; we then move on (Section 3) to describe the applications we have built.

2 From theory...

Realistic machine learning As opposed to the traditional classification schema to predict one out of a few elbow/wrist/hand configurations, *simultaneous/proportional* control [8] has the more ambitious goal of providing graded control over many degrees of freedom of the robotic artifact at the same time. Such a complex form of control must, however, be complemented in several ways. In particular, new ways of non-invasive intention detection [7] must be investigated (examples of this are computer vision [10], ultrasound imaging [14], tactile and pressure sensing [2]). A common framework for all these interfaces (and the joint usage of them, whenever possible and required) is still missing, but testing them must definitely be carried out either in the field, that is in the clinics and on patients, or in lab conditions, but trying to avoid the common pitfalls associated with abstract performance measures, e.g., claiming superiority of an approach because of a 5% increase in offline classification accuracy.

Surprisingly, one approach we have found ideal for all these tasks is simple least-squares regression (in the regularised form of Ridge Regression, RR [6]). Using RR, given a training set of (sample,target) pairs X, a linear model of the intended

forces, $f(x) = w^T x$ can be built, where the weight vector w is exactly calculated in closed form as $w = (X^T X + \lambda I)^{-1} X^T y$. This approach is fast and bounded in space, and is easily made incremental using a rank-1 update method such as the Sherman-Morrison formula or the Cholesky update. The term *incremental* is here used in a crucial sense: each model found by RR can be updated with a new (sample,target) pair with a reasonable computational effort; and the updated model is equivalent to the model which would have been obtained by RR, as if all samples (including the new one) had been available as a batch since the beginning.

Incremental learning in this sense means that the model can take into account shifts and changes in time of the underlying input space; instead of modeling the changes, one can "learn them away" by temporarily switching to data gathering and incorporating the new knowledge in the old model. This opens up the possibility of online correcting the inaccuracies in the prediction, one typical example being given by sEMG. As sEMG gathers the level of muscle activation, its signal will change not only due to fatigue, electrode displacement and sweat — problems which the community already has tried to accommodate in various ways — but also whenever a heavy ovject is grasped and lifted, or whenever the arm/body posture changes. In that case, incremental learning only needs new example sEMG patterns to be shown to the system, e.g., the pattern representing a power grasp of an object weighing a few kilos. This pattern is in general different from the one obtained by power grasping a lightweight object; and given the right ground truth values, it will be seamlessly incorporated in the model, making the grasp stable in the future. In our framework, provided that the relationship between the input space and the required control signals is linear, this makes RR ideal to work online: new signal samples can be acquired to update the model whenever required by the subject, without the need to store all samples previously seen [14]. This *de facto* blurs the ominous distinction between training phase and prediction — one can switch back and forth from training to prediction, at the subject's will.

The non-linear case can be handled by adding to RR the so-called *Random Fourier Features* (RFF, [3]), an instance of the kernel trick in which the linear regression problem is solved in a higher-dimensional space induced by a non-linear transformation. The models obtained by RR-RFF have the form $f(x) = w^T \phi(x)$, where ϕ is a computationally feasible non-linear mapping. Surprisingly, all the above-mentioned good features of RR carry on to RR-RFF, at a slightly higher computational cost for updating the models and for prediction; in particular ϕ can simply be "plugged in" onto the RR model calculation: $w = (\phi(X)^T \phi(X) + \lambda I)^{-1} \phi(X)^T y$.

Moreover, the interpolation and generalisation properties of RR and RR-RFF have been proved effective in the above-mentioned works [14, 3] by training on minimal and maximal activations only, obtained using a visual stimulus. The models so obtained have comparable accuracy to those obtained in ideal conditions, meaning that the system based upon RR-RFF is usable in practice.

Interfaces for assistive robotic arms A crucial point in most investigations on HMIs for the disabled is that there is no real need to gather "proper" ground truth to build a good model. In prosthetic hand control, one possible scenario is that of having the prosthesis autonomously move into a certain configuration and asking the subject to try and enact that configuration: gathering the (sample,target) pairs in this situation and updating the corresponding model will yield the desired behaviour of the control system. Moreover, there is no limit to the updates to the model: if the perceived prediction accuracy is no longer enough, the experimenter — or the subject himself, once the system has been deployed outside the laboratory — can just switch back to the data-gathering phase and update.

For controlling assistive robotic arms, we believe that a natural and intuitive control scheme is highly desirable. Generating goal-directed robot arm movement is a complex task, which can be simplified by commanding the robot in task coordinates. Still, a multi-dimensional interface is needed to move the robot in 3D space. If the bandwidth of the biological signals is high enough, a 1 to 1 mapping, i.e., signals from a limb directly used to control the robotic arm, can be achieved, allowing for intuitive control.

We demonstrated this natural and intuitive control on two different interfaces: one based upon intracortical neural recordings in a patient with tetraplegia, and one based upon sEMG recorded from subjects with severe spinal muscular atrophy (SMA). Whereas an intuitive interface helps the user to operate a robotic system, modern robotic concepts offer a variety of ideas to further increase the usability of an assistive device.

Adding local shared autonomy To provide support to the user of an assistive robotic system in task execution, we are developing a robotic framework that integrates *soft robotic features* to provide safety and supportive behavior in object interaction. The goal is to provide an easy-to-use robotic system for people with physical disabilities and thereby enable them to perform simple tasks of daily living. The framework consists of a fully torque-controlled robotic hand arm system velocity-controlled via an HMI and a binary trigger signal. Furthermore, it consists of an assistive planner which modulates the robots behavior based upon the HMI input and the current state of the robot. Currently, we exploit the torque sensing capabilities of the robotic system to detect the state of action within a task and then assist in task execution. In the future work, this framework shall be extended with a vision system, to potentially provide more sophisticated supportive behavior.

Figure 1 depicts a schematic overview of the devised framework. Its core component, the assistive planner, has access to a set of functionalities stored in a *library of skills*. A skill, e.g., picking up a cylindrical object, is an activity started by the user via a binary trigger signal. Skills are parameterized by information (e.g., the diameter of the object to be grasped) gathered from a world model. The world model also provides information related to safety features to the robotic system, e.g., the position of the user and the allowed workspace. The framework also consists of a feedback provider, which extends the feedback available to the user beyond visual information. The feedback provider features audible feedback based on the

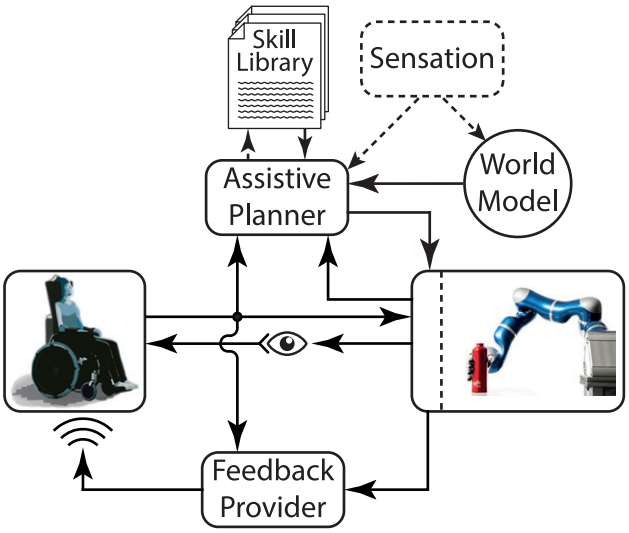

Figure 1: An assistive framework for a torque controlled robotic hand-arm system to support people with physical disabilities.

assistive planner and the state of the robot, e.g., in case of contact with workspace limits.

At the current state of development, the world model is static and manually defined in accordance with the task to achieve. Currently the skill library consists of three predefined skills, which can be used to grasp a bottle, drink from it and safely put it back on a table. The internal sensing capabilities of the robotic system can be used to evaluate the current state within a skill. For instance, stable grasping of the bottle is ensured from the torque sensing of the hand, when the user activates the grasping skill. Another example of this supportive behavior is given when the user wants to put the bottle back on the table. Once the according release skill is activated, the robot will move downwards until contact with the table is detected by the collision detection algorithm. Only after this contact has been established, the hand opens and thereby releases the object. To provide further support, a retract motion of the robot is executed automatically to safely release the object.

3 ...to practice

A neural interface to control a robotic arm We used the assistive framework mentioned in Subsection 2 with a tetraplegic patient within the Braingate2 clinical trial [5]. Using an intracortical microelectrode array, we recorded neural spiking activity from the hand-arm region of the participant's M1 motor cortex. From these signals, the intended upper limb movement was decoded and used to directly control the Cartesian velocity of the robotic arm. In the experiments we conducted, the participant was able to autonomously serve herself a drink for the first time after her brain stem stroke, which she suffered approximately 14 years prior to this research (see Figure 2 as well as [16, 5]).

Figure 2: Screenshots from video footage showing the subject during the first successful completion of the drinking task (reprint from [5]).

sEMG in a case of neurodegenerative disease Turning to a non-invasive interface, we have exploited the sEMG signals stemming from residual arm muscle fibers, which can be voluntarily activated but which do not suffice to move the limbs. We recorded residual sEMG from two subjects with spinal muscular atrophy, a disease leading to death of motor neurons in the spinal cord. In combination with the above mentioned machine learning methods, a natural control scheme has been developed, to allow for translational control of a robotic hand arm system [15]. To gather ground truth data for system training, we use a paradigm based on visual stimuli. In this, the subject is asked to monitor predefined motions of the robotic arm and perform muscular activation that shall be associated with the observed movement direction. After training a Neural Network on this data, the subjects could control a full dynamics simulation of the DLR Light-weight Robot III on a 3D monitor, using the associated EMG activation.

The short-term plan is that of combining the newly developed sEMG-based interface with the above described assistive framework, and conduct experiments not only in the robotic simulation but with the real robotic system.

Teleoperation via sEMG RR-RFF have been used to demonstrate a very stable form of grasping control on the teleoperated humanoid platform called TORO [12]. The system achieved a success rate of up to 95% when deployed in a daily-living-activites setup. We applied force control on all 5 motors of one *i-LIMB Ultra* hand prosthesis [4] (Figure 3 shows the setup); moreover, the same approach was later on applied to two *Azzurra* mechanical hands by Prensilia, fixed on two wrist/hand splints that intact subjects would use to manipulate objects in an environment modeled after the Southampton Hand Assessment Procedure [9]. In that experiment we showed that incremental learning was required, although it represented only a fraction of the total time of the experiment.

Playing a virtual piano via ultrasound The incrementality of RR has also been exploited to convert ultrasound

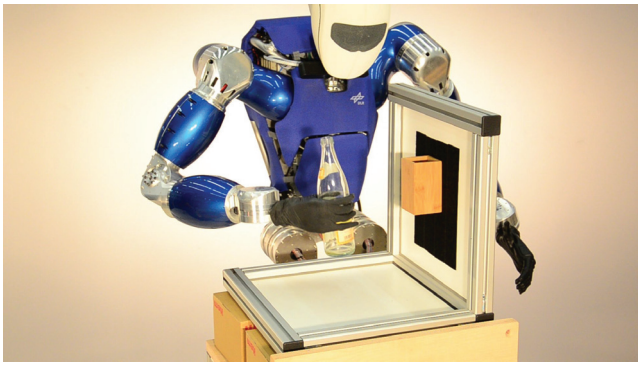

Figure 3: The teloperated TORO setup while performing pick'n'place actions (reprint from [4]).

images of the forearm into finger forces. The result is the *Ultraharmonium*, a virtual dynamic keyboard-based instrument [1] which is going to be used for rehabilitation of wrist/hand impairment as well as for handling complex regional pain syndrome and phantom-limb pain. In this work, for the first time we also used questionnaires to obtain a subjective evaluation of the experience by the involved subjects, revealing that the "game" was perceived as natural and exciting. We think this is an essential point: to involve the subject in the training of the machine, as well as inducing him to learn how to properly use the machine. Figure 4 shows the setup we used.

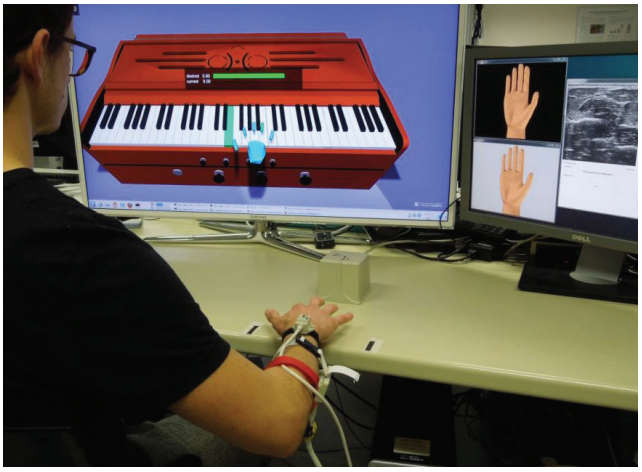

Figure 4: The Ultraharmonium setup: playing a virtual keyboard instrument using ultrasound images of the forearm (reprint from [1]).

4 Discussion and conclusions

Rehabilitation robotics is about human beings and restoring their pre-disease functions. We have the feeling that, at the time of writing, the dexterity of the robotic artifacts is way ahead of the control possibilities. To the aim of improving the situation, we have for the past few years turned our attention to simultaneous, proportional, incremental and natural control. The main idea is that of reading one or more types of bodily signals in real time, and converting them to signals which will control the mechanical artifact proportionally. Natural and incremental control means that one must be able to update the model built so far by the control system, in order to take into account the changes in the signals and the new situations which can arise. The patient must in the end be able to control the robot "by desiring so".

The take-home lesson that our experience has so far taught us is that such a system must be literally designed *around the human subject*, inducing him to produce the right patterns; measuring his performance with a concrete accuracy metrics; and tailoring the system (signals, sensors, processing method, robotic artifact) on the patient himself. Close cooperation with rehabilitation institutes and facilities is, for the engineer, paramount, in order to foster the human contact with the subjects. All in all, the machine-learning methods employed to control such artifacts must be brought out of the laboratories, and in the clinics. Only by practical application will we learn what the optimal systems look like.

References

[1] Claudio Castellini, Katharina Hertkorn, Mikel Sagardia, David Sierra González, and Markus Nowak. A virtual piano-playing environment for rehabilitation based upon ultrasound imaging. In *Proceedings of BioRob - IEEE International Conference on Biomedical Robotics and Biomechatronics*, pages 548–554, 2014.

[2] Claudio Castellini and Vikram Ravindra. A wearable low-cost device based upon force-sensing resistors to detect single-finger forces. In *Proceedings of BioRob - IEEE International Conference on Biomedical Robotics and Biomechatronics*, pages 199–203, 2014.

[3] Arjan Gijsberts, Manfredo Atzori, Claudio Castellini, Henning Müller, and Barbara Caputo. The movement error rate for evaluation of machine learning methods for sEMG-based hand movement classification. *IEEE Transactions on Neural Systems and Rehabilitation Engineering*, 22(4):735–744, 2014.

[4] Arjan Gijsberts, Rashida Bohra, David Sierra González, Alexander Werner, Markus Nowak, Barbara Caputo, Maximo Roa, and Claudio Castellini. Stable myoelectric control of a hand prosthesis using non-linear incremental learning. *Frontiers in Neurorobotics*, 8(8), 2014.

[5] L.R. Hochberg, D. Bacher, B. Jarosiewicz, N.Y. Masse, J.D. Simeral, J. Vogel, S. Haddadin, J. Liu, S.S. Cash, P. van der Smagt, et al. Reach and grasp by people with tetraplegia using a neurally controlled robotic arm. *Nature*, 485(7398):372–375, 2012.

[6] Arthur E. Hoerl and Robert W. Kennard. Ridge regression: Biased estimation for nonorthogonal problems. *Technometrics*, 12:55–67, 1970.

[7] N. Jiang, S. Došen, K.-R. Müller, and D. Farina. Myoelectric control of artificial limbs - is there a need to change focus? *IEEE Signal Processing Magazine*, 29(5):148–152, 2012.

[8] Ning Jiang, K.B. Englehart, and P.A. Parker. Extracting simultaneous and proportional neural control information for multiple-dof prostheses from the surface electromyographic signal. *IEEE Transactions on Biomedical Engineering*, 56(4):1070–1080, 2009.

[9] C. M. Light, P. H. Chappell, and P. J. Kyberd. Establishing a standardized clinical assessment tool of pathologic and prosthetic hand function: Normative data, reliability, and validity. *Archive of Physical Medicine and Rehabilitation*, 83, 2002.

[10] M. Marković, S. Došen, C. Cipriani, D. Popović, and D. Farina. Stereovision and augmented reality for closed-loop control of grasping in hand prostheses. *J Neural Eng.*, 11(4):epub, 2014.

[11] S. Micera, J. Carpaneto, and Stanisa Raspopović. Control of hand prostheses using peripheral information. *IEEE Reviews in Biomedical Engineering*, 3:48–68, Octobre 2010.

[12] C. Ott, O. Eiberger, M.A. Roa, and A. Albu-Schaeffer. Hardware and control concept for an experimental bipedal robot with joint torque sensors. *Journal of the Robotics Society of Japan*, 30(4):378–382, 2012.

[13] B. Peerdeman, D. Boere, H. Witteveen, R. Huis in 't Veld, H. Hermens, S. Stramigioli, H. Rietman, P. Veltink, and S. Misra. Myoelectric forearm prostheses: State of the art from a user-centered perspective. *Journal of Rehabilitation Research & Development*, 48(6):719–738, 2011.

[14] David Sierra González and Claudio Castellini. A realistic implementation of ultrasound imaging as a human-machine interface for upper-limb amputees. *Frontiers in Neurorobotics*, 7(17), 2013.

[15] Jörn Vogel, Justin Bayer, and Patrick van der Smagt. Continuous robot control using surface electromyography of atrophic muscles. In *Intelligent Robots and Systems (IROS), 2013 IEEE/RSJ International Conference on*, pages 845–850. IEEE, 2013.

[16] Jörn Vogel, Sami Haddadin, John D Simeral, Sergey D Stavisky, Daniel Bacher, Leigh R Hochberg, John P Donoghue, and Patrick van der Smagt. Continuous control of the DLR Light-weight Robot III by a human with tetraplegia using the braingate2 neural interface system. In *Experimental Robotics*, pages 125–136. Springer, 2014.

[17] Kiri Wagstaff. Machine learning that matters. In John Langford and Joelle Pineau, editors, *Proceedings of the 29th International Conference on Machine Learning (ICML-12)*, ICML '12, pages 529–536, New York, NY, USA, July 2012. Omnipress.

Session 6

Interfaces & Haptic Feedback

Chair: Dr. Emmanuel Vander Poorten, University of Leuven

Wednesday, October 15th

11:00 – 12:00

Evaluation of the effect of a robotized needle holder on ergonomics and skills

Thierry Bensignor[1,2,3], Brice Gayet [1,2,3,4] and Guillaume Morel[1,2,3]
1. Sorbonne Universités, UPMC Univ Paris 06, UMR 7222, ISIR, F-75005, Paris, France
2. INSERM, U1150, AGATHE-ISIR, F-75005, Paris, France
3. CNRS, UMR 7222, ISIR, F-75005, Paris, France
4. Institut Mutualiste Montsouris, Digestive Surgery Department, France

I. AIMS

In laparoscopic surgery, the surgeon meets technical and ergonomics problems that do not exist in open surgery, because of the limited number of degrees of freedom of the instruments. Some tasks, such as sutures, become technically difficult to realize. Furthermore, on long term, this induces, for a lot of surgeon, muscolo-skeletal pain of the upper members and the neck due to vicious positions [1]. New robotized types of instruments seek to overcome those two troublesome issues.

We have developed, in partnership with the Endocontrol Company, a 5mm robotized needle holder, named Jaimy, which has 2 intracorporeal degrees of freedom, Yaw-Roll, controlled by a joystick placed on an ergonomic handle [2–4]. The tip of the instrument can bend from 0° to 80° and his jaws can turn on themselves with a speed controlled through the joystick deviation (Fig1).

To our knowledge Jaimy is the only 5mm robotized laparoscopic needle-holder developed. Another robotized needle holder, Robot Dex (Dexterite Surgical, Annecy, France) was developed, but it is a 10mm device. Our co manipulated instrument allows the surgeon to perform his intervention in sterile condition next to the patient and with a haptic feedback, unlike telemanipulated surgical robot such as the DaVinci Surgical Robot (Intuitive Surgical, Inc., Sunnyvale, CA, USA). Haptic feedback is an important sensitive information for the surgeon during suturing to preclude tissue traumatism. Besides, the robotization of laparoscopic instrument avoids the use of a knee joint between the handle and the shaft to control the distal DOF. Non robotized instrument with such interface have been created in the past decade but this type of interface is hard to control and can thus offset the advantage of intracorporeal DOF [7].

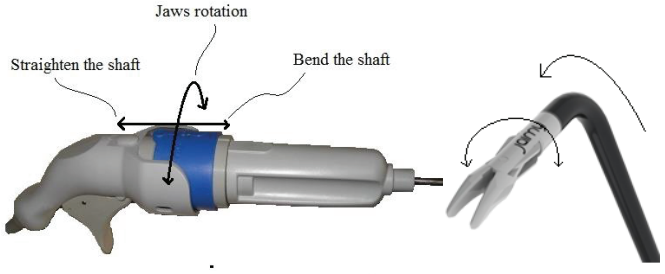

Figure 1: Jaimy, a robotized needle holder

The aim of this study is to evaluate if this needle holder increases the surgical skills and the surgeon ergonomics for diverse kinds of standard surgical tasks.

II. METHODS

This is a randomized cross-over study that is stratified on the level of expertise. Each subject is separated between two groups: resident surgeon and senior surgeon. We compare Jaimy to a standard laparoscopic needle holder (Karl Storz). Each subject has to make a set of 3 limited time exercises on a pelvitrainer with a 0° degree optics. They perform the exercises whether with Jaimy (*J*) first and then with the classic laparoscopic needle holder (*NH*) – after at least 2 hours of cooldown to avoid practice bias – or in the inverse order. The non-dominant hand uses a classic grasper or another needle holder.

The 3 exercises are:

1. Pegboard gripping exercise: the set is composed of 2 pegboard and 6 pegs. The 6 pegs are taken one by one from a pegboard with the dominant hand, then transfer to the other hand and place on the other pegboard. This was then reversed. We measure the number of peg transfer and the number of fallen peg.
2. Hexagonal suture: with a 2/0 Vicryl, a suture around a hexagonal pattern is made. The suture has to go through entrance and exit dots. We measure the quantity of stitches and the precision of entry and exit of each stitch.
3. Suture and knots: one stitch is made through an entry and an exit dots on a frontal axis and then 1 double knot follow by 2 simple knots are realized. We measure the distance between the entry and the exit of the stitch and the dots and also the quantity and quality of the knot.

Ergonomics of the dominant arm is evaluated by motion capture and surface electromyography. Five markers for motion capture are positioned on the subject: hand, forearm, arm, acromion and sternum, together with a marker on the instrument and a reference marker on the pelvitrainer. The Polaris system is used to record markers positions with a 15Hz frequency. A calibration for each articulation, made at the beginning of the session, allows finding the centers of the articulation using a spherefit algorithm. Then the angles between the different segments of the upper limb are calculated for every moment: angle between the arm and the vertical, elevation of the shoulder, angle between the arm and

the forearm, rotation of the forearm and angle between the hand and the forearm.

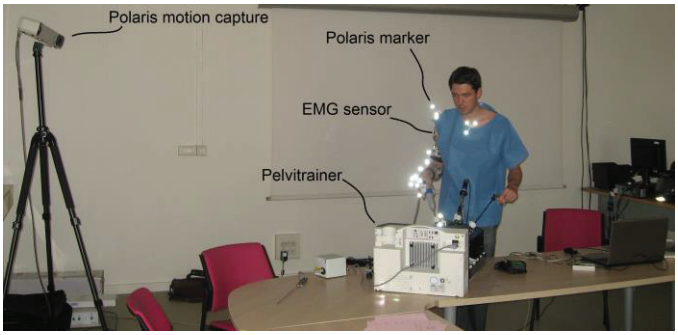

Figure 2: experimental setup

An ergonomic score of the dominant upper limb, the RULA-score (*RULA*) (Table 1), developed by Persons & al, can be calculated, as every angle corresponding to a value [2,5]. This score ranges from 4 to 15 and will increase when ergonomics decreases. We calculate the RULA-score for each exercise and the mean of the 3 exercises.

TABLE I
INDIVIDUAL POSTURE SCORES TO COMPUTE THE ERGONOMIC SCORE

Upper-arm score	*Arm elevation angle (0° when arm down)*
1	0–45°
3	45–90°
5	>90°
+1	if shoulder is raised by >10 mm
Forearm score	*Elbow flexion angle (0° when arm and forearm aligned)*
1	60-100°
2	<60°; >100°
+1	if hand crosses body midline or is out to side
Wrist posture score	*Wrist flexion angle (0° when forearm and hand aligned)*
1	-5–5°(neutral)
2	-15–-5°; 5–15°
3	<-15°; >15°
+1	if wrist deviation angle >5°
Wrist twist score	*Forearm rotation angle*
1	-45–45°
2	<-45°; >45°

Table 1: RULA-score

Additionally, EMG data is collected with the TeleMyoDTS system and the MyoResearch software. EMG data's are collected with a 1000 Hz frequency. Six muscular groups of the dominant arm are evaluated: the flexor carpi ulnaris, the extensor carpi radialis, the biceps brachialii, the triceps, the deltoid and the trapezes. The maximal voluntary contraction of each muscle is recorded at the beginning of the session and is used as a reference to normalize every recording as a percentage of this maximum voluntary contraction. Then the EMG data is full wave rectified and filtered using a Butterworth low-pass filter with a cut off frequency of 10 Hz on Matlab. Finally we can measure the Cumulative Muscular Workload (*CMW*) of each muscle group, which is the area under the curve of the filter EMG signal and can be translated into the work made by each muscle.

The tip of the instrument localization enables the measure of surgical skills. The indicators are the length travel by the tip of the instrument (*Length*) and the number of movements (*Mov*) during each exercise or the total ofthe3 exercises.

We also use a scoring system specific to each exercises to evaluate the performances. This score has been developed by Menhadji & al [6]. It is composed of a quantitative score (*Quant*) and a qualitative score (*Qual*). Their product is the global score (*Global* = *Quant x Qual*) and assessed the performance of each exercise.

III. RESULTS

14 surgeons were included in this study, 8 senior surgeons and 6 residents. 7 were randomized in doing the exercises with Jaimy then with the classical instrument and 7 did the inverse process. 12 subjects are right-handed and 2 are left-handed. Only one surgeon has already use Jaimy before.

I.A Ergonomics

Figure 3 presents the results for the RULA score. The mean RULA-score for the three exercises is statistically better with Jaimy (*RULA-score_J* = 8.67 ± 1.05) than with the classic needle-holder (*RULA-score_NH* = 10.09 ± 1.44) ($p < 0.001$).

For the Peg-Board exercise, the observed performance is better for Jaimy but this is not statistically significant (9.13 ± 1.48 vs 9.68 ± 1.45; $p = 0.056$). For the 2 sutures exercises the difference is statistically significant and in favor of Jaimy. *RULA_J* = 8.58 ± 1.27 versus *RULA_NH* = 9.98 ± 1.49 ($p < 0.001$) for the hexagonal suture and *RULA_J* = 8.16 ± 1.1 versus *RULA_NH* = 9.93 ± 1.67 ($p < 0.001$) for the frontal suture.

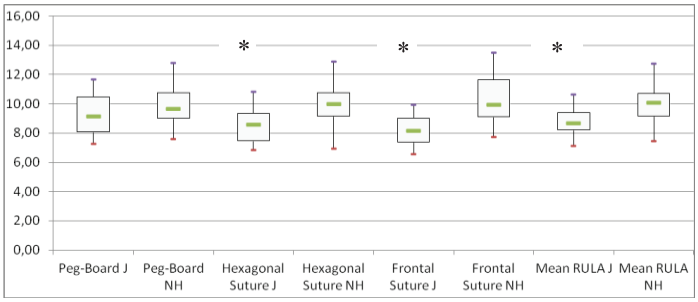

*Figure 3: RULA score; *: $p < 0.05$*

III.B Muscular workload

For 4 muscular groups (extensor carpi radialis, biceps brachialii, deltoid and trapezes), there is no significant difference between using Jaimy and the classic needle-holder. The *CMW* on the three exercises is in favor of the classic needle-holder for the flexor carpi ulnaris, with *CMW* for Jaimy and the needle holder respectively of 15.96 ± 7.06 vs 9.85 ± 2.74 ($p < 0.001$) and for the triceps, with *CMW* of 18.72 ± 9 vs 11.93 ± 8.55 ($p = 0.026$).

III.C Skills

There is no statistically significant difference between the two instruments for the total number of movement, *Mov_J* = 343.1 ± 57 vs *Mov_NH* = 322.9 ± 31 (p = 0.88).

Meanwhile, the path length of the tip of the instrument is shorter with Jaimy than with the classic needle-holder, *Length_J* = 926.52 cm ± 189.38 vs *Length_NH* = 1131.5 cm ± 224.9 (p = 0.006).

III.D Performance

The performance for each exercises are summarized in the figure 4.

The Peg-Board exercise score is in favor of the classic needle-holder, with *Global_J* = 22.5 ± 9.31 versus *Global_NH* = 34.5 ± 9.77 (p = 0.002). There is no difference for the qualitative score but quantitative score is better with the needle-holder.

The global hexagonal suture score is not statistically different, with scores of *Global_J* = 18 ± 7.46 versus *Global_NH* = 16 6 ± 6.08 (p = 0.13), because the quantitative and the qualitative scores are not in favor of the same instrument. The qualitative score is better with Jaimy *Qual_J* = 3 ± 0.55 versus *Qual_NH* = 2 ± 0.47 (p = 0.003) and the quantitative score is better with the classic instrument, *Quant_J* = 6 ± 2 versus *Quant_NH* = 8 ± 2.14 (p = 0.034). Finally, the frontal suture score is better with Jaimy with *Global_J* = 26 ± 7.97 versus *Global_NH* = 15 ± 5.86 (p < 0.001), with a superiority in both the qualitative and quantitative score.

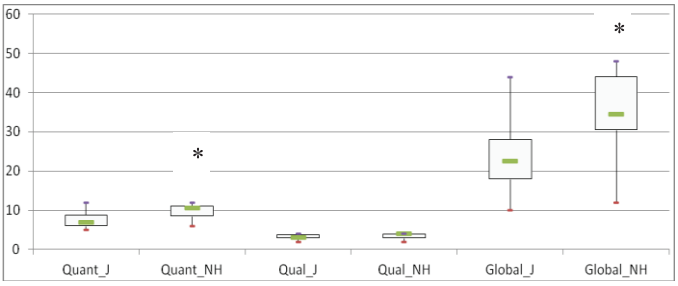

*Figure 4A: Peg Board scores; *: p<0.05*

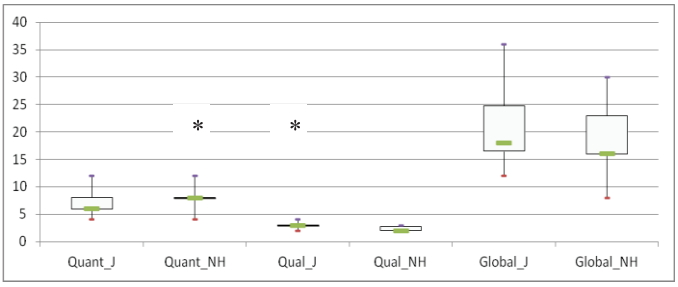

*Figure 4B: Hexagonal sutures scores; *: p<0.05*

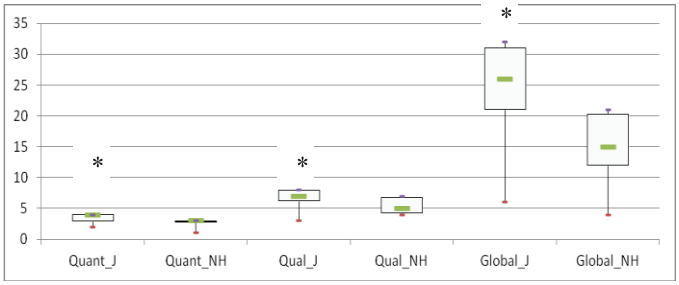

*Figure 4C: Frontal sutures scores; *: p<0.05*

IV. DISCUSSION AND CONCLUSION

Most of the different indicators computed show a positive impact on the use of a Jaimy robotic needle holder as compared to a conventional instrument. More particularly, this study shows that a robotized needle-holder such as Jaimy allows the surgeon to have a better posture during difficult sutures. The quality of the suture is also increased, thanks to the added intracorporeal degrees of freedom.

It is very important to notice that all the subjects were having some experience on surgery with classical instruments, but not with Jaimy (except for one subject). Thus, these results on significant posture improvement and significant quality of suturing improvement also demonstrate the intuitiveness of the use of the instrument.

Three individual results did not show the superiority of Jaimy.

Firstly, the measure of the flexor carpi ulnaris activity showed a higher level with Jaimy: this muscular group is mainly used here for closing the jaws through the trigger. This function is technically realized, in both instruments, in the same way (mechanically). However, during the experiments, the trigger in Jaimy was tuned with a high stiffness which has been clearly identified, from isolated tests, as the source of the high activity of the flexor carpi ulnaris. This observed difference will thus be easily corrected and has nothing to do with the robotic functions of the instrument (distal mobility).

Secondly, for the Pegboard exercise, performance is higher with the conventional instrument. A careful observation has shown that, during this exercise, surgeons tended to use the distal mobility of the instrument even though it was not necessary. For this reason they lost time “playing” with the instrument and were able to achieve less steps of the overall task. It is hypothesized that this behavior mostly came from the fact that the surgeon wanted to test the new instrument and to see if it could be of some use for this exercise, rather than focusing on rapidly completing the task. Once again, this observation seems to have little impact on the interest of using a Jaimy needle holder for surgery.

Thirdly, for the first suturing exercise, the quantity of suture achieved with the standard instrument was slightly higher (with statistical signfiance) than with Jaimy. One could conclude that using Jaimy slows down the suturing. In fact, a careful observation shown that the time used to position the needle in the jaws was higher with Jaimy, while the suturing by itself was faster with Jaimy. Indeed, surgeons rapidly understood that the last robotized DoF of Jaimy can produce a

very well controlled movement for the needle at a cost: the needle shall be precisely perpendicular to the jaws. Meanwhile, this constraint is looser with a conventional instrument, leading to a less precise needle grasping phase. This is also consistent with the other performance result for the same exercise: with Jaimy, the quality of the sutures is significantly higher.

In summary, this study proves that the use of robotized laparoscopic instrument such as Jaimy increases the postural comfort, the skills of the surgeon and most of the performance indicators, even when the surgeon uses it for the first time while he/she is trained with the conventional instrument. It was remarkable to observe almost no learning curve for the use of Jaimy.

The study also allowed identifying two minor technical problems: jaw trigger stiffness, which is already solved and needle positioning in the jaws, which will soon be eased by the development of jaws that favor, by the shape, perpendicularity.

V. ACKNOWLEDGEMENT

This work was partially supported by French state funds managed by the ANR within the Investissements d'Avenir programme (Labex CAMI) under reference ANR-11-LABX-0004 and through the FUI Fluoromis project.

VI. REFERENCES

[1] Berguer R, Forkey DL, Smith WD. Ergonomic problems associated with laparoscopic surgery. Surg Endosc. 1999 May;13(5):466–8.

[2] Herman B, Zahraee a. H, Szewczyk J, Morel G, Bourdin C, Vercher J-L, et al. Ergonomic and gesture performance of robotized instruments for laparoscopic surgery. 2011 IEEE/RSJ Int Conf Intell Robot Syst. Ieee; 2011 Sep;1333–8.

[3] Zahraee AH, Paik JK, Szewcyzk J, Morel G. Towards the Development of a Hand-Held Surgical Robot for Laparoscopy. :1–9.

[4] Zahraee AH, Paik JK. Robotic Hand-Held Surgical Device : Evaluation of End-Effector ' s Kinematics and Developpement of Proof-of-Concept Prototypes. :1–8.

[5] Person JG, Hodgson a J, Nagy a G. Automated high-frequency posture sampling for ergonomic assessment of laparoscopic surgery. Surg Endosc. 2001 Sep;15(9):997–1003.

[6] Menhadji A, Abdelshehid C, Osann K, Alipanah R, Lusch A, Graversen J & al. Tracking and assessment of technical skills acquisition among urology residents for open, laparoscopic, and robotic skills over 4 years: is there a trend? J endourol. 2013 June; 27(6): 783-9.

[7] Martinec D, Gatta P, Zheng B, Denk PM, Swanström LL. The trad-off between flexibility and maneuverability: task performance with articulating laparoscopic instruments. Surg Endosc. 2009; 23(12): 2697-701.

Towards Intuitive Operation of a Robotic Catheter

A. Devreker, S. Portoles Diez, A. Gijbels, B. Rosa,
J. Vander Sloten, E. Vander Poorten, D. Reynaerts
Department of Mechanical Engineering
Katholieke Universiteit Leuven
Leuven, Belgium

H. De Praetere, P. Herijgers
Experimental Cardiac Surgery
University Hospital Leuven
Leuven, Belgium

***Abstract*—Advances in miniaturized surgical instrumentation are key to less invasive and safer medical interventions. Also in cardiovascular procedures interventionalists turn more and more towards catheter-based interventions, treating patients considered unfit for more invasive approaches. Improvements in design and steerability can further reduce the level of invasiveness of catheter-based interventions e.g. by improved control over interaction forces tissue damage can be limited. Operation times and exposure to radiation can be reduced by improving the steerability of the catheter. This abstract presents recent work in this direction. A novel hydraulically actuated catheter is introduced and efforts to devise intuitive mappings between a joystick input device and the new catheter are reported. Experimental results show an encouraging steerability of the novel robotic catheter. Whereas at present superiority of one mapping is obtained compared to the other, it is expected that further improvements by additional visual guidance or by embedding partial autonomy will further improve the ease of use.**

***Keywords*—robotic catheter, artificial muscle, teleoperation, catheter control, TAVI**

I. Introduction

Reducing invasiveness of surgical techniques has always been a major concern in the medical community. However, the advantages for the patient associated to MIS (Minimally Invasive Surgery) come at a substantial cost, namely a significant increase in procedural complexity. This is mainly caused due to a lack of visualization and the loss of direct access to the surgical site. Advances in miniaturized, dexterous and reliable surgical robotic instrumentation could overcome aforementioned complications. A large spectrum of robots has been designed for this purpose in the past[1].

Also in cardiovascular procedures MIS has brought considerable benefits. Thanks to technological improvements, weak patients suffering from severe aortic stenosis, previously classified as inoperable, can now be operated using a trans-catheter approach: Transcatheter Aortic Valve Implantation (TAVI) [2]. Despite the risks associated with radiation exposure, fluoroscopy is still the main imaging technique used during TAVI surgery [3]. Current valve delivery systems, such as the NovaFlex+ Transfemoral System (by Edwards Lifescience) only provide a single manually controllable bending motion. Due to the poor controllability and the high stiffness, surgeons cannot insert these devices directly into the vasculature. A combination of guidewires and supporting sheets need to be introduced to clear the way for the delivery catheter. What is worse is that every placement step takes place under X-ray guidance. Also, the risks of plaque disruption, puncture of tissue, tissue damage forms an important concern for TAVI surgeries[4], [5].

This paper presents a novel inherently compliant sensorised active robotic catheter. Both a position sensor and IVUS (IntraVascular UltraSound) sensor are integrated in this catheter which allows it to reconstruct the catheter's environment in real-time in a radiation-free manner[6]. The robotic catheter was interfaced and integrated into a dedicated robot control framework so that it can be remotely controlled by a haptic device. Given the large kinematic dissimilarity between the master robot (joystick) and the robotic slave (catheter) it is not straightforward at all to come up with an intuitive mapping between joystick inputs and catheter motion. This paper reports on the work that was conducted to come up with such a mapping. After describing the overall setup of the system (section II), a pair of mappings are introduced and motivated (section III). Section IV introduces some initial experimental results that were conducted with this system. Finally, conclusions are drawn and directions for further work sketched in section IV.

II. Robotic Catheter Teleoperation System

Navigating in a delicate and deformable environment such as the human vasculature requires superior dexterity compared to what classical robotic structures can provide. Thanks to their miniaturizability continuum robots provide here an attractive opportunity[7]. The 7mm diameter robotic catheter presented in this paper is made up of a continuum backbone actuated by fluidic muscles which provide three distal actuated degrees of freedom (DOF). The catheter body is further clamped in a catheter driver which takes care of the catheter's insertion movement and allows rotation of the catheter about its neutral axis. The available DOFs are controlled by a 4DOF haptic joystick that was designed for MIS applications. The different components of the robotic catheter teleoperation system are explained in the following.

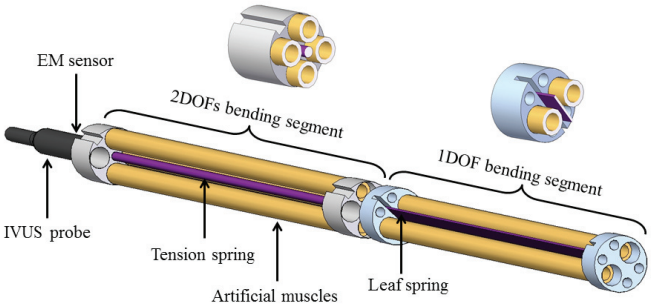

Fig. 1. Configuration of the catheter with two bending segments, an ultrasound probe and a position sensor. One of the four muscles of the more distal bending segment is not represented for better clartiy. Cross sections of both bending segments are also shown.

A. Actuation principle

The insertion of the catheter into the patient body is currently done manually during TAVI procedures. In our setup the actuation of this proximal DOF is provided by a catheter driver. The latter uses a pair of rollers driven by a motor to propel the catheter clamped between them. The same driver also controls the rotation of the catheter about its neutral axis.

The actuation of the three distal DOFs is ensured by pneumatic artificial muscles (PAM) which have the advantage of being inherently more compliant than other actuation principles. PAM are characterized by a high power density and have been extensively studied and used in the literature [8][9]. The muscles used have already been presented in previous work of the author [10]. Fig.1 presents the global configuration of the distal catheter tip and its local actuation and sensors. The three DOFs are distributed over two bending segments located at the tip of the catheter. A first 70mm long segment provides the two most distal DOFs. It is composed of four PAM distributed around a 0.9mm diameter axi-symmetric tension spring which acts as a 2DOF return spring. By actuating the corresponding muscles this segment can bend in two directions. A second 60mm long segment allows the actuation of a third DOF. The latter antagonist structure is made up of two muscles and a 1DOF leaf spring. The 3rd DOF was designed to improve the passage by the catheter of the aortic arch, however at this point and in the presented work the focus is limited to steering of the two most distal DOFs. This choice simplifies the steering as both bending DOFs are collocated, yet it still is not trivial as the overall control requires managing of the combination of the proximal (global) and distal (local) DOFs. In future work the control of the 3rd bending segment will be addressed as well.

B. Integrated sensors

In order to provide a better visualization to the surgeon, an intra-vascular ultrasound (IVUS) probe was disassembled and mounted at the tip of the robotic catheter (black in Fig. 1). The probe used is a Visions PV 8.2 manufactured by Volcano Corporation. In the original tool lumen of this IVUS probe, an electromagnetic position sensor was embedded. The position sensor used is a 6DOFs Aurora sensor developed by NDI Medical. Thanks to the information provided by both sensing technologies, the catheter tip can be accurately located and a 3D model of the aorta can be reconstructed[6].

C. Haptic joystick

The robotic catheter was interfaced and integrated with a dedicated surgical robotic control platform so that it can be tele-operatively controlled using a haptic device. The joystick that was used is the 4DOFs joystick that has been described in [11] and is depicted in Fig.2. It provides three rotational DOFs and one DOF in translation. The 4DOF joystick was designed for MIS applications in general and seems particularly suited for controlling robotic catheters where the translation DOF could command the insertion. The three rotational DOFs allow experimenting with various mappings to control the distal local actuation. Two potentially interesting mappings are described in the next section.

III. Control Strategies

The kinematic dissimilarity between the master robot and the robotic slave complicates the steering and as such forms a major motivation for the research towards intuitive mappings. Since the workspaces differ considerable in size the use of rate control is considered. Indeed, during TAVI surgery, the catheter is inserted in the patient body at the level of the groin and brought up to the aortic annulus by following the aorta and crossing the aortic arch. The insertion length, close to one meter, is thus ten times larger than the available and usable stroke of the joystick DOFs. For rotation/bending DOFs the range is similar and rate control is not needed here. An extra element to be considered is that the developed prototype provides more controllable DOFs than the joystick offers. For the presented work, two different mapping were investigated. The mappings are presented in Fig.3 and Fig.4 and explained below.

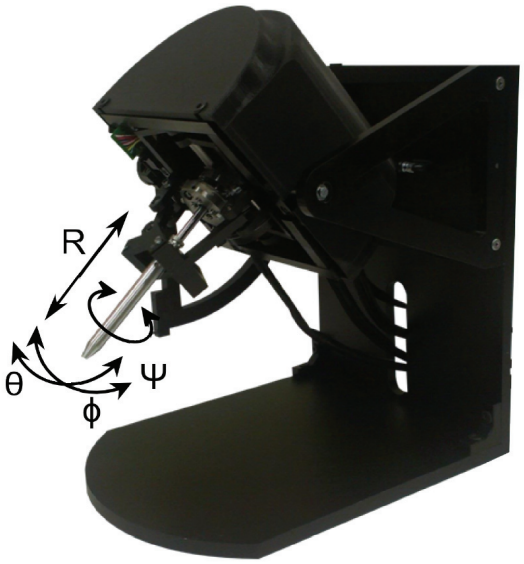

Fig. 2. The insertion of the catheter is controlled by the translational DOF R of the joystick. For the distal DOFs of the catheter, either master joint angles φ and θ, or φ and Ψ are used.

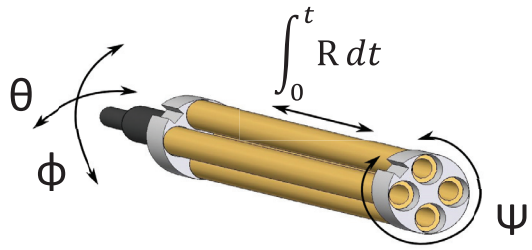

Fig. 3. Sketch of 'direct joint-based mapping'. The symbols indicate the motion generated by the different DOFs R, ϕ, θ, Ψ of the haptic joystick (as depicted in Fig.2) the insertion and the rotation of the catheter are controlled similarly to current manual OR practice. The two additional bending segments are controlled with the two other rotational DOFs ϕ, θ of the joystick.

A. *Direct joint-based mapping*

The first mapping was designed so that the hand movements of the user – for the proximal DOFs - are similar to gestures a surgeon would perform during a real TAVI procedure.
For the insertion of the catheter and thus the control of the catheter driver, the translational DOF R of the joystick is used. Given the difference in range in this DOF, and in order to keep a relatively good precision, the control of the catheter insertion uses rate control. The orientation about the neutral axis of the catheter is controlled using the joystick's joint angle Ψ. By initial alignment of the joystick handle and the catheter body, real-life steering conditions are reproduced.
The pressure levels in the pneumatic muscles, and thus the distal DOFs, are directly related to the corresponding master joint angles ϕ and θ, as depicted in Fig.2 and Fig.3, an upwards movement of the joystick induces an upwards bending of the catheter tip.

B. *Spherical distal mapping*

The basic idea behind the second mapping is to decouple the orientation of the bending plane of the catheter (i.e. the orientation of the plane wherein the bending takes place) from the bending amplitude. The orientation of the bending plane is controlled by the joystick's joint angle Ψ. The bending amplitude is mapped to the joint angle ϕ. This mapping is represented in Fig. 4. The assumed advantage of this mapping is that it would allow the user to precisely adjust the bending orientation while keeping the bending amplitude constant. This could especially be advantageous when crossing the aortic arch of which the curvature is approximately constant.
Similar to the case of the direct joint-based mapping, the insertion is controlled with the translation R of the joystick. The rotation of the catheter about its neutral axis is now mapped to the joint angle θ.

IV. Experimental Test

In order to test the developed catheter and to compare the implemented mappings a number of experiments have been conducted. During experiments the user was asked to insert the developed catheter into a flexible transparent 3D mockup of the aorta using the robotic catheter teleoperation system described in this paper. Both mappings were tested 5 times. The user was an experimented cardiac surgeon.

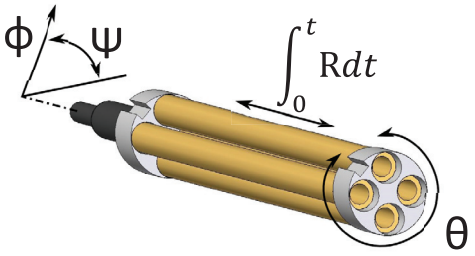

Fig. 4. Sketch of the 'spherical distal mapping' which allows the user to independently control the bending angle and the bending amplitude.

A. *Setup description*

The overall setup layout is represented in Fig. 5. The mockup and the joystick were placed on an operating table. An articulated arm, clamped to the table, holds the catheter driver in front of the 3D mockup. A display showing the IVUS images was located in front of the operator. The 3D mockup, also visible in Fig. 5, was about 20cm long and 12cm wide. It was a silicone aorta constructed from real patient data. Each of the experiments started with the catheter tip inserted in the mockup at the level of the descending aorta. The subject was asked to steer the catheter up to the center of the aortic valve as fast as possible while trying not to put high forces on the aorta itself. The user could visually estimate the contact force between the catheter and the mockup by observing the deformation of the latter. For each insertion the coordinates of the position sensor, the IVUS images, as well as joystick joint angles were recorded.

B. *Results*

The trajectory followed by the EM sensor for a single insertion, overlapped with a representative 3D model of the aorta, is shown on Fig. 6. The time to completion was defined as the time it took the user to steer the catheter originally placed at the level of the descending aorta to the center of the aortic valve. For both mappings the user managed to reach the goal in less than 70s. For the conducted experiments it was found that the average completion time was 10s shorter for the direct joint-based mapping than for the spherical distal mapping. The overall results of the experiments are summarized in Table 1.

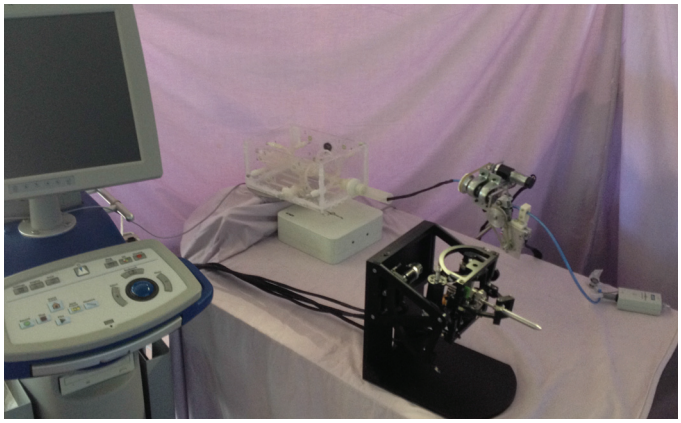

Fig. 5. While steering the catheter the user could directly see the IVUS images as well as the position of the catheter tip thanks to the transparency of the 3D mockup.

TABLE I. EXPERIMENTAL RESULTS

Mapping	*Number of experiments*	*Total time [s]*	*Mean [s]*	*Std. Dev. [s]*
direct joint-based	5	203.4	40.68	12.12
spherical distal	5	263.9	52.78	14.73

After the experiments the user was positively surprised by the steerability of the catheter. However, due to the U-shape of the aorta, once the aortic arch crossed, catheter motion reverses with respect to user input commands. This inversion combined with a build-up of rotational motion of the catheter about its neutral axis did cause some confusion to the user. At such point the user could not easily predict the movement of the catheter anymore. Overall, at least for the limited number of experiments that were conducted, the spherical distal mapping was found less intuitive by the user due to the indirect mapping of the respective DOFs. This can explain the difference in completion time. The user was interestingly mentioning that both mappings have their advantages depending on the insertion level. The aortic arch was, as predicted, easier to cross with the spherical based mapping, while the catheter tip was more easily positioned at the center of the aortic valve with the direct joint-based mapping. Additional experiments as well as more advanced data analysis would help analyzing the proposed mappings in more detail.

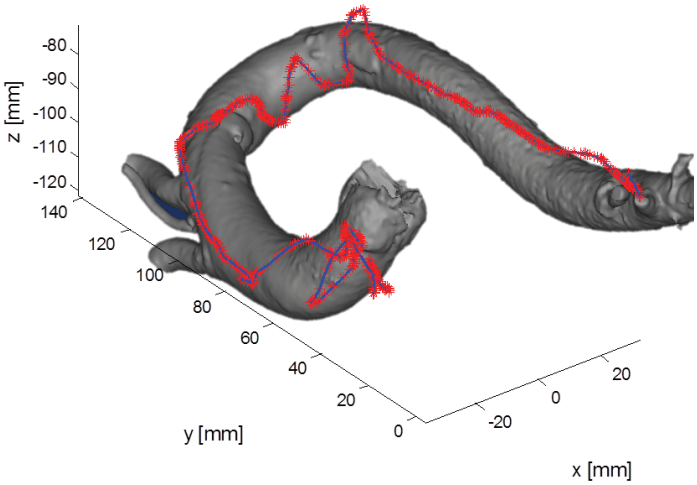

Fig. 6. 3D path followed by the EM position sensor placed at the tip of the catheter. This insertion took 43s and the user was using the direct joint based mapping.

V. CONCLUSION AND FUTURE WORK

This paper describes a first study on the development of dedicated mappings for steering novel inherently compliant sensorised active robotic catheters. Initial results show successful navigation through an artificial mockup and suggest superior performance of a direct mapping. Further experiments should be conducted to exclude possible learning effects. Also, the use of the 1DOF bending segment is expected to increase the overall navigation performance. More in depth experiments, characterization of the system and development of new mappings are also topics for the future.

ACKNOWLEDGMENTS

This research has been supported by the European Commission's 7th Framework Programme FP7-ICT, by the project CASCADE under grant agreement No.601021, and by the fund for Scientific Research-Flanders (FWO – G.0B48.13).

REFERENCES

[1] J. M. Albani, "The role of robotics in surgery: a review.," *Mo. Med.*, vol. 104, no. 2, pp. 166–172, Apr. 2007.

[2] R. R. Makkar, G. P. Fontana, H. Jilaihawi, S. Kapadia, A. D. Pichard, P. S. Douglas, V. H. Thourani, V. C. Babaliaros, J. G. Webb, H. C. Herrmann, and others, "Transcatheter aortic-valve replacement for inoperable severe aortic stenosis," *N. Engl. J. Med.*, vol. 366, no. 18, pp. 1696–1704, 2012.

[3] A. M. Kasel, S. Cassese, A. W. Leber, W. von Scheidt, and A. Kastrati, "Fluoroscopy-guided aortic root imaging for TAVR:'follow the right cusp' rule," *JACC Cardiovasc. Imaging*, vol. 6, no. 2, pp. 274–275, 2013.

[4] J. B. Plotkin, R. J. Siegel, and R. Beigel, "Plaque disruption during transcatheter aortic valve replacement," *Eur. Heart J. - Cardiovasc. Imaging*, vol. 15, no. 1, pp. 117–117, Jan. 2014.

[5] A. Aminian, J. Lalmand, and B. El Nakadi, "Perforation of the descending thoracic aorta during transcatheter aortic valve implantation (TAVI): An unexpected and dramatic procedural complication," *Catheter. Cardiovasc. Interv.*, vol. 77, no. 7, pp. 1076–1078, Jun. 2011.

[6] C. Shi, S. Giannarou, S.-L. Lee, and G.-Z. Yang, "Intravascular Modeling and Navigation for Transcatheter Aortic Valve Implantation," presented at the 3rd Joint Workshop on New Technologies for Computer/Robot Assisted Surgery (CRAS), Verona, Italy, 2013.

[7] S. Iqbal, S. Mohammed, and Y. Amirat, "A guaranteed approach for kinematic analysis of continuum robot based catheter," in *Robotics and Biomimetics (ROBIO), 2009 IEEE International Conference on*, 2009, pp. 1573–1578.

[8] E. G. Hocking and N. M. Wereley, "Analysis of nonlinear elastic behavior in miniature pneumatic artificial muscles," *Smart Mater. Struct.*, vol. 22, no. 1, p. 014016, Jan. 2013.

[9] B. Tondu and P. Lopez, "Modeling and control of McKibben artificial muscle robot actuators," *Control Syst. IEEE*, vol. 20, no. 2, pp. 15–38, 2000.

[10] A. Devreker, E. Vander Poorten, A. Gijbels, P. T. Tran, H. De Praetere, P. Herijgers, J. Vander Sloten, and D. Reynaerts, "Towards Fluidic Actuation for Catheter-Based Interventions," presented at the ACTUATOR 2014, Bremen, Germany, 2014, pp. 173–176.

[11] A. Gijbels, E. B. Vander Poorten, P. Stalmans, H. Van Brussel, and D. Reynaerts, "Design of a Teleoperated Robotic System for Retinal Surgery," presented at the 2014 IEEE International Conference on Robotics & Automation (ICRA), Hong Kong, China, May 31 - June 7, pp. 2357 – 2363.

Toward User-Friendly Robotic Assistance for Enhancing Accuracy and Safety of Reconstructive Microsurgery

L. Vanthournhout, B. Herman, J. Duisit, F. Château, J. Szewczyk, B. Lengelé, and B. Raucent

***Abstract*— Reconstructive microsurgery enables extraordinary procedures such as breast reconstruction, face allograft, or torn member saving. However, several gestures require a precision that goes beyond human dexterity. An ergonomic robotic assistance is being developed to push back the current frontiers of microsurgery and scale it down to the sub-millimeter scale of so-called super-microsurgery. The robot would be integrated transparently and intuitively into standard procedures performed under a microscope, so as to make super-microsurgery safer with limited additional cost.**

I. Context and Objectives

Since the first vascular anastomosis (see Fig. 1) defined at the beginning of last century by A. Carrel, important advances have been made in microsurgery: Tissue autograft, face allograft, torn member saving, hand surgery, etc. None of this could be performed without several major technological innovations such as operating microscope that offers up to 50x magnification [1] and the adaptation of instruments and suturing wires, whose diameter may be smaller than 15 μm. However, several gestures require a precision that goes beyond human dexterity [2], [3]. For this reason, microsurgery procedures such as free flap reconstructions are extremely challenging and remain not very widespread. In particular, the DIEP (deep inferior epigastric perforator) [4] is a complex surgical act of breast reconstruction that consists in removing a vascularized skin flap (with fat tissue) from the patient's lower abdomen, and transplanting it on the breast after a tumor resection (see Fig. 2). At the moment, this procedure requires to cut deeply into the abdominal muscles and to remove a piece of rib from the chest to access blood vessels large enough to be anastomosed. The poor accessibility of the deep surgical sites and the high accuracy required restricts the use of this promising technique in surgical routine. Providing surgeons with a device to assist them in performing safely microanastomoses on sub-millimeter vessels closer from skin could decrease invasiveness of DIEP and other free flap reconstructions, and make these surgical procedures feasible by most microsurgeons.

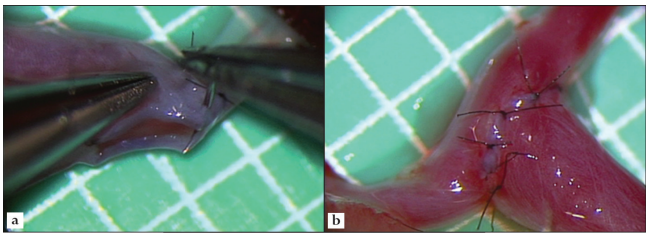

Fig. 1. Microanastomosis on graph paper (from [1].)

A couple of exploratory studies with the Da Vinci surgical system (Intuitive Surgical, Inc.) showed feasibility and highlighted the benefits of robotic assistance for very delicate microsurgery gestures [5], [6]. This teleoperated system allows a motion downscaling and decreases tremor magnitude. However, the Da Vinci system is expensive to purchase and to use. It is also very cumbersome and takes the surgeon away from the operative field. Image magnification provided by the stereo-endoscope might not be sufficient for microsurgery. Furthermore, its kinematics is primarily dedicated to intra-abdominal minimally invasive surgery, and is not really suitable for open microsurgery. Finally, instruments developed by Intuitive for microsurgery are much larger and cumbersome than manual instruments. Besides this commercial system, several research prototypes have been developed in various laboratories. A telemicrosurgery system developed at Tokyo university for open neurosurgery [7] is also efficient but shares most of the Da Vinci's limitations. The RAMS system from Jet Propulsion Laboratory is also devoted to microsurgery, and is notably smaller than aforementioned systems. Yet, no performance improvement has been observed with respect to manual surgery while operative time is doubled [8]. A master-slave system for reconstructive microsurgery has been recently developed by Eindhoven University of Technology [9] but trials with vessels are not reported yet, and because of the selected kinematics, accuracy, velocity and workspace do not appear to be sufficient for our applications.

This work was supported own funds from UCL and ISIR.

L. Vanthournhout, B. Herman, and B. Raucent are with the Center for Reserach in Energy and Mechatronics, Institute of Mechanics, Materials, and Civil Engineering, Université catholique de Louvain, Louvain-la-Neuve, Belgium, and with Louvain Bionics, Université catholique de Louvain, Belgium. lena.vanthournhout@uclouvain.be.

J. Duisit is with Morphology Research Group and with Experimental Surgery and Transplantation Group, Institute of Experimental and Clinical Research, Université catholique de Louvain, Bruxelles, Belgium.

F. Château is with Department of Plastic and Reconstructive Surgery, Cliniques universitaires Saint-Luc, Université catholique de Louvain, Bruxelles, Belgium.

J. Szewczyk is with Institute for Intelligent Systems and Robotics, Universit Pierre et Marie Curie Paris 06 – CNRS, Paris, France.

B. Lengelé is with Morphology Research Group, Institute of Experimental and Clinical Research, Université catholique de Louvain, Bruxelles, Belgium, and with Department of Plastic and Reconstructive Surgery, Cliniques universitaires Saint-Luc, Université catholique de Louvain, Bruxelles, Belgium.

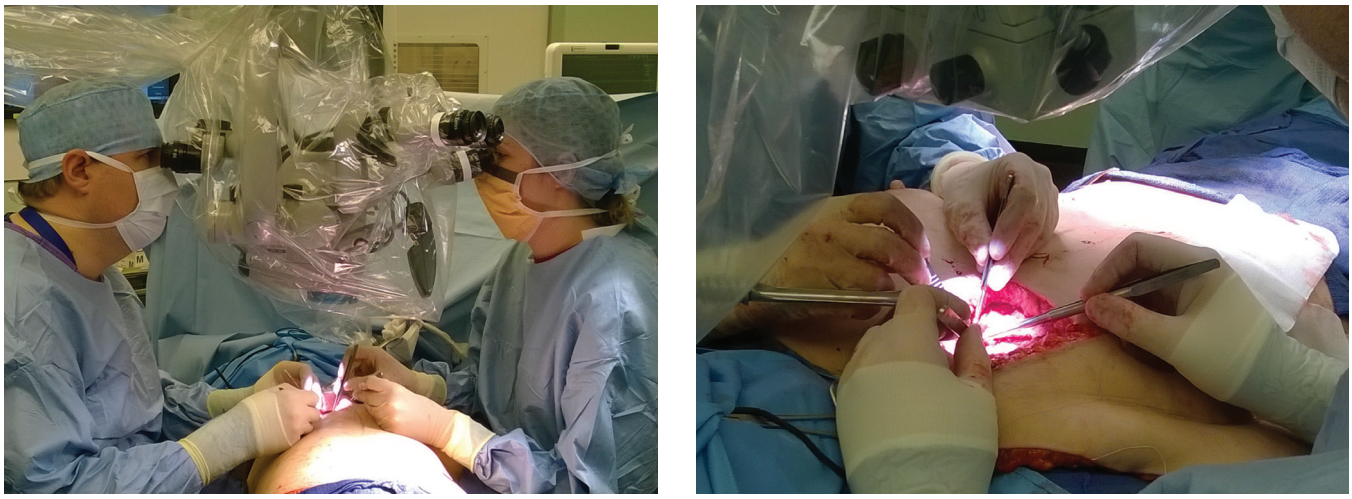

Fig. 2. Microsurgeons at work during a DIEP procedure.

Currently available teleoperation interfaces also suffer from a main limitation often raised by microsurgeons. The scaling factor is generally set constant during a gesture or even during the entire procedure. Yet, if a large reduction factor increases accuracy and decreases tremor magnitude, it also slows down gestures. In addition, the limited working range of the master arms forces surgeons to de-clutch and re-center the arms several times during some gestures (e.g. for pulling a wire over several centimeters). As a consequence, operative time is increased [7], [10], which is a common cause of non acceptance of robotic technology for surgery. This problem of procedure duration is even more severe in the particular case of free flaps, since the surgeon must perform arterial and venous anastomoses rapidly to restore blood flow in graft as soon as possible, and avoid its deterioration. Several authors therefore indicate the need for an more advanced interface allowing a variable scaling factor that could be adjusted manually or even automatically to the complexity of ongoing task [3], [6], [7], [10].

In this context, we aim at bringing both technologically and economically viable solutions to the accuracy and dexterity problems that still reserve microsurgery to few highly-skilled surgeons. Our goal is also to push current microsurgery boundaries and open the way to super-microsurgery, which requires a gesture accuracy close to 0.01 mm so as to achieve anastomoses on sub-millimeter vascular structures (thin pedicles of perforator flap, lymphatic vessels). This paper reports our current work towards the design of a robotic system for microsurgery that would be integrated easily in current microsurgery protocols. It should allow the surgeon to sit next to the patient and work under a conventional microscope. Careful attention must therefore be paid to the robot topology and dimensions, to avoid visual field obstruction while offering a sufficient workspace.

II. Instruments Motion Quantification

Workspace covered by microsurgery instruments, along with their velocity and acceleration, were recorded experimentally so as to set our robot requirements.

A. Experimental Protocol

Two microsurgeons performed a micro-anatomosis on rat adrenal aorta (1.7 mm outer diameter) from zone exposure until anastomosis permeability verification. Position, orientation, and instruments usage were recorded with three devices: (see Fig. 3):

1) A standard camcorder mounted on a tripod to analyze the global workflow and distinguish useful from unnecessary instruments motion (e.g. distinguish valid microsurgery gesture from microscope adjustment, instrument change, surgeon distraction).
2) A 3D tracking system (MicronTracker ®) to localize tip position and orientation of instruments. For this purpose, instruments were equipped with optical markers. Surgeons stated that these sensors did not change the instruments behavior and did not alter the gestures.
3) A microscope-mounted camcorder to record minute details of the surgical site.

Non-relevant instrument motions detected on camcorders recordings were excluded manually from the 3D tracking system data.

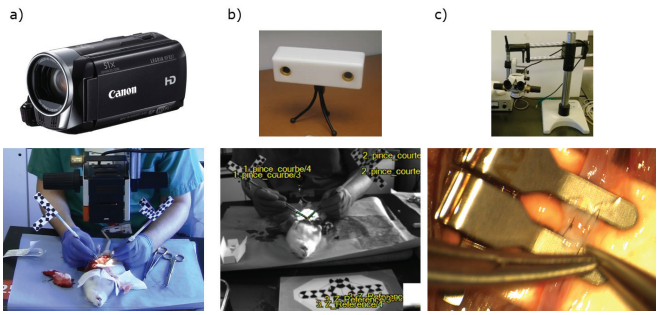

Fig. 3. Devices used for recording position, orientation, and insrtuments usage during a micro-anastomosis: a) Standard camcorder; b) 3D tracking system (MicronTracker); c) Microscope-mounted camcorder.

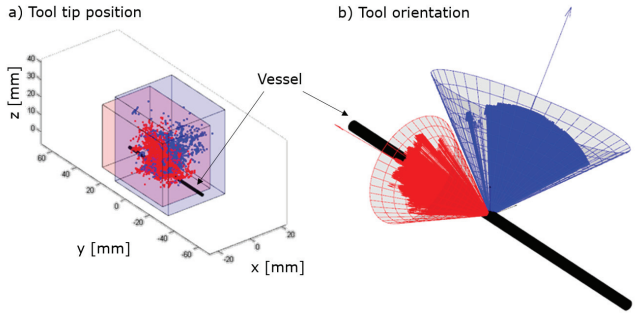

Fig. 4. Microsurgery instruments tip position and orientation with respect to anastomosis center. Surgeon is positioned on y-positive side perpendicular to vessel.

B. Results

Positions and orientations obtained are depicted in Fig. 4. Velocities and accelerations were then derived. To excluding some pick measurments assumed not to be representative only 99.9% of velocity measurements and 99.8% of acceleration measurements were taken into account. Table I gives an overview of the main results.

TABLE I

MICROSURGERY INSTRUMENTS TIP POSITION, ORIENTATION, VELOCITY, AND ACCELERATION DURING ADRENAL AORTA MANUAL ANASTOMOSIS ON RAT.

	Δ Position/Orientation	Velocity	Acceleration
x	37 mm	100 mm/s	410 mm/s^2
y	52.5 mm	100 mm/s	410 mm/s^2
z	48 mm	100 mm/s	410 mm/s^2
ψ (yaw)	135 deg	105 deg/s	570 deg/s^2
θ (pitch)	135 deg	100 deg/s	540 deg/s^2
ϕ (roll)	360 deg	125 deg/s	780 deg/s^2

III. ROBOT TOPOLOGY

Robotic assistance for improving gesture accuracy can be implemented according to two principles: comanipulation and teleoperation. Comanipulaton can filter tremors and has the advantage of being truly intuitive to use: The surgeon simply holds the instrument, as usual, and its motions are smoothed by the robot that can act in parallel such as the SteadyHand [11] or the robot developed at KULeuven [12], or be inserted serially between instrument handle and effector as in the Micron [13]. Telemanipulation, in addition, can scale motions. This feature might not be required for slow pointing tasks as in retinal microsurgery, but is likely to prove useful for more complex gestures that would remain difficult to achieve with human fingers dexterity, even with active tremor cancellation and motion damping. For this reason, the system to be designed will be based on a teleoperation architecture, although the master console should be kept as small as possible to fit on the operating table, as the system proposed in [9].

Robot needs at least 7 degrees of freedom: Six to have sufficient dexterity and the seventh to open/close manipulated tools. We decided to decouple tool tip position from orientation because accuracy requirements are very high in position ($10\mu m$) but low in orientation (in the order of 1-2 deg), where human dexterity is already sufficient. So we chose a XYZ Cartesian structure for positioning and a spherical wrist with concurrent axes crossing at tool tip, with the last rotation coincident with the self-rotation of the instrument (see Fig. 5). This kinematics can match naturally the required position accuracy and offers a sufficient angular amplitude while remaining rather compact. It has already been implemented successfully in the Robotol system [14] devoted to middle-ear microsurgery, and seems to be a good starting point for the design of our own system.

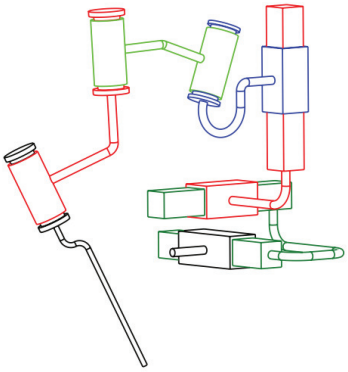

Fig. 5. Considered kinematic structure (from [14]).

IV. GEOMETRICAL AND KINEMATIC OPTIMIZATION

A. Optimization Process

Based on the specifications above, an optimization of seven geometric parameters of the wrist structure is performed. A brute force optimization algorithm tests all possible parameters combinations and checks the following criteria:

- **Constraint 1:** All positions orientations measured previously must be reachable;
- **Constraint 2:** Contact with environment must be avoided;
- **Constraint 3:** Robot cannot pass inside surgeon's visual field;
- **Objective 1:** Distance to environment should be as large as possible;
- **Objective 2:** Dexterity should be as high as possible;
- **Objective 3:** Robot must, as much as possible, leave room for an assistant surgeon to work in front of the main surgeon. This objective is reflected by maximizing the distance between the robot and the vertical plan between the two surgeons (y=0 with respect to Fig. 4). The larger the distance is the better it is.

The solutions that cannot fulfill constraints 1, 2 ou 3 are rejected while the others form the set of admissible solutions and are classified regarding their score associated to objectives 1, 2 and 3.

B. Results

200 millions of solutions were evaluated. The set of admissible solutions has got a Pareto Surface (i.e.: the sub-set comprising of all non-inferior solutions with respect to the three objectives) which is represented on Fig. 6. As depicted also on Fig. 6, the particular solution n1247 stands for a good final choice as it presents balanced scores between the 3 objectives. The robot structure corresponding to this particular solution is shown on Fig. 7.

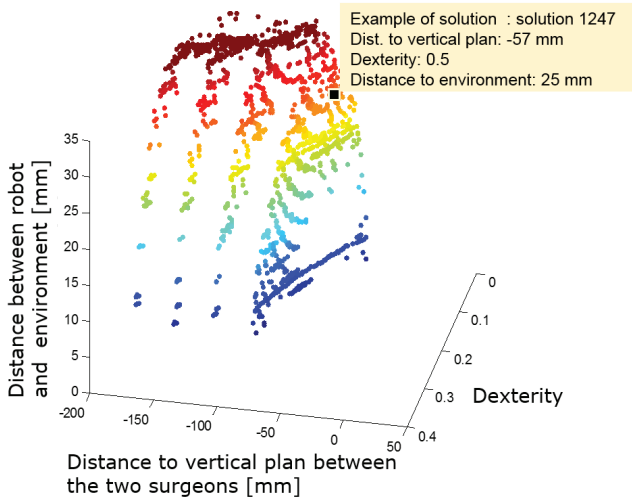

Fig. 6. Point of spherical wrist dimensions optimization Pareto surface.

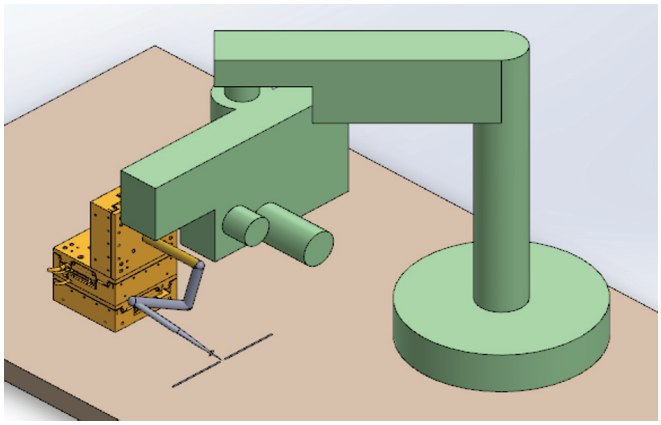

Fig. 7. SolidWorks representation of solution 1247 in its environment.

V. Conclusions and Future Work

Optimization process is still under refinement and the best solution will then be selected to offer a good balance between the three objectives. A prototype will be designed and built subsequently. Our attention will then focus on the control interface in order to make robot use as fast and intuitive as possible. As stated above, this is essential in therapeutic gestures assistance. Indeed interaction modes between surgeons and robot are a decisive factor in the system acceptance by users, as demonstrated by the large diffusion of the Da Vinci surgical system that offers a comfortable and intuitive interface, despite little evidence of its clinical interest. In particular, we'll propose different interaction modes between surgeon and robot and study their impact on system performance from the point of view of ergonomics, usability, executed gestures accuracy, and task duration.

Acknowledgement

Authors would like to thank all members of reconstructive, maxillofacial, and otolaryngology microsurgery teams of Cliniques universitaires Saint-Luc who took part in discussions, observations and experiments. Authors are also grateful to Prof. Pierre Gianello and his team from Experimental Surgery Laboratory (CHEX, UCL), to Prof. Jean-Paul Dehoux, and to all colleagues from the CEREM and ISIR for their help and support in this project.

References

[1] N. Matsumura, N. Hayashi, H. Kamiyama, M. Kubo, T. Shibata, S. Okamoto, Y. Horie, H. Hamada, and S. Endo, "Microvascular anastomosis at 30-50 magnifications (super-microvascular anastomosis) in neurosurgery," *Surgical Neurology International*, vol. 2, no. 1, p. 6, Jan. 2011.

[2] C. Riviere, R. Rader, and P. Khosla, "Charasteristics of hand motion of eye surgeons," *Proc. 19th Annual Conference of the IEEE Engineering in Medicine and Biology Society*, pp. 1690–1693, Oct. 1997.

[3] B. Safwat, E. Su, R. Gassert, C. Teo, and E. Burdet, "The role of posture, magnification, and grip force on microscopic accuracy," *Ann Biomed Eng*, vol. 37, no. 5, pp. 997–1006, Mar. 2009.

[4] C. Lepage, A. Paraskevas, K. Faramarz, and L. Lantieri, "Reconstruction mammaire par lambeau libre diep (deep inferior epigastric perforator)," *EMC (Elsevier Masson SAS, Paris)*, 2006.

[5] R. Katz, G. Rosson, J. Taylor, and N. Singh, "Robotics in microsurgery: use of a surgical robot to perform a free flap in a pig," *Microsurgery*, vol. 25, no. 7, pp. 566–569, Sep. 2005.

[6] P. Liverneaux, S. Berner, M. Bednar, S. Parekattil, G. Ruggiero, and J. Selber, *Telemicrosurgery: robot assisted microsurgery*. Springer, 2013.

[7] M. Mitsuishi, A. Morita, N. Sugita, S. Sora, R. Mochizuki, K. Tanimoto, Y. Baek, H. Takahashi, and K. Harada, "Master-slave robotic platform and its feasibility study for micro-neurosurgery," *Int J Med Robot Comput Assist Surg*, vol. 9, no. 2, pp. 180–189, Jun. 2013.

[8] P. Le Roux, H. Das, S. Esquenazi, and J. Kelly, "Robot-assisted microsurgery: a feasibility study in the rat," *Neurosurgery*, vol. 48, no. 3, pp. 584–589, Jun. 2001.

[9] R. Cau, "Design and realization of a master-slave system for reconstructive microsurgery," Ph.D. dissertation, Eindhoven University of Technology, Feb. 2014.

[10] S. Salcudean, S. Ku, and G. Bell, "Performance measurement in scaled teleoperation for microsurgery," in *CVRMed-MRCAS'97*, Grenoble, Mar. 1997, pp. 789–798.

[11] A. Üneri, M. A. Balicki, J. Handa, P. Gehlbach, R. H. Taylor, and I. Iordachita, "New steady-hand eye robot with micro-force sensing for vitreoretinal surgery," in *Proceedings of the 3rd IEEE RAS & EMBS International Conference on Biomedical Robotics and Biomechatronics (BioRob)*, Tokyo, Japan, Sep. 2010, pp. 814–819.

[12] A. Gijbels, N. Wouters, P. Stalmans, H. Van Brussel, D. Reynaerts, and E. Vander Poorten, "Design and realisation of a novel robotic manipulator for retinal surgery," in *Proceedings of the IEEE/RSJ International Conference on Intelligent Robots and Systems (IROS)*, Tokyo, Japan, Nov. 2013, p. 35983603.

[13] R. MacLachlan, B. Becker, J. Cuevas Tabare?s, G. Podnar, L. Lobes, and C. Riviere, "Micron: An actively stabilized handheld tool for microsurgery," *Robotics, IEEE Transactions on*, vol. 28, no. 1, pp. 195–212, Feb 2012.

[14] M. Miroir, Y. Nguyen, J. Szewczyk, O. Sterkers, and A. Grayeli, "Design, kinematic optimization, and evaluation of a teleoperated system for middle ear microsurgery," *The Scientific World Journal*, Jun. 2012.

Using Vibrations for Haptic Feedback Discrimination in Teleoperation

Adrian Ramos
Advanced Robotics Department
Istituto Italiano di Tecnologia
Via Morego 30, 16163 Genova, Italy
adrian.ramos@iit.it

Domenico Prattichizzo
Department of Information Engineering and Mathematics
Universita degli Studi di Siena
Via Roma 56, 53100 Siena, Italy
prattichizzo@dii.unisi.it

***Abstract*—The European project ACTIVE aims at developing an integrated redundant robotic platform for neurosurgery. During tele-operation, the surgeon perceives on a haptic device the interaction of the tool with the brain tissue by means of a force/torque sensor mounted on the slave. Moreover, active constraints prevent damage to eloquent areas and assist the surgeon by constraining and directing his motions. Having two sources of haptic feedback, and only one haptic device through which it can be displayed makes it difficult to distinguish between the two sources. In this extended abstract, we formalize the problem and propose a solution based on vibratory feedback. The platform that we've set up in order to take our findings from virtual reality to teleoperation is described, as well as the current work we're performing in order to cover not only forbidden region active constraints, but also guidance forces.**

I. Introduction

While performing an operation, surgeons must rely on their senses to understand the environment they are dealing with, and be able to react to unforeseen situations. In traditional surgery, the surgeon is situated very close to the operating scene, and gets the stimuli conveyed directly through the tools he uses (microscope, scalpel, endoscope, etc...).

In robotic surgery, it is frequent to have the surgeon situated further away from the patient, so as to leave enough room for the robot, and to place the surgeon in front of a master station from which he will control the slave robot (for example, [1], [2]). In such case, the surgeon doesn't interact directly with the tissue anymore, but through a computer/robotic interface that transmits the stimuli from the operating scene to the master console. This gives rise to many difficulties (lag time, limited resolution, possible instabilities, etc...) but also allows to augment the senses of the surgeon.

When it comes to touch, the interaction that takes place between the robot and the operating scene can be measured by a force sensor, and then conveyed back to the surgeon through a haptic interface. Augmentation usually consist in adding *active constraints* [3] (also called *virtual fixtures* [4]), that either guide the surgeon in the operation (*guidance fixtures*) or assist him in staying away from potentially dangerous areas (*forbidden region fixtures*). A recent survey can be found in [5].

When using both a sensor on the robot and virtual feedback to assist the surgeon, the main issue is that we have two sources of haptic feedback, but only one haptic device through which we can render forces. In this work, we tackle the problem of rendering these two sources of feedback in a way that is clear and beneficial to the operator at the master console.

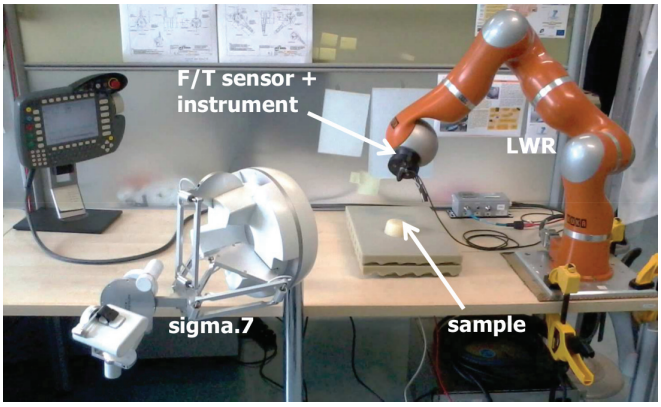

Fig. 1: Teleoperation setup

II. Combining sources of feedback

When two different sources of feedback are used simultaneously, they will have to be rendered in some way at the user's hand. If the feedback sources never return non-null forces simultaneously (for example, if guidance forces are only present when the robot moves in free space), conflict is unlikely to arise, as only one source is rendered at a time. When both sources return non-zero forces, a straightforward approach is to just sum both forces. This is expected to work well if both forces are orthogonal (for example keeping the user on a given plane while manipulation tissue orthogonal to it), since it could be simple to tell the forces apart. It also works if one of the forces is much higher than the other (a very stiff forbidden surface, for example), and is supposed to overcome the other.

If we are interested in keeping the operator aware of the two sources, they should somehow be distinguishable. Just adding them will create a resulting force with a different direction and magnitude. We propose to overlay vibrations on top of one of the sources to make it easily distinguishable from the other. We will see separately how to tackle forbidden region and guidance virtual fixtures.

A. Forbidden regions

When implementing forbidden region active constraints, together with force feedback coming from tissue interaction, there are a couple of design choices to consider. The first is: where should we use vibration, on the tissue feedback, or on the virtual feedback? It's important for the surgeon to distinguish as clearly as possible any unexpected force on the tissue, so we consider it's best to preserve this source of feedback as close to the original as possible. On the other hand, the virtual feedback is already something *synthetic*, so we consider it's the best candidate to modify. On the other hand, we consider a forbidden region as a critical region that must not be penetrated, so it's important to make it very easily distinguishable, and prevent the surgeon from entering it.

In previous work [6], we experimented in virtual environments, where part of the environment was supposed to represent a physical reality, and other virtual surfaces represented forbidden regions. We showed how in certain scenarios, just adding both sources of feedback naively would cause the user to fail to notice certain elements that he touched. In order to overcome this, we first thought about rendering one source of feedback kinesthetically (render continuous forces), while the other source would be rendered by having a vibration convey the magnitude of its force. This indeed made it very clear as to what was virtual and what was supposed to be real, but since we're not able to perceive the direction of vibrations, the direction of the virtual force was lost. Since we used kinesthesia to render the physical objects (tissue in the case of surgery), and vibration for the active constraints, big penetrations into the forbidden regions, would be frequent. This was highly undesirable.

In later work [7], we proposed a better solution to render the virtual constraints. We would *overlay* a vibrating component on top of virtual force. The vibration amplitude would be proportional to the magnitude of the virtual force, with a small positive offset at the moment of contact to make it easily distinguishable. Through an experimental study, we found that users could easily distinguish the two sources of feedback, without increasing the penetration into the forbidden regions, which was our goal.

B. Guidance forces

In the area of guidance forces, the problems we face are of another nature. Forbidden regions should prevent the user from reaching a dangerous area, therefore generating force that resist the surgeon's motion. On the other hand, a guidance force should help the surgeon reach a certain goal. The difference is that in the first case, motion is impeded, while in the second, a motion should be encouraged. The surgeon should be at all times in control of the slave, and having the haptic interface *push* his hand in a certain direction is deemed dangerous.

The use of vibrations to guide the surgeon is an attractive one, since the average energy exchange with the hand is zero. The higher the frequency used, the lower the oscillations it will cause on the hand. However, as we previously saw, vibration will not convey the sense of direction that we want to transmit to the operator. The solution that we propose to solve this problem is that of asymmetric pulses, where the master device displays a short strong force in one direction, followed by a longer lower force in the opposite direction. This creates the illusion of being pushed or pulled in the direction of the strong, short pulse. This concept has been employed on un-grounded portable [8] and wearable [9] devices, where it is clear that there is no net energy transferred to the hand.

We've done preliminary experiments where a clear sensation of pulling or pushing in a direction can be felt. Even if the haptic device is released, its vibrations are hardly perceivable, and it won't slide towards the direction of the pushing. Psychophysical studies with more subjects will be performed to study the usefulness of the illusion in clinically relevant scenarios.

III. The platform

In order to take our experiments from a virtual scenario to an actual teleoperation setup, we've prepared a platform that comprises a Light Weight Robot (LWR) from KUKA as slave, and a Sigma 7 from Force Dimension as the master. A 6DOF force/torque sensor (ATI Nano17) is mounted on the LWR to measure the forces at the tool tip of the slave. The setup is shown in figure 1, and has been designed in the framework of the European project ACTIVE [10].

On the master side, the displacement of the haptic device is read, filtered and down-scaled. The filtering is necessary to remove vibrations introduced by the vibratory feedback techniques mentioned in the previous sections. The positions are used to control the slave, which measures its interaction forces with the environment through the force/torque sensor. The measured forces are filtered to remove mechanical vibrations of the robot at 190Hz and 50Hz (empirically measured, due to cooling fans) and upscaled. Using the pose of the end effector, the forces are rotated to the slave's reference frame, and fed back to the operator.

Time delays are inevitable, and in order to guaranty safety and stability of the system, a passivity observer and controller is implemented, following the theory and algorithms in [11]. The observers measure the amount of energy that enters and escapes the system through both the slave and master side, and limit the output of any of the sides when the system is about to become active. Without a passivity controller, hard contacts are extremely unstable (causing big and violent bounces), while keeping a constant contact force on soft tissue can destabilize the system (the motion and force scaling playing a key factor on the maximum allowable stiffness before we lose stability).

Figure 3 shows how the passivity layer is situated in the system. The difference in contact with a soft tissue (the silicon sample shown in figure 1) with and without the passivity controller is shown in figure 2. It can be seen how the contact is unstable in figure 2a, and that it becomes much more stable in 2b, where the haptic master doesn't bounce anymore.

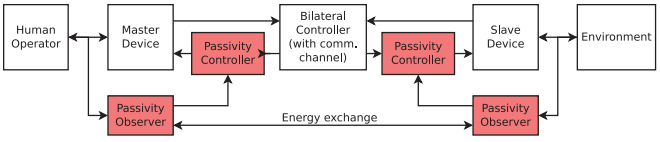

Fig. 3: Passity layer

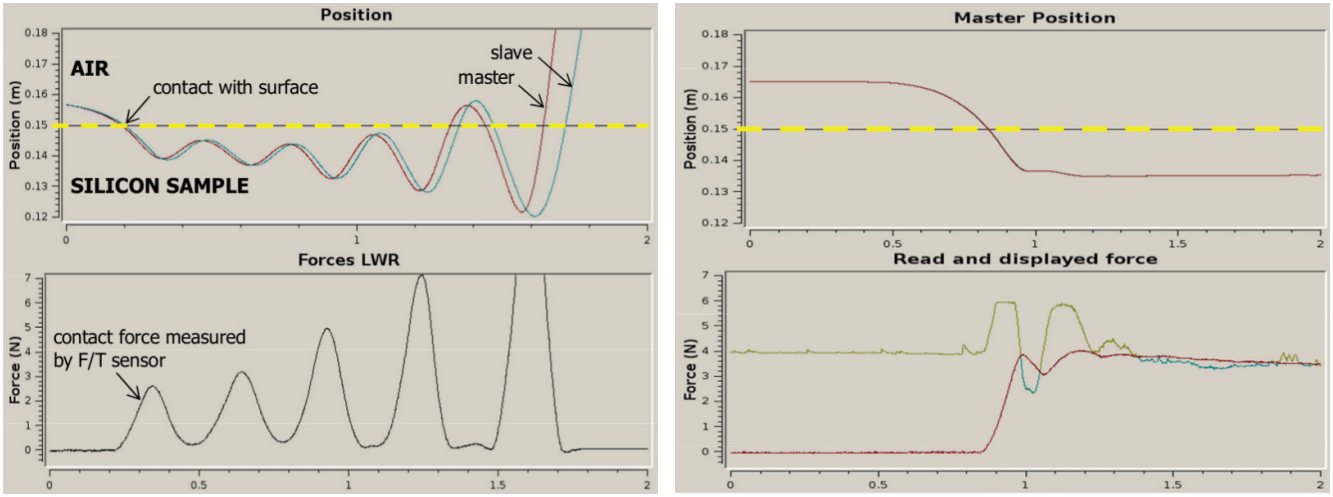

(a) Passivity Off

(b) Passivity On

Fig. 2: (a) recorded force sensor data (black) and position data in vertical direction (perpendicular to contact surface) for master (red line) and slave (green) devices during contact with a silicon sample located at 0.15m (yellow dashed line), without passivity controller and (b) recorded position data of master device (slave is slightly shifted in time but not shown) with force sensor signal (red), the upper bound of the applicable force as calculated by the passivity controller (yellow) and force actually rendered by the haptic device (green when visible, otherwise red).

Having a working and stable platform will allow us to extend our work on vibratory feedback that had been done up to now only in virtual scenarios to the teleoperation domain. Preliminary tests have been performed, in which a simple planar forbidden region is introduced inside the silicon sample shown in figure 1, a couple of centimeters below its surface. The *hidden* virtual feature becomes very easy to distinguish from other unexpected stiff features buried in the tissue, due to the use of vibration.

IV. Conclusion

We have presented for the state of our research concerning the use of vibrations for haptic feedback in robotic assisted surgery. When tool-tissue interaction forces are available via a force sensor, it is important to keep them unmodified to maximize the realism of this feedback at the surgeon's hands. Vibrations are used to modify the virtual forces originating from active constraints. The cases of forbidden region and guidance virtual fixtures are treated differently, since the goal of each is different and requires separate considerations. The teleoperation platform that has been set-up in accordance to our needs in the ACTIVE project was described, together with the considerations we've taken for its stability. This paves the way to new experiments that will be conducted in order to study the usability of our approach in medical scenarios.

Acknowledgment

This work has been supported by the European Commission with the Collaborative Project no. FP7-ICT-2009-6-270460, "ACTIVE: Active Constraints Technologies for Ill-defined or Volatile Environments".

References

[1] A. D. Greer, P. M. Newhook, and G. R. Sutherland, "HumanMachine Interface for Robotic Surgery and Stereotaxy," *IEEE/ASME Transactions on Mechatronics*, vol. 13, no. 3, pp. 355–361, Jun. 2008.

[2] B. Kuebler, U. Seibold, and G. Hirzinger, "Development of actuated and sensor integrated forceps for minimally invasive robotic surger." *The international journal of medical robotics + computer assisted surgery : MRCAS*, vol. 1, no. 3, pp. 96–107, Oct. 2005.

[3] B. Davies, M. Jakopec, S. Harris, F. Rodriguez y Baena, A. Barrett, A. Evangelidis, P. Gomes, J. Henckel, and J. Cobb, "Active-Constraint Robotics for Surgery," *Proceedings of the IEEE*, vol. 94, no. 9, pp. 1696–1704, Sep. 2006.

[4] O. A. Abbott J.J., Marayong P., *Haptic Virtual Fixtures for Robot-Assisted Manipulation*, ser. Springer Tracts in Advanced Robotics, S. Thrun, R. Brooks, and H. Durrant-Whyte, Eds. Berlin, Heidelberg: Springer Berlin Heidelberg, 2007, vol. 28.

[5] S. A. Bowyer, B. L. Davies, and F. Rodriguez y Baena, "Active Constraints/Virtual Fixtures: A Survey," *IEEE Transactions on Robotics*, vol. 30, no. 1, pp. 138–157, Feb. 2014.

[6] A. Ramos, C. Pacchierotti, and D. Prattichizzo, "Vibrotactile stimuli for augmented haptic feedback in robot-assisted surgery," in *2013 World Haptics Conference (WHC)*. IEEE, Apr. 2013, pp. 473–478.

[7] A. Ramos and D. Prattichizzo, "Vibrotactile Stimuli for Distinction of Virtual Constraints and Environment Feedback," *Eurohaptics*, Jun. 2014.

[8] T. Amemiya and T. Maeda, "Directional Force Sensation by Asymmetric Oscillation From a Double-Layer Slider-Crank Mechanism," *Journal of Computing and Information Science in Engineering*, vol. 9, no. 1, p. 011001, 2009.

[9] T. Amemiya and H. Gomi, " Distinct pseudo-attraction force sensation by a thumb-sized vibrator that oscillates asymmetrically," *Eurohaptics*, Jun. 2014.

[10] www.active-fp7.eu/index.php, 2014.

[11] M. Franken, S. Stramigioli, S. Misra, C. Secchi, and A. Macchelli, "Bilateral Telemanipulation With Time Delays: A Two-Layer Approach Combining Passivity and Transparency," *IEEE Transactions on Robotics*, vol. 27, no. 4, pp. 741–756, Aug. 2011.

Session 7

Continuum & Soft Robots (I)

Chair: Dr. Arianna Menciassi, Scuola Superiore Sant'Anna

Thursday, October 16th

8:45 – 10:00

A new bio-inspired, antagonistically actuated and stiffness controllable manipulator

Agostino Stilli, Farahnaz Maghooa, Helge A Wurdemann and Kaspar Althoefer, *Member, IEEE*

I. INTRODUCTION

Robotic manipulators can be divided into different classes, including discrete, serpentine and continuum robots [1]. Most robots in use today have a number of discrete and usually rigid links connected by simple joints. Our work though has been inspired by biology [2], [3] - specifically by the octopus, with its soft tentacles and virtually infinite number of degrees of freedom (DoFs). Biological studies show that the octopus is capable of actuating the different types of muscles in such a way that it can control the stiffness of its arms, enabling the animal to catch fish, move stones or even walk across the seabed. Taking inspiration from the antagonistic behaviour of octopus arms, our robot manipulator makes use of two fundamental actuation means, pneumatic actuation and tendon-based actuation, able to oppose each other and thus capable of varying the arms' stiffness over a wide range. Our robot arm can be said to employ two main actuation mechanisms in a hybrid fashion - intrinsic (pneumatics in our case) and extrinsic (tendon actuation in our case) [1], [4].

As it is the case for other robots developed recently, we use extrinsic actuation based on tendons to achieve bending away from the longitudinal axis of the robot arm. Tendons that are attached at the tip and intermediate points of the arm are pulled by externally situated motors controling the length of each tendon see e.g. Intuitive. The overall DoF depends on the number of integrated tendons and fix points along the manipulator [5]. Other manipulators whose links are moved by tendons are [6]–[10]. Most tendon-driven robot manipulators cannot lengthen or shorten their structure longitudinally [11], [12].

While most current robot arms make use of only one type of actuator such as tendons or motors integrated with the robot joints, our robot arm employs two actuation mechanisms. The tendon based mechanism is combined with pneumatic actuators to allow for antagonistic control. The pneumatic actuation which can be considered intrinsic actuation provides our arm mainly with extension capability. Other robot arms that are entirely based on pneumatic actuation have been developed in the past. One example of an intrinsic pneumatic actuation principle employed in a robot arm is the Octarm manipulator equipped with a set of McKibben actuators connected in series and in parallel [13]. Another example is the universal joint based robot for minimally invasive surgery (MIS) [14]; each finger-like segment is driven by 7 micro-motors leading to a miniaturized manipulator arm with an outer diameter of 12 mm. Another robot arm that is actuated pneumatically is the soft robot arm developed as part of the EU-funded project STIFF-FLOP. STIFF-FLOP focuses on exploring the mechanisms of the octopus and attempts to extract relevant biological features to develop medical robotics systems for MIS [15] with integrated sensors [16]–[18]. The STIFF-FLOP robot arm is made up of silicon segments with each segment being equipped with a set of parallel compressible chambers; the current prototype consists of two segments arranged in series [19].

Stiffness variation can be realised with an additional chamber within the silicone body filled with granular that can be jammed by applying a vacuum [20]. Hence, the control of the stiffness of the robot?s body is achieved by extending the overall robot system through the introduction of an additional type of actuator.

The concept of polymeric artificial muscles proposed in [21] to actuate a robot manipulator was furthered in [22] by integrating granule-filled chambers which when exposed to

(a) (b)

Fig. 1. Prototype of the new bio-inspired, antagonistically actuated and stiffness controllable manipulator in the (a) stiff and elongated and (b) entirely shrunk state.

*The work described in this paper is partially funded by the Seventh Framework Programme of the European Commission under grant agreement 287728 in the framework of EU project STIFF-FLOP.

Agostino Stilli, Farahnaz Maghooa, Helge A Wurdemann and Kaspar Althoefer are with King's College London, Department of Informatics, Centre for Robotics Research, Strand, London, WC2R 2LS, United Kingdom k.althoefer@kcl.ac.uk

Farahnaz Maghooa is with Polytech UPMC, Paris, France and the University of Pierre and Marie Curie (UPMC) farah.maghooa@laposte.net

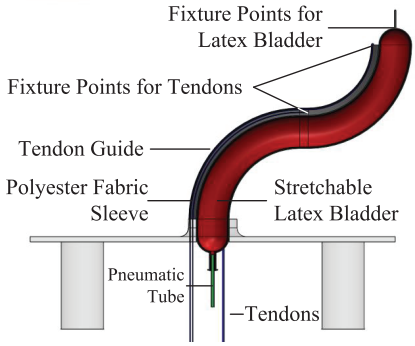

Fig. 2. Section view of the manipulator's structure.

varying degrees of vacuum could actuate, soften and stiffen the manipulator's joints.

Appropriately fusing two different actuation mechanism often allows enhanced manipulation capabilities above single-type actuation approaches [4] - enhanced control of the manipulator's configuration, stiffness and compliance can be observed. Such a hybrid robot concept is the one described in [23]; the authors created a system where pneumatic actuators are combined with an electro-mechanical actuation mechanism. Also, the work by Immegal [24] aims at bringing together extrinsically and intrinsically actuation principles. The idea of fusing pneumatic and tendon-driven actuation was also explored in [25] - in their work, each robot segment is made up of a pressurizable inner hose inside a surrounding hose and a set of cables attached to aluminum plates at the top and base of each of the many segments.

Here, we propose to fuse pneumatic and tendon-driven actuation mechanisms in an entirely soft outer sleeve realising a hybrid actuation mechanism, to realize a new type of robotic manipulator that can collapse entirely, extend along its main axis, bend along the main axis and vary its stiffness. The proposed robot arm is inherently flexible manufactured from segments that consist of an internal stretchable, air-tight balloon and an outer, non-stretchable sleeve preventing extension beyond a maximum volume. Tendons connected to the distal ends of the robot segments run along the outer sleeve allowing each segment to bend in one direction when pulled. The developed robot arm is depicted in Figure 1. The results from our study show the capabilities of such a robot and the main advantages of the proposed technique when compared to traditional, single-actuation type robot manipulators.

II. DESIGN OF THE HYBRID ACTUATION MECHANISM

A. Structure and Assembly of the Manipulator

A section view of the robot arm is depicted in Figure 2. There are three main parts that make up the overall robot structure: an inner stretchable air chamber, an outer, non-stretchable (but compactable) fabric sleeve and triplets of nylon tendons per each of the two segments. The outer sleeve is 20 cm in length and has a diameter of 23 mm, when fully inflated. Since the outer fabric cannot stretch, the outer sleeve keeps the inner balloon from extending indefinitely and restricts it in radial direction to a maximum diameter of 23 mm. During transition from complete deflation to maximum inflation, the manipulator is capable only of extending along its main axis (translational extension). The manipulator stiffness is varied by changing the tendon length - hence, pulling the tendons in at a certain air volume, the outer sleeve will shorten, whilst increasing its stiffness, and vice versa.

In our robot, the extrinsic actuators, i.e. the tendons are guided through specific fabric channels on the outside of the manipulator sleeve, 120° apart along the circumference of the robot's cylindrical body. In our two-segment experimental system, a triplet of tendons are attached to the distal end of the manipulator and another tendon triplet connected the mid-section of the robot - hence, the two segments of our manipulator can be actuated individually, Figures 2 and 3.

B. Active Motion Control Setup

Figure 3 shows the setup of the entire robotic system. A pressure regulator (SMC ITV0010-3BS-Q) is used to control the air pressure in inner balloon from 0.001 MPa to 0.1 MPa, allowing the controlled inflation and deflation of the balloon. An air compressor (BAMBI MD Range Model 150/500) is employed to provide the required pressure.
The tendons are operated via a pulley system of a 6.4 mm radius driven by DC motors (Maxon RE-max 24) via a gear (Maxon Planetary Gearhead GP 22 C), allowing us to apply a torque of up to 2 Nm and a force of up to 312.5 N at the outer edge of the used pulleys.

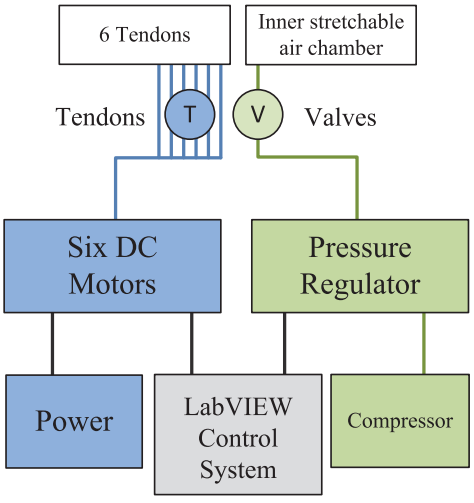

Fig. 3. Active motion control architecture involving tendon and pneumatic actuation.

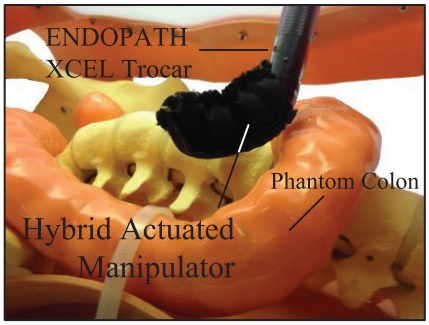

Fig. 4. The manipulator is squeezed through an ENDOPATH XCEL Trocar (18 mm diameter) and actuated.

A DAQ card (NI USB-6211) and LabVIEW software are used to control the motors and pressure regulators taking input from a joystick (Logic 3 JS282 PC Joystick) for remote control of the overall system. In addition, a button is used to regulate the pressure inside the robot's air chamber. In the conducted experiments, we used the joystick to control the tendons and thus steer the manipulator whilst keeping the pressure in the balloon constant. Thus, most of our experiments allowed controlling the robot's motion whilst keeping the pressure and, hence, stiffness, constant - see [26].

III. DISCUSSION AND CONCLUSIONS

We present here a new hybrid and antagonistic actuation system for a robotic manipulator fusing pneumatic with tendon-driven actuation. Being inspired by the biological role model, the octopus, our antagonistic actuation system aims at modeling the octopus' way of using its longitudinal and transversal muscles in its arms: activating both types of muscles, the octopus can achieve a stiffening of its arms.

Our concept goes beyond state-of-the-art in the field of soft robotics: our robot is mainly made of thin sleeve-like components filled with air to achieve a fully-extended state, and thus can be shrunk to a considerably small size when entirely deflated. This capability to move between these two extreme states make the robot a particularly useful candidate for applications such as MIS or search and rescue. Our experimental study shows that the our manipulators, indeed, is capable to bend, to morph from entirely inflated to completely shrunk as well as to squeeze through narrow openings.

REFERENCES

[1] G. Robinson and J. Davies, "Continuum robots - a state of the art," in *IEEE International Conference on Robotics and Automation*, 1999.

[2] Y. Gutfreund, T. Flash, G. Fiorito, and B. Hochner, "Patterns of arm muscle activation involved in octopus reaching movements," *The Journal of Neuroscience*, vol. 18, no. 15, p. 5976598, 1998.

[3] C. Laschi, B. Mazzolai, V. Mattoli, M. Cianchetti, and P. Dario, "Design of a biomimetic robotic octopus arm," *Bioinspiration and Biomimetics*, vol. 4, pp. 1–8, 2009.

[4] I. D. Walker, "Robot strings: Long, thin continuum robots," in *IEEE Aerospace Conference*, 2013.

[5] I. Gravagne, C. Rahn, and I. D. Walker, "Large deflection dynamics and control for planar continuum robots," *IEEE/ASME Transactions on Mechatronics*, vol. 8, no. 2, pp. 299–307, 2003.

[6] D. Camarillo, C. Milne, C. Carlson, M. Zinn, and J. Salisbury, "Mechanics modeling of tendon-driven continuum manipulators," *IEEE Transactions on Robotics*, vol. 24, no. 6, pp. 1262–1273, 2008.

[7] H. Watanabe, K. Kanou, Y. Kobayashi, and M. Fujie, "Development of a "steerable drill" for acl reconstruction to create the arbitrary trajectory of a bone tunnel," in *IEEE/RSJ International Conference on Intelligent Robots and Systems*, pp. 955–960, 2011.

[8] M. Moses, M. Kutzer, H. Ma, and M. Armand, "A continuum manipulator made of interlocking fibers," in *IEEE International Conference on Robotics and Automation*, 2013.

[9] L. Kratchman, M. Rahman, J. Saunders, P. Swaney, and R. W. III, "Toward robotic needle steering in lung biopsy: a tendon-actuated approach," in *Medical Imaging: Visualization, Image-Guided Procedures, and Modeling*, 2011.

[10] S. Sanan, J. Moidel, and C. Atkeson, "A continuum approach to safe robots for physical human interaction," in *International Symposium on Quality of Life Technology*, 2011.

[11] R. Cieslak and A. Morecki, "Elephant trunk type elastic manipulator - a tool for bulk and liquid type materials transportation," *Robotica*, vol. 17, pp. 11–16, 1999.

[12] A. Deshpande, J. Ko, D. Fox, and Y. Matsuoka, "Control strategies for the index finger of a tendon-driven hand," *The International Journal of Robotics Research*, vol. 32, no. 1, pp. 115–128, 2013.

[13] S. Neppalli, B. Jones, W. McMahan, V. Chitrakaran, I. Walker, M. Pritts, M. Csencsits, C. Rahn, and M. Grissom, "Octarm - a soft robotic manipulator," in *IEEE/RSJ International Conference on Intelligent Robots and Systems*, 2007.

[14] J. Shang, D. Noonan, C. Payne, J. Clark, M. Sodergren, A. Darzi, and G.-Z. Yang, "An articulated universal joint based flexible access robot for minimally invasive surgery," in *International Conference on Robotics and Automation*, pp. 1147–1152, 2011.

[15] A. Jiang, E. Secco, H. Wurdemann, T. Nanayakkara, P. Dasgupta, and K. Athoefer, "Stiffness-controllable octopus-like robot arm for minimally invasive surgery," in *3rd Joint Workshop on New Technologies for Computer/Robot Assisted Surgery*, 2013.

[16] Y. Noh, S. Sareh, J. Back, H. Wurdemann, T. Ranzani, E. Secco, A. Faragasso, H. Liu, and K. Althoefer, "A three-axial body force sensor for flexible manipulators," in *IEEE International Conference on Robotics and Automation*, 2014.

[17] S. Sareh, A. Jiang, A. Faragasso, Y. Noh, T. Nanayakkara, P. Dasgupta, L. Seneviratne, H. Wurdemann, and K. Althoefer, "Bio-inspired tactile sensor sleeve for surgical soft manipulators," in *IEEE International Conference on Robotics and Automation*, 2014.

[18] Y. Noh, E. Secco, S. Sareh, A. F. H.A. Wurdemann, J. Back, H. Liu, E. Sklar, and K. Althoefer, "A continuum body force sensor designed for flexible surgical robotic devices," in *IEEE Engineering in Medicine and Biology Society*, 2014.

[19] M. Cianchetti, T. Ranzani, G. Gerboni, I. de Falco, C. Laschi, and A. Menciassi, "Stiff-flop surgical manipulator: Mechanical design and experimental charaterization of the single module," in *IEEE/RSJ International Conference on Intelligent Robots and Systems*, 2013.

[20] A. Jiang, T. Aste, P. Dasgupta, K. Althoefer, and T. Nanayakkara, "Granular jamming with hydraulc control," in *ASME International Design Engineering Technical Conferences & Computers and Information in Engineering Conference*, 2013.

[21] D. Caldwell, G. Medrano-Cerda, and M. Goodwin, "Control of pneumatic muscle actuators," *IEEE Control Systems*, vol. 15, 1995.

[22] A. Jiang, G. Xynogalas, P. Dasgupta, K. Althoefer, and T. Nanayakkara, "Design of a variable stiffness flexible manipulator with composite granular jamming and membrane coupling," in *IEEE/RSJ International Conference on Intelligent Robots and Systems*, 2012.

[23] D. Shin, I. Sardellitti, and O. Khatib, "A hybrid actuation approach for human-friendly robot design," in *IEEE International Conference on Robotics and Automation*, pp. 1747–1752, 2008.

[24] G. Immega and K. Antonelli, "The KSI tentacle manipulator," in *IEEE International Conference on Robotics and Automation*, 1995.

[25] B. Jones, W. McMahan, and I. Walker, "Design and analysis of a novel pneumatic manipulator," in *IFAC Symposium "Advances in Automotive Control"*, 2004.

[26] A. Stilli, H. Wurdemann, and K. Althoefer, "Shrinkable, stiffness-controllable soft manipulator based on a bio-inspired antagonistic actuation principle," in *IEEE/RSJ International Conference on Intelligent Robots and Systems (IROS)*, 2014.

Biphasic Media Variable Impedance Actuation Application in Human Robotics Interaction

Bo Han, Matteo Zoppi, *Member, IEEE,* and Rezia Molfino, *Member, IEEE,*

Abstract—A major application today is in robotic systems expected to interact safely and friendly with humans and the environment. This paper presents a concept of soft serial links actuator- variable impedance actuator using a combination of fluid and gas to realize the adaptation of the position and stiffness. Because of the high power density, simple structure and low cost, the variable impedance actuator using biphasic media can be realized with the architecture of a common hydraulic piston in micro and meso-scale and application spanning from minimum invasive robotics surgery to robotics locomotion legs, arms and dexterous hands. The schematic of serial links actuator of biphasic media is presented and model design application in fields such as robot assisted surgery, daily life service robot, industrial robot involved with human and environment interaction are analyzed respectively. The dynamic model and control strategy are built and application cases listed with the innovation concept.

Keywords—Variable Impedance Actuator, Human Robotics Interaction.

1 Introduction

In the growing fields of rehabilitation robotics, prosthetics, wearable robotics, and walking robotics, variable impedance actuators (VIAs) are being designed and implemented because of their ability to minimize large forces due to shocks, to safely interact with the user, and their ability to store and release energy in passive elastic elements. This thesis describes the state of the art in the design of actuators with adaptable passive compliance.

The working principles of the different existing designs are explained and compared. According to mechanism design and function, the VSA are divided into four groups: equilibrium-controlled stiffness, antagonistic-controlled stiffness, structure-controlled stiffness (SCS), and mechanically controlled stiffness. In classical robotic applications, actuators are preferred to be as stiff as possible to make precise position movements or trajectory tracking control easier (faster systems with high bandwidth). The biological counterpart is the muscle that has superior functional performance and a neuro-mechanical control system that is much more advanced at adapting and tuning its parameters. The superior power-to-weight ratio, force-to-weight ratio, compliance, and control of muscle, when compared with traditional robotic actuators, are the main barriers for the development of machines that can match the motion safety, and energy efficiency of human or other animals.

One of the key differences of these systems is the compliance or spring-like behavior found in biological systems [1]. In this paragraph, we present different types of variable stiffness actuators according to their function and structure. Most actuators with controllable stiffness consist of two classical stiff actuators that can be easily dimensioned for the required force or torque. Applications requiring adaptable compliance can be divided into two groups: those for robot-human interaction and those to adjust natural dynamics. The distinction between these groups depends on the primary use of the compliance within the application.

1.1 Variable impedance in Human Robotics interaction

Industrial robots are heavy machines actuated by stiff systems, and they do not give or comply in a collision, thereby inducing severe damage. Therefore, for safety reasons, these devices are placed in a human-free environment. However, for some applications, it is useful to have robots and

- *R. Molfino is with the Department of Mechanical and Automation Engineering, University of Genova, Genova, Italy, 16145. E-mail: see http://www.pmar.robotics.unige.it/people*
- *B. Han and M. Zoppi are with University of Genova.*

Manuscript received May 19, 2014; revised Jul 11, 2014.

humans fulfilling tasks together [3]. This requires safer robots, which can be achieved by designing compliant joints. However, with a compliant joint, it is harder to place the tool center point in an exact position or to track a specific trajectory accurately. In this case, an actuator with adaptable compliance can act stiff during precise positioning at low speeds (grasping and placing an object) and compliant when positioning is not as important when moving at higher speeds (moving from one position to another) [4]. Most robotic toys are actuated by stiff electrical drives. This inflexible movement results in the typical artificial way of moving and interacting. Especially for cuddly toys such as Huggable [5] or Anty [6], a compliant, natural movement is preferred.

Therefore, robots that can assist in the rehabilitation process are being proposed, e.g., Lokomat [7] and Auto ambulator, which impose gait like motion patterns to the legs of a patient. Paraplegic patients and stroke survivors often suffer from severe spasms. When using stiff actuators, undesired motions, such as those caused by spasms, can cause large actuator forces that could potentially harm the leg. Adding compliance to the actuation system can naturally absorb large position errors, thus preventing damage to the system and insuring safety of the wearer. Additionally, in the beginning of the rehabilitation process, a relatively low stiffness might be preferred for safety, and stiffness could be gradually raised when the patient has regained a certain level of control over their legs. The Automated Locomotion Training using an Actuated Compliant Robotic Orthosis project (ALTACRO) [8] intends to build a gait rehabilitation robot with adaptable compliance. This field is growing rapidly with many compliant systems: Bowden cables [9] gravity balanced systems [10] ankle devices that use series elastic actuators (SEAs) [11] and robotic tendons [12].

1.2 Robotics safety factors involving environment around

Robot safety involves several different considerations and depends on many factors, ranging from software dependability, to possible mechanical failures, to human errors in interfacing with the machine, etc. A thorough hazard analysis and risk evaluation should be performed according to methodical procedures specifically for different domains of application: these methods are receiving growing attention from both the scientific community and international standardization bodies. General hazard management considerations are very broad, of course, and fall beyond the scope of this thesis. A robot arm that has to interact with humans needs a very important safety design considerations. Under no circumstances should the robot arm cause harm to people in its surroundings, directly or indirectly, in regular operation or in failures. A type of risk is the situation in which, in an unspecified instant, during the execution of a preplanned robot arm movement, a collision between a link of the arm and a human occurs. The quantitative analysis of the trade-off between such risk and the performance obtainable is one of the objectives of robot safety. Such analysis has a strong impact on how robot mechanisms and controllers should be designed for human interactive applications, giving rise to a paradigm shift in robot design [13], which will be examine in detail.

1.3 Human-robotics safety evaluation criterion

As already stated, we will only focus on a particular aspect of safety of robot manipulators, which is against unexpected collisions by the manipulator with a human operator. In the worst case, impacts could happen anywhere on the manipulator structure and on the body of the operator, and at any time during the execution of a planned trajectory. The severity of injuries caused by collisions is a well studied subject in biomechanics, with particular regard to such domains as car accidents or sports, though only very recently these studies have been applied to robotics [14]. Researchers have developed several standard indices of injury severity, including the Gadd Severity Index (GSI), the Head Injury Criterion (HIC) [15], the ”3 ms” criterion, the Viscous Injury Response (VC), or the Thoracic Trauma Index (TTI). Most of these are related to a basic tolerance limit curve developed at Wayne State University (the WSUTL) on the basis of data experimentally acquired from animal and cadaver head collision tests. The WSUTL is a curve plotting head accelerations versus impact duration, indicating that very intense head acceleration is tolerable if it is very brief but that much less is tolerable if the pulse duration exceeds 10 or 15 ms (as the time exposure

to cranial pressure pulses increases, the tolerable intensity decreases).Gadd plotted the WSUTL curve in log-log coordinates, obtaining a straight line of slope -2.5, and proposed accordingly a severity index as:

$$GSI = \int_0^t \alpha^{2.5} d\tau \tag{1}$$

where α is the head acceleration in g, and the integral is extended to the whole duration of collision. A GSI value of 1,000 is generally considered to be the threshold level or tolerance limit for serious head injury. Versace [15] proposed a mathematical refinement of the GSI known as the Head Injury Criterion (HIC), which is defined as:

$$HIC = T[\frac{1}{T}\int_0^t \alpha(\tau) d\tau]^{2.5} \tag{2}$$

where T is conventionally the final time of impact. As the choice of this time is often difficult, it is recommended to consider the worst-case HIC at varying T, which corresponds to taking T equal to the time at which the head reaches its maximum velocity v(T) (typically, T$\leq$15 ms). An HIC value of 1,000 or greater is typically associated with extremely severe head injury; a value of 100 can be considered suitable to normal operation of a machine physically interacting with humans. A generalization of the HIC to collisions with other parts of the body can be considered whereby the 2.5 coefficient is replaced by other empirically determined values α(see, for example, [17]) and, assuming the operator is standing still before the impact, one can write:

$$HIC' = T^{1-\alpha} v(T)^{\alpha} \tag{3}$$

In general, evaluation of the above severity indices is numeric, based on either experimental or simulated data. However, it is instructive to compute the most widely used index, the HIC, for the basic case of a single rigid joint moving at uniform velocity v before impact.

2 SCHEMATIC AND MODELING

Consider the VIA in Fig. 1 in a known initial state. The VIA moves to another state: call q^A and q^B the volumes of liquid moving in/out the chambers A and B, respectively (positive if inlet and negative if outlet); p^A and p^B are the final pressures in the

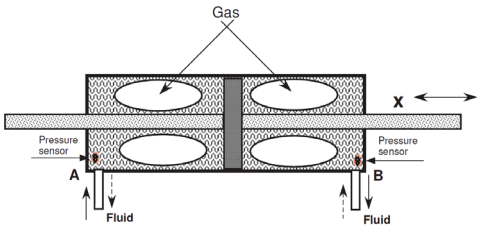

Fig. 1: **The schematic of variable impedance actuator using biphasic media**

chambers. Suppose the movement of the piston is in the direction of the chamber B, no external force is applied to the piston and the type and mass of the gas fraction in both chambers is the same. Four cases apply, depending on the relation between q^A and q^B: (1) if $q^A = -q^B$, the piston moves of an amount proportional to q^A and the initial and final stiffness are identical (because the volumes of the gas fractions at the two sides of the piston remain constant); (2) if $q^A > -q^B$, the actuator increases its stiffness and the piston moves of an amount smaller than in the case (1) (the pressures in both chambers increase and the gas fractions in both chambers reduce their volumes); (3) if $q^A < -q^B$, the stiffness decreases and the piston moves of an amount larger than in the case (1) (the pressures in both chambers decrease and the gas fractions in both chambers expand); (4) if $q^A = q^B$, the stiffness in the final state is higher than in the initial state and there is no displacement of the piston. If the cylinder moves toward side A, vice versa. In case of external force applied to the piston, the four cases above apply but there with a difference of pressure between the two chambers proportional to the ratio between the external force and the surface of the piston. For more details, refer to [2].

2.1 Mathematic model of the serial links actuator using biphasic media

The schematic in Fig. 2 represents the functioning principle used in the actuator to achieve the variation of stiffness. The gas behaves like a nonlinear spring. Two hydraulic servo pumps are used to move liquid inside-outside the chambers and so drive the mobile part of the actuator, represented by the black longer vertical stick in the middle. Two pressure sensors are mounted on the chambers to measure the instantaneous pressures of the fluid inside.

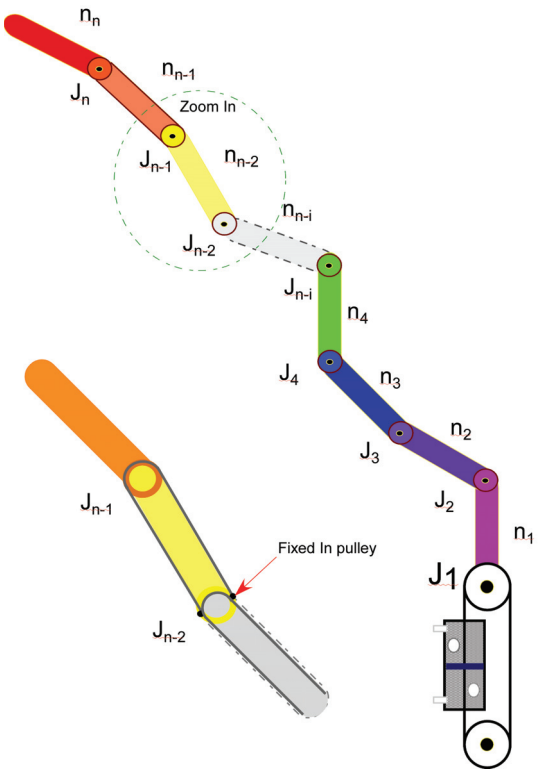

Fig. 2: Schematic of the serial links actuator using biphasic media

The serial links actuator is modeled referring to the schematic in Figure 2. The following differential equations hold, linking the output motion θ_i(described in this case by the displacement $x = r_1\theta_1$ of the piston, r_i is the radius of pulley) to the joint J_i, p^A and p^B, and gas volumes, V^A and V^B, and torque T_i in the pulley where T_1 is the active torque and T_2 is the load torque from joint J_2:

$$I_1\ddot{\theta}_1 + \mu_1\dot{\theta}_1 = T_1 - T_2 \tag{4}$$

$$r_1\theta_1 = x \tag{5}$$

$$m\ddot{x} + \mu_0\dot{x} = (p^A - p^B)S - \frac{1}{r_1}T_1 \tag{6}$$

Let m the mass of the piston; I the moment of inertia(meaning by piston the output link of the actuator); S the net area of the piston (on which fluid pressures acts), being identical for both chambers; θ_i the angle displacement of the joint J_i link and $\dot{\theta}_i$ and $\ddot{\theta}_i$ the first and second derivative of θ_i in the time; x the displacement of the piston and $\dot{x}$ and $\ddot{x}$ the first and second derivative of x in the time; μ_i a damping coefficient related to the friction of the J_i pulley ; μ_0 a damping coefficient related to the viscosity and dissipative properties of the fluid; $C^A{=}p^AV^A$ and $C^B{=}p^BV^B$ are the ideal gas constant in the chambers A and B respectively.

Considering the joint J_2 and there is no relative slip between cable and pulley, we get the dynamic equation as below:

$$I_2\ddot{\theta}_2 + \mu_2\dot{\theta}_2 = T_2 - T_3 \tag{7}$$

$$r_2\theta_2 = r_1\theta_1 \tag{8}$$

Where the T_2 is the active torque and T_3 is the load torque from joint J_3. Refer to the zoom in part of Figure 2, the driving cables are coupled each other. This means that the cables transfer torque in joint J_{n-1} through pulley but fixed in the pulley of joint J_{n-2}. We realize the VIA function through the serial links actuator.

Considering the joint J_i and the J_n, we get the dynamic equation as below:

$$I_i\ddot{\theta}_i + \mu_i\dot{\theta}_i = T_i - T_{i+1} \tag{9}$$

$$r_i\theta_i = r_{i-1}\theta_{i-1} \tag{10}$$

$$I_{i+1}\ddot{\theta}_{i+1} + \mu_{i+1}\dot{\theta}_{i+1} = T_{i+1} - T_{i+2} \tag{11}$$

$$r_{i+1}\theta_{i+1} = r_i\theta_i \ \ldots\ldots \tag{12}$$

$$I_n\ddot{\theta}_n + \mu_n\dot{\theta}_n = T_n \tag{13}$$

$$r_n\theta_n = r_{n-1}\theta_{n-1} \tag{14}$$

Where the T_i is the active torque and T_{i+1} is the load torque from joint J_{i+1}. Combine the Eq.s 4, 7, 9, 11, ... 13, we get the equation as below:

$$r_n\ddot{\theta}_n\sum I_i r_i^{-1} + r_n\dot{\theta}_n\sum \mu_i r_i^{-1} = T_1 \tag{15}$$

Using dynamic equilibrium and combining with the expressions in Eq.s 4, 5, 6 and combine 15, (Original derivation to the equation of state of a hypothetical ideal gas reference [3]) we obtain:

$$\begin{aligned}&(\sum I_i r_i^{-1} + mr_1)r_n\ddot{\theta}_n + (\sum \mu_i r_i^{-1} + \mu_0 r_1)r_n\dot{\theta}_n \\ &= \frac{C^A S r_1}{V^A(0) - q^A + Sr_n\theta_n} - \frac{C^B S r_1}{V^B(0) - q^B - Sr_n\theta_n}\end{aligned} \tag{16}$$

where q^A, q^B, and θ, are functions(Simplified model without consideration of centrifugal force, Coriolis force, gravity and Coulomb friction because of the low velocity application.) of the time. The structure of this nonlinear differential equation is $U(t, q^A, q^B, \theta, \dot{\theta}, \ddot{\theta}) = 0$.

When the actuator is in equilibrium under an external torque, the difference between the pressures in the two chambers is related to the value of the external torque by the geometry and the design of the actuator. In the design shown in Figure 2, the external torque is proportional to the difference of pressure through the surface area of the piston and radius : $T = (p^A - p^B)Sr_1$. In statics, for any given external torque, the values of the pressures in the two chambers may be any provided that their difference is the one required to balance the external torque.

The instantaneous stiffness $K(\theta)$ of the actuator (of the link) is the derivative of the external torque applied to it with respect to the angle displacement. In our case the stiffness is a function of the volumes of liquid moved q^A and q^B; Considering ideal the gas, its expression is $K(\theta_n)$:

$$
\begin{aligned}
&= \frac{\partial T}{\partial \theta} \\
&= -\left(\frac{C^A (Sr_1)^2}{(V^A(0) - q^A + Sr_n\theta_n)^2} + \frac{C^B (Sr_1)^2}{(V^B(0) - q^B - Sr_n\theta_n)^2} \right) \\
&= -\left(\frac{(p^A Sr_1)^2}{C^A} + \frac{(p^B Sr_1)^2}{C^B} \right)
\end{aligned} \tag{17}
$$

According to Eq. (17), it is possible and easy to adapt the stiffness to a desired value or to specific actuation requirements using q^A and q^B as control variables because we can get the pressure value in the chambers of cylinder using transducer.

2.2 Impedance control

As illustrated in the schematic of Fig. 1 and mathematic model Eq. (16)∼ (17), the stiffness and displacement of the piston can be controlled through the flows of liquid in the chambers.

Physically, this corresponds to piston displacements and volumes q^A and q^B such that the volume of the gas fraction in the left or right chamber reduces to zero (assuming that the liquid is incompressible). Following the ideal gas model used, with gas volume tending to zero the gas pressure and stiffness tend to infinity. For any assigned q^A and q^B, the configurations with gas volume equal to zero are on the boundary of the range of motion of the piston.

In the special case of same type and mass of gas in the two chambers, $c^A = c^B = c$ and $V^A(0) = V^B(0) = V(0)$; Eq. (17) simplifies to:

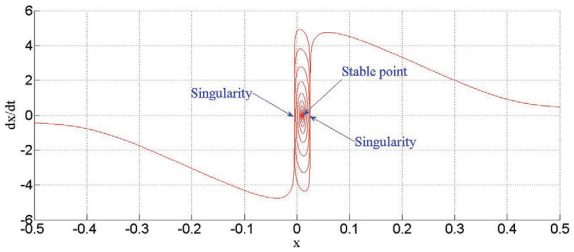

Fig. 3: Working range of the actuator and detail of the singularity and stable point

$$
m\ddot{x} + \mu\dot{x} = c\frac{q^A - q^B - 2Sx}{(V(0) - q^A + Sx)(V(0) - q^B - Sx)}S \tag{18}
$$

The singular point is now at $\dot{x} = 0$ and $x = (q^A - q^B)/2S$.

At this preliminary stage of the investigation of the actuator, we have applied a simple PID controller with controlled variables q^A and q^B with the aim to investigate through examples the controllability of the VIA concept proposed. The measured quantities are the position of the piston and the pressures in the two chambers. The pressures are used to calculate the current stiffness of the actuator using Eq.s (17). Since the position of the link piston depends on $q^A - q^B$ and the stiffness on $q^A + q^B$, two PID controllers are used relating the control flows $\dot{q}^A$ and $\dot{q}^B$ to the position error e^θ and stiffness error e^K as follows:

$$
\begin{aligned}
\dot{q}^A + \dot{q}^B &= K_{p\theta}e^\theta + K_{d\theta}e^\theta + K_{i\theta}e^\theta \\
\dot{q}^A - \dot{q}^B &= K_{pK}e^K + K_{dK}e^K + K_{iK}e^K
\end{aligned} \tag{19}
$$

From Eq.s (19), $\dot{q}^A$ and $\dot{q}^B$ are easily expressed as functions of e^θ, e^K and the proportional, derivative and integral gains.

The schematic of the control is shown in Fig. 4. The response of the actuator is simulated using all sets of equations presented above, grouped in a block having $\dot{q}^A$ and $\dot{q}^B$ as input and, as output, the link position θ and the pressures p^A and p^B. A separate block calculates K from p^A and p^B. θ and K are subtracted to the task-desired values at each control loop, generating the errors e^θ and e^K used in the two PIDs for the generation of $\dot{q}^A$ and $\dot{q}^B$.

The adaptive fuzzy control consists of two parts, one is the conventional PID controller and the other is fuzzy controller, two input and three output fuzzy

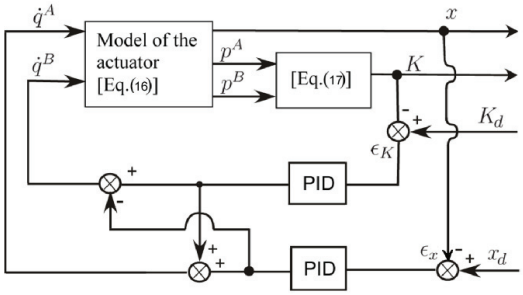

Fig. 4: Schematic of the duel PID control loop

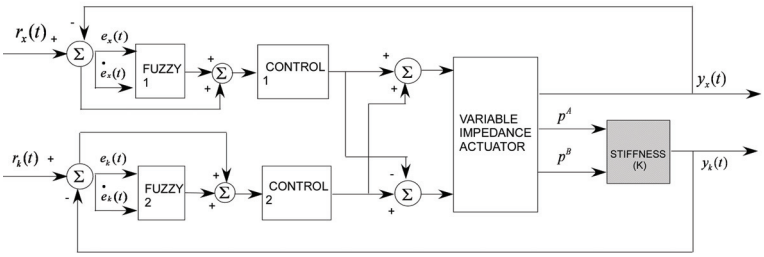

Fig. 5: Schematic of the adaptive fuzzy control loop

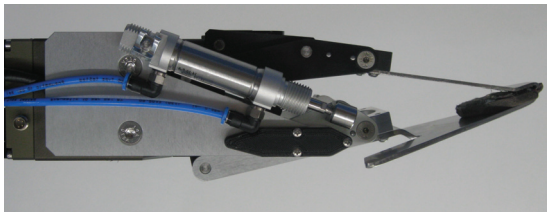

Fig. 6: **The application of VIAs in garment gripper**

adaptive PID controller is designed in this chapter. The inputs are the error and the error rate. The outputs are the Kp, Ki and Kd values.The objective is to find the fuzzy relations among Kp, Ki , Kd, error, and error rate. With continual testing, the three output parameters are adjusted online so as to meet different requirements and achieve good stability. Variable PID controller adds the output value of the fuzzy controller and default PID values.

As we have discussed in paragraph above, the adaptive fuzzy control can adjust the parameters of PID online, especially, there are huge overshot when the encountering unexpected load torque big enough. Although many researchers in VIAs field proposed good methods to control the actuator, there are still some flaws in suspending. Hereby, we have applied a adaptive fuzzy PID controller with controlled variables q^A and q^B with the aim to control the system robust, stable and precisely, as shown in Fig. 5. The measured quantities are the position of the piston and the pressures in the two chambers. The pressures are used to calculate the current stiffness of the actuator using Eq.s (17). Since the position of the piston depends on $q^A - q^B$ and the stiffness on $q^A + q^B$, in order to adjust the PID parameters online in real time, two fuzzy controller knowledge base are configured. And also, two PID controllers are used relating the control flows $\dot{q}^A$ and $\dot{q}^B$ to the position error ε_θ and stiffness error ε_K as follows:

3 Application Cases

The VIA is realized and implemented in the CloPeMa gripper as shown in Fig. 6 with two linear motors and four small cylinders connected to the two big cylinders assembled on the gripper. The stiffness of the VIA with respect to the displacement of the two big cylinders are connected with two blue tubes which inject or release liquid respectively. Considering the linkage length at rotation joint of gripper, the relative stiffness at the fingertip is a round 1/8 of the VIA stiffness. Hence, the expected stiffness range at the fingertip is from 2.5 N/m to 25 N/m.

The applications of VIA using biphasic media can be used in such field such as robotics hand which can grasp fragile objects and robotics arm which can avoid collision with human body and environment around. In this case, the pressure sensor and encoder are used to control the stiffness and angular displacement. For example, the rethink robotics company baxter robot is friendly interact with human because of the arm driving involved passive elastic joint as shown in Fig. 7. However, the stiffness is fixed and not stable in high speed. We are considering replace the passive elastic spring joint with VIA using biphasic media. And also, minimally invasive robotics surgery (MIRS), using VIA between the kinematic modules can do less harm to human body.

As shown in the Figure 2, assume that the $n = 3$,

Fig. 7: Baxter robot friendly interacts with human for the low stiffness arm

the finger has 3 joints and each joint can rotate in the coupled way. In this model, we can use the pulley cable combined with biphasic media VIAs to drive the motion of each joint and realize the dexterous hand performance. As is known, when the single finger has redundancy and touches with the object, the joints can cause restoring force and torque as shown in Eq.s (20)

$$\begin{aligned}\tau =& J_\theta^T K_F J_\theta \delta\theta \\ =& K_\theta \delta\theta \end{aligned} \tag{20}$$

Where the J_θ is orthogonal matrix. In order to avoid slip between finger and object, the finger should apply a bias force f_b. And then, the impedance control formulation as shown in Eq.s (21)

$$\tau = K_\theta \delta\theta + J_\theta^T f_b \tag{21}$$

In which the stiffness errors ΔK and joint position errors $\Delta\theta$ are controllable and depend on control parameters Q(liquid flow).

$$\begin{bmatrix} Q^A \\ Q^B \end{bmatrix} = \begin{bmatrix} K_\theta & K_s \\ -K_\theta & K_s \end{bmatrix} \begin{bmatrix} \Delta\theta \\ \Delta K \end{bmatrix} \tag{22}$$

In order to realize the stable grasp of given object, we need to use joint torque apply in object by using n fingers. As shown in the Fig.s 8, we simplify the model to 3 pair of torque and force stiffness that driving by finger joint torque. The restoring force can balance 3 DoF of translation and

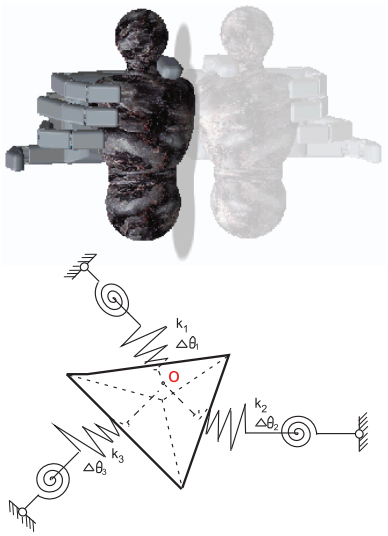

Fig. 8: Robotics hand grasp model using biphasic media VIAs

restoring torque can balance 3 DoF of rotation. On the condition of stable state with disturbing force, the redundancy finger is helpful. Based on the object gravity center, the resultant of forces, torques and internal force stiffness matrix

$$\Lambda = K_O \delta\chi_O \tag{23}$$

The robotics hand impedance control formulation as below

$$\begin{aligned}\Gamma =& J_\theta^T W^T K_o W J_\theta \delta\Theta \\ =& K_\theta \delta\Theta \end{aligned} \tag{24}$$

And also, if bias force Λ_b was applied, Eq.s (24) can be replaced with

$$\Gamma = K_\theta \delta\Theta + J_\theta^T W^T \Lambda_b \tag{25}$$

Every actuator can drive the 3 joints of one finger at the same time using cables parallel connection which means the 3 cables connecting 3 joints parallel but driving by the same actuator. The robotics hand has five fingers which actuated by five actuators independently. This way simplifies the control model and actuation structure. Combined with the mathematic model of the hand grasp, the

robotics hand can use 5 actuators to realize the adjustment of fingers impedance and posture. Because of the compact structure and high power density, this should be a very innovation way.

APPENDIX A

Appendix one text goes here.

APPENDIX B

ACKNOWLEDGMENTS

The authors would like to thank the Ministry Of Education University And Research Directorate-General, Scientific Research Programmes, Italy.

REFERENCES

[1] R. Alexander, *Three uses of springs in legged locomotion*, Int. J.Robot. Res. Vol 9, no.2: 53-61, **1990**.

[2] Bo Han, Matteo Zoppi, Rezia Molfino.Variable impedance actuation using biphasic media. *Mechanism and Machine Theory*, *62*, 1-12, **2013**.

[3] M. Zinn, O. Khatib, B. Roth, and J. Salisbury, Playing it safe [human friendly robots]. *IEEE Robot. Automat. Mag*, *11*, 12-21, **2004**.

[4] A. Bicchi and G. Tonietti, Fast and soft arm tactics: Dealing with the safety-performance trade-off in robot arms design and control. *IEEE Robot. Automat. Mag*, *11*, 22-33, **2004**.

[5] W. Stiehl, C. B. L. Lieberman, J. Breazeal, M. Lalla, and L. Wolf, Design of a therapeutic robotic companion for relational, affective touch. *IARP-IEEE/RAS-EURON Joint Workshop on Techn*, Rome, Italy, **2005**.

[6] J. Saldien, K. Goris, B. Vanderborght, B. Verrelst, R. Van Ham,D. Lefeber, Anty: The development of an intelligent huggable robot for hospitalized children. *Proc. 9th Int. Conf. Climbing and Walking Robots and the Support Technologies for Mobile Machines*, **2006**.

[7] S. Jezernik, G. Colombo, T. Keller, H. Frueh, and M. Morari, Robotic orthosis lokomat: A rehabilitation and research tool. *Neuromodulation*, *Vol 6*, 108-115, **2003**.

[8] P. Beyl, M. Van Damme, R. Van Ham, R. Versluys, B. Vanderborght, D. Lefeber, An exoskeleton for gait rehabilitation: Prototype design and control principle. *Proc. IEEE Int. Conf. Robotics and Automation*, 20372042, **2008**.

[9] J. Veneman, R. Kruidhof, E. Hekman, R. Ekkelenkamp, E. Van Asseldonk, and H. van der Kooij, Design and evaluation of the lopes exoskeleton robot for interactive gait rehabilitation. *Trans. Neural Syst. Rehabil. Eng.*, *Vol 15*, 379-386, **2007**.

[10] S. K. Banala, S. K. Agrawal, A. Fattah, V. Krishnamoorthy, W.-L. S. Hsu, and K. J. Rudolph, Gravity-balancing leg orthosis and its performance evaluation. *IEEE Trans. Robot.*, *Vol 15*, 1228-1239, **2006**.

[11] H. Blaya and J. A. Herr, Adaptive control of a variable-impedance ankle-foot orthosis to assist drop-foot gait. *IEEE Trans. Neural Syst. Rehabil. Eng.*, *Vol 12*, 24-31, **2004**.

[12] K. W. Hollander, R. Ilg, T. G. Sugar, and D. Herring, An efficient robotic tendon for gait assistance. *J. Biomech. Eng.*, *Vol 128*, 788-791, **2006**.

[13] A. Bicchi, S. Lodi Rizzini, and G. Tonietti, Compliant design for intrinsic safety: General issues and preliminary design. *Proc. IEEE/RSJ Int. Conf. Intell. Robots and Syst.*, 18641869, Maui, Hawaii, **2001**.

[14] M. Zinn, O. Khatib, B. Roth, and J.K. Salisbury, A new actuation approach for human friendly robot design. *Proc. Int. Symp. Experimental RoboticsISER02*, Sant'Angelo d'Ischia, Italy, **2002**.

[15] J. Versace, A review of the severity index. *Proc. 15th Stapp Car Crash Conf.*, 771796, New York, **1971**.

[16] G.O. Njus, Y.K. Liu, and T.A. Nye, The inertial and geometrical properties of helmets. *Med. Sci. Sports Exerc.*, *Vol 16*, 498-505, **1984**.

[17] D.W.A. Brands, Predicting brain mechanics during closed head impactNumerical and costitutive aspects. *Ph.D. dissertation*, University of Eindhoven, Netherlands **2002**.

Rezia Molfino Professor, Member, IEEE, University of Genova

Bo Han PhD, Research Associate, PMAR, University of Genova

Matteo Zoppi PhD, Researcher, PMAR, University of Genova

An Actuated, Flexible Endoscope for Laser Surgery inside the Larynx

Dennis Kundrat, Andreas Schoob, Lüder A. Kahrs, Tobias Ortmaier
Institute of Mechatronic Systems
Leibniz Universität Hannover
30167 Hanover, Germany
dennis.kundrat@imes.uni-hannover.de

***Abstract*— Transoral laser surgery focuses on contact-less treatment of disorders of the vocal folds. To overcome limitations of common microscopic interventions, current research focuses on the development of endoscopic laser scalpels. This paper presents a flexible robot for laser phonomicrosurgery. In detail, the design of endoscopic shaft, multi-functional tip and actuation are described. First insertion trials on a phantom and human cadavers have been conducted successfully demonstrating that proper view onto the vocal folds can be established essential for intraoperative laser planning and cutting.**

***Keywords*—** *Laser Phonomicrosurgery, Continuum Robot, Multi-functional Distal Tip*

I. Introduction

Laser surgery inside the larynx is commonly performed with extension of the neck and suspension laryngoscopy by inserting a straight rigid laryngoscope through the oral cavity and oropharynx to expose the glottic region. Gold standard for this procedure is a microscopic based approach [1]. Patel et al. integrated a laser beam deflecting mechanism based on Risley prisms into a rigid endoscopic device with one degree of freedom (DoF) at the tip [2]. We are currently developing the first flexible robot for endoscopic laser phonomicrosurgery with several DoF [3] (see Fig. 1). The design of our endoscope was inspired by Simaan et al. [4]. Our endoscopic device will be combined with an overall control and surgeon-machine interface as well as a small scale beam deflector [5,6]. In this contribution we present our system components and current maneuverability with articulation examples.

Fig. 1. Schematic drawing of the intented use of our new endoscope for laser surgery inside the larynx.

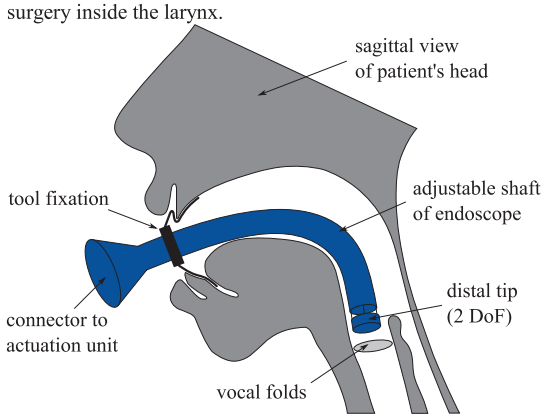

This research has received funding from the European Union FP7/2007-2013 under grant agreement µRALP - n°288663.

II. Methods

The actual prototype of our endoscope consists out of three main components:

1. A multi-functional distal tip with motorized two DoF,
2. a shaft with a manually adjustable and a rigid section

   as well as
3. an actuation unit controlling 1. and 2.

Tip and shaft have a diameter of 19 mm and a length of approx. 15 cm (see Fig. 2). The overall structure has a central backbone and three further concentric tubes, all out of Nitinol (NiTi). The multi-functional tip encases two cameras, light guides, further channels for tools, suction and irrigation as well as space for a micro beam deflector for laser cutting of tissue (see Fig. 3). The tip is articulated in two DoF by the concentric push/pull wires. The wires are guided inside tubes that allow for bending of the shaft. Wires and tubes are moved inside the actuation unit (see Fig. 4).

Fig. 2. Adjustable shaft of the endoscope with articulated tip.

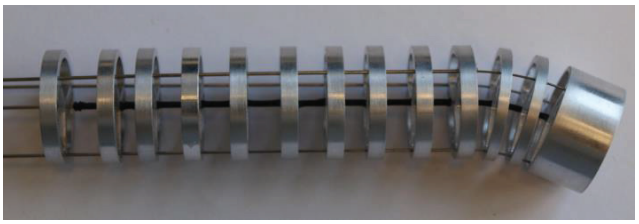

Fig. 3. Multi-fuctional tip with encased two cameras, two light guides and preparation of the electrical connection of the laser beam deflector. A Front cover in combination with inserted windows (right photograph) seal the tip .

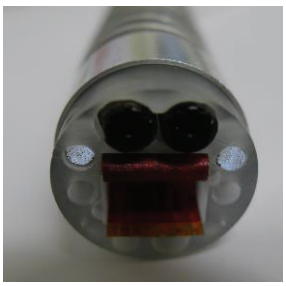

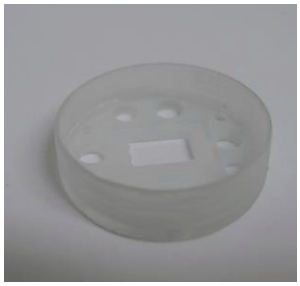

Fig. 4. Overall endoscope with actuation unit. Three motors for the articulation of the tip are mounted on a sliding carriers that are translated by a rotary knob and allow for bending of the shaft section.

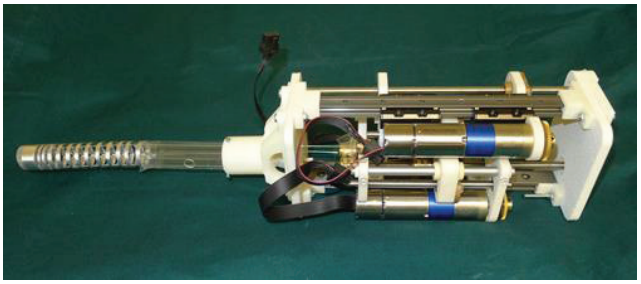

The actuation of the tip is controlled by software buttons or with a 3D mouse. The low level control algorithms are implemented on an embedded PC which is attached to the housing of the actuation unit. During phantom and cadaver trials the endoscope is held at the actuation unit manually by hands or is fixated on an articulated arm.

During cadaver experiments protection against water, blood, etc. is achieved by closing the tip with a window and a front cover. The flexible shaft is equipped with a silicone cover and the actuation unit is put into a bag.

III. Results

The manually actuated shaft is able to bend to a 90° position. Additionally, motorized movements of the tip are feasible in two DoF with each ±30°. Velocities were limited to protect the hardware for safety reasons. Movements of the tip are visualized in Fig. 5.

Insertion of the endoscope into the larynx of a phantom and cadavers was successfully achieved. Surgeons as well as engineers were able to manipulate the endoscopic shaft during insertion and to adjust the field of view by moving the distal tip. This facilitated proper stereoscopic visualization of the vocal folds. Adjunct views obtained from the left camera are illustrated in Fig. 6.

Fig. 5. Movement of the motorized tip of the endoscope.

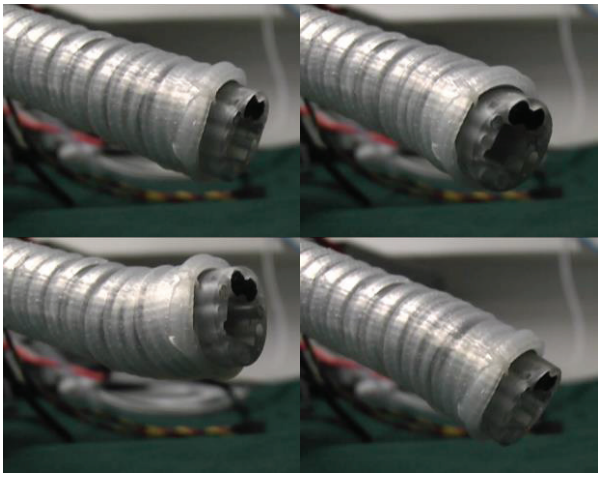

Fig. 6. Left camera views onto the vocal folds obtained from insertions into two human cadavers.

IV. Conclusion and Outlook

We build a hybrid-actuated, flexible endoscope and were able to visualize structures like the vocal folds inside the larynx. First insertion trials were successfully conducted on a phantom and human cadavers. We observed that movability is quite limited inside confined structures like the glottis region. Thus, future prototypes will focus on reducing the overall diameter and on integrating of laser delivering fibers as well as micro beam deflection to the distal tip.

Acknowledgment

We thank all members of the µRALP consortium (www.microralp.eu) helped e.g. in specifications and during discussions about the presented prototype as well as during the cadaver trials. We further thank Jannek Hisleiter for his Bachelor Thesis on electrical design and kinematics.

References

[1] L. Hinni, J. Salassa, D. Grant, B. Pearson, R. Hayden, A. Martin, H. Christiansen, B. Haughey, B. Nussenbaum, W. Steiner, “Transoral laser microsurgery for advanced laryngeal cancer,” Arch Otolaryngol Head Neck Surg 133(12):1198–1204, 2007.

[2] S. Patel, M. Rajadhyaksha, S. Kirov, Y. Li, and R. Toledo-Crow, “Endoscopic laser scalpel for head and neck cancer surgers,” in Proc. SPIE 8207, 2012.

[3] D. Kundrat, A. Schoob, L.A. Kahrs, T. Ortmaier, “Flexible robot for laser phonomicrosurgery,” in Proc. First International Symposium on Soft Robotics 2014, ISBN 978-3662445051.

[4] N. Simaan, R. Taylor and P. Flint, “A dexterous system for laryngeal surgery - multi-backbone bending snake-like slaves for teleoperated dexterous surgical tool manipulation,” in Proc. IEEE International Conference on Robotics and Automation, pp. 351–357, 2004.

[5] L.S. Mattos, N. Deshpande, G. Barresi, L. Guastini, G. Peretti, “A novel computerized surgeon-machine interface for robot-assisted laser phonomicrosurgery,” Laryngoscope. 124(8):1887-94, 2014.

[6] S. Lescano, D. Zlatanov, M. Rakotondrabe, and N. Andreff, “Kinematic analysis of a meso-scale parallel robot for laser phonomicrosurgery,” in Proc. Second Conference on Interdisciplinary Applications in Kinematics, 2013.

Modular integration of a 3 DoF F/T sensor for robotic manipulators

Emanuele Lindo Secco, Yohan Noh*, Sina Sareh, Helge Wurdemann, Hongbin Liu, Kaspar Althoefer
Dept. of Informatics, Centre for Robotics Research
King's College London, UK
Email (*corresponding author): yohan.noh@kcl.ac.uk

***Abstract*— Robot assisted surgery and minimally invasive robotic surgery inherently entail that the hands of the surgeon indirectly interact with the patient tissues and organs even if the operator is out of the affected body. Hence, transferring sensor information from the inside of the patient to the outside of the surgeon may certainly improve the perception of the robotic end-user. To this aim – within the EU framework of the STIFF-FLOP project (STIFFness controllable Flexible and Learnable Manipulator for Surgical Operations), we developed a novel design of miniaturized and magnetic resonance compatible sensors for force and torque real-time measurements in robotic surgery. The sensor design has a hollow shape, whose geometry allows its integration and embedding within snake-like surgical robots and modular devices. According to typical requirements and specifications of a surgical procedure, the sensor operates in a range of force and torque of 0-5 N and 0-5 N·cm, respectively. Due to a customized tool and calibration procedure, an error of less than 15% of sensor range can be obtained. This novel transducer may advance force and haptic feedback in robot assisted and minimally invasive surgeries.**

Keywords—force sensor; minimally invasive surgery; hollow design; MR compatibility sensin; keyhole surgery.

I. INTRODUCTION

During laparoscopic procedure, robot assisted surgery and minimally invasive robotic surgery (MIS), surgeons are going into the human body of the patient with tools which are remotely interfering with their operating hands [1-3]. Therefore, set of visual instruments are usually employed to make surgeons able to achieve the surgical tasks. Usually, these instruments supply a real-time stream of visual information through local or remote docking stations, providing that external monitors are available and one or more cameras are embedded within the surgical tool. Such an approach means that all information - which are usually transferred into the hands of the surgeon during an open surgical procedure - are implicitly replaced and surrogated by means of a unique senor channel, namely the visual one. Undoubtedly, vision is one of the most relevant sensors in human being. Nevertheless - due to the typical tasks of surgery, which usually requires direct palpation of human tissues, vessels and organs - touch sensitivity fulfills a not negligible role [4]. As a result, even if these concerns are largely discussed within the medical community, supplementary information procured from further sensor modalities may be beneficial while exploiting robotic surgery.

To this aim, within the EU framework of STIFF-FLOP Project - which develops new concepts and class of robotic devices for MIS based on STIFFness controllable Flexible and Learnable Manipulator for Surgical Operations [5] – a novel force and torque (F/T) sensor was conceived. The F/T sensor is easily integrated in a modular fashion within STIFF-FLOP manipulator [6, 7]; thanks to its optimized design, it can be easily adapted and employed within other surgical manipulators having a snake-like and hollow configurations. The sensor contains an interesting sets of peculiarities: small size, reproducible design (due to a 3D printing-base manufacturing process), magnetic resonance compatibility; it also allows cables and other linkages to passing through its structure internally, thanks to its geometry which is built externally and covers the peripheral area of the robot only.

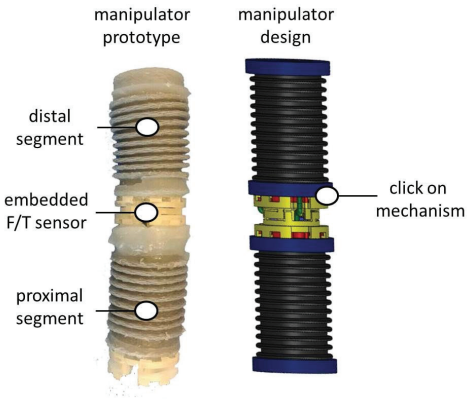

Fig. 1. STIFF-FLOP two segments manipulator with its own modualr strucutre and the embedded 3 d.o.f. F/T sensor.

II. THE 3 D.O.F. F/T SENSOR

A. Sensor design

Sensor design and characteristics originate from a set of preliminary and desired specifications and requirements:

Biocompatibility – a device, which has to be fully compatible vs. surgical application is desirable, therefore it has to avoid electric power and wires, as well as to elude the presence of any metal components (in order to pursue whole compatibility with magnetic resonance scans).

Modularity - the sensor structure should inherently allow the structural connection between the modules of the surgical manipulator. Hopefully, it should also leave an internal room (i.e. auxiliary channel) which may be used to accomplish other

surgical tasks like the introduction of tools or actuators for a biopsy or other assignments.

Degree of freedom (d.o.f.) – from a sensorial viewpoint, the transducer should be able to measure applied forces as well as torques with a good S/N ratio and precision as it is required by a surgical task.

In line with these specifications, a ring-shape device has been designed as it is shown in Fig. 2. The device was plotted with the Solid Works software environment (by Dassault Systèmes Corp.) and manufactured in PROJET VisiJet® EX200 material (by 3D SYSTEM Co. Ltd) with a 3D printer (ProJet HD3000, by Print It 3D Ltd). The sensor structure is made a 3 d.o.f. plate, which is supported by 3 equally distributed cantilevers at 120° on the circular shape (Fig. 2, left panel). This structure allows measuring longitudinal force, F_z, and two torques in the orthogonal plane (M_x and M_y, Fig. 2, left panel). The principle behind the F/T measurements lays on the displacement estimation of each distal section of the 3 cantilevers. The displacement is transduced into a light intensity modulation, which is obtained by means of 3 couples of optical fibres (one for each cantilever), namely emitting and receiving fibres coupled with a digital amplifier FS-N11MN Fiber Optic Sensor (by Keyence Co., Ltd). Finally, the light modulation is performed through 3 reflective mirrors, which are fixed on each tip of the cantilever (Fig. 2, right panel). The whole sensor restrained within the size of 33x13 mm.

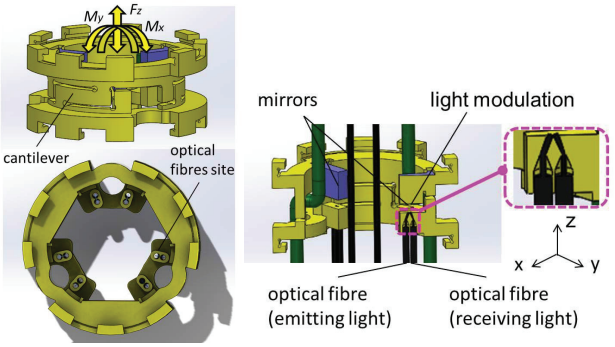

Fig. 2. Sensor design and geomtry (left panel) and its principle of functioning (right panel).

B. *Sensor integration*

Design of a 2-segmentsSTIFF-FLOP manipulator is shown in Fig. 1: a modular structure contains 3 air chamber actuators within each module plus an auxiliary channel allowing tubes to pass through the manipulator internally. On the periphery of the sensor, a click-on mechanism is embedded, which matches with a similar coupled structure designed in the manipulator (Fig. 1, right panel): the mechanism allows connecting multiple actuated modules by introducing force sensors in between each couple of consecutive segments..

C. *Sensor performance*

A specific tool and procedure for the calibration of each sensor and release of main characteristics was designed: the tool allows loading different weights on the sensor which stress the cantilever plates with different forces and torques [6]. A Multiple Linear Regression (MLR) method is then applied to sensor data to infer 3x3 calibration matrix (K_{calib}): this latter one establishes the relationship between the F/T output (F_z, M_x, M_y) and input signals (i.e. the 3 measurements of light intensity, as retuned from the FS-N11MN amplifiers, aset of 3 voltage levels, V_1, V_2 and V_3). Therefore it holds:

$$\begin{bmatrix} F_z \\ M_x \\ M_y \end{bmatrix} = [K_{calib}] \cdot \begin{bmatrix} V_1 \\ V_2 \\ V_3 \end{bmatrix} \qquad (1)$$

The final sensor operative range, in terms of force and torque, is from 0 to 5 N and from 0 to 5 N·cm, respectively; proper MLR estimation of K_{calib} entails a maximum absolute error of force and torque of less than 0.3 N and 0.1 N·cm, respectively.

III. Conclusion

A novel bio-compatible and metal free F/T sensor for robotic and minimally invasive surgery has been presented. The sensor was originally designed for a specific family of manipulators within the EU STIFF-FLOP project. Nevertheless, due to its hollow shape, size and performance , the proposed device lends itself to be used and embedded in different surgical robots.

Current sensor performances are constrained within a maximum percentage error of less than 15% of its range . Due to the sensor manufacturing process and material, a deeper analysis of its properties linearity and hysteresis should be performed, as it was already proposed for similar devices and applications [8-10].

IV. References

[1] W. Reynolds, “The First Laparoscopic Cholecystectomy”, JSLS 5:89-94, 2001.

[2] A. Rané, G. Y. Tan, A. K. Tewari, “Laparoendoscopic single-sitesurgery in urology: is robotics the missing link?”, BJU International, 2009; pp. 1041–1043.

[3] N. Simaan, K. Xu, A. Kapoor, W. Wei, P. Kazanzides, P. Flint, and R. Taylor, "A System for Minimally Invasive Surgery in the Throat and Upper Airways", Int. J. Robotics Research, vol. 28- 9, pp. 1134-1153, June 2009.

[4] I.B. Wanninayake, E.L. Secco, L.D. Seneviratne, K. Althoefer (2013), A Novel Probe Designed to Estimate Soft Tissue Stiffness in MIS, Workshop on Cognitive Surgical Robotics, IEEE IROS 2013.

[5] M. Cianchetti, T. Ranzani, G. Gerboni, I. De Falco, C. Laschi, A. Menciassi,”STIFF-FLOP Surgical Manipulator: mechanical design and experimental characterization of the single module”, IEEE/RSJ 2013, pp. 3576-3581, 2013.

[6] Y. Noh, S. Sareh, J. Back, H. Würdemann, T. Ranzani, E.L. Secco, A. Faragasso, H. Liu, K. Althoefer (2014), A Three-Axial Body Force Sensor for Flexible Manipulators, IEEE ICRA 2014, pp. 6388-6393.

[7] Y. Noh, E.L. Secco, S. Sareh, H.A. Würdemann, A. Faragasso, J. Back, H. Liu, E. Sklar, K. Althoefer, A Continuum Body Force Sensor Designed for Flexible Surgical Robotic Devices, IEEE EMBC 2014.

[8] P Puangmali, H Liu, LD Seneviratne, P Dasgupta, K Althoefer, ”Miniature 3-axis distal force sensor for minimally invasive surgical palpation”, Mechatronics, IEEE/ASME Transactions on 17 (4), 646-656.

[9] P Polygerinos, P Puangmali, T Schaeffter, R Razavi, LD Seneviratne, “1) Novel miniature MRI-compatible fiber-optic force sensor for cardiac catheterization procedures”, IEEE ICRA 2010, pp. 2598 – 2603.

[10] Panagiotis Polygerinos, Dinusha Zbyszewski, Tobias Schaeffter, Reza Razavi, Lakmal D Seneviratne, Kaspar Althoefer,” MRI-compatible fiber-optic force sensors for catheterization procedures”, IEEE Sensors Journal, pp. 1598-1608, 2010.

A novel sensorized catheter for precise stenotic heart valve targeting:

an application of the Medyria Trackcath Catheter Positioning System

Anita Di Iasio. Theresa Visarius, Gianluca Martena, Mauro M. Sette
Medyria AG
Winterthur, Switzerland
Mauro.Sette@medyria.com

***Abstract*— Crossing a stenotic aortic valve with a guidewire can be a time consuming and risky step during valvuloplasty or before implanting a heart valve stent. The blind advancement of a guidewire is associated with adverse effects that can potentially be prevented by improved catheter guidance. This work presents the design and performance testing of a novel sensorized catheter used to facilitate the crossing of a stenotic aortic valve with a guidewire. The sensing system is based on two technologies that allow the measurement of blood flow velocity simultaneously with the automatic identification of anatomical features. This study presents data where the system was able to recognize the center of a stenotic heart valve and allow the alignment of the catheter tip with the valve center, facilitating guidewire traversal. The clinical introduction of this catheter guidance technology is expected to minimize surgical risk and improve heart valve disease management.**

Keywords*— *percutaneous aortic valve, blood flow velocity, catheters, sensing, cardiovascular, stroke.

I. Introduction

We are living in an exciting era, in which many cardiac pathologies that in the past were treated with an open surgical approach, now can be managed with minimally invasive techniques. One such pathology is the aortic valve stenosis, affecting up to 7% of the population over the age of 65 in western countries (McRae, Rodger, & Bailey, 2009), with a trend towards increased prevalence. The state of the art minimally invasive technique used to treat aortic valve stenosis is catheter based. Here, in sequential surgical steps, elongated tools are passed from a remote access point through vasculature to the surgical site in the heart. The initial step is the advancement of a soft guidewire across the stenotic valve (Figure 1). This guidewire then serves as a rail on which other catheters are advanced. The initial placement of this guidewire is a delicate and time consuming task that can lead to adverse effects such as detachment of atherosclerotic plaques, calcium deposits, or secondary thrombus, resulting in stroke. A recent prospective study showed a 3% incidence of clinical stroke and a 22% incidence of new defects on magnetic resonance imaging after retrograde left ventricular catheterization for aortic stenosis (Chambers et al., 2004).

As suggested by the two surgeons leading the clinical part of the CASCADE project (EU-FP7), it is urgent to develop methods for the safer and faster crossing of the native aortic valve, thus reducing the risk for the patient and reducing the time required for the preparatory steps of the interventional procedure. To address this unmet clinical need, Medyria has developed a catheter prototype integrating the Trackcath Catheter Positioning System (CPS), a unique technology that allows catheter navigation in the cardiovascular system.

The aim of this study was to evaluate the performance of the Medyria CPS when guiding a catheter across a stenotic aortic valve in an anatomical mock-up that simulates the interventional procedure.

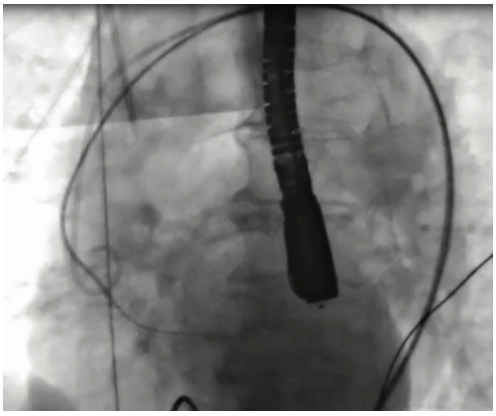

Figure 1: Placement of guidewire through a stenotic valve.

II. Materials and Methods

A. *Trackcath CPS*

The Trackcath CPS consists of a sensing unit (Figure 2) and processing unit (Figure 3). The sensor is a platinum flow velocity sensor integrating a temperature compensation scheme. The sensor pad size is 1mm x 6mm with a thickness of 30 µm. This allows the easy integration of the sensor with any type of catheter. Six wires of 100 µm diameter connect the sensor to the control unit. The control unit is connected via USB to a PC which runs the software for the processing of the flow velocity signals.

Figure 2: CPS - Flow velocity sensor.

Figure 3: CPS - control unit.

B. Catheter prototype integrating Medyria CPS

An Amplatz guiding catheter normally used for guiding the catheter through the valve has been equipped with the flow velocity sensor on its tip (Figure 4).

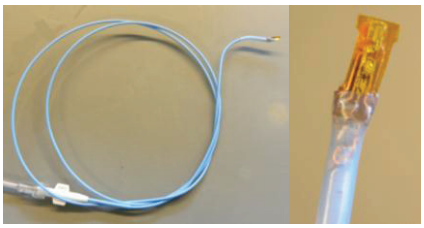

Figure 4: Amplatz catheter (right) equipped with flow velocity sensor on the tip (left).

C. Mock-up of the aorta with perfusion

A rigid plastic 3D printed model of the aortic arch produced by Materialise (Leuven, Belgium) was used for simulating the geometry of the anatomy. The aortic stenosis was simulated adding a metallic ring at the aortic valve resulting in a central circular opening of 5mm. The system was perfused with water kept in circulation by a peristaltic pump (Figure 5), the pump is a prototype developed by Medyria (Winterthur, Switzerland) within the framework of the CASCADE project, it has the ability for generating controlled flow profiles that resemble the flow within the aorta.

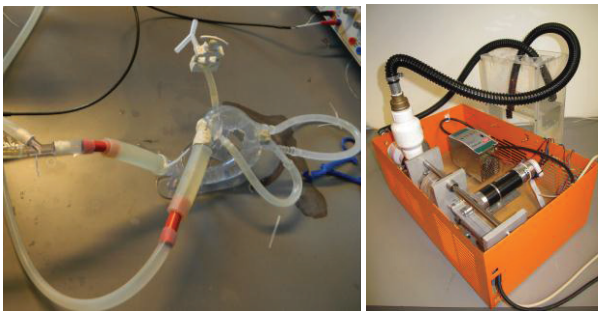

Figure 5: Mock-up aorta model (left) and peristaltic pump (right).

D. Acquisition and data processing

The catheter was advanced into the model up to the ascending aorta. The area in front of the aortic valve was scanned moving the catheter along two trajectories; in the plane parallel to the valve, and pushing/pulling along the aorta. While moving the catheter, the flow sensor was connected to the controlling unit and the flow signal was processed with the Trackcath CPS algorithm. The flow velocity was displayed as relative velocity with respect to a baseline velocity. The baseline velocity was acquired by positioning the sensor in a region of the aorta far from vascular side branches or other structures that could interfere with the plug flow profile.

III. Results

Figure 6 shows the flow velocity acquired while scanning with the tip of the catheter on a plane parallel to valve opening plane. The two peaks represent when the catheter tip is aligned with the center of the valve.

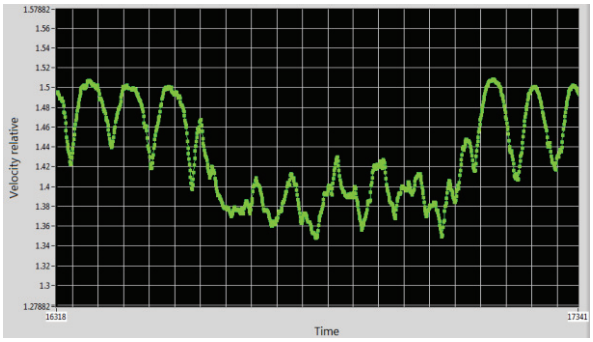

Figure 6: Acquisition made while scanning parallel to the valve plane.

Figure 7 shows the flow velocity acquired while scanning from distal to proximal towards the valve. The flow velocity gradually increases as the sensor approaches center of the valve and recognizes a maximum flow.

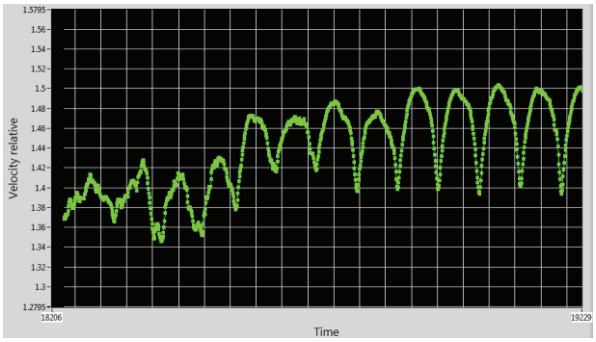

Figure 7: Flow velocity acquired while scanning from distal to proximal during advancement towards the valve.

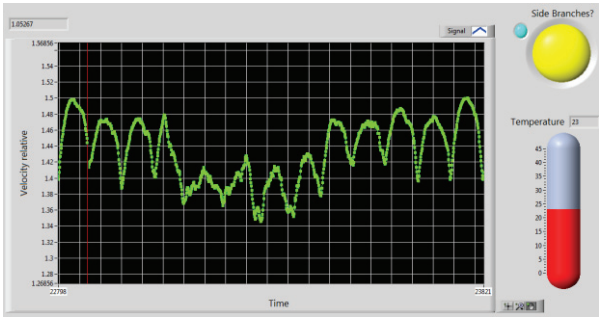

Figure 8: Trackcath CPS identifying the probability of locating the anatomical landmark (yellow light).

The Trackcath CPS was able to identify the position of the appropriate anatomical landmark. A yellow signal indicated when the catheter approached the center of the valve (Figure 8) and a green signal indicated when the catheter was aligned with the center of the valve (Figure 9).

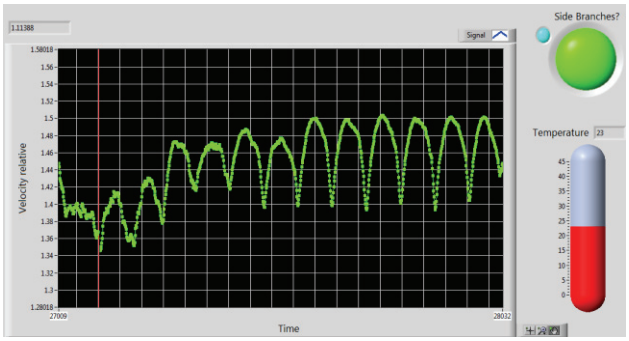

Figure 9: Trackcath CPS has identified the position of the anatomical landmark (green light).

IV. Discussion and Conclusion

The Trackcath CPS technology can precisely target the center of a stenotic aortic valve in the model system described. Additionally, this pilot study demonstrates that the system accurately measures the flow pattern in the proximity of the valve. The signal can be automatically processed with the aim of finding the flow peak in an automatic way. Our next foreseen steps will involve the quantification of accuracy for valve center tracking in comparison to the existing technique used clinically. This novel technology aims to improve the safety of guiding a catheter across a stenotic heart valve by reducing morbidity and mortality associated with procedure as well as minimizing surgical time.

Acknowledgements

The project was partially founded by the European Commission EU-FP7-ICT Cascade project n.601021.

References

Chambers, J., Bach, D., Dumesnil, J., Otto, C., Shah, P., & Thomas, J. (2004). Editorial : Crossing the Aortic Valve in Severe Aortic Stenosis : No Longer Acceptable ?

McRae, M. E., Rodger, M., & Bailey, B. a. (2009). Transcatheter and transapical aortic valve replacement. Critical Care Nurse, 29(1), 22–37; quiz 38. doi:10.4037/ccn2009553

Session 8

Continuum & Soft Robots (II)

Chair: Dr. Kaspar Althoefer, King's College London

Thursday, October 16th

10:30 – 11:30

STIFF-FLOP surgical manipulator: design and preliminary motion evaluation

Iris De Falco, Matteo Cianchetti and Arianna Menciassi
The BioRobotics Institute, Scuola Superiore Sant'Anna, Pisa, Italy
{i.defalco; m.cianchetti; a.menciassi}@sssup.it

***Abstract*—This paper presents a soft multi-module manipulator for minimally invasive surgery (MIS). The design and the materials are bioinspired and try to reproduce some biological capabilities of the octopus, such as elongation, omni-directional bending and stiffness variation. Embedded fluidic chambers allow to pneumatically actuate the manipulator in order to achieve a 3-D motion, while a variable stiffness mechanism based on the granular jamming phenomenon allows to control the stiffness of the arm. The design of three modules integration and the fabrication phases as well as a preliminary study on the 3-module manipulator performance are reported. Elongation and bending have been experimentally evaluated. The arm is 165 mm long and it is able to elongate up to 53.3% of the initial length and to bend up to 248 degrees depending on the combination of the actuated chambers.**

Keywords*—minimally invasive surgery, soft robot, pneumatic actuation, modular robot.

I. Introduction

In the last years surgical procedures have improved with the aim of reducing the invasiveness of traditional medical techniques [1]. Minimally invasive surgery (MIS) has successfully developed with laparoscopic operations, that are based on the access into the abdomen cavity by 4 or 5 trocars. Several dedicated accesses are necessary because traditional tools are elongated but they have a very limited flexibility. In order to reduce the number of the trocars, more tools can be inserted from a single access (single port laparoscopy, SPL), *i.e.* the umbilical one, or through natural entrance as in natural orifices translumenal endoscopic surgery (NOTES), avoiding external visible scars [2]; anyhow these solutions increase the difficulty of the surgical operations [3, 4]. These limitations are at the base of the development of innovative instrumentation with redundant degrees of freedom (DOFs) that ensure more motility and dexterity during insertion, control and operations. Articulated tools are able to reach and work in different districts of the body [5-8] in NOTES or SPL [9-11]. Articulated robots can be used for optimizing surgical operations and also as retraction systems, often necessary in surgery [12]. New technologies allow to design flexible tools which are safer than the traditional ones thanks to their compliance with the tissues [13]. Some examples of flexible manipulators permit to gain a specific configuration when the working site is reached, but generally they lack stability and the contact with the surrounding tissues is not controlled [14].

The growing interest in the study of biological soft structures, such as the octopus arm and the elephant trunk, allowed the development of new technologies of fabrication and use of new materials to design manipulators with controllable stiffness (from highly compliant to rigid) [15]. The biological inspiration represents an input for the design of more deformable and flexible manipulators, with a redundant number of DOFs and mechanisms to control their stiffness. This leads to the possibility of controlling the interaction with an object and then with a biological tissue. Several solutions have been proposed in order to design a soft multi-articulated robot, and normally actuation systems are based on cables, passive springs [16], pneumatic elements, tendons [17, 18] or smart materials such as shape memory alloys [19]. However, these studies do not resolve the request of combining softness with the generation of large forces.

This work presents the design of a soft manipulator taking inspiration by the octopus biological capabilities, and that is able to elongate, to bend in any direction, to be passively squeezed and to tune its stiffness.

II. Design and Fabrication of the Manipulator

The STIFF-FLOP manipulator is based on a modular architecture that integrates multiple basic units, each characterized by the same capabilities in terms of 3D motion and force generation. The design of the first prototype of the manipulator is shown in Fig. 1.

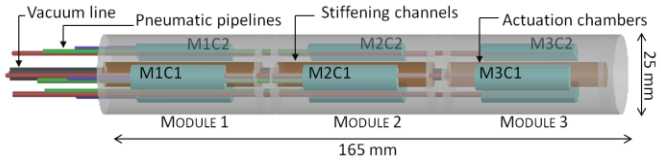

Fig. 1. Overall sketch of the manipulator design.

The overall length is 165 mm and the diameter is 25 mm. These dimensions are not yet compatible with MIS procedures, but at this first stage the research has been more focused on the feasibility and the proof of the modular concept. In the next developmental phase they will be optimized for an application in a real medical scenario. The single module of the arm has a length of 50 mm and consists of an elastomeric cylinder made of Ecoflex 0050 silicone (Smooth-On). Three embedded fluidic chambers are internally

This work has been supported by the EC with the STIFF-FLOP FP7-ICT-2011.2.1 European Project (#287728).

arranged at 120 degrees and they actuate the module when inflated and controlled by external valves. The actuation of one single chamber or two chambers simultaneously allows the omni-directional bending, while the inflation of all three chambers elongates the module. A central channel is dedicated to the granular jamming mechanism [21] based on a Latex membrane incorporating granular material. When an external pump activates the vacuum in this channel, the granular matter compacts, thus increasing the internal friction and thus allowing to vary and control the stiffness of the module. A detailed explanation of the single module performance is reported in [22].

The multi-module manipulator integrates three modules, as visible in Fig. 1. Pneumatic actuation supplies the pressure in the modules thanks to nine pipelines (Cole-Parmer). The tubes have an external diameter of 1.5 mm and they are made of soft silicone which maintains flexibility when the manipulator moves. Thanks to their flexibility, it has been possible to insert the tubes inside the actuation chambers with a length longer than the chambers one (Fig. 2) in order to minimize the tubes elongation and guarantee the module functionality.

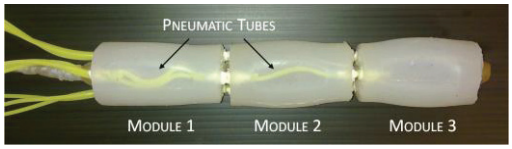

Fig. 2. First phase of three modules integration. The arrangement of the pneumatic tubes inside the actuation chambers is indicated.

Three tubes pressurize MODULE 1, while the other six pass through the chambers of this module and go to the other modules, thus supplying the pressure in the same way. For this reason, the distal modules are different from the proximal modules, which is the richest in number of passing pipes. The tubes are fixed to the bottom and the top of each module with soft Teflon around thus avoiding possible air leakages also during motion. Three stiffening channels, one for each module, are inserted in the manipulator. They are serially connected; they allow to control the stiffness of the manipulator without selection of the specific module, by activating a certain vacuum level in the vacuum line. The configuration of the tubes for supplying pressure and for activating vacuum makes the manipulator not yet completely modular because every module is bounded to the next one by tubes. Thus in this context the concept of modularity has to be intended from a functional (each module has the same functionalities) rather than structural point of view. In next works, the manipulator will be re-designed in order to pass from the current multi-module structure to a modular one, thus obtaining independent modules easily connectable.

The connection with pneumatic pipelines and the integration of the stiffening channels represent the first phases of fabrication of the manipulator. Then the consecutive modules have to be connected. The junction between two modules is not actuated and it does not include the granular jamming based stiffening channel. It has been designed in order to minimize its non-active effect on the system performance and not to prevail on that. A stiffer material and a small length have been considered to minimize the displacement of this zone when the manipulator works: when in soft state, the rigid junctions do not interfere with the softness of the modules; when in stiff state, the junctions contribute to the stiffness of the entire structure. The silicone Dragon Skin 10 (Smooth-On) has been chosen for this purpose and has been moulded between the modules for a length of 5 mm. The final step of the fabrication consists of the integration of a crimped braided sheath around the manipulator, fixed at the base and the tip. The sheath allows to increase the motion capabilities, thus avoiding the lateral expansion of the fluidic actuators when actuated.

The manipulator represents a closed system where every element is designed inside the basic structure of silicone and protected by it and the external sheath. This configuration guarantees that if an actuation chamber or the stiffening channel breaks, possible dispersion of particles is avoided. However, the low pressures needed for the chambers inflation make the breaking of the chambers a very unlikely event and for the central channel the dispersion of material is almost impossible because a Latex membrane and a thick silicone layer confine the granular matter inside the manipulator.

III. PERFORMANCE OF THE MANIPULATOR

For a preliminary characterization of the manipulator, the performance in terms of elongation and bending have been studied. The tip of the arm has been tracked for different cases relative to different values of pressure and different combinations of actuated chambers. The manipulator has been fixed at the base in a configuration similar to a hypothetic medical scenario, in which the base of the arm stops at the abdominal wall and the tip is free to move in the abdomen. As shown in Fig. 3, a 6-DOF tracking probe has been fixed on the tip of the arm and the different positions during the motion have been acquired with the Aurora EM tracking system.

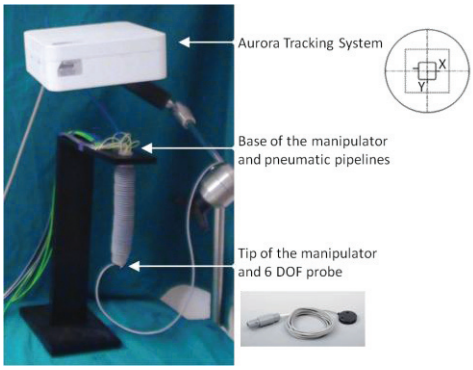

Fig. 3. Set up for the tracking of the tip position during manipulator motion.

For each position 100 samples have been acquired and afterwards elaborated. The tip has been tracked during elongation and bending movements by supplying different values of pressure to the chambers. The range of pressure is 0 – 650 mbar with steps of 50 mbar, that means fourteen tip positions acquired. The pressure 650 mbar represents the maximum actuation pressure for the single module, as discussed in [22].

Considering the different structure of the modules, mainly due to the different number of tubes inside the chambers, the

manipulator has been tested by actuating firstly the single modules in order to assess their performance. In the case of elongation, MODULE 1 has been actuated with the fourteen pressures cited before, while the other two modules were passive; the tip position has been acquired. The same tests have been carried out by actuating MODULE 2, and finally MODULE 3. The elongation of the single modules is 29 mm for MODULE 1, 30 mm for MODULE 2 and 31 mm for MODULE 3. The difference between the elongation can be associated to the number of tubes that slightly limit the motion of the proximal module. Moreover, the different values of elongation can be in part due to the fabrication method that is not yet completely repeatable at this level.

Fig. 4 shows the position of the tip during the manipulator elongation, that means all the modules (thus all nine chambers) are actuated in the same instant with the same pressure.

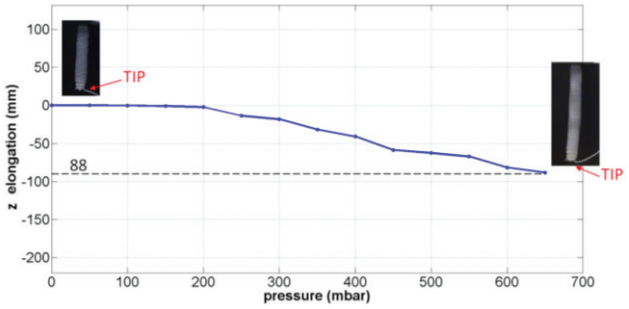

Fig. 4. Elongation of the manipulator when all the modules are simultaneously actuated with the same pressure. In the insets initial and final configurations are shown.

From Fig. 4, it is possible to notice that a significant elongation starts to be visible beyond 200 mbar and it increases up to 650 mbar for a maximum elongation of 88 mm, that means an elongation of 53.3 % and a final length of the manipulator of 253 mm. Looking at the elongation of the single modules, the overall elongation corresponds to their sum. This means that the external sheath, shared between the modules, has a length sufficient to guarantee the right elongation of each module.

Also for the bending, the single modules have been tested in order to identify possible interesting behaviours. Moreover, both the cases of 1-chamber and 2-chamber bending have been tracked. Fig. 5 (Top) shows the tip position when the chambers M1C1, M2C1 and M3C1 (as indicated in Fig. 1) are separately actuated; the same test is carried out in the case of 2-chambers actuation (Fig. 5 Bottom). In the case of 1-chamber bending, the tip is able to describe larger trajectories than the case of 2-chamber bending. This means the possibility to cover different spaces and reach the same position in different ways. Fig. 6 (Top) shows the bending of the manipulator when the chambers M1C1, M2C1 and M3C1 are simultaneously actuated with the same pressures, as discussed before. The fourteen positions of the tip have been acquired to calculate the bending angle for each one. The bending angle is the angle between the orthogonal line to the base and to the tip of the manipulator, as indicated in Fig. 6.

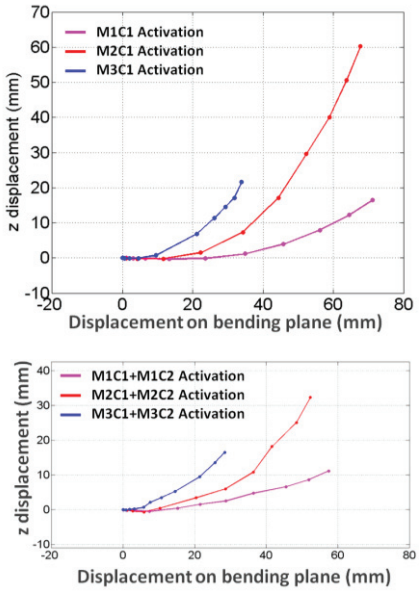

Fig. 5. Tip position during the bending of the single modules. Top: 1-chamber bending. Bottom: 2-chamber bending.

For a pressure of 650 mbar the tip bends of 248 degrees respect to the initial position of the manipulator. In the case of 2-chamber bending the following chambers are actuated: M1C1, M1C2, M2C1, M2C2, M3C1, M3C2. As shown in Fig. 6 (Bottom), the manipulator describes around the half of the trajectory described in 1-chamber bending case and the tip bends of 85 degrees.

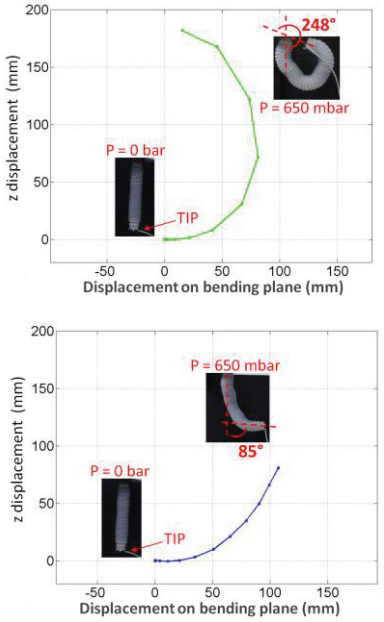

Fig. 6. Top: Tip positions during 1-chamber bending of the manipulator. Bottom: 2-chamber bending of the manipulator. In the insets the initial and the final configurations are reported, respectively for 0 bar and 650 mbar.

The values of length and bending of the manipulator are suitable for an abdominal procedure and compatible with the dimensions of the current tools used in laparoscopy [23]. Due to the placement of the manipulator with the tip going down, as during the entrance of a medical tool in the abdominal

cavity, the gravity force influences the behaviour of the manipulator. Theoretically, every module is able of larger bending, but the action of the gravity force limits the trajectory of the tip, as reported in the curves of Fig. 5 and Fig. 6. A theoretical study of the tip position of the manipulator will be carried out, by eliminating the gravity effect and thus obtaining a theoretical model for the bending.

IV. Conclusion

In this work a new manipulator for MIS has been presented. In Section II the design and the fabrication phases have been illustrated. The arm takes advantage of three soft units connected to form a modular structure. This configuration allows to obtain a flexible and redundant manipulator characterized by more dexterity than the traditional tools used in laparoscopic procedures. The manipulator is long 165 mm. It is pneumatically actuated by fluidic chambers, three inside each module. The arrangement of the actuators and an external braided sheath allow to elongate and bend the manipulator in every direction.

A central channel is dedicated to the granular jamming based stiffening mechanism providing a stiffness control of the modules.

Preliminary tests on the performance of the manipulator allowed to study the 3-D motion. The overall elongation of the manipulator, respect to the initial length, is of around 53 % when it is actuated with the maximum pressure. This allows to reach a maximum length of 253 mm that is a tool length compatible for an operation in the abdomen. The different possibilities of bending, due to the several combinations of the chambers actuation, permits to reach different positions. 1-chamber bending allows the tip manipulator to bend of 248 degrees, while in the case of 2-chambers bending the tip describes 85 degrees.

From a first evaluation of the controllable stiffness, the system permits to control the arm up to a Young Modulus of 0.91 MPa [24]. It is worth mentioning that future works will include a more detailed work on the stiffness manipulator when the vacuum in the stiffening channels is applied. Stiffness properties will be studied in combination with the motion in order to assess the potentiality of the manipulator in MIS procedures.

In addition, future works will focus on the miniaturization of the manipulator and the design of a functional tip in order to obtain a device suitable for applications in a real working scenario.

References

[1] A. Forgione, “In vivo microrobots for natural orifice transluminal surgery. Current status and future perspectives”, Surg Oncol, vol. 18, pp. 121-129, 2009

[2] D. J. Scott, S. J. Tang, R. Fernandez, R. Bergs, M. T. Goova, I. Zeltser, F. J. Kehdy, J. A. Cadeddu, “Completely transvaginal NOTES cholecystectomy using magnetically anchored instruments”, SurgEndosc, vol. 21, pp. 2308-2316, 2007

[3] V. Vitiello, S. Lee, T. Cundy, G. Yang, “Emerging Robotic Platforms for Minimally Invasive Surgery”, IEEE Rev Biomed Eng. vol.6, pp.111-126, 2013

[4] L. Vyas, D. Aquino, C.-H. Kuo, J. S Dai, P. Dasgupta, “Flexible Robotics”, BJU International 107, pp.187-189, 2011

[5] A. Degani, H. Choset, A. Wolf, M.A. Zenati, “Highly articulated robotic probe for minimally invasive surgery”, Proceedings of IEEE International Conference on Robotics and Automation, pp.4167-4172, 2006

[6] W. Wei, X. Kai, N. Simaan, “A Compact Two-armed Slave Manipulator for Minimally Invasive Surgery of the Throat”, International Conference on Biomedical Robotics and Biomechatronics, IEEE/RAS-EMBS pp.769-774, 2006

[7] A. Bajo, L.M. Dharamsi, J.L Netterville, C.G.Garrett, N. Simaan, “Robotic-assisted micro-surgery of the throat: The trans-nasal approach”, IEEE International Conference on Robotics and Automation (ICRA), pp.232-238, 2013

[8] J. Burgner, P.J. Swaney, R.A. Lathrop, K.D. Weaver, R.J. Webster, “Debulking From Within: A Robotic Steerable Cannula for Intracerebral Hemorrhage Evacuation”, IEEE Transactions on Biomedical Engineering, vol.60, no.9, pp.2567-2575, 2013

[9] A. Rané, G. Y. Tan, and A. K. Tewari, “Laparoendoscopic single-site surgery in urology: is robotics the missing link?”, BJU International, pp. 1041–1043, 2009

[10] A. Bajo, R.E. Goldman, W. Long, D. Fowler, N. Simaan, “Integration and preliminary evaluation of an Insertable Robotic Effectors Platform for Single Port Access Surgery”, IEEE International Conference on Robotics and Automation (ICRA), pp.3381, 3387, 2012

[11] J. Shang, D.P. Noonan, C. Payne, J. Clark, M. H. Sodergren, A. Darzi, G.Z. Yang, “An articulated universal joint based flexible access robot for minimally invasive surgery”, IEEE International Conference on Robotics and Automation (ICRA), pp.1147-1152, 2011

[12] G. Tortora, T. Ranzani, I. De Falco, P. Dario, A. Menciassi, "A Miniature Robot for Retraction Tasks under Vision Assistance in Minimally Invasive Surgery", Robotics 3, no. 1: 70-82, 2014

[13] C. Laschi, M. Cianchetti, “Soft Robotics: new perspectives for robot bodyware and control”, Frontiers in Bioengineering and Biotechnology, 2(3), 2014

[14] A. Loeve, P. Breedveld, J. Dankelman, “Scopes too flexible...and too stiff”, *Pulse*, IEEE, vol. 1, no. 3, pp. 26 -41, 2010

[15] K. Smith, W. M. Kier, “Trunks, tongues, and tentacles: Moving with skeletons of muscle”, American Scientist 77 (1), pp. 28-35, 1989

[16] I. Walker, “Some issues in creating “invertebrate” robots”, International Symposium on Adaptive Motion of Animals and Machines, 2000

[17] G. Immega, K. Antonelli, “The ksi tentacle manipulator”, IEEE International Conference on Robotics and Automation, vol. 3, pp. 3149-3154 vol.3, 1995

[18] W. McMahan, B. Jones, I. Walker, “Design and implementation of a multi-section continuum robot: Air-octor”, IEEE/RSJ International Conference on Intelligent Robots and Systems, pp. 2578–2585, 2005

[19] C. Laschi, B. Mazzolai, M. Cianchetti, L. Margheri, M. Follador, P. Dario, “A Soft Robot Arm Inspired by the Octopus”, Advanced Robotics (Special Issue on Soft Robotics), 26 (7) pp. 709-727, 2012

[20] http://www.stiff-flop.eu/

[21] N.G. Cheng, M.B. Lobovsky, S.J. Keating, A.M. Setapen, K.I. Gero, A.E. Hosoi, K.D. Lagnemma, “Design and Analysis of a Robust, Low-cost, Highly Articulated manipulator enabled by jamming of granular media”, IEEE International Conferrence on Robotics and Automation (ICRA), 2012

[22] M. Cianchetti, T. Ranzani, G. Gerboni, I. De Falco, C. Laschi, A. Menciassi, “STIFF-FLOP Surgical Manipulator: mechanical design and experimental characterization of the single module”, Proceedings of IEEE/RSJ International Conference on Intelligent Robots and Systems (IROS), 2013

[23] R. K. Mishra, “Laparoscopic Hernia Repair”, chap. 3, p. 47, 2013.

[24] I. De Falco, M. Cianchetti, A. Menciassi, “A soft and controllable stiffness manipulator for minimally invasive surgery: preliminary characterization of the modular design”, accepted for Annual International Conference of the IEEE Engineering in Medicine and Biology Society (EMBC), 2014

Manipulability of Robotic Catheters

Phuong Toan Tran*, Emmanuel Vander Poorten*, Gabrijel Smoljkic*, Caspar Gruijthuijsen*,
Paul Herijgers†, Dominiek Reynaerts*, Jos Vander Sloten*
*Department of Mechanical Engineering, KU Leuven,
†Experimental Cardiac Surgery, University Hospital Leuven, Leuven, Belgium

***Abstract*—For the last decades, the interest for the development and application of continuum robots within the field of minimally invasive surgery has gained in popularity, as the compliance of such robots contributes to the patient safety when operating in delicate environments. However, due to the complex interaction with their surrounding environment and the absence of a closed-form inverse kinematics, precise position control remains challenging. This abstract presents a finite difference approach that uses a quasi-static predictive model to estimate and solve the differential kinematics of robotic catheters in a constrained environment. Preliminary analysis is performed in a simulation environment to characterize the kinematic performance of robotic catheters.**

I. Introduction

For the last years, the interest for continuum robots has significantly increased in the scientific community. In particular, continuum robots are gaining in popularity in the field of minimally invasive surgery, where their ability to bend and conform to complex, deformable and delicate environments contributes to make the operation safer. However, their intrinsic compliance also makes precise position control of such robots difficult.

With traditional robots made of rigid links, the inverse kinematics of the robot can be expressed in a closed form and thus can be solved to achieve precise position control. However, this is not the case for the kinematics of continuum robots, as the robot pose depends on the complex interaction between the robot and the environment. The nature of this interaction being specific to the surgical application, this paper focuses on endovascular interventions where a robotic catheter is inserted from a single vascular access site and navigates through a constrained environment – the vasculature – until reaching a target location. In particular, TAVI (transcatheter aortic valve implantation) aims to treat stenosis of an aortic valve by implanting a stent-mounted bioprosthetic valve delivered on-site by a catheter. Departing e.g. from the femoral artery, the catheter navigates up to the aorta and the aortic arch until reaching the stenotic native valve where the implant is released [1]. In such scenario, as the catheter advances in the vasculature, it exerts forces on the environment because of its actuation, thus deforming the environment, but is also subject to the environmental forces that tend to bend and deform the catheter to constrain it inside the vasculature geometry. These complex interaction forces are distributed along the catheter and depend on the vessel and catheter geometry, as well as their respective material properties. A correct and precise formulation of the kinematics of continuum robots evolving in such constrained environment should then incorporate all these factors.

Previous work in the literature focuses on solving the differential kinematics of continuum robots, as it can be expressed with a set of differential equations relating the external and internal forces acting on the robot to the robot pose [2]–[4]. Although the Cosserat rod theory from which this set of differential equations is derived can take into account the distributed external forces acting along the entire robot shaft, these methods are practically limited to the consideration of external forces only acting on the catheter tip. The measure of the distributed force interactions along the entire catheter would indeed require a sensitive skin with a high resolution and accuracy over the whole catheter surface, which is beyond the current state of the technology.

Other groups focused on autonomous steering based on alternative sensory information (such as position sensing based on electromagnetic trackers) to help steering the catheter when reaching a bifurcation [5]–[7]. However, these methods focus on controlling the catheter tip, thus neglecting the complex interaction that can arise over the rest of the catheter body. Current commercial system, such as the Niobe Magnetic Navigation System (Stereotaxis) or the Sensei Robotic System (Hansen Medical), present the same limitations.

This paper proposes a finite difference approach to estimate the differential kinematics of a robotic catheter based on a quasi-static predictive model [8]–[12] that incorporates the complex interaction between the environment and the whole body of the robotic catheter. This model estimates the changes of the catheter shape and interaction forces resulting from specific changes in the robot joint variables. The estimated catheter shape and interaction forces are iteratively computed based on a minimum argument of the system's (catheter and environment) energy. This model uses a pre-operative geometrical model and lumped material model of the vasculature in which the vasculature surface is spanned with orthogonal linear springs. Gravity is incorporated and friction is described by the Coulomb friction model. The catheter is represented as series of rigid beams that are interconnected by torsional springs that represent the intrinsic bending stiffness of the catheter. When a change in the robot joint variables occurs, the catheter-vasculature system will tend to evolve ("relax") towards a new state of equilibrium that corresponds to a minimum energy state of the whole system. Such a model can then be used to cope with the lack of sufficient sensory information and estimate the differential kinematics of the robotic catheter.

In the remaining of this paper, Section II details the proposed finite difference approach for solving the differential kinematics of a robotic catheter navigating inside a vasculature and characterizing its manipulability. Section III presents results of the described method in simulation. Finally, section

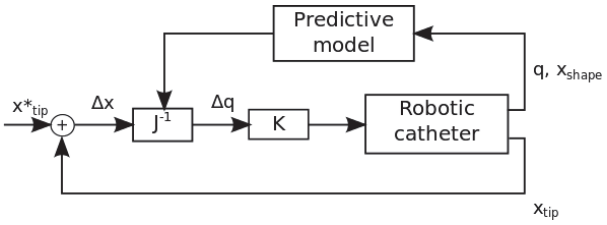

Fig. 1. Control scheme incorporating the estimated Jacobian $\hat{J}$. The current shape $\boldsymbol{x_{shape}}$ and state $\boldsymbol{q}$ of the catheter are sent to the predictive model to estimate the Jacobian matrix $\hat{J}$ of the system. The deviation $\boldsymbol{\Delta x} = \boldsymbol{x^*_{tip}} - \boldsymbol{x_{tip}}$ is calculated by comparing the current position $\boldsymbol{x_{tip}}$ of the catheter tip to its desired position $\boldsymbol{x^*_{tip}}$. This deviation is then corrected with the joint actuations $\boldsymbol{\Delta q} = \hat{J}^{-1}\boldsymbol{\Delta x}$, which are scaled by K before being sent to the robot. Note that care should be taken to account for scenario where J becomes close to singular.

IV concludes by discussing directions for future developments.

II. Finite difference approach for differential kinematics of robotic catheters

A. Jacobian estimation

Obtaining an accurate kinematic map of the robotic catheter in a constrained vascular environment requires knowledge of the interactions between the catheter and the environment. The quasi-static predictive model described in [8]–[12] is used to estimate the changes of the catheter shape and interaction forces resulting from specific changes in the robot joint variables. Since the input joint variables used by the predictive model depend on the type and possible degrees of freedom (DoFs) of the robot, we focus on three actuations that are typical in robotically steered catheters : catheter tip bending q_b, catheter rotation q_r and catheter insertion and retraction q_t. By virtually imposing finite movements (i.e. finite changes in the robot joint variables) in the predictive model and recording the resulting predicted changes of the catheter shape, it is possible to estimate a Jacobian matrix to solve the differential kinematics of the robot. Focusing on point position control, the estimated Jacobian matrix J linearly relates the changes in the joint variables $\boldsymbol{\Delta q} = (\Delta q_t, \Delta q_r, \Delta q_b)^t$ and changes in the Cartesian position of the to-be-controlled point $\boldsymbol{\Delta x} = (\Delta x, \Delta y, \Delta z)^t$ as follows:

$$\boldsymbol{\Delta x} = J\boldsymbol{\Delta q} \tag{1}$$

Thus, by locally probing the predictive model with different input actions, such as $\boldsymbol{\Delta q_0} = (\Delta q_t, 0, 0)$, $\boldsymbol{\Delta q_1} = (0, \Delta q_r, 0)$ and $\boldsymbol{\Delta q_2} = (0, 0, \Delta q_b)$, it is possible to acquire for each state of the catheter-vessel system an estimated input-output model in the form of a Jacobian matrix :

$$\hat{J} = \left[\frac{\boldsymbol{\Delta x_0}}{\Delta q_t} \quad \frac{\boldsymbol{\Delta x_1}}{\Delta q_r} \quad \frac{\boldsymbol{\Delta x_2}}{\Delta q_b}\right] \tag{2}$$

with $\boldsymbol{\Delta x_0}$, $\boldsymbol{\Delta x_1}$ and $\boldsymbol{\Delta x_2}$, the finite changes in $\boldsymbol{x}$ resulting respectively from $\boldsymbol{\Delta q_0}$, $\boldsymbol{\Delta q_1}$ and $\boldsymbol{\Delta q_2}$. This estimated Jacobian matrix $\hat{J}$ can then be used to decide appropriate actions of the robotic catheter in a conventional control scheme (see Fig.1).

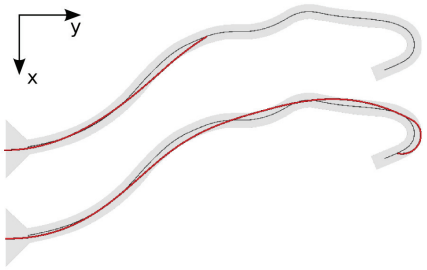

Fig. 2. Catheter insertion with position control of the catheter tip to follow the vessel centerline, with a zero friction coefficient. The catheter shape and the vessel centerline are respectively represented by red and black lines. Top : insertion length of 330mm. Bottom: insertion length of 695mm.

B. Manipulability analysis

In classical robotics, the concept of manipulability refers to the ability of a kinematic chain to rapidly adjust its end-effector in any direction of its workspace in response to given velocities in its current state. Given the joint variables $\boldsymbol{q}$, the Jacobian matrix $J(\boldsymbol{q}) \in \mathbf{R}^{m\times n}$ and its singular value decomposition $J(\boldsymbol{q}) = U\Sigma V^t$ where $U = [\boldsymbol{u_1}, ..., \boldsymbol{u_m}] \in \mathbf{R}^{m\times m}$, $V \in \mathbf{R}^{n\times n}$ and $\Sigma \in \mathbf{R}^{m\times n}$ is a diagonal matrix containing the m singular values σ_i $(i = 1, ..., m)$ of J, the manipulability of the robot at a state $\boldsymbol{q}$ is defined as [13]:

$$w_m = \sqrt{\det(J(\boldsymbol{q})J^t(\boldsymbol{q}))} = \prod_{i=1}^{m}\sigma_i \tag{3}$$

The Jacobian matrix can be geometrically interpreted as a mapping that transforms a unit hypersphere in differential joint space into an ellipsoid in differential workspace with principal semi-axes $\sigma_i\boldsymbol{u_i}$. This ellipsoid is called the manipulability ellipsoid. To calculate the manipulability ellipsoid resulting from the mapping of a non-unit hypersphere, the Jacobian needs to be normalized by the radius of the hypersphere as described in [13]. While the manipulability is proportional to the volume of the manipulability ellipsoid, the inverse of the condition number of the Jacobian matrix

$$w_c = \frac{\min_i\sigma_i}{\max_i\sigma_i} \tag{4}$$

gives a measure of the directional uniformity of the manipulability ellipsoid.

In the context of a finite difference approach estimating the differential kinematics, the manipulability ellipsoid corresponding to a certain robot state can be derived from the estimated Jacobian $\hat{J}$ (Section II-A), or directly built by probing the hypersphere in differential joint space using the above mentioned predictive model and recording the corresponding changes in workspace.

III. Results

The aforementioned predictive model is used as a simulation environment in combination with the control scheme described in Fig.1 to virtually steer the tip of a robotic catheter along a predefined trajectory. Similar to [12], a 2D virtual vasculature is generated by projecting in a plane the 3D shape of an aorta acquired with MR scans. The target trajectory is

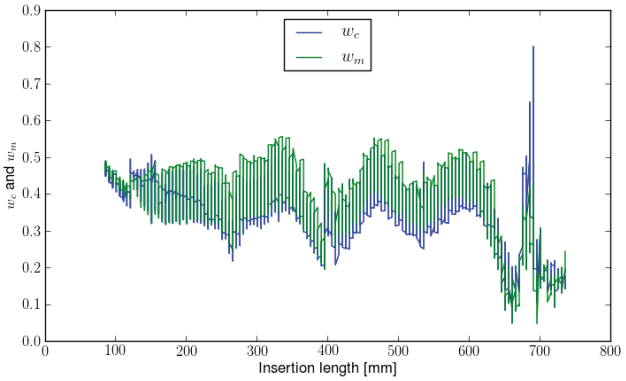

Fig. 3. Kinematic indices w_c and w_m during a controlled insertion of the robotic catheter in the vessel with the vessel centerline as target. Friction coefficient is zero.

chosen as the centerline of the resulting 2D vessel (see Fig. 2). The catheter is modeled as a 2-DoFs continuum robot with insertion and tip bending. The length of the local actuator at the catheter distal tip is 70mm.

We first present results without simulating friction in the environment. Fig. 3 shows the kinematic indices w_c and w_m computed from the estimated Jacobian $\hat{J}$ during the catheter insertion with a zero friction coefficient and $\Delta q_t = 1$mm and $\Delta q_b = 1$degree. Both indices are following the same trend, oscillating between 0.2 and 0.55 until reaching the aortic arch (which correspond at an insertion length of 650mm) where both indices drop because of the constraints the environment imposes on the catheter. This can be illustrated by Fig.4. As mentioned in Section II-B, the Jacobian can be geometrically interpreted as a mapping between a hypersphere in differential joint space and an ellipsoid in differential workspace. In our 2D case without friction, the probing circle is shown in the left part of Fig.4. The resulting mapping in differential workspace for different catheter states (insertion length of 330mm and 695mm, as shown in Fig.2) in the middle and right parts of Fig.4. The yellow curves are directly built from the probing in joint space, while the green curves results from the singular decomposition of the estimated Jacobian $\hat{J}$. The probing order is indicated by the numbered annotations. When the constraints imposed by the environment on the catheter are relatively small (top part of Fig.2 and middle part of Fig.4), the ellipsoid is symmetric and the approach described in Section II-A provides a good approximation of the actual Jacobian matrix. However, when constraints imposed by the environment become large (bottom part of Fig.2 and right part of Fig.4), w_c and w_m are relatively small and the ellipsoid flattens, indicating that there is one direction of preference motion in joint space. In this case, as the local actuator of the catheter lies against the vasculature, bending is more difficult than insertion or retraction. The ellipsoid is then asymmetric, denoting a different behavior in insertion and retraction. In such case, approximating the Jacobian with the method described in Section II-A might not be sufficient. More involved approaches might then be required to take this phenomenon into account.

Fig.5 shows the probed manipulability ellipsoid for different probing radii r_s in differential joint spaces for an inserted length of 695mm.

Finally, Fig.6 presents the estimated manipulability ellip-

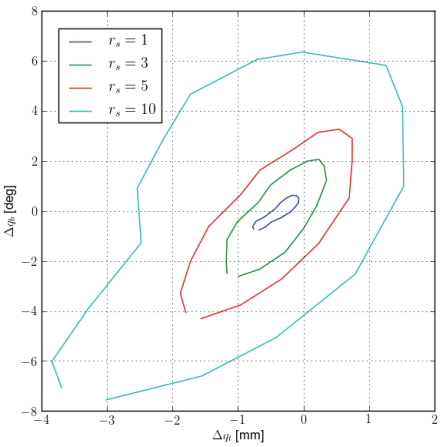

Fig. 5. Manipulability ellipsoid of the robotic catheter estimated by probing hyperspheres of different radii r_s in differential joint space for an inserted length of 695mm.

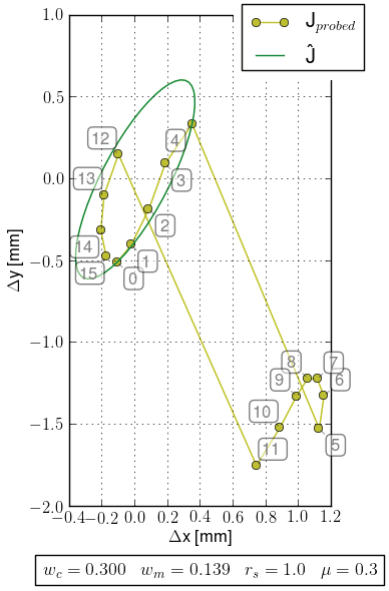

Fig. 6. Manipulability ellipsoid computed from the estimated Jacobian $\hat{J}$ (green) and manipulability ellipsoid resulting from a systematic probing of the unit circle in differential joint space (yellow) for an inserted length of 710mm and a friction coefficient of 0.3. The order of probing on the unit circle is as in Fig.4. The values of w_c and w_m are respectively 0.3 and 0.139.

soids when friction (friction coefficient 0.3) is incorporated in the predictive model and for an inserted length of 710mm. For such insertion length, the catheter tip is located at the same position as the case without friction but with a 695mm insertion length. As in Fig.4, the ellipsoids in Fig.6 result from probing a unit circle in differential joint space. When incorporating friction, the probed ellipsoid (yellow curve) clearly separate the insertion case from the retraction case. We hypothesize that this might be due to the fact that, in a very constrained environment, a retraction of the catheter causes the tip to first move forwards before going backwards. Although the friction is expected to increase the asymmetry of the ellipsoid, the reasons for such behavior remains unclear to the authors. This might indicate the presence of artefacts in the predictive model that is used.

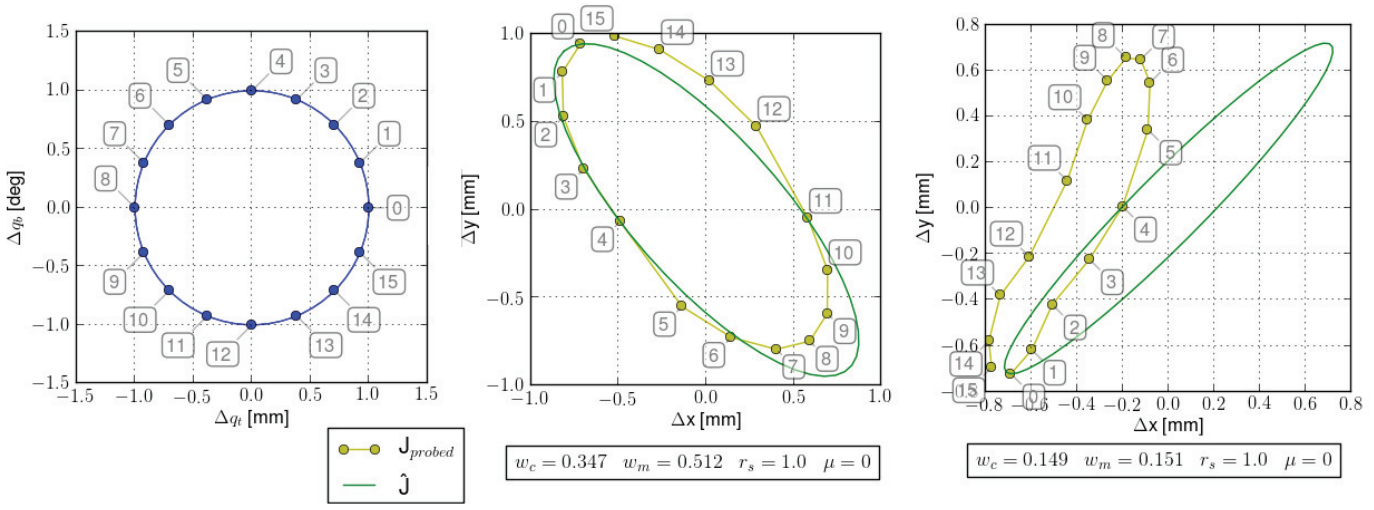

Fig. 4. Estimation of the manipulability ellipsoids of the robotic catheter with no friction. The ellipsoids are drawn in a frame parallel to the world coordinate frame used during simulation (see Fig.2). The direction of positive bending is parallel to the z axis of the world coordinate frame. Left : unit circle of radius r_s in differential joint space $(\Delta q_t, \Delta q_b)$. Middle : Manipulability ellipsoid (green), $w_c = 0.347$ and $w_m = 0.512$ computed from the estimated Jacobian $\hat{J}$ and manipulability ellipsoid resulting from a systematic probing of the unit circle in differential joint space (yellow) for an inserted length of 330mm (see top of Fig.2). The order of the probing is indicated by the annotated numbers. Right : idem, but for an inserted length of 695mm (see bottom of Fig.2). The values of w_c and w_m are respectively 0.149 and 0.151.

IV. Conclusion

In this paper, a finite difference approach has been presented to estimate and solve the differential kinematics of a robotic catheter constrained in a vascular environment. An analysis of the manipulability of robotic catheters in such environment showed that, in highly constrained environments, the manipulability of the robots becomes asymmetric, thus calling for the development of more involved control schemes. Although the analysis contained in this paper is limited to the control of the catheter tip, the method can be extended for shape control as it can be applied for any point of the catheter – given that the catheter incorporates enough local DoFs to control its shape. Future work includes the development of an experimental setup including a deformable mock-up and robotic catheter to investigate further and validate the proposed approach.

Acknowledgment

This research was supported by the EU's Seventh Framework Programme under GA No. 601021 (CASCADE).

References

[1] C. R. Smith, M. B. Leon, M. J. Mack, D. C. Miller, J. W. Moses, L. G. Svensson, E. M. Tuzcu, J. G. Webb, G. P. Fontana, R. R. Makkar, M. Williams, T. Dewey, S. Kapadia, V. Babaliaros, V. H. Thourani, P. Corso, A. D. Pichard, J. E. Bavaria, H. C. Herrmann, J. J. Akin, W. N. Anderson, D. Wang, and S. J. Pocock, "Transcatheter versus surgical aortic-valve replacement in high-risk patients." *The New England journal of medicine*, vol. 364, no. 23, pp. 2187–98, Jun. 2011.

[2] D. C. Rucker and R. J. Webster, "Computing Jacobians and compliance matrices for externally loaded continuum robots," in *2011 IEEE International Conference on Robotics and Automation*, no. 3. IEEE, May 2011, pp. 945–950.

[3] D. C. Rucker and R. J. Webster III, "Statics and Dynamics of Continuum Robots With General Tendon Routing and External Loading," *IEEE Transactions on Robotics*, vol. 27, no. 6, pp. 1033–1044, Dec. 2011.

[4] J. Burgner, D. C. Rucker, H. B. Gilbert, P. J. Swaney, P. T. Russell, K. D. Weaver, and R. J. Webster, "A Telerobotic System for Transnasal Surgery." *IEEE/ASME transactions on mechatronics : a joint publication of the IEEE Industrial Electronics Society and the ASME Dynamic Systems and Control Division*, vol. 19, no. 3, pp. 996–1006, Jun. 2013.

[5] R. S. Penning, J. Jung, N. J. Ferrier, and M. R. Zinn, "An evaluation of closed-loop control options for continuum manipulators," in *2012 IEEE International Conference on Robotics and Automation*. IEEE, May 2012, pp. 5392–5397.

[6] J. Jayender, M. Azizian, and R. Patel, "Autonomous Image-Guided Robot-Assisted Active Catheter Insertion," *IEEE Transactions on Robotics*, vol. 24, no. 4, pp. 858–871, Aug. 2008.

[7] C. Ji, Z.-G. Hou, and X.-L. Xie, "Guidewire navigation and delivery system for robot-assisted cardiology interventions," in *IEEE 10th International Conference on Cognitive Informatics and Cognitive Computing (ICCI-CC'11)*. IEEE, Aug. 2011, pp. 330–335.

[8] M. K. Konings, E. B. van de Kraats, T. Alderliesten, and W. J. Niessen, "Analytical guide wire motion algorithm for simulation of endovascular interventions." *Medical & biological engineering & computing*, vol. 41, no. 6, pp. 689–700, Nov. 2003.

[9] T. Alderliesten, M. K. Konings, and W. J. Niessen, "Simulation of minimally invasive vascular interventions for training purposes." *Computer aided surgery : official journal of the International Society for Computer Aided Surgery*, vol. 9, no. 1-2, pp. 3–15, Jan. 2004.

[10] ——, "Robustness and complexity of a minimally invasive vascular intervention simulation system," *Medical Physics*, vol. 33, no. 12, p. 4758, 2006.

[11] ——, "Modeling friction, intrinsic curvature, and rotation of guide wires for simulation of minimally invasive vascular interventions." *IEEE transactions on bio-medical engineering*, vol. 54, no. 1, pp. 29–38, Jan. 2007.

[12] G. Smoljkic, C. Gruijthuijsen, J. V. Sloten, and E. V. Poorten, "Towards Intraoperative Use of Surgical Simulators : Evaluation of Catheter Insertion Models," in *3rd Joint Workshop on New Technologies for Computer/Robot Assisted Surgery*, Verona, 2013, pp. 45–47.

[13] T. Yoshikawa, "Manipulability of Robotic Mechanisms," *The International Journal of Robotics Research*, vol. 4, no. 2, pp. 3–9, Jun. 1985.

Rapid Prototyping of Rod-Driven Continuum Robots for Medical Applications

Dennis Kundrat, Andreas Schoob, Lüder A. Kahrs, Tobias Ortmaier
Institute of Mechatronic Systems
Leibniz Universität Hannover
30167 Hanover, Germany
dennis.kundrat@imes.uni-hannover.de

***Abstract*—The application of continuum robots in robotic surgery has evolved within recent years. This paper presents preliminary steps towards rapid prototyping of customized rod-driven continuum robots. Design, fabrication, and preliminary results are described. Objectives are adaptive and cost-effective fabrication of prototypes as well as decreased production time.**

I. Introduction

Minimally invasive surgery has evolved in a variety of surgeries. More recently, the evolution resulted in disciplines such as natural orifice transluminal endoscopic surgery (NOTES), robotic surgery (e.g. da Vinci, Intuitive Surgical, CA, USA) or use of task-specific devices for treatment and diagnosis.
The need for improved intra-operative dexterity, stability, and flexibility for surgical instruments is associated with on-going developments.
This work addresses an alternative design and fabrication of rod-driven continuum robots as potential device for medical applications. The objective of this work is to analyse the hypothesis: customized rod-driven continuum robots for medical applications are able to manufacture with rapid-prototyping methodology exclusively?
We present preliminary steps towards customized continuum segments with modularized design fabricated with a combination of recent rapid prototyping technologies.

II. State of the Art

In this section we describe state of the art design concepts and principles of existing systems for medical and industrial applications. Furthermore, we introduce our associated endoscopic robot and requirements of the recent development.

A. Design Concepts

Continuum robots represent a physical structure with typically constant curvature comprising actuated and adaptable (multiple) backbones. Mechanical compliance to external loads resulting from interaction with the environment (e.g. in anatomical cavities) is another remarkable feature. Walker highlights the combination of aforementioned properties to utilize this type of robot in surgical applications in order to perform with superior dexterity as well as gentle interaction [1].
A wide range of design principles is currently existing and an excerpt is presented briefly in the following. Systems based on a high number of serially and rigidly linked elements (i.e. snake-like units or pseudo continuum robots) have slowly reached steps to commercialization [2], [3].
Recent continuum robots are classified with regard to actuation principles such as external, internal, and hybrid methods. Simaan et al. developed an externally rod-driven continuum robot for delicate tasks in laryngeal and urological applications comprising a fixed central backbone and three concentrically actuated secondary backbones [4], [5]. Further approaches employ tendon-actuated springs [6] or inflated flexible tubes [1].
A recent principle is based on the combination and telescoping of concentric NiTi tubes (active cannulas) with task-specific curvatures [7]. Roppenecker et al. propose monolitic designs based on external tendon-driven structures with different shapes and structures (e.g. springs or flexible hinges) additively manufactured with selective laser sintering (SLS) [8]. However, material properties in combination with size constraints limit durability and force transmission.
Further devices employ intrinsic actuation. The use of three integrated pneumatic chambers in combination with a separate sheath and central channel for stiffness adaptation forms the fundamental design of the STIFF-FLOP project [9]. This principle shows a reduced internal lumen due to channels and chambers for pneumatic actuation as well as space for granular jamming. In this regard smart memory alloy (SMA) and electro active polymers (EAP) have been used in a variety of systems [1], [10]. In general, these principles require high voltage or currents restricting an application inside the human body.
To the best of our knowledge no research group has addressed the presented combination of rod-driven actuation and flexible continuum structure without central backbones.

B. Development of endoscopic robot

We address an application of continuum segments in the field of endoscopic laser surgery in the laryngeal region as described in [11]. Primary objectives of the recent development considering aforementioned state of the art are:

- Compliant but stable architecture to minimize trauma and injuries to soft tissue
- Increased internal lumen for integration of instrumentation (e.g. optical fibres for laser beam delivery)
- Modularization and scalability for providing a task-specific kit
- Encapsulated combination of sheath and bending continuum

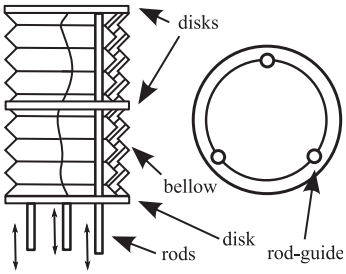

Fig. 1. Schematic drawing of exemplary design for rod-driven continuum segment with three disks and circumferentially and equally spaced rod alignment.

Our endoscopic robot consists of two continuum segments and is driven by a customized actuation unit providing four degrees of freedom (DoF) with motorized and manual actuation.

III. Materials and Methods

Based on the work presented in [11], specifications were determined regarding medical and technological constraints. We advanced the design to simplify manufacturing, increase the available lumen and optimize stiffness as well as potential biocompatibility. We derived from state of the art systems following specific requirements:

- Large internal lumen
- Diameter of less than 20 mm
- Push/pull actuation with rods
- No risk of hydraulic or pneumatic leakage
- Rapid prototyping as dominant fabrication

A. Design Overview

As described in Sec.II-A, we focus on a combination of rod-driven architecture and flexible continuum to provide an encapsulated device. The basic principle is schematically illustrated in Fig. 1. In this regard, three major design components have been identified and analysed: rod-guiding disks, design of continuum elements connecting disks, and rod-guidance in-between disks. The diameter and thickness of rod-guiding disks have been determined to 18.5 mm and 2.5 mm, respectively. Several designs have been proposed incorporating specific bellow shapes (e.g. triangular, s-shaped, and u-shaped) based on the results of [12]. Furthermore, cylindrical structures and embedded springs have been considered. We select silicone (polydimethylsiloxane (PDMS)) as continuum element due to high flexibility, simple processing, and biocompatability. Internal and external rod guidance have been considered in aforementioned designs. Reduction of friction and optimized circular bending is expected from rod guidance with additional spacing disks. This includes circumferentially aligned holes (see Fig. 1) which have been extensively proposed for tendon and rod-driven continuum robots.

B. Manufacturing

Selected designs have been manufactured by applying selective laser sintering (SLS), fused deposition modeling (FDM), and silicone casting. The manufacturing process includes three consecutive steps:

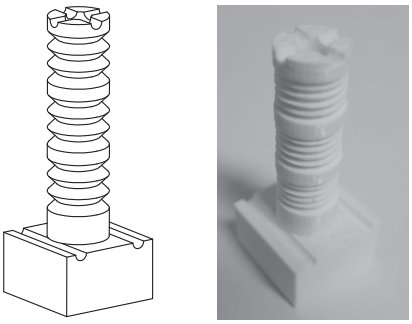

Fig. 2. CAD model and FDM prototype of exemplary core

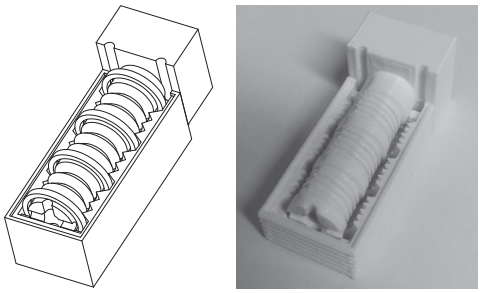

Fig. 3. Exemplary CAD model and FDM prototype with inserted SLS disks of core and drag (cope and rods removed for visualization purposes)

1) *Design of structural parts:* Dependent on the selected design (see Sec. III-A) rod-guiding disks and/or spring-connected components are specifically dimensioned, exported to STL format and fabricated with FDM (Replicator 2X, Makerbot Industries, USA) or SLS (EOS M280, EOS GmbH, Germany), respectively.
2) *Design of silicone mould:* Moulds for silicone casts were designed according to specific dimensions and geometric properties as described in Sec. III-A. In general, established methods for mould design have been applied for optimized casting. After design of the mould cavity with boolean subtraction, wall thickness of the mould cavity was examined to be larger than 1 mm in order to enable demoulding without component damage. The parting line was defined symmetrically. Afterwards, blind and open risers were added to dispense enclosed air. Consecutive silicone feeding to the mould cavity is implemented with a pouring basin on a suitable wall. Exemplary mould designs with inserted core are shown in Fig. 2 and 3.
3) *Silicone casting:* Initially, moulds are treated with releasing agent to minimize the risk of component damage while demoulding. After preparation of two-component silicone and insertion of spacing disks, the cast process is started by continuously feeding the material to the mould cavity. End disks are glued to rods. Prototypes with different properties are shown in Fig. 4.

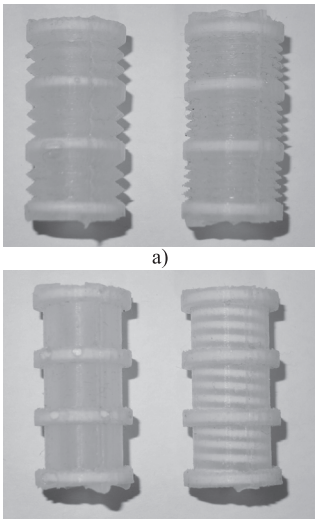

Fig. 4. Prototypes of casted continuum segments with a) different bellow geometries and b) tubular shape and embedded SLS spring

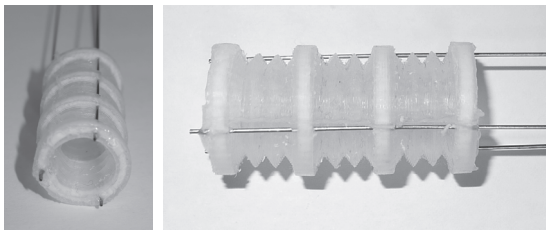

Fig. 5. Proof-of-concept prototype for experimental evaluation (outer diameter 18.5 mm) with NiTi tubes.

C. Experimental setup

A test bench was implemented to assess the bending behaviour of a single continuum module incorporating three sub-segments divided by two disks. Preliminary evaluation and proof-of-concept of the aforementioned methodology was conducted with manual actuation, i.e. translational movement of the rods.

IV. Results and Discussion

Preliminary experiments described before have been applied to the sample shown in Fig. 5 in order to characterize kinematic and mechanical boundaries. After manufacturing of structural parts and moulds the average fabrication time is approx. 3 h. Bending from 0° to 90° was achieved with manual actuation (see Fig. 6). Stiffness can be modified with structural modifications as presented in Fig. 4.

V. Conclusion

This contribution describes methods for design and manufacturing of modular rod-driven continuum segments. The proposed work-flow focuses on reduced fabrication time, modular design, and low-cost applications. To our knowledge this is the first work towards rod-driven continuum segments without central backbone. Preliminary experiments have shown proof-of-concept and further optimization is dedicated to structural design, actuation, and kinematic models.

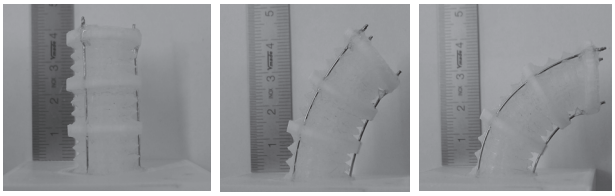

Fig. 6. In-plane bending of prototype from 0° to 90°.

Acknowledgment

This research has received funding from the European Union FP7 under grant agreement μRALP - n° 288663. We further thank Alexander Michailik and Benjamin Vollmann for their assistance in design and manufacturing.

References

[1] I. D. Walker, "Continuous backbone continuum robot manipulators," *International Scholarly Research Notices*, vol. 2013, Jul. 2013. [Online]. Available: http://www.hindawi.com/journals/isrn/2013/726506/abs/

[2] C. M. Rivera-Serrano, P. Johnson, B. Zubiate, R. Kuenzler, H. Choset, M. Zenati, S. Tully, and U. Duvvuri, "A transoral highly flexible robot: Novel technology and application," *Laryngoscope*, vol. 122, no. 5, pp. 1067–1071, May 2012.

[3] J. Shang, C. Payne, J. Clark, D. Noonan, K.-W. Kwok, A. Darzi, and G.-Z. Yang, "Design of a multitasking robotic platform with flexible arms and articulated head for minimally invasive surgery," in *IEEE/RSJ International Conference on Intelligent Robots and Systems (IROS)*, 2012, pp. 1988–1993.

[4] N. Simaan, R. Taylor, and P. Flint, "A dexterous system for laryngeal surgery - multi-backbone bending snake-like slaves for teleoperated dexterous surgical tool manipulation," in *IEEE International Conference on Robotics and Automation*, 2004, pp. 351–357.

[5] A. Bajo, R. Pickens, S. Herrell, and N. Simaan, "Constrained motion control of multisegment continuum robots for transurethral bladder resection and surveillance," in *IEEE International Conference on Robotics and Automation (ICRA)*, 2013, pp. 5837–5842.

[6] J. Mehling, M. Diftler, M. Chu, and M. Valvo, "A minimally invasive tendril robot for in-space inspection," in *IEEE/RAS-EMBS International Conference on Biomedical Robotics and Biomechatronics*, 2006, pp. 690–695.

[7] R. Webster, A. Okamura, and N. Cowan, "Toward active cannulas: Miniature snake-like surgical robots," in *IEEE/RSJ International Conference on Intelligent Robots and Systems*, 2006, pp. 2857–2863.

[8] D. Roppenecker, A. Pfaff, J. Coy, and T. Lueth, "Multi arm snake-like robot kinematics," in *IEEE/RSJ International Conference on Intelligent Robots and Systems (IROS)*, 2013, pp. 5040–5045.

[9] M. Cianchetti, T. Ranzani, G. Gerboni, I. De Falco, C. Laschi, and A. Menciassi, "STIFF-FLOP surgical manipulator: Mechanical design and experimental characterization of the single module," in *IEEE/RSJ International Conference on Intelligent Robots and Systems (IROS)*, 2013, pp. 3576–3581.

[10] I. Walker, M. Darren, A. Dawson, F. Tamar, W. Frank, C. Grasso, T. Roger, D. Hanlon, E. Hochner, M. William, F. Kier, C. Christopher, G. Pagano, D. Christopher, H. Rahn, M. Qiming, and I. Zhang, "Continuum robot arms inspired by cephalopods," in *SPIE Proceedings Vol. 5804*, 2005.

[11] D. Kundrat, A. Schoob, B. Munske, and T. Ortmaier, "Towards an endoscopic device for laser-assisted phonomicrosurgery," in *Proceedings of The Hamlyn Symposium on Medical Robotics*, 2013, pp. 55–56.

[12] J. Wilson, "Mechanics of bellows: A critical survey," *International Journal of Mechanical Sciences*, vol. 26, no. 1112, pp. 593 – 605, 1984. [Online]. Available: http://www.sciencedirect.com/science/article/pii/0020740384900134

A new strategy to build a fully modular soft manipulator for MIS

G. Gerboni, T. Ranzani, M. Cianchetti, G. Ciuti, A. Menciassi
The BioRobotics Institute
Scuola Superiore Sant'Anna,SSSA
Pisa, Italy
g.gerboni@sssup.it

***Abstract*— Soft robotics is currently considered very promising in the medical field, especially in Minimally Invasive Surgery (MIS), since it can combine high dexterity and compliance in the same manipulator, thus resulting in devices that are safer than rigid-link robots when getting in contact with tissues. However the construction, miniaturization and control of such manipulators are severally affected by the number of modules composing the whole structure. This limitation can be overcome by using a full modular architecture. In our design, the whole manipulator is thought to be built by means of several simpler, yet independent, modules, which can be easily added/removed to the manipulator, depending on the task. Each module has a fluidic elastic actuator (FEA) and it is equipped with its own actuation unit to internally control the fluidic power and generate the related movements, such as the bending/elongation of the actuator. The actuation unit comprises switching valves, a wireless microcontroller and a fluidic distribution system embedded directly into the module's soft body, thus each module results to be a free standing portion of the whole manipulator.**

I. Introduction

Research in robotics is recently moving more and more towards soft technologies. To the ultimate extent of avoiding control complexity and poor environment adaptability of conventional robots, which are traditionally built of rigid links and joints, new strategies of actuation by employing compliant and high deformable materials are becoming appealing among the robotics community [1]. Thanks to their low stiffness and high flexibility, soft actuators are sometimes more efficient in producing high displacements than conventional rigid actuators. At the same time, given their inherently compliant body, they are also safer in interacting with the environment to such an extent that they can even adsorb most of the energy when facing unexpected impacts. This characteristic is, perhaps, one of the most valuable feature of soft robots, because it allows to use highly simplified mathematical models of the actuator's behavior, which would otherwise become too computational complex given the continuity and non-linearity of the their body. Thus, in principle, their motion planner controllers can be less accurate since, when moving, the actuator will not generate serious damages to the surrounding structures. All these peculiar proprieties have recently brought the interest towards soft robots, especially regarding applications with uncertain environments and requiring the interaction with delicate objects. This is the case of surgery, Minimally Invasive Surgery (MIS) in particular, where there is the combined need for high dexterity and safe instrumentation.

Several soft robots have been developed taking Nature as a source of inspiration: the octopus arm is, above all, an explicative example that demonstrates how a high dexterous soft structure can accomplish difficult tasks, such as manipulation, squeezing and grasping, in a safe yet efficient way [1]. On the same bio-inspired trend, a flexible manipulator for MIS has been under development within the STIFF-FLOP project (http://www.stiff-flop.eu/). The STIFF-FLOP manipulator [6], differently from its SMA actuated predecessor (the OCTOPUS [1]), exploits fluids for its actuation and it employs serially connected FEAs (Fluidic Elastomeric Actuators) to form an articulating arm which is also able to continuously modulate its stiffness. FEAs are one of the most exploited strategies of actuation in soft robotics [2]. They are essentially a bulk of elastomeric material, generally silicone, which can be moved in several directions by producing the expansion of fluidic chambers embedded in various areas of the bulk [2]. These chambers are commonly inflated by supplying pressurized fluid (air, water, oil, etc.). FEAs translate the chamber's pressurization into mechanical power, thus yielding a displacement of their structure. Fig. 1a shows how the FEAs' power is managed. Besides the main fluidic power line (blue arrow) there is also an ancillary line (red arrow), i.e. the electric power line, for the fluidic power distribution among different FEA's chambers. While in conventional electric

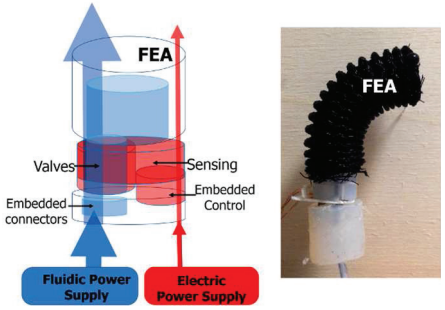

Fig.1 Left: FEA's architecture and Power Supply system. Right: Prototype of a single module performing one directional bending by means of its own actuation unit integrated at its base.

The work has been supported by the European Commission with the STIFF FLOP FP7-ICT-2011.2.1 (#287728).

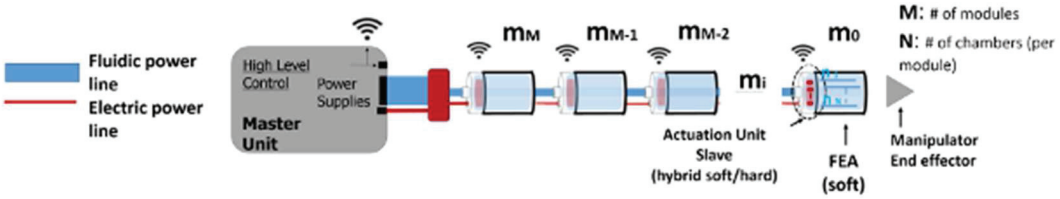

Fig.2. System architecture of a modular manipulator with FEAs.

actuators (DC/AC motors, Shape Memory Alloys, etc.) the production of mechanical work results from the conversion of the electric energy they receive from the supply, FEAs do not involve a local transduction (electric-mechanic), but they exploit all the supplied fluidic energy to produce the final work. In that sense FEAs are more efficient as actuators, and the resulting actuation is only dependent on the actuator's geometry and/or materials, and not on the energy conversion ratio. Being a secondary source, used just for control, the electric energy is supplied in a relatively small amount making this actuators even safer for a possible application in MIS devices. Additionally FEAs are extremely versatile since they can employ the fluidic power using a broad range of possible designs. But, first of all, they are relatively cheap both in terms of row materials and manufacturing/production processes, making them suitable even for disposable instrumentation.
Nevertheless, they also present a few drawbacks which are not currently turning in favor of the soft actuator's progression in the robotic field. Firstly the poor stiffness of their soft links may eventually represent a problem when considerable high forces have to be produced by the arm. To this aim, a few attempts to enhance the otherwise low rigidity of these actuators can be found in [2], in which there are examples where the compliant elastomeric material is combined with rigid fibers or rods, and also in [6], where a jamming based stiffening mechanism has been introduced and combined with the elastomeric structure. However the main limitation regarding the employment of FEAs is the fluidic power supply system itself, which notoriously requires pipes, connectors and valves that are bulky components, often made by rigid, or simply different, materials in comparison with the soft ones of the actuator. This aspect is of relevant importance when the FEAs have to be miniaturized to be implemented, for example, into small and modular devices and their dimensions become comparable or even smaller than the piping system.

Modularity is another emerging branch of robotics, according to which complex and high performing robots are just the result of a composition of several simpler units that all together can accomplish the complex actuation of the whole robot structure. This approach is quite well established for traditional rigid-link robots: Harada *et al.* in [4] reports an overview of how a modular approach can help in the construction and actuation of complex high dexterous robots inside the human body by means of smaller wireless controllable magnetically assembled units. However, while in solely electrical powered robots most of the difficulties related to the modular approach seem to be solved, in fluidic actuated robots (built with several FEAs) several issues are still open. One over all is, again, their dependence on fluidic power, which is challenging to be integrated in a fully modular system [5]. This paper presents an innovative approach in addressing the actuation of a fully modular soft manipulator made up of FEAs. An overview of the whole system concept is presented in the next paragraph (section II), while the single module's architecture, its components design and integration are explained in detail in section III. Preliminary results on the achievements of the first prototype's module are reported in section IV.

II. System Overview

As mentioned in the introduction, modular robotics allows developing high dexterity but also reliable manipulators. The strength of modularity relays in having simpler and uniform units, or modules, which can be easily connected together as well as controlled by the master unit, no matter their arrangement nor their total amount. Therefore all the units must share the input signals from the central control, as well as from the other modules, in the same way. In the case of fluidic actuators, such as FEAs, these shared signals are of both fluidic and electric kinds since two are the sources of energy they need for functioning. In the proposed architecture of a flexible and soft modular manipulator for MIS, each module has two only inputs and outputs, as in Fig.2. From the two input lines a module can gain respectively the fluidic and electric power for its actuation. The outputs, instead, serve to carry out the two power lines and make them again available for the following module. The standard method traditionally used for controlling robots made up of fluidic actuators uses a parallel instruction paradigm [2][6], where each chamber in each FEA is addressed by an externally placed proportional valve from which a long pipe reaches the specific chamber. In that way the central system controls proportionally and in a parallel all the DOFs of all the FEAs. Since each module can have up to N chambers, it then requires N valves supplied with a likewise number of pipes, which are passed through the other proximal modules. Even if this is the faster and easier solution to be implemented, as well the more intuitive approach for controlling these robots, it impedes the realization of a fully modular system with all modules with the same geometry. In modular robotics, indeed, any addition and/or subtraction of a new unit should have the minimum impact on the rest of the structure, as well as on the central system control. In the parallel control paradigm, instead, both the central system and each unit are influenced by a change in the number of units. The more M (the number of modules) changes, the more each module begins to differ from the others because of the numerous pipes passing through it. In combination to that, also the central system needs to manage more proportional lines (for the respective $N \times M$ chambers). To this purpose, a simple relation can underline the difference among the modules due to the piping system. By indicating by

m_i the *i-th* module, which is a generic unit between the distal (m_1) and the proximal (m_M) units, we can define Qi, (the number of pipes passing through the *i-th* module), as follows:

$$Q_i = (i \cdot N) - N \; ; \qquad 1 < i < M \qquad (1)$$

From (1) one can evince that with high values of *M*, either the complexity of the control system and the amount of pipes passing through the more proximal modules (Q_i) become unmanageable. Most important, any change (increase/decrease) of *M* introduces differences among different placed modules, which will not be free to be connected everywhere and every time, depending on the specific task that the final manipulator has to accomplish. To let the system becoming independent on the total number of modules (*M),* as well as on the internal chamber setting in each module (and so from *N*), the fluidic control system of each unit has to be entirely moved on board the module. In this way each unit preserves the same number of inputs/outputs, which is exactly the number of the energy sources required for its functioning. In other words, a module would become a standalone unit combining a FEA with its own fluidic control system. Moving just the valves on board the module, however, does not make it completely independent. The valve control, indeed, has still to be separately managed by the central system, by using controlling wires, which again depends on both *M* and *N* and that have to pass through the other modules anyway. To circumvent this additional dependence on the final number of controlling wires, each unit should be required to manage its set of *N* valves control locally, without the need of physical connections with the central system. Therefore, each module needs to incorporate a sort of distributed intelligence able to both communicate with the high level controller and distribute the control signals received among the unit's valves with low level embedded control loops. To satisfy this requirement we can take advantage from wireless technology, which offers the opportunity to manage the electric control signals between the main control system (the master) and each module (slave unit), as shown in Fig.2, without additional wiring. Using this control strategy only a single electric line (red line) is needed and it serves just for providing the electric energy for the internal fluidic control and it is in common for all the modules. This line would be avoided in the case of modules already equipped with batteries, as future vision. With such architecture the control paradigm shifts from a parallel instructions paradigm, where each chamber was addressed with a centralized and proportional controlled line, to a serial instructions control paradigm. In the proposed strategy all the modules receive the regulated pressure from one main line coming from the central system and then each on board valve is wireless controlled to locally direct the pressurized flow to the relative chamber.

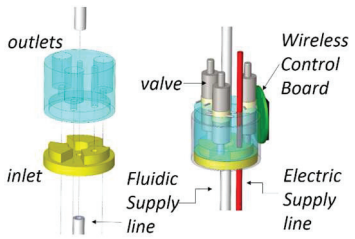

Fig. 3. Left: exploded view of the two connector's halves. Right: actuation unit assembly.

III. Single Module with Embedded Actuation Unit

The envisioned architecture of each module should present the four main components of a generic FEA as in the proposed scheme of Fig.1: the fluidic actuation system (essentially the FEA addressed by its embedded fluidic power control with valves and connectors), a perception system (with embedded sensors for monitoring the fluidic pressure, which drives the actuation), an embedded control system (with proper driving electronics to connect to the valves system as well as to the sensing part); each connected to the corresponding power source. It follows the description of how these components will be practically implemented into a single module. For the first prototype only the parts regarding the actuator and the embedded fluidic control system will be explored, leaving apart and for future developments the sensing system. As core of the actuation there is the FEA, which in the specific case is represented by a miniaturized version of the fluidic actuator of the STIFF-FLOP single module [6]. The design of this specific FEA involves a basic architecture with silicone cylinder (12 mm in diameter) with three embedded chambers, able to steer in 3D, as well as longitudinally elongate, upon the differential or simultaneous pressurization of these chambers. The cylinder is also surrounded by a bellow shaped braided sheath (black in Fig.1. right) which enhances the module performances in terms of bending and elongation capabilities. Besides the FEA, which is completely soft, the module comprises also its distributed actuation unit, which is a hybrid structure of soft and hard components, namely a silicone-embedded channeling system and metallic valves controlled by a miniaturized PCB board. The approach of combining hard components with soft structures has been already explored by other groups working on soft robotics [3], underlining the powerful of this apparently unconventional combination. By merging hybrid soft-hard components we can take the advantages as well as circumvent the disadvantages of both. Hard components are notoriously reliable, repeatable and often already optimized for a low power consumption functioning. On the other hand, soft materials are compliant, therefore safer, and high deformable so they potentially make larger displacements and, eventually produce relatively high force nevertheless the soft structure. Furthermore, given their high versatility and ease of fabrication, they can assume an infinite number of shapes and configurations depending on the specific need. In our case, the main advantages of employing hard components, such as the valves embedded in the soft body of the FEA, lies in both their stable and optimized behavior in a miniature size and their ease of interfacing with a likewise miniaturized control system.

The main constituents building up the module's actuation unit will be descripted hereinafter, while Fig. 4 presents a pictorial view of their integration.

A. Embedded connectors (single inlet-multi outlets)

According to the scheme of Fig.2 each module gains the fluidic power from the single supply line (in blue), which runs through the whole manipulator. Since the fluid has to reach all the chambers inside the FEA, at the inlet of each actuation unit a sort of ramification of the main line is necessary. In particular

each module has to produce at least *N* branches from this single line, to connect the fluid supply to each valve inlet.

Standard commercially available connectors do not offer enough geometry variety, hence a custom connector with branched channels and thought for being constructed directly into the soft material has been developed. By taking as source of inspiration the techniques used for developing microfluidic circuits [7], we optimized a slightly modified method to fabricate a custom fluidic channeling system directly integrated into the elastomeric bulk of material which is also composing the FEA. This method essentially involves the production, by molding, of the two halves of the channeling system, respectively depicted in yellow and transparent blue in Fig 3. The bottom half (yellow) has dedicated grooves on its upside, which allows the distribution of fluid towards the outputs (valve's inlets). These grooves are all connected to a central hole, which serves for connecting the inlet pipe. The top half (in blue) has three outlet ports for the valves on the upside, while it can perfectly mate the bottom half at its downside, as shown in the exploded view of Fig.3 (left). The two halves are finally hermetically sealed by pouring an additional outer layer of silicone around the two merged parts, visible in Fig.3 (right). To guarantee a minimum expansion of the inner channels due to the FEA's driving pressure, thus creating therefore negligible loading losses, the embedded connectors were developed by using a stiffer silicone in the areas surrounding the channels.

B. *Embedded valves and wireless system control*

Developing efficient and reliable but also miniaturized and soft valves is still an open issue in the state of the art [2], thus commercially available, but rigid, highly miniaturized solenoid latching two-ways valves (*Lee Products Ltd, UK*) have been selected. The choice of employing a bi-stable mechanism (latching) for the valve actuation is justified by the need of having low power consumption components to be integrated on the single module. The valves need power just for switching (open-closed passage) with a duration of 1 ms, leading to a total powering consumption of about 1.8 mJ per switch. They are small (3 mm as maximum diameter) and lightweight (300 mg each), thus up to three valves can be easily be integrated into the actuation unit of its associated FEA (close-ups of Fig.4) Given the conceived control logic, two-way valves act as simple logic gates which connect or isolate the corresponding chamber from the common line, whose pressure is proportionally regulated from the master unit. Therefore by controlling both the main pressure line and the valves, each chamber can be inflated or deflated. A preliminary test on the maximum input pressure these valves can resist in a closed state. They experimentally demonstrated to tolerate up to 15 psi (with less than 2% of leakages) of input pressure, which is far above the actuation pressure range (0-8 psi) of the current FEA.

The custom made PCB electronic board, shown in Fig 4 (center), is devoted to the low level control of each unit. The main component of the board is the miniaturized wireless microcontroller (CC2430, *Texas Instruments*, USA) which integrates a telemetry module (i.e. 2.4 GHz IEEE 802.15.4 and ZigBee® systems) and is combined to dedicated drivers (A3901, *Allegro Microsystems LLC, USA*) for the valves. The board sizes 10.8 mm in diameter and 2.3 mm in thickness and

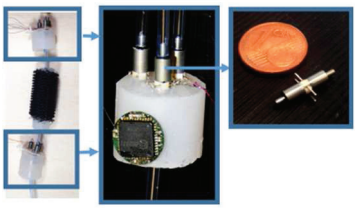

Fig.4. Actuation-unit assembly. Left: exploded of soft modular manipulator's main components (FEA and actuation units). Centre: single actuation unit with valves and embedded connectors. Right: valve.

is also able to manage data from sensing systems (due to the availability of dedicated input on the microcontroller with the ADC converter), which has not yet been integrated on the current prototype.

IV. RESULTS AND CONCLUSIONS

Fig.1 (right) reports as an illustrative example, one module which is actuated in one bending of its DOFs by means of the integrated actuation unit with valves, electronic board and embedded connectors. Future works envisage a detailed study of the static and dynamic behavior of each module for evaluating important actuation parameters, such as the accuracy, actuation speed, stability, etc. The preliminary results of the integration process proved the feasibility of the fully modular approach. In particular pressure tests on the custom made silicone embedded connectors showed their reliability in functioning as well as repeatability in fabrication. Among five connectors all fabricated with the same procedure, just one turned out to produce high pressure losses (up to 3% of the supplied pressure).

In order to build a soft manipulator which has a fully modular architecture, the current work aimed at demonstrating the integration of all the components involved in the actuation of a single independent module. Connectors, valves and embedded control circuit have been added on board of a single FEA module, composing its own actuation unit and making it independent from the structure of other modules composing the final manipulator. Furthermore, by using the wireless link for controlling each module, the single module's design and performance optimization can be done completely regardless the total amount of units which will be included into the final manipulator.

REFERENCES

[1] Laschi C, Cianchetti M. (2014)"Soft Robotics: new perspectives for robot bodyware and control." *Frontiers in Bioengineering and Biotechnology*.

[2] A. De Greef, et al. (2009)"Towards flexible medical instruments: Review of flexible fluidic actuators." *Prec. Engineering*.

[3] A. A. Stokes, et al.. (2014)"A Hybrid Combining Hard and Soft Robots." *Soft Robotics.*

[4] K. Harada, et al. (2010)"A reconfigurable modular robotic endoluminal surgical system: vision and preliminary results." *Robotica*.

[5] C. D.Onal, D. Rus. (2012). "A modular approach to soft robots." *IEEE Conference Biomedical Robotics and Biomechatronics (BioRob).*

[6] M. Cianchetti, et al. (2013)"STIFF-FLOP Surgical Manipulator: mechanical design and experimental characterization of the single module." *IEEE Conference on Intelligent Robots and Systems (IROS).*

[7] M.A. Eddings, M.A. Johnson, B.K. Gale. (2008)"Determining the optimal pdms-pdms bonding technique for microfluidic devices." *J. Micromech. Microeng.*

Session 9

Ontologies and Software

Chair: Dr. Tamás Haidegger, Óbuda University

Thursday, October 16th

14:30 – 15:30

Task Ontology Validation in Surgical Robotics

Fabrizio Boriero, Marta Capiluppi, Riccardo Muradore and Paolo Fiorini
Università degli studi di Verona
Strada le Grazie 15 - 37134 Verona
{fabrizio.boriero,marta.capiluppi,riccardo.muradore,paolo.fiorini}@univr.it

***Abstract*—In this paper we present a method introducing the validation phase in the context of robotic-assisted surgery. We propose here a method which, starting from medical knowledge, is able to perform validation of a surgical robot, either telemanipulated or autonomous, during the task execution. This validation method takes into account the operator skills and can be used for training and for evaluating the safety of a surgical tool.**

I. Introduction

The execution of a surgical task implies considerable effort and psychological stress for surgeons. New technologies appeared in the last 20 years to support nurses and surgeons within the operating rooms [1]) and the complexity of such systems is expected to increase in the early future. A possible drawback of this "technology-oriented" surgery is related to the need of coordinating in a seamless way heterogeneous hardware, software and middleware. The design of more sophisticated software architectures is the crucial point to successfully integrate heterogeneous subsystems and a possible high form of embedded intelligence.

An example of a possible solution to handle complexity in surgical robots was proposed in [2] where a robot had to insert in an autonomously way a needle in the human body (in this case a phantom). A robotic software architecture was designed to coordinate sensing, low/high level controllers, reasoning and human-robot interfaces to plan and perform the task.

In parallel with the work done by the EU projects BRICS (www.best-of-robotics.org/) and RoboEarth (www.roboearth.org) for mobile and service robotics, during the project Eurosurge (FP7-ICT-2011-7, www.eurosurge.eu) we proposed a workflow to execute simple surgical tasks exploiting the *a priori* surgical knowledge (provided by interviews with surgeons and radiologist) during the surgery planning phase [3]. The ontology-based paradigm proposed in the Eurosurge project is based on

1) a *ComponentOntology* that describes the interface of software components by means of models, and
2) a *TaskOntology* that describes the different phase of the surgical task.

Task ontology was already used in other research fields (e.g. web services [4]) but it was never applied for surgical operation planning.

From the workflow described in [5], we are able to verify that a surgical system is performing the task we designed it for. Nevertheless, we did not evaluate the surgical specifications. This means that we have to introduce the operator in the loop, in order to check if our system meets the user specifications. To this end, we introduce in this paper a basic validation procedure for surgical robots and tools. Since our architecture is component-based, the validation procedure can start from each component specification in the surgical field. In other words, to check if the system is performing correctly from the surgical specifications point of view, we apply boundaries on certain variables related to the components.

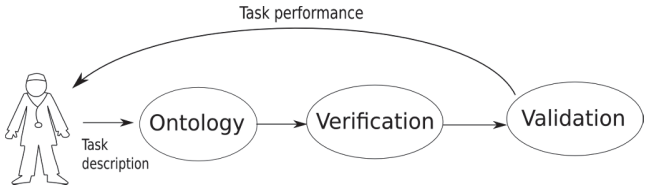

Fig. 1. This picture show the general work-flow.

We describe a robotic surgical task as a chronological sequence of actions; each action is characterized by a set of parameters that allows to define when its execution can be considered "safe" according to the best-practice in surgery (i.e. literature) and the information given by expert surgeons. Figure 1 shows the proposed workflow. The most important phase is the definition of the boundaries where the measurements collected during the execution should stay (i.e. upper and lower bounds of some physical variables). Examples of these values are the time of application of a given tool (e.g. the electrosurgical knife), the operating temperature of a cryoablation needle or the distance of a tool from a human organ. Once we have defined the steps to accomplish the operation and the parameters used to validate the task-ontology, it is possible to perform the off-line verification process as proposed in [5] and then the validation phase. *Validation*, in this context, consists of the "run-time" comparison between the nominal parameters of some variables described by surgeons and the actual measurements of the same variables collected during the execution of the operation. If the important variables remain within the defined boundaries (i.e. parameters), then the operation can be declared "valid". We call "Checker" the software module dedicated to such comparison.

This validation procedure allows to re-use the previously designed TaskOntology enriched with the boundaries related to some specified parameters. Notice that both the parameters and their safety/goodness values are specified by the medical knowledge and experience. To this end, the validation procedure can be performed online during the task execution and these parameters can be adjusted with respect to the ability and skills of the operator. Hence, the same procedure can be used in the training phase to validate the students level of expertise.

II. Scenarios

To clarify the concept proposed in the previous section, we describe few scenarios where the integration of the validation process within the planning and the execution of a robotic surgical task is important.

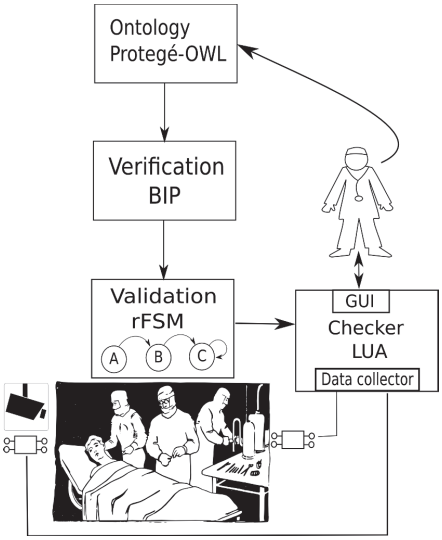

Fig. 2. This figure shows the steps managed by the software architecture during a supervised surgical intervention.

The first example is the validation of a surgical task performed by a surgeon as shown in Figure 2. An expert surgeon describes using the "OWL" language ([6]) the surgical intervention. The description contains all the steps of the operation, the boundaries of the critical values such as the minimum distance of a scalpel from an artery, the maximum execution time, etc. This description is translated by an automatic tool in a language, like BIP [7], which formally verifies the correctness of some properties like "reachability" or "deadlocks presence". Once the verification has provided a positive outcome, it is possible to translate the OWL description into a finite state machine (FSM). The FSM is a supervisor controlling the robotic architecture; a common choice for implementing the FSM in a software architecture is by using the "rFSM" toolbox [8]. When the finite state machine is created, it is possible to execute the surgical intervention.

During the training phase, a student performs the desired task and the data from the sensors available in the operating room (such as trackers, timers, force sensors) are collected by the software components that send the data to the "Checker" module that validates at run-time the execution of the student comparing his/her performance with the set of parameters (conditions and bounds) defined in the pre-operative phase. If some constraints are not respected, a graphical user interface can notify to the trainer surgeon that the actual execution differs from the correct execution. This workflow allows to create a feedback to increase the safety of the task performed.

In the second scenario we can imagine either that the robotic system is autonomous or that the user is expert. Here the same validation procedure is used for validating the robotic system during a surgical task instead of validating the skills of a student during training. As shown in Figure 3, a software system coordinates the robotic arms based on the measurements and events coming from the sensing system. The finite state machine defined in the pre-operative phase has a twofold use: it is implemented in the Validation block as before and the same FSM is also present in the Coordination block. The FSM copy is used by the Coordination block to control, monitor and coordinate the all components of the robotic architecture.

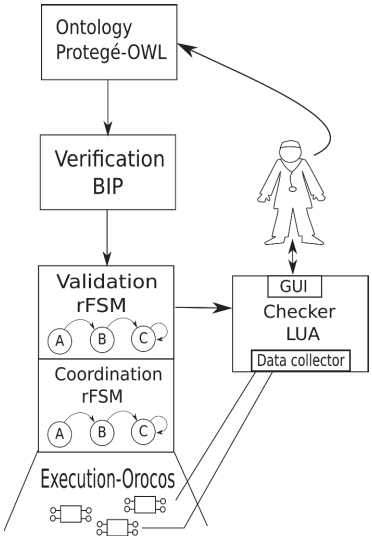

Fig. 3. This figure shows the steps managed by the software architecture during an automated surgical procedure.

To effectively handle the low-level software components it is worth designing the architecture complying with the "Component-based" paradigm ([9] [10]) such as OROCOS [11] or ROS [12]. During the execution of the procedure in this scenario, the information will be gathered from the robots during the task and the data can be compared with their nominal parameters defined in the ontology. The role of the surgeon is to supervise the operation performed by the "Checker" software module. In case of unexpected events and situation that the autonomous system cannot manage, the surgeon is informed by a graphical user interface. Then he/she can interact with the software architecture by activating emergency procedures or, at the end to the surgical procedure, updating the design parameters in the ontology for the future procedures. This update will not affect the verification procedure, which has not to be repeated.

III. Conclusion

In this article we proposed the validation phase for an ontology-driven software architecture that starts from the knowledge of the surgeons to validate the execution of a surgical intervention by the Task-ontology module. The proposed method and guidelines shall be implemented in future developments using formal methods and be tested on more realistic experiments involving surgeons and radiologists.

References

[1] K. C. Curley, "An Overview of the Current State and Uses of Surgical Robots," *Operative Techniques in General Surgery*, 2005.

[2] C. S. Marcello Bonfe, Fabrizio Boriero, Riccardo Dodi, Paolo Fiorini, Angelica Morandi, Riccardo Muradore, Liliana Pasquale, Alberto Sanna, M. Bonfe, F. Boriero, R. Dodi, P. Fiorini, A. Morandi, R. Muradore, L. Pasquale, A. Sanna, and C. Secchi, "Towards automated surgical robotics: A requirements engineering approach," *2012 4th IEEE RAS & EMBS International Conference on Biomedical Robotics and Biomechatronics (BioRob)*, pp. 56–61, Jun. 2012.

[3] E. D. Momi, P. Roberta, S. Luzie, J. Raczkowsky, F. Boriero, M. Capiluppi, and P. Fiorini, "EuRoSurge Workflow: From ontology to surgical task execution," *3rd Joint Workshop on New Technologies for Computer/Robot Assisted Surgery*, 2013.

[4] V. X. V. Tran and H. Tsuji, "OWL-T: A task ontology language for automatic service composition," in *Proceedings - 2007 IEEE International Conference on Web Services, ICWS 2007*, no. Icws, 2007, pp. 1164–1167.

[5] M. Capiluppi, L. Schreiter, Fiorini, J. Raczkowsky, and W. Heinz, "Modeling and verification of a robotic surgical system using Hybrid Input/Output Automata," *European Control Conference*, pp. 4238–4243, 2013.

[6] D. McGuinness and F. V. Harmelen, "OWL web ontology language overview," *W3C recommendation*, pp. 1–22, 2004.

[7] T. Abdellatif, S. Bensalem, J. Combaz, L. de Silva, and F. Ingrand, "Rigorous design of robot software: A formal component-based approach," *Robotics and Autonomous Systems*, vol. 60, no. 12, pp. 1563–1578, Dec. 2012.

[8] M. Klotzbuecher and H. Bruyninckx, "Hard real-time Control and Coordination of Robot Tasks using Lua," Tech. Rep., 2011.

[9] D. Brugali and P. Scandurra, "Component-based robotic engineering (part i)," *Robotics & Automation Magazine, IEEE*, vol. 16, no. 4, pp. 84–96, 2009.

[10] D. Brugali and A. Shakhimardanov, "Component-based robotic engineering (part ii)," *Robotics & Automation Magazine, IEEE*, 2010.

[11] H. Bruyninckx, "Open robot control software: the OROCOS project," in *International Conference on Robotics and Automation 2001*. IEEE, 2001, pp. 2523–2528.

[12] M. Quigley, B. Gerkey, K. Conley, J. Faust, T. Foote, J. Leibs, E. Berger, R. Wheeler, and A. Ng, "ROS : an open-source Robot Operating System," in *ICRA. IEEE International Conference on Robotics and Automation*, no. Figure 1, 2009.

A New ROS Interfaced Haptic Library with an Example of Application

Emidio Olivieri and Leonardo S. Mattos
Department of Advanced Robotics, Istituto Italiano di Tecnologia, Genova, Italy
Email: Emidio.Olivieri@iit.it, Leonardo.DeMattos@iit.it

***Abstract*—This paper presents a new C++ library for the development of software for haptics technologies. It was created to overcome limitations in existing solutions, including the lack of support for Linux for many devices and the burdensome integration with ROS. The main features of the new library include the possibility of designing and adding in real-time new haptic devices, objects and effects, the connectivity with ROS, and the availability of a Qt-OpenGL widget for the visualization of the scene. The new library outperforms existing solutions, such as CHAI3D, both in framerate and haptic smoothness. An example of application is shown, which uses the new library to introduce haptic feedback in a teleoperated laser surgery system.**

I. Introduction

This C++ based library was created to overcome limitations of already existing solutions. For example, the OpenHaptics Toolkit [1] is not well maintained, supports just a few devices and the code is not accessible. The CHAI3D libraries [2] are open source software; however they lack in the support of hardware-software combinations, for example only Force Dimension products are supported on Linux and Mac-OS; also, the graphic rendering is written in GLUT, which is not standard OpenGL; finally, the computation is too slow when processing high-resolution meshes. The Haptik Library [3] is probably the best suited open source software for general purpose but it comes without graphic rendering, which has to be manually implemented; also, the Linux port lacks many features compared with the Windows version and is not maintained.

To realize the library, a physical engine based on instantaneous force calculation has been written and basic interfaces have been designed. Then, a few examples of haptic device handlers, objects and effects have been implemented. Also, messaging over ROS [4] has been introduced to allow easy introduction of haptic devices in already existing robotic software.

II. Library Structure

The structure of the library is presented below.

A. Haptic World Class

The central class is `HapticWorld`. It coordinates all the elements that are added in real-time. It is an event-driven interface, with asynchronous methods accessible from the main program, and three timers: one of them checks if the graphic scene is rotated and accordingly updates the graphic rendering, one publishes available messages on ROS, and one computes force feedback for all the haptic devices connected.

HapticWorld class

```
class HapticWorld : public QGLWidget {
public:
  HapticWorld(QWidget* parent = 0);
  void addHapticDevice(HdHandler* device);
  void addHapticElement(HapticElement* element);
  void addRosPublisher(RosPublisher* publisher);
  void addRosSubscriber(RosSubscriber* subscriber);
  void shutdown();
protected:
  /*[...]*/
};
```

It must be noted that it is a `QGLWidget`. Thus, it can be included in Qt GUIs or shown as a separated window. If the widget is not shown, both haptic feedback and ROS messaging continue to work.

- `addHapticDevice` is used to add the handler of an haptic device which can interact with the scene.
- `addHapticElement` allows to insert a new object or effect in the world.
- `addRosPublisher` and `addRosSubscriber` include the parts intended to send and receive messages over ROS.
- `shutdown` is used to kill the haptic callback and the ROS thread before closing the application.

B. Drawable Items

Haptic devices and elements are considered drawable, in the sense that they need to be drawn somewhere in the scene.

DrawableItem abstract class

```
class DrawableItem {
public:
  DrawableItem(float alpha=1.0f);
  virtual void initGL();
  virtual void draw() = 0;
  float getAlpha();
  void setAlpha(float alpha);
protected:
  float alpha;
};
```

The abstract method `draw` must be implemented for each derived class. It is called during the OpenGL updates of `HapticWorld` (if the widget is shown).

The virtual method `initGL` should be overridden if something has to be initialized before calling the drawing method. As it is, it just returns without doing anything.

An implementation with transparency support is recommended. To allow it the floating number `alpha` was introduced. It can be set in the constructor or with the `setAlpha`

method and read from `getAlpha`. Its value ranges from 0.0, that means fully transparent, to 1.0 that stands for completely opaque.

C. ROS Publishers and Subscribers

For full integration with ROS, two abstract classes have been designed. An implementation of `RosPublisher` is used to send messages.

ROSPUBLISHER ABSTRACT CLASS

```
class RosPublisher {
public:
  virtual void advertise(ros::NodeHandle& node) = 0;
  virtual void publishAction() = 0;
};
```

The `advertise` method must be implemented to advertise a topic on the given ROS node handle. The `publishAction` method is called periodically and is used to send messages over the advertised topic. A `RosSubscriber` is used to receive messages.

ROSSUBSCRIBER ABSTRACT CLASS

```
class RosSubscriber {
public:
  virtual void subscribe(ros::NodeHandle& node) = 0;
};
```

In the implemented class, the `subscribe` method should connect a topic to a particular callback. Both interfaces allow handling several topics at the same time.

D. Haptic Device Handlers

The abstract class `HdHander` has to be implemented to use a new haptic device.

The `HdHander` has a native coordinate system, which should correspond to the built-in coordinates of the device, and a transformed one, that maps the coordinates of the haptic peripheral to the world coordinates, optionally rotating them.

HDHANDLER ABSTRACT CLASS

```
class HdHandler: public DrawableItem, public RosPublisher {
public:
  HdHandler(Mat9 iRot, Vec3 iTra, float alpha=1.0f);
  void transform(float transfMatrix[16]);
  void resetTransform();
  Vec3 getTransformedPosition();
  virtual Vec3 getPosition() = 0;
  Vec3 getTransformedVelocity();
  virtual Vec3 getVelocity() = 0;
  Mat9 getTransformedRotation();
  virtual Mat9 getRotation() = 0;
  virtual bool getButton(unsigned char i) = 0;
  virtual unsigned char getButtonNumber() = 0;
  void setTransformedForce(Vec3 force);
  virtual void setForce(Vec3 force) = 0;
  virtual void advertise(ros::NodeHandle& node);
  virtual void publishAction();
  virtual void draw();
  virtual void shutdown() = 0;
protected:
  /*[...]*/
};
```

It implements the `RosPublisher` interface. The `advertise` and `publishAction` methods are used to send on the topics `Position`, `Velocity` and `Rotation` the transformed kinematics of the haptic device, and on the topic `Buttons` a numeric value, corresponding to the combination of buttons pressed.

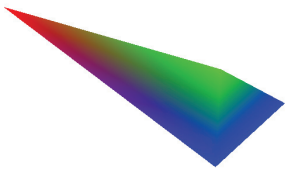

Figure 1. `HdHandler` graphic drawing – the red vertex is the position, the green one is a rotation reference (e.g. in the reference system of the Sensable Phantom Omni it points in the directions of the buttons)

There is also a default implementation of the method `draw` (that can be further overridden in the handler implementation) that paints a colored pyramid in the transformed position and orientation, as in Figure 1.

The parameters of the constructor are the initial rotation (a 3×3 matrix) and translation (a 3-D vector) of the haptic reference system, and the initial transparency of the drawing. The geometrical transformation can be altered by the `transform` methods (which requires the new 4×4 rotation matrix, column major) and reset to the initial one with the `resetTransform` method.

The abstract methods `getPosition`, `getVelocity`, `getRotation`, `getButton`, `getButtonNumber`, and `setForce` must be implemented to get the device inputs and set the force feedback in the device coordinates (the transformation is handled by the library with the `--Transformed--` methods).

The `shutdown` method is intended to release the haptic device resources before closing the program.

The only example of haptic device handler that has been implemented so far is the one for the Sensable Phantom Omni. The methods cited above are implemented in a specific way for this device, by the means of the low level functions of the OpenHaptics Toolkit. In addition the `getInstance` method is used to get a unique instance of the class, if the device is ready, otherwise a void pointer is returned.

PHHANDLER CLASS

```
class PhHandler : public HdHandler {
public:
  static PhHandler* getInstance();
  void initGL();
  void draw();
  void shutdown();
  Vec3 getPosition();
  Vec3 getVelocity();
  Vec3 getAcceleration();
  Mat9 getRotation();
  void setForce(Vec3 force);
  bool getButton(unsigned char i);
  unsigned char getButtonNumber();
protected:
  /*[...]*/
};
```

E. Objects and Effects

Objects and effects are inserted in the scene using implementations of the same abstract class, `HapticElement`.

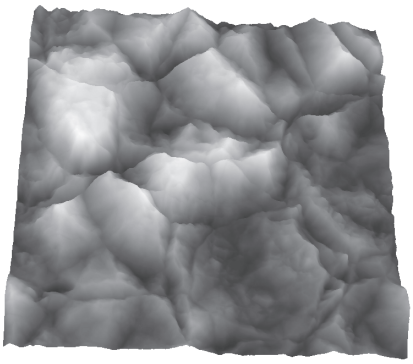

Figure 2. An example of `HeightmapElement` – a gray scale image is mapped to a depth map where darker means deeper

HAPTICELEMENT ABSTRACT CLASS

```
class HapticElement : public DrawableItem {
public:
  HapticElement(float alpha=1.0f);
  virtual Vec3 computeInteractionForce(HdHandler* h) = 0;
};
```

It is a `DrawableItem`: initial transparency is set in the constructor and the `draw` method can be implemented if needed.

The `computeInteractionForce` method should be implemented to evaluate the interaction of the object or effect with a haptic device handler, and to return the corresponding 3-D force. This method is pure virtual and thus it doesn't put any limitation: for each class implemented, the programmer is supposed to decide and to implement the physical laws.

An example of an object is a height-map mesh.

HEIGHTMAPELEMENT CLASS

```
class HeightMapElement : public HapticElement, public
    RosSubscriber {
public:
  HeightMapElement(float keepInArea=-1.0f,
                   float stiffness=-1.0f,
                   float magnetic=-1.0f,
                   float damping=-1.0f);
  void subscribe(ros::NodeHandle& node);
  void changeMap(const meshConstPtr& msg);
  Vec3 computeInteractionForce(HdHandler* h);
  void draw();
protected:
  /*[...]*/
};
```

It subscribes to a ROS topic to receive point-clouds in a certain format. Every time that one is received, the `changeMap` callback is used to change the rendered mesh, as shown in Figure 2.

The force feedback is the composition of the different force types selected in the constructor:

- `keepInArea` is the stiffness of the four transparent walls enclosing the haptic device in the vertical space over or below the mesh.
- `stiffness` is the stiffness of the mesh.
- `magnetic` is a force that pushes the device towards the surface from both sides, the further it is, the stronger the effect.
- `damping` is a damping effect, increasing below the surface.

Each force type is ignored if its value is negative.

An example of haptic effect is the device friction compensation. In this case the `draw` method is empty (it doesn't draw anything) and the force computed is proportional to the velocity of the haptic device `h` and to the `friction` coefficient to be compensated (given in the constructor).

FRICTIONCOMPENSATIONEFFECT CLASS

```
class FrictionCompensationEffect : public HapticElement {
public:
  FrictionCompensationEffect(float friction);
  virtual void draw();
  Vec3 computeInteractionForce(HdHandler* h);
protected:
  /*[...]*/
};
```

III. EXAMPLE OF APPLICATION

In this section an application example in the context of robotic laser surgery is presented. It uses the Sensable Phantom Omni both for simulating the touch of the surface (stiffness and damping effect) and to drive the surgical laser during a procedure. In this application, a virtual scapel is added to the scene and used to guide the surgical laser. Friction is reduced to provide the impression of using a real scalpel to cut the tissue. The 3-D reconstructed image of the surgical scene is sent via ROS to a `HeightmapElement` and the position of the haptic device is sent back to the laser micromanipulator. The 3-D graphical output is presented to the user as in Figure 3.

The haptic simulation of a high density mesh has outperformed CHAI3D both in framerate and in haptic smoothness.

EXAMPLE OF APPLICATION

```
int main(int argc, char *argv[]) {
  ros::init(argc, argv, "PhantomInputDevice");
  QApplication a(argc, argv);
  HapticWorld world(0);
  PhHandler* phHandler = PhHandler::getInstance();
  if(phHandler != 0) {
      world.addHapticDevice(phHandler);
      world.addRosPublisher(phHandler);
  } else {
    ROS_WARN("Phantom device not ready");
  }
  HeightMapElement hMap(-1.0f, 0.3f, -1.0f, 1.5f);
  world.addHapticElement(&hMap);
  world.addRosSubscriber(&hMap);
  FrictionCompensationEffect fcEffect(0.6f);
  world.addHapticElement(&fcEffect);
  world.show();
  a.exec(); //this ends when the window is closed
  return 0;
}
```

This example improves the work about haptic shape perception of 3-D reconstructed surface for laser surgery presented in [5] adding visual feedback. We believe that giving visual and haptic feedback together during laser surgery will increase the surgeons' hand-eye coordination and thus improve the safety of the surgical procedure.

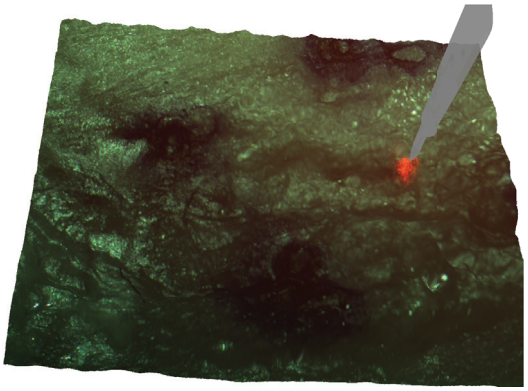

Figure 3. Example of application built with the library

IV. Conclusion

A new haptic library and an example of use have been presented. This library makes use of very generic interfaces, well suited for the addition of new device handlers, objects and effects. The connection with ROS is easy and the library outperforms exisiting solutions such as the CHAI3D both in terms of framerate and haptic smoothness when processing high density meshes. The example shown uses the new library to introduce haptic feedback in a robotic laser surgery system.

Future improvements to this library include the possibility to use two Phantoms at the same time, writing new haptic handlers for different devices, adding torque support. New objects and effects to be used in the scene will also be written. This library will be distributed for free or as open software for the benefit of the community.

Acknowledgment

Funding from the EU FP7 under grant agreement RALP n 288663.

References

[1] B. Itkowitz, J. Handley, and W. Zhu, "The OpenHaptics™ Toolkit: A Library for Adding 3D Touch™ Navigation and Haptics to Graphics Applications," in *First Joint Eurohaptics Conference and Symposium on Haptic Interfaces for Virtual Environment and Teleoperator Systems (World Haptics 2005)*. IEEE, March 2005, pp. 590–591.

[2] F. Conti, F. Barbagli, D. Morris, and C. Sewell, "CHAI: An Open-Source Library for the Rapid Development of Haptic Scenes," Hands-On-Demo at the World Haptics Conference, March 2005.

[3] M. De Pascale and D. Prattichizzo, "The Haptik Library," *IEEE Robotics & Automation Magazine*, vol. 14, no. 4, pp. 64–75, December 2007.

[4] M. Quigley, K. Conley, B. Gerkey, J. Faust, T. Foote, J. Leibs, R. Wheeler, and A. Y. Ng, "Ros: an open-source robot operating system," in *ICRA workshop on open source software*, vol. 3, no. 3.2, 2009, p. 5.

[5] E. Olivieri, A. Schoob, L. A. Kahrs, and L. S. Mattos, "Haptic shape perception of 3-D reconstructed surface for laser surgery," in *Workshop on Robotic Microsurgery and Image-Guided Surgical Interventions at the 2014 IEEE International Conference on Biomedical Robotics and Biomechatronic (BioRob 2014)*, August 2014, p. 16.

Towards Open Source Surgical Robotics

S. Jordán, Á. Takács, J. Tar, I. Rudas and T. Haidegger*

Antal Bejczy Center for Intelligent Robotics, Óbuda University, Budapest, Hungary

*also with the Austrian Center for Medical Innovation and Technology (ACMIT), Wiener Neustadt, Austria

{jordan@irob.; takacs@irob.; tar@nik.; rudas@; haidegger@irob.}uni-obuda.hu

***Abstract*—As the field of Computer-Integrated Surgery is becoming more mature, initiatives arise to harmonize research, and provide widely accepted de facto standards and platforms facilitating the sharing of knowledge and know-how. Open source projects offer great opportunity to extend the reach of a small community, thus numerous projects were started recently to develop a core hardware and software infrastructure for the needs in the field the surgical robotic. This paper provides a brief overview of the most important platforms and initiatives based on their availability, functions and active support of the user group.**

I. Introduction

Robot manufacturers consider hardware design and software programs their key asset, protecting it in various ways, especially in highly competitive areas, such as medical robotics. However, the research community definitely needs accessible platforms and solutions to achieve consensus regarding future development. High-level robot controllers, such as the Real-Time Application Interface (RTAI) for Linux have already been available [1]. Recently, a much appreciated rise of the open source efforts can be witnessed in the domain of Computer-Integrated Surgery (CIS); both public investment resulted in general open know-how, and some key industrial stakeholders decided to support these efforts.

II. Medical Robot Software

In this work, free and open source options are reviewed, where one has complete control over the software components, which allows customizations of the program code. In addition, there usually exists a developer community, which continuously develops and maintains the software.

A. 3D Slicer

3D Slicer[1] is probably the most popular open source software that can be used for image processing and visualization, particularly for medical images [2]. The software is available for Windows, Linux and Mac OS X. The operation of the Slicer 3D relies on the NA-MIC kit and other software components such as Tcl/Tk, VTK and ITK [3]. VTK (Visualization Toolkit) and ITK (Insight Segmentation and Registration Toolkit) components are described later.

3D Slicer has been employed in numerous research and clinical projects [4]. Using the OpenIGTLink, robotic platforms were serviced for brain tumor removal [3] to prostate biopsy [5]. The software was used as part of an Open Core Control software for surgical robots, which shows the flexibility of the 3D Slicer [6]. Not only the position of the actuators can be visualized, but one can also specify control boundaries that cannot be crossed during the intervention—also called as virtual fixtures.

B. Visualization Toolkit (VTK)

Visualization Toolkit is also for free, used for image processing, visualization, 3D computer graphics volume rendering, scientific visualization and information visualization [7]. The software can be modified and expanded with other modules thanks to the object oriented design [8]. Programs can be created in C++ Python, Java and Tcl language, and 3D Slicer is built to the top of VTK.

C. Insight Segmentation and Registration Toolkit (ITK)

ITK is for image segmentation and image registration [9]. It has a vast collection of algorithms for analyzing biomedical images, which was made within the framework of the Visible Human Project [10]. The 3D Slicer is using ITK, as a component.

D. Computer Integrated Surgical Systems and Technology (CISST)

CISST is a collection of libraries which can be a useful tool in the field of CIS and any medical robotic application. These libraries and functions are used by the Surgical Assistant Workstation. It supports interchangeability, therefore the devices that meet the basic requirements are becoming interoperable with each other [11].

E. The Image-Guided Surgery Toolkit (IGSTK)

IGSTK supports the development of image-guided applications [12], where intra-operative tracking is involved. It provides the following main features [13]:

- read and display medical images,
- interface to common tracking ,
- GUI and visualization capabilities,
- multi-slice axial view,

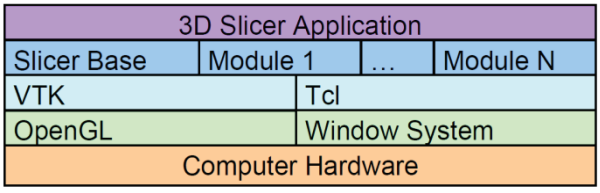

Figure 1. The modularity of Slicer 3D [5].

[1] http://slicer.org

- four-quadrant view (axial, sagittal, coronal or 3D),
- point based registration,
- robust common internal services for logging, exception-handling and problem resolution[2].

F. *Medical Imaging Interaction Toolkit (MITK)*

MITK is for the development of interactive medical software for image processing. MITK expands VTK and ITK with some interactive components [14]. Thus, the combination of these increases the versatility of the platforms. The most prominent module of the program is the interactive segmentation.

G. *Public software Library for UltraSound (PLUS)*

PLUS is yet another open software platform written is C++ and built on the NA-MIC Kit [15]. The PLUS software package contains a lot of tools that are related to the ultrasound calibration and processing, supporting optical and electro-magnetic trackers and ultrasound imaging devices [16]. In the future, PLUS will be equipped with da Vinci support, where the research interface is already in an advanced stage.

H. *Nat. Alliance for Med. Image Computing (NA-MIC)*

The NA-MIC[3] kit is not a standalone software, rather a collection of tools and methodologies [17]. It contains several software packages which have been described already (ITK, VTK and 3D Slicer).

I. *Surgical Assistant Workstation (SAW)*

While creating an experimental robotic surgical system, many different components can be (re-)used. These devices can be integrated using SAW, from Johns Hopkins University (JHU). It supports the most common tools of CIS, such as stereo viewers, haptic devices, tracking systems, the 3D Slicer, various research robots and most prominently, the da Vinci (Intuitive Surgical Inc.) master console and robotic arms [18]. It was written in C++ and the research was mostly funded by the National Science Foundation (NSF). Thanks to its modular structure, the SAW can be easily expanded with new components in a research system. As a result, many different devices can be integrated into one: e.g., a snake robot could be controlled with a da Vinci console for laryngeal surgery [19] at JHU (Fig. 2).

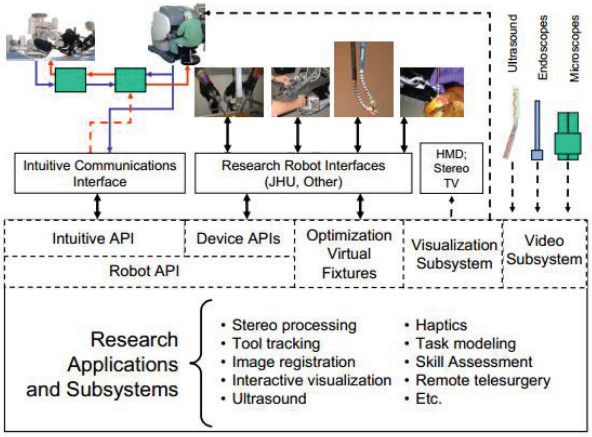

Figure 2. Architecture of the Surgical Assistant Workstation [19]

J. *The Common Toolkit (CTK)*

The goal of CTK[4] is to support biomedical image computing, the scope of current CTK development efforts includes *DICOM support*, *DICOM Application Hosting*, *Widgets* and *Plugin Framework*.

K. *NifTK*

NifTK is a platform, combining NiftyReg, NiftySim, NiftyRec and NiftySeg via the viewer NiftyView, developed at the Center for Medical Image Computing at UCL[5].

III. System-related APIs

While the academic community typically tries to develop generic solutions supporting a wide range of components and devices, some manufacturers developed particular APIs for their own system. For example, Medtronics' intra-operative navigation systems feature a StealthLink research interface [20].

The da Vinci Surgical Systems that is deployed most widely globally is not provided with open access by default. A user cannot retrieve any data from robot, the components and the programs cannot be changed, and there is no information about of the basic operating principle. (This is also due to liability issues.) Some limited information can be recorded with data collection tools [21]. Yet, these systems become transparent using open source software, once their manufacturer allows access to it [22]. (See Section V.)

IV. Research hardware environment

Fundamental research cannot easily be accomplished with closed systems, but there are examples, where closed systems became partially accessible for researchers. In the case of the da Vinci, there exists a real-time stream of kinematic and user event data from the robot that can be read, also known as the da Vinci Application Programming Interface (API)[6]. However, the total replacement of certain closed components of the robot (including the complete controller) can transform the da Vinci into an open source platform, as it is discussed in Section V.

One of the most successful open source robots is the Raven II, a former competitor to the da Vinci [23]. The development started more than 10 years ago at the University of Washington, supported by DARPA. With the help of the National Institutes of Health (NIH), 8 robots have been built and distributed to North-American and European sites. It has an open control architecture, based on the Robot Operating System (ROS)[7]. Applied Dexterity Ltd. was founded to sell the robot as a research platform, and to build the community. Current price of the system is around $300k.

[2] http://www.igstk.org
[3] http://www.na-mic.org
[4] http://www.commontk.org/index.php/Main_Page
[5] http://cmic.cs.ucl.ac.uk/home/software/
[6] http://surgrob.blogspot.hu/2009/11/da-vinci-news.html
[7] http://www.ros.org

Other groups decided to use general purpose robot arms for surgical mock applications, such as the WAM Arm from Barrett Technology Inc[8].

V. THE DA VINCI RESEARCH KIT

One of the most capable, recently realized platform is the da Vinci Research Kit (dVRK). It is a collection of retired, first-generation da Vinci robot components with additional open source control electronics and open source software.

A. Hardware components

The dVRK consists of the following parts[9]:

- 2 da Vinci Master Tool Manipulators (MTMs)
- 2 da Vinci Patient Side Manipulators (PSMs)
- A stereo viewer
- A foot pedal tray
- Manipulator Interface Boards (dMIBs)
- Basic accessory kit.

These are the original, unmodified mechanical components, thus a functional da Vinci Classic can also be transformed into a DVRK. Since the da Vinci is a commercial system, some of the components are still not available to researchers. The system does not include a number of other items, such as the Endoscopic Camera Manipulator (ECM), but these are not strictly necessary. Even for research operations, however, control electronics and control software are essential.

JHU, Worcester Polytechnic Institute (WPI) and their partners decided to create a new, open controller [24]. (The source files of the control electronics are also available online[10].) The system is equipped with an IEEE 1394a Firewire interface that is capable of a communication speed of 400 Mbit/sec. It is important to create a real-time connection between devices, which is desirable for a surgical robot system, so it can be operated with the necessary degree of security. The control box consists of two pieces of FPGA and two pieces of Quad Linear Amplifier (QLA). This assembly is sufficient for driving one robotic tool (Fig. 3). If one wants to operate 2 da Vinci Master Tool Manipulators (MTMs) and two da Vinci Patient Side Manipulators (PSMs) then four boxes of control electronics are needed—consisting of 8 pieces of FPGAs and QLAs in total.

The da Vinci research kit follows the centralized computation and distributed I/O idea [25]. This means that only the control electronics maintain contact with the peripheral inputs and outputs and all calculations are performed centrally by a main computer, which is located at the control units. The central unit is usually a Linux-based computer, which is extended by a real-time component.

B. Low level software architecture overview

The firmware of the FPGA modules is available on the internet, which can be freely modified, thanks to the BSD license[11].

[8] http://www.barrett.com/robot/products-arm.htm
[9] http://research.intusurg.com/dvrkwiki/index.php?title=Main_Page
[10] http://jhu-cisst.github.io/mechatronics/
[11] http://jhu-cisst.github.io/mechatronics/ website

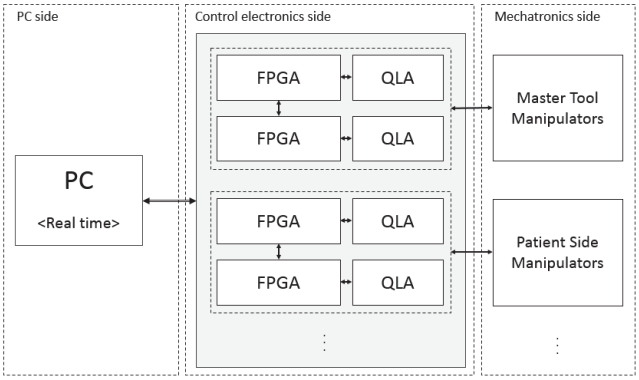

Figure 3. Schematic representation of the hardware structure

The connection through the firewire cable can be implemented with standard Linux C++ libraries and there is a solution to realize a real-time software subsystem over firewire (RT-FireWire) [26]. In this case, the computer and the FPGA modules are capable of communicating with each other.

Linux is the preferred PC side operating system for its open access. Furthermore, there also exists a real-time extension to Linux, called RTLinux, which basically is a Linux OS that runs under the control of a hard real-time microkernel [27]. This means that all of the computational deadlines have to be respected during operation.

The software architecture of a surgical robotic system can be divided into five functional layers (I-V) and three development layers (A-C), presented in Fig. 4 [28]. The development layers are stratified by the complexity of the programming language tools used. The functional layers are sorted by the complexity of their function. Owing to the centralized computation, all of the functional layers are implemented on the PC side.

One must be aware of this grouping, because the various software pages in different levels are represented in different ways. Therefore, they are also connected with each other in various ways.

Once the components are pieced together, the robot can be used at a completely open research platform thanks to the extensive high-level software support provided by the SAW and CISST libraries[12].

VI. THE FUTURE ROADMAP

The dVRK is a great advancement in the field of open source surgical robotics, since it fees the access to a clinically used system. A research community has been formulated around the 17 DVRK systems currently deployed, having regular open meetings and workshops[13]. In Europe, prior FP7 actions of the EU have already given a boost to synchronized robotics research (e.g., the EuroSurge[14], I-SUR[15], ACTIVE[16] projects.), or the Joint Workshop on Computer/Robot Assisted Surgery (CRAS)[17] series. Further, the IEEE Robotics and

[12] https://trac.lcsr.jhu.edu/cisst/wiki/ /sawIntuitiveResearchKitTutorial
[13] http://research.intusurg.com/dvrkwiki/ /index.php?title=Main_Page
[14] http://www.eurosurge.eu/eurosurge/
[15] http://www.isur.eu/isur/
[16] http://active-fp7.eu/
[17] http://www.cras2014.eu/about.html

Automation society has also created a study group[18] for the generalization of surgical robotics, and soon, a workgroup for surgical robotics ontologies is to be established[19]. This is expected to have a great impact on the entire field, given the generally increased governmental interest and support towards open source research.

VII. Conclusion

Open source surgical robotics promises to make surgery safer and more effective, and stimulate further innovation in the field. The paper reviewed the currently available software and hardware platforms, and provided some highlights to their features and projects realized on the top of them. It is expected that the prominence and significance of open medical research will grow tremendously in the future, largely relying on these technologies.

Acknowledgment

T. Haidegger is a Bolyai Fellow of the Hungarian Academy of Sciences.

References

[1] L. Dozio and P. Mantegazza, "Real-time distributed control systems using RTAI," in Proc. of the 6th IEEE Intl. Symp. on Object-Oriented Real-Time Distributed Computing, Hakodate, 2003, pp. 11–18.

[2] Pieper, S., Halle, M., & Kikinis, R. (2004, April). 3D Slicer. In Biomedical Imaging: Nano to Macro, 2004. IEEE International Symposium on (pp. 632-635).

[3] Arata, J., Tada, Y., Kozuka, H., Wada, T., Saito, Y., Ikedo, N., ... & Fujimoto, H. (2011). Neurosurgical robotic system for brain tumor removal. International journal of computer assisted radiology and surgery, 6(3), 375-385.

[4] Haidegger, T., Kovacs, L., Fordos, G., Benyo, Z., & Kazanzides, P. (2008, January). Future trends in robotic neurosurgery. In 14th Nordic-Baltic Conference on Biomedical Engineering and Medical Physics (pp. 229-233). Springer Berlin Heidelberg.

[5] A. Lasso, J. Tokuda, N. Hata, G. Fichtinger, Robot-assisted MRI-guided prostate biopsy using 3D Slicer. NA-MIC Tutorial Contest, 2010. Available: http://www.na-mic.org/Wiki/images/4/43/DBP2JohnsHopkinsTransRectalProstateBiopsy.pdf

[6] Arata, J., Kozuka, H., Kim, H. W., Takesue, N., Vladimirov, B., Sakaguchi, M., ... & Fujimoto, H. (2010). Open core control software for surgical robots. International journal of computer assisted radiology and surgery, 5(3), 211-220.

[7] Kitware, About Visualization Toolkit, http://www.vtk.org/VTK/project/about.html, 2014

[8] Schroeder, W. J., Avila, L. S., & Hoffman, W. (2000). Visualizing with VTK: a tutorial. Computer Graphics and Applications, IEEE, 20(5), 20-27.

[9] Kitware, About Insight Segmentation and Registration Toolkit, http://www.itk.org/ITK/project/about.html, 2014

[10] U.S. National Library of Medicine, The Visible Human Project – Appplications,
http://www.nlm.nih.gov/pubs/factsheets/visible_human.html, 2014

[11] Deguet, A., Kumar, R., Taylor, R., & Kazanzides, P. (2008, September). The cisst libraries for computer assisted intervention systems. In MICCAI Workshop on Systems and Arch. for Computer Assisted Interventions, Midas Journal.

[12] Gary, K., Ibanez, L., Aylward, S., Gobbi, D., Blake, M. B., & Cleary, K. (2006). IGSTK: an open source software toolkit for image-guided surgery. Computer,39(4), 46-53.

[13] IGSTK. What is IGSTK? Available: http://public.kitware.com/IGSTKWIKI/index.php/What_is_IGSTK, 2014

[14] MITK. The Medical Imaging Interaction Toolkit (MITK), Available: http://www.mitk.org/MITK, 2014.

[15] Lasso, A., Heffter, T., Pinter, C., Ungi, T., Chen, T. K., Boucharin, A., Fichtinger, G. (2011, October). PLUS: An open-source toolkit for developing ultrasound-guided intervention systems. In 4th Image Guided Therapy Workshop (Vol. 4, p. 103).

[16] Lasso, A., Heffter, T., Pinter, C., Ungi, T., & Fichtinger, G. (2012). Implementation of the PLUS open-source toolkit for translational research of ultrasound-guided intervention systems. MICCAI-Systems and Architectures for Computer Assisted Interventions, 1-12.

[17] Pieper, S., Lorensen, B., Schroeder, W., & Kikinis, R. (2006, April). The NA-MIC Kit: ITK, VTK, pipelines, grids and 3D slicer as an open platform for the medical image computing community. In Biomedical Imaging: Nano to Macro, 2006. 3rd IEEE International Symposium on (pp. 698-701). IEEE.

[18] CISST, System Requirements for Surgical Assistant Workstation ,Available: https://www.cisst.org/main/images/c/cd/SAW-SystemRequirements-Rev2.pdf, 2007

[19] Vagvolgyi, B., DiMaio, S., Deguet, A., Kazanzides, P., Kumar, R., Hasser, C., & Taylor, R. (2008, September). The surgical assistant workstation. In Proc MICCAI Workshop: Systems and Architectures for Computer Assisted Interventions.

[20] StealthLink Manual v09, Medtronic, 2005

[21 Reiley, C. E., Lin, H. C., Yuh, D. D., & Hager, G. D. (2011). Review of methods for objective surgical skill evaluation. Surgical endoscopy, 25(2), 356-366.

[22] Leven, J., Burschka, D., Kumar, R., Zhang, G., Blumenkranz, S., Dai, X. D., ... & Taylor, R. H. (2005). DaVinci canvas: a telerobotic surgical system with integrated, robot-assisted, laparoscopic ultrasound capability. In Medical Image Computing and Computer-Assisted Intervention (MICCAI), pp. 811–818, 2005

[23] IEEE Pulse.Surgical Robots in Space: Sci-fi and Reality Intersect, Available: http://pulse.embs.org/july-2014/surgical-robots-space-sci-fi-reality-intersect/, 2014.

[24] AIM WPI. daVinci Surgical Robot Robot Research System (dVRK), Available: http://aimlab.wpi.edu/research/projects/daVinci_Robot_Research_System, 2014.

[25] Chen, Z., Deguet, A., Taylor, R. H., DiMaio, S., Fischer, G. S., & Kazanzides, P. (2013, August). An open-source hardware and software platform for telesurgical robotics research. In MICCAI Workshop on Systems and Arch. for Computer Assisted Interventions, Midas Journal: http://hdl. handle. net/10380/3419.

[26] Zhang, Y., Orlic, B., Visser, P., & Broenink, J. (2005). Hard real-time networking on FireWire.

[27] Barabanov, M., & Yodaiken, V. (1996). Real-time linux. Linux journal, 23.

[28] Kazanzides, P., Chen, Z., Deguet, A., Fischer, G. S., Taylor, R. H., & DiMaio, S. P. An Open-Source Research Kit for the da Vinci R Surgical System. In Pro of the IEEE International Conference on Robotics & Automation (ICRA), Hong Kong, pp. 6434-6439, 2014.

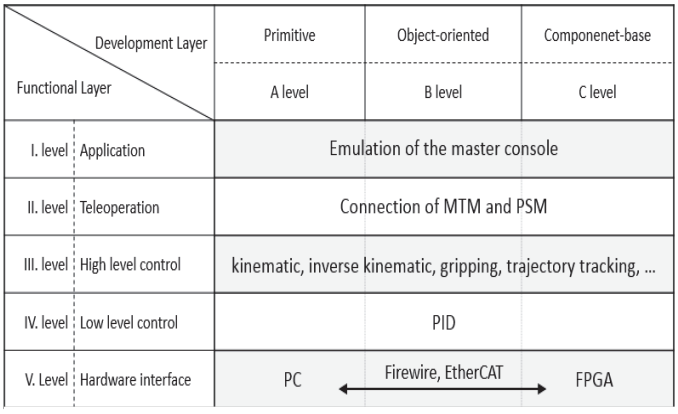

Figure 4. Stratification of the software architecture

[18] http://www.ieee-ras.org/about-ras/ras-calendar/event/529-ieee-ras-standards-committee-industry-connections-surgical-robotics-meeting
https://sites.google.com/site/ieeerasmedicalrobotics/

[19] Follow http://surgrob.blogspot.com/ for more updates.

Robot visualisation concept in 3D Slicer for image-guided interventions

Sebastian Tauscher*, Alexander Fuchs*, Thomas Neff†, Lüder Alexander Kahrs*, Tobias Ortmaier*
*Institute of Mechatronics Systems
Leibniz Universiät Hannover
Appelstrasse 11 a, 30169 Hannover, Germany
Email: Sebastian.Tauscher@imes.uni-hannover.de
†KUKA Laboratories GmbH
Zugspitzstrasse 140, 86165 Augsburg, Germany

***Abstract*—Current surgical navigation systems are visualising the tool pose relative to pre- or intraoperative image data. When a robot is used for positioning, further information is available, but often not utilised. In this paper, a visualisation concept of a robot for image-guided therapy interventions including its pose, the current state as well as the measured forces at the tool center point is presented. This information can be used for navigation purposes and force monitoring. Furthermore, the visualisation of the current robot state gives the surgeon a direct and intuitive feedback on the current system state, e.g. if the robot is position or impedance controlled and if virtual fixtures are active.**

I. Introduction

In surgical navigation systems the pose of the tool is displayed relative to pre- or intraoperative images. When a robotic systems is used for tool positioning, further information is available, but often not included in the navigation display. By visualising additional information such as the measured force at the tool tip, e.g. a drill tool or a grasping device, useful information about the current contact forces can be provided to the surgeon. Furthermore, a feedback of the current state of the robot can be helpful for the surgeon, e.g. which virtual fixtures are activated, which zone is active, and if requested transitions are succesfully performed.

II. Materials

In the following section, the setup consisting of a light weight robot (LWR) with an open interface for image-guided therapy (IGT), an exemplary state machine for IGT, and a customised 3D Slicer module for visualisation and state control is described. Further information about the interface, the state machine, and the 3D Slicer modul were published in previous papers [1], [2].

A. Light Weight Robot

The LWR was used due to its applicability to the field of robot assisted surgery. On the one hand, it is reconfigurable while holding the pose of the end effector caused by the kinematic redundancy. On the other hand, the LWR is able to estimate the external forces at the tool center point (TCP) based on integrated torque sensors in each joint and, hence, can be directly used for the given purpose without any additional hardware. In prelimanary studies an open interface concept based on the OpenIGTLink protocol was developed (Fig. 1) and three general groups of interfaces were identified: visualisation, state-control, and sensor. The visulaisation interface allows for transmission of the pose of each joint of the robot as transformation matrix. The state-control interface provides a cyclic bidirectional communication with an is-alive-check used to operate a finite state machine running on the robot control by string commands (see TABLE I). The OpenIGTLink Protocol was used due to its small footprint and its broad usage [3]. The state machine and the two interfaces are described below.

TABLE I: List of the states as well as their command and acknowledge parameters for the exemplary state machine (img = image space, rob = robot base coordinate system; 0 = free, 1 = aware, 2 = locked)

state	parameter (command)	parameter (acknowledge)
IDLE	-	-
Free	-	-
Virual-Fixtures	coordinate frame = {img, rob}; geometry = {cone, plane}; position vector = $x;y;z$; normal vector = $n_x;n_y;n_z$; cone angle = α;	geometry = {cone, plane}; active zone = {0, 1, 2};
Path	coordinate frame = {img, rob}; destination = $x;y;z;A;B;C$;	active zone = {0, 1, 2}; reached target = {true, false}
MoveTo	coordinate system = {img, rob}; destination = $x;y;z;A;B;C$;	reached target = {true, false}

1) Simple IGT state machine: This examplary state machine provides states typically needed for IGT interventions with robot systems (see Fig. 2). In the *Free* state the robot can be moved manually and freely by the surgeon and, hence, can be utilised for registration purposes. For the prepositioning phase the two impedance controlled states *VirtualFixtures* and *Path* were defined. In the first one, the workspace is restricted by active constraints [4] of a plane or cone geometry. In the second one, the robot can be moved on a linear path in cartesian space towards a target point. The *MoveTo* state can be used for the autonomous movement of the robot and, thereby, is predestined for the targeting phase of a surgical procedure such as drilling. In the *IDLE* state, the robot is holding its position with maximum stiffness.

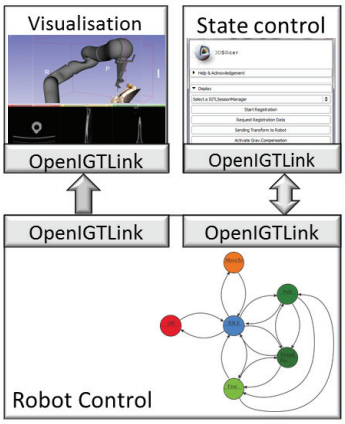

Fig. 1: Interface concept for the integration of an robot into an image-guided therapy system

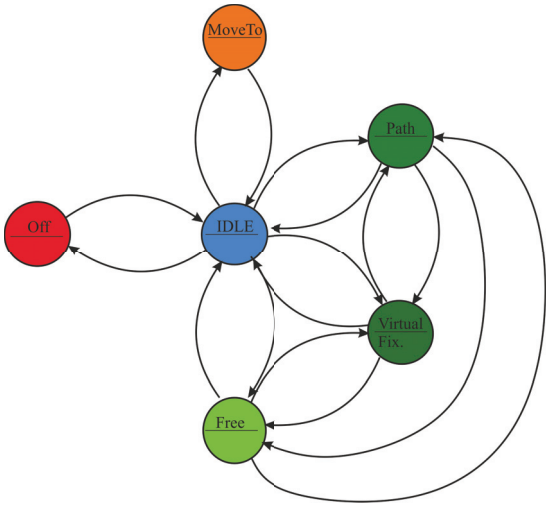

Fig. 2: Simple state machine example of a robot for image-guided therapy

2) LWRStateControlIF: For the communication with an external control system an open interface based on OpenIGTLink was developed and described previously [1]. Via this interface, command strings of the type "CommandName;p_1;p_2;..;p_n" can be received by the robot control and are mirrored back towards the state control including additional information about the robot state. In TABLEI, the command set and the parameters contained in the acknowledge strings for the exemplary state machine are given.

3) LWRVisualisationIF: In addition to the state control interface a visualisation interface was developed. This allows for sending transformation matrices from the robot control to a visualisation software. In first performance tests it was shown that a visualisation of the robot pose is possible with update rate ≥ 60 Hz and a latency ≤ 100 ms [2] including the whole visualisation process.

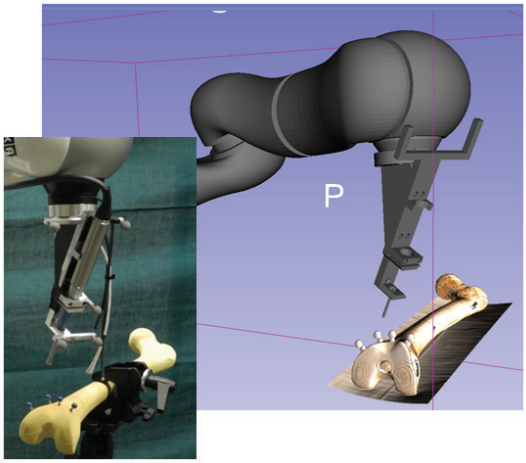

Fig. 3: Visualisation of the robot relative to the target in 3D Slicer and the experimental setup

B. LightWeightRobotIGT

LightWeigthRobotIGT[1] is a control and visualisation 3D Slicer module developed for the LWR. This module enables a cyclic communication with the state machine running on the robot control via the described interfaces. Commands used for operating the state machine, to activate or deactivate the visualisation interface, and to shut down the state machine are supported. The parameters $p_1, .., p_n$ needed for the proper initialisation of the different states can be set as well.

III. Visualisation Concept

In this section, the visualisation concept of a robot for image-guided therapy is presented. This concept includes the representation of forces, the pose, and the current robot state. The focus of this paper is set to the force display and the visualisation concept for the robot state.

A. Robot configuration

For the visualisation of the robot configuration the position of each joint relative to the robot base coordinate frame is sent from the robot control via the *LWRVisualisationIF* interface represented by the homgeneous transformation matrix ${}^{i}\mathbf{T}_{\mathrm{Base}}$. A STL file of each part of the LWR and the used tool is loaded to the 3D Slicer scene and automatically connected to the corresponding transformations. Thereby, the robot is automatically visualised in the base coordinate system. To visualise the robot in relation to the target region, which is normally displayed in image space or CT-base coordinate frame respectively, the transformation ${}^{\mathrm{Base}}\mathbf{T}_{\mathrm{CT}}$ needs to be connected with and observed by all models of the LWR (see Fig. 3).

B. Forces

To represent the information of a force the following aspects are important: the force application point, the absolute value of the force, and the direction in which the force is

[1] https://github.com/SNRLab/LightWeightRobotIGT

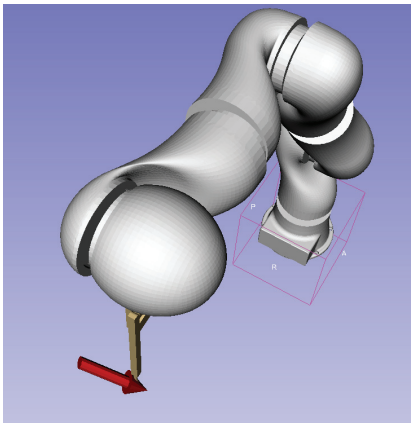

Fig. 4: Force visualisation at the tool center point of LWR

applied. The force vector contains two of these details and the current pose of the robot is known to the robot control. For the display of vectors, arrows are an intuitive way, hence, a 3D arrow is chosen for this purpose.
The orientation of the force vector can be represented by a rotational matrix, which describes the rotation from the robot base coordinate to a coordinate frame with the z-axis in the direction of the force vector $\mathbf{f}$. This rotation can be computed by

$$^{\text{Base}}\mathbf{R}_{\text{Force}} = \mathbf{R}_x(\phi)\mathbf{R}_y(\theta) \tag{1}$$

with the two euler angles

$$\phi = -\arcsin\frac{f_x}{||\mathbf{f}||_2} \text{ and} \tag{2}$$

$$\theta = \arctan\frac{f_y}{f_z}. \tag{3}$$

The third rotation around the z-axis is not needed for the visualisation, because the chosen object is symmetric to the z-axis. By adding the translation $^{\text{Base}}\mathbf{t}_{\text{TCP}}$ from the base coordinate system to the force application point the homogenous transformation matrix $^{\text{Base}}\mathbf{T}_{\text{Arrow}}$ from the robot base to the coordinate frame at the tool center point with the z-axis in direction of the force vector is given by

$$^{\text{Base}}\mathbf{T}_{\text{Arrow}} = \left(\begin{array}{c|c} ^{\text{Base}}\mathbf{R}_{\text{Arrow}} & ^{\text{Base}}\mathbf{t}_{\text{TCP}} \\ \hline (0\ 0\ 0) & 1 \end{array}\right). \tag{4}$$

For the representation of the force the magnitude is of importance as well. This can be included by multiplying the rotation matrix $^{\text{Base}}\mathbf{R}_{\text{Force}}$ with the absolute value of the force vector. Thereby, the force vector orientation, position, and size can be described by the similar transformation

$$^{\text{Base}}\mathbf{A}_{\text{Arrow}} = \left(\begin{array}{c|c} ||\mathbf{f}||_2\,^{\text{Base}}\mathbf{R}_{\text{Arrow}} & ^{\text{Base}}\mathbf{t}_{\text{TCP}} \\ \hline (0\ 0\ 0) & 1 \end{array}\right). \tag{5}$$

Thereby, a linear transformation including all necessary information for force representation is defined, which can be used to transform a 3D arrow, so that the arrow tip points to the force application point in the direction of the force vector. The size of the 3D object is proportional to the absolute value of the force (see Fig. 4). An advantage of this concept is that the OpenIGTLink TRANSFORM data type can be used and, thus, the *LWRVisualisationIF* interface.

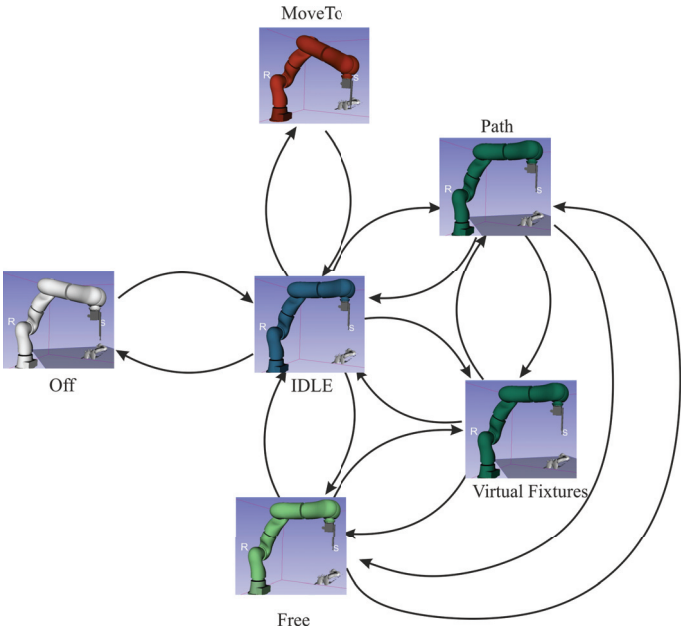

Fig. 5: Visualisation concept of the current state of the robot by a color coding for the different states (IDLE = blue; VirtualFixtures/PathImp = dark green; Free = green; MoveTo = orange)

C. Current robot state

To give an intuitive and direct feedback of the current robot state to the surgeon a color coding for the robot states and the active zones of the virtual fixtures was developed for the examplary state machine (see Fig. 5 and Fig. 6). Therefor, the received acknowledge string is read and according to the information the display in 3D Slicer is adapted.

1) Impedance based states: For the *Free* state a light green was used, whereas for the *VirtualFixtures* and *Path* state a darker green was used (see Fig. 5). Futhermore, the active virtual fixture is displayed in relation to the robot and changes its color according to the active zone of the active constrains. The used constraint concept distinguishes three zones: *free*, *aware*, and *locked*. Here, a colour coding from blue to red is used (Fig. 6).

2) Position controlled states: For the position based state *IDLE* the robot colour is changed to a dark blue. In the state *MoveTo* orange is used because this colour is widely understood as an alarm signal and, hence, gives a warning to the surgeon that the robot is now moving autonomously.

IV. Conclusion

In this paper a visualisation concept was developed and implemented for the experimental setup consisting of a LWR with an open interface extension and a 3D Slicer module. By using this interface concept information about the measured force and the current robot state could be directly displayed in 3D Slicer in relation to images of the target regions. Thereby, an intiutive feedback on the current state and the success of the requested transition is given to the user. Furthermore the active virtual fixtures are automatically displayed in relation

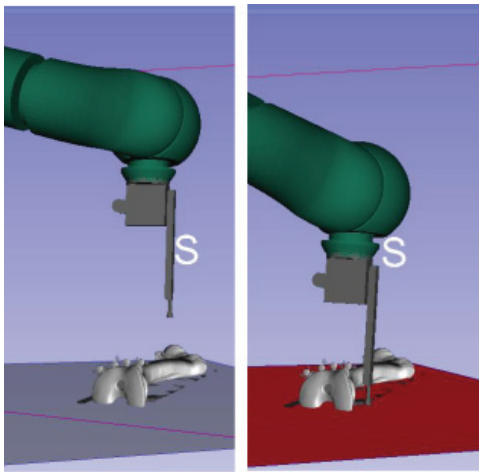

Fig. 6: Visualisation concept of a active planar virtual fixtures in the two zones *free* (left) and *locked* (right)

to the robot and the target region and their position can be checked as well.

Acknowledgment

The authors thank Nobuhiko Hata and Junichi Tokuda for the cooperation as well as the organizers of the NAMIC 2013 Summer Project Week. This work is funded by KUKA Laboratories GmbH (Augsburg, Germany).

References

[1] Tauscher S, Neff T, Ortmaier T *Interface concept for the integration of a robot into an image-guided therapy system*, Proceedings of the 27th International Congress on Computer Assisted Radiology and Surgery,8(51), 192-193, (2013)

[2] Tauscher S, Tokuda J, Schreiber G, Neff T, Hata N, Ortmaier T *OpenIGTLink Interface for state control and visualisation of a robot for image-guided therapy systems*,3rd ed. International Journal of Computer Assisted Radiology and Surgery, (DOI) 10.1007/s11548-014-1081-1, (online first, 2014)

[3] Tokuda J, Fischer GS, Papademetris X, Yaniv Z, Ibanez L, Cheng P, Hata N. *OpenIGTLink: an open network protocol for image-guided therapy environment*, The International Journal of Medical Robotics and Computer Assisted Surgery, 5(4), 423-434, 2009.

[4] Jakopec M, Rodriguez y Baena F, Harris SJ, Gomes P, Cobb J, Davies BL . *The hands-on orthopaedic robot* IEEE Transactions on Robotics and Automation, 19(5), 902-911, 2003.

Session 10

Cognitive Robotics

Chair: Dr. Leonardo Mattos, Istituto Italiano di Tecnologia

Thursday, October 16th

16:00 – 16:30

Towards Autonomous Robotic Catheter Navigation Using Reinforcement Learning

Abraham Temesgen Tibebu*, Bingbin Yu*, Yohannes Kassahun*, Emmanuel Vander Poorten†, Phuong Toan Tran†
*Faculty 3 - Mathematics and Computer Science, University of Bremen
Robert-Hooke-Str. 5, D-28359 Bremen, Germany
†Department of Mechanical Engineering, University of Leuven
Celestijnenlaan 300B, B-3001 Heverlee, Belgium
Email: Abraham.Tibebu@uni-bremen.de

I. Abstract

Autonomous navigation with robotic catheter, which can be seen as a specialization of continuum robots, inside the aorta is a challenging task due to the deformable and dynamic nature of the aorta and due to the fact that the geometry varies considerably from patient to patient. A reinforcement learning (RL) method, Q-learning, is applied to navigate inside the aorta. The knowledge learned by the robotic catheter in a given 2D aorta mesh is transferred by means of the action value function to a modified 2D aorta mesh. In the first mesh, for testing with the knowledge from training on the first mesh, the action value function is initialized using the knowledge from the first mesh. In the second mesh, for testing with the knowledge from training on the second mesh, the action value function is initialized using the knowledge from the second mesh. In the second mesh, for testing transferability of training knowledge from the first mesh to the second mesh, the action value function is initialized using the knowledge from training on the first mesh. The initial result shows that the knowledge transferred from the first mesh to the second mesh by using action value function enables autonomous navigation in the second mesh. The initial result shows also that the RL algorithm does not depend on the 2D aorta mesh but rather depends on the robotic catheter which learns the knowledge.

II. Experimental Setup

The experiment is done using a catheter simulator provided by University of Leuven which has both a 2D aorta mesh as an environment and a simulated catheter as a robot shown in Figure 1. The catheter simulator employs a minimum-energy principle to compute the next state from the current state and the current action [1]. The current state $\boldsymbol{s}_t$ is defined as a B-spline representation of L 3D points from catheter simulator where L is the number of nodes. L varies depending on the length of the catheter. For learning the catheter-aorta interaction modeling, the B-spline representation has 30 nodes. The touch state $\boldsymbol{t}_t$ is defined by comparing the distance between the nodes of the catheter and the wall of the aorta with a predefined threshold distance t_{tr}. If the measured distance is less than t_{tr}, then it is considered as touching and if the measured distance is greater than t_{tr}, then it is considered as not touching. The action space consists of three types of actions: translation, bending and rotation. The translation actions are of two types: push and pull. The bending actions are also of two types: bending left and bending right. Due to 2D aorta mesh, the rotation actions are not considered.

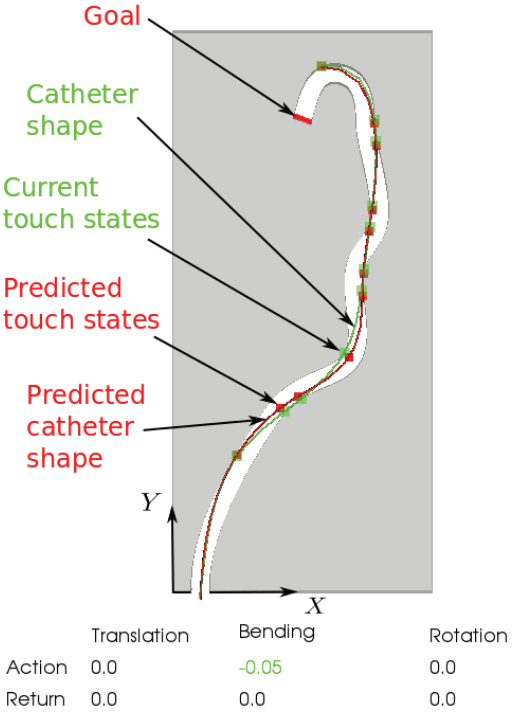

Fig. 1. The catheter simulator: The current state which is the current catheter shape is shown with a green spline curve and the predicted catheter shape is shown with a red spline curve. The touch states of the catheter nodes for the current state are shown with green mini squares. The touch states for the catheter nodes of the predicted catheter shape are shown with red mini squares. The goal for autonomous navigation is shown with a red bar at the beginning portion of the ascending aorta.

The model has six components: touch state $\boldsymbol{t}_t \in \Re^{30\times1}$, entrance point $\boldsymbol{p}_e \in \Re^{3\times1}$, tip point $\boldsymbol{p}_t \in \Re^{3\times1}$, current state $\boldsymbol{s}_t \in \Re^{90\times1}$, current action $\boldsymbol{a}_t \in \Re^{3\times1}$ and reward $r_t \in \Re^{1\times1}$.

During training, the catheter simulator is started by considering the initial state and the initial action as current state and current action respectively. Every time after updating the model with the current state and current action which are inputs to the catheter simulator, the current state is updated

with the next state which is output of the catheter simulator. Similarly after generating the next action, the current action is updated with the next action. An episode of the training phase is completed when the tip of the catheter reaches the goal. After performing a required number of episodes, the training phase is completed.

During testing, the catheter simulator is started by taking the initial state and the initial action as current state and current action respectively. After executing the current action, the next state is perceived. The optimal action for the next state is selected and the next reward is calculated. The action value function for the current state and current action is updated. Every time after updating the model with the current state and current action which are inputs to the catheter simulator, the current state is updated with the next state which is the output of the catheter simulator and the current action is updated with the optimal action which is the next action.

III. METHOD

Reinforcement learning (RL) is a goal oriented learning from the interactions between the actor, which is the robotic catheter, and the environment, which is the 2D aorta mesh [2]. In RL the actor learns what to do and how to map situations to actions in order to maximize a reward. The cost function which is used to calculate the reward is shown in Equation (1).

$$r(n) = \begin{cases} -100 & \text{if tip touches the wall of the aorta and action is push} \\ 100 & \text{if tip touches the wall of the aorta and action is pull, bend or rotation} \\ -200 & \text{if tip touches not and action is pull, bend or rotation} \\ 200 & \text{if tip touches not and action is push} \\ M & \text{if tip reaches goal} \end{cases} \quad (1)$$

where M is a large positive constant.
The return is calculated as a discounted sum of rewards using Equation (2) [2].

$$\mathbb{R}_t = \sum_{i=1}^{N} \gamma^{i-1} r_{t+i} \quad (2)$$

where N is total number of steps and γ is discount rate.
The action value function $\mathbb{Q}^{\pi}(\boldsymbol{s}_t, \boldsymbol{a}_t)$ is defined as the expected return when starting from current state $\boldsymbol{s}$, taking action $\boldsymbol{a}$ and following policy π which is a mapping from current state $\boldsymbol{s}$ to current action $\boldsymbol{a}$ to be taken [2]:

$$\mathbb{Q}^{\pi}(\boldsymbol{s}_t, \boldsymbol{a}_t) = \mathbb{E}_{\pi}\left[\mathbb{R}_t | \boldsymbol{s}_t = \boldsymbol{s}, \boldsymbol{a}_t = \boldsymbol{a}\right] \quad (3)$$

During training for a given number of episodes, the training data is generated for a policy π and a joint probability distribution (JPD)

$$p(\boldsymbol{t}_t, \boldsymbol{p}_e, \boldsymbol{p}_t, \boldsymbol{s}_t, \boldsymbol{a}_t, r_t) \quad (4)$$

is learned [3]. The return is calculated for each state and action per episode and the model is updated. For the action value function which has three components (current state $\boldsymbol{s}_t$, current action $\boldsymbol{a}_t$ and return $\mathbb{R}_t$), the JPD

$$p(\boldsymbol{s}_t, \boldsymbol{a}_t, \mathbb{R}_t) \quad (5)$$

is learned. Monte Carlo (MC) which is one way of solving RL problems by applying averaging returns is used for training. The pseudocode for training using MC method is

```
initialization;
while not the last episode do
    generate an episode using policy π;
    if an episode is completed then
        calculate the return ℝ_t for each state s_t and
        action a_t in the episode;
        update ℚ(s_t, a_t) with ℝ_t;
        increment an episode counter;
    else
    end
end
```

Algorithm 1: The pseudocode for training using MC method

Q-learning is an off-policy Temporal-Difference control algorithm [2].

$$\mathbb{Q}(\boldsymbol{s}_t, \boldsymbol{a}_t) \leftarrow \mathbb{Q}(\boldsymbol{s}_t, \boldsymbol{a}_t) + \alpha\left[r_{t+1} + \gamma \max_{\boldsymbol{a}} \mathbb{Q}(\boldsymbol{s}_{t+1}, \boldsymbol{a}) - \mathbb{Q}(\boldsymbol{s}_t, \boldsymbol{a}_t)\right] \quad (6)$$

where α is step size and γ is discount rate. If α is 1, Equation (6) is simplified to

$$\mathbb{Q}(\boldsymbol{s}_t, \boldsymbol{a}_t) \leftarrow r_{t+1} + \gamma \max_{\boldsymbol{a}} \mathbb{Q}(\boldsymbol{s}_{t+1}, \boldsymbol{a}) \quad (7)$$

The action value function $\mathbb{Q}(\boldsymbol{s}_t, \boldsymbol{a}_t)$ is updated in each step using Equation (7).

During testing using Q-learning method until the catheter reaches its goal, the catheter shape is perceived and the return is calculated using Expression (3). The action with a maximum return is executed. After executing the optimal action, the next catheter shape is perceived. The optimal action for the next state is selected and the next reward is calculated to update action value function of the current catheter shape and current action using Equation (7). Then the current state is updated with the next state and the current action is updated with the optimal action. The pseudocode for testing using Q-learning method is

```
initialization;
perceive the current state s_t;
select an optimal action a* = arg max_a ℚ(s_t, a);
update a_t with a*;
while tip of catheter not in goal state do
    execute a_t;
    perceive the next state s_{t+1};
    select an optimal action a* = arg max_a ℚ(s_{t+1}, a);
    calculate the next reward r_{t+1};
    update ℚ^π(s_t, a_t) with r_{t+1} + γℚ(s_{t+1}, a*);
    update s_t with s_{t+1};
    update a_t with a*;
end
```

Algorithm 2: The pseudocode for testing using Q-learning method

To calculate analytically the quantity given by Expression (3), we used a mixture of Gaussians for modeling the joint probability distribution given by Expression (5). Mixture of Gaussians are discussed in-depth in the book by Mclachlan and Peel [4]. The values for the constants used in the method are shown in Table I.

TABLE I. Values for constants used in the method

Constants	Values
γ	0.9
α	1
t_{tr}	$4mm$
M	$5 * 10^5$

IV. Results

In Figure 2, 2D aorta meshes used during training and testing are shown. To get mesh II, mesh I has been modified in abdominal aorta, descending thoracic and aortic arch parts. The boundaries for sectioning the aorta are shown in Figure 2. Five episodes have been run for training and testing.

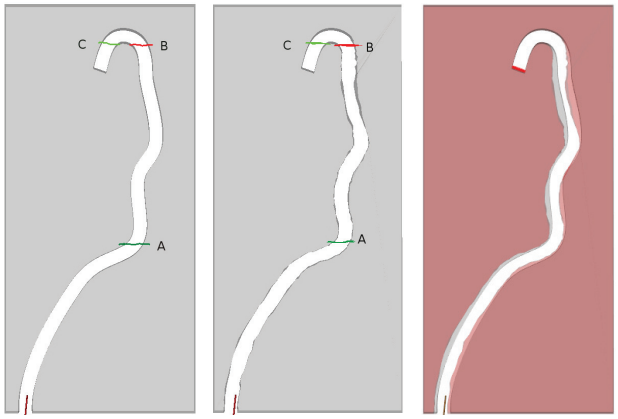

(a) (b) (c)

Fig. 2. The 2D meshes used in the experiment during training and testing. A is a boundary for transition from abdominal aorta to descending thoracic aorta or vice versa. B is a boundary for transition from descending thoracic aorta to aortic arch or vice versa. C is a boundary for transition from aortic arch to ascending aorta or vice versa. In order to show the modifications made on mesh I to get mesh II, the two meshes are superimposed. The color of mesh II has been changed to red for contrast.

The result of testing using Q-learning for three runs is shown in Figure 3. In Figure 3a, the average of the three runs for testing on mesh I with action value function initialized from training on mesh I is shown with thick red line and the three runs are shown with thin red lines. The vertical error bars shown with red represents the standard deviation of the three runs shown with thin red lines. The training on mesh I is shown with black line. In Figure 3b, the average of the three runs for testing on mesh II with action value function initialized from training on mesh II is shown with thick red line and the three runs are shown with red thin lines. The vertical error bars shown with red represents the standard deviation of the three runs shown with thin red lines. The average of the three runs for testing on mesh II with action value function initialized from training on mesh I is shown with thick green line and the three runs are shown with thin green lines. The vertical error bars shown with green represents the standard deviation of the three runs shown with thin green lines. The training on mesh II is shown with black line.

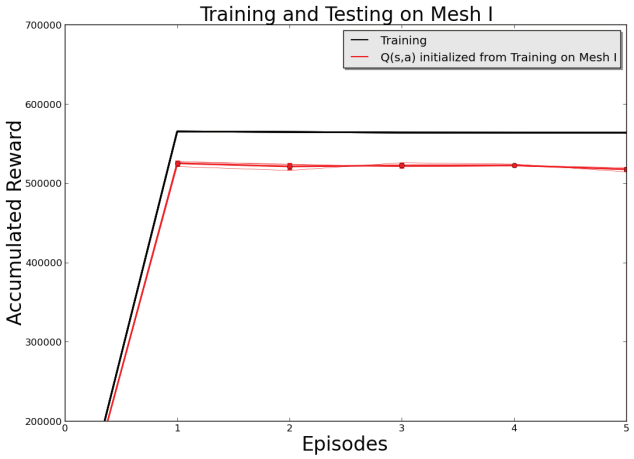

(a)

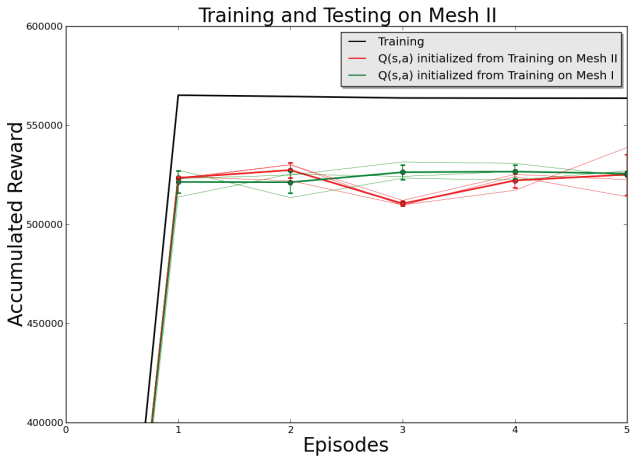

(b)

Fig. 3. In the pictures, accumulated reward versus episodes is plotted for training and testing using mesh I (a) and using mesh II (b) where $Q(s, a)$ is action value function.

As shown in Figure 3a when RL algorithm is tested in mesh I by initializing action value function with training from mesh I, it could not reach the level of the accumulated reward of the training within five episodes. The percentage discrepancy D_p is calculated using Equation (8)

$$\mathrm{D}_p = \frac{|X_e - X_t|}{X_t} * 100\%, \tag{8}$$

where X_e is experimental value and X_t is theoretical value. The percentage discrepancy between training in mesh I which is taken as X_t and testing in mesh I which is taken as X_e at the fifth episode is 8.21%. The reason for not reaching the level of the accumulated reward of the training is the cost function defined in Equation (1) does not reward some catheter aorta interactions correctly. One of such catheter aorta interactions

is that if the tip of the catheter touches the left wall of the aorta (i.e. the wall of the aorta where x-coordinate of the catheter tip is greater than x-coordinate of the wall of the aorta provided that the catheter is in the abdominal aorta or the descending thoracic aorta as shown in Figure 2) and the next action is bend left, according to the cost function the reward is 100 instead of -100. The wrong reward will affect updating the action value function of the current catheter shape and current action using Equation (7).

As shown in Figure 3b when RL algorithm is tested in mesh II with action value function initialized from training on mesh I, it rose above the level of the accumulated reward of testing with action value function initialized from training on mesh II within three episodes. The percentage discrepancy between testing with action value function initialized from training on mesh II which is taken as X_t and testing with action value function initialized from training on mesh I which is taken as X_e at the fifth episode is 0.1%.

The higher the number of the accumulated reward is, the safer the autonomous navigation inside the aorta is. A higher number of accumulated reward indicates less number of occurrence for catheter tip touching the wall of the aorta.

V. CONCLUSION

The initial result shows that by using RL algorithm, the skill learned in one environment can be transferred to another environment. Because of the differences in size and shape of aorta from patient to patient such transferability of skills are very crucial for navigating autonomously in aorta. As future work, the RL method will be extended to 3D and human knowledge or prior knowledge will be added for obstacle avoidance. Further the extended RL method will be tested in a 3D rigid mock-up.

ACKNOWLEDGMENT

This research has been funded by the European Commission's 7th Framework Programme FP7-ICT, by the project CASCADE under grant agreement No.601021.

REFERENCES

[1] G. Smoljkic, C. Gruijthuijsen, J. Vander Sloten, and E. Vander Poorten, "Towards Intraoperative Use of Surgical Simulators: Evaluation of Catheter Insertion Models," in *Proceedings of the 3rd Joint Workshop on New Technologies for Computer/Robot Assisted Surgery (CRAS)*, 2013, pp. 45–47.

[2] R. S. Sutton and A. G. Barto, *Reinforcement learning: An introduction*. MIT Press, 1998.

[3] Y. Kassahun, B. Yu, and E. B. Vander Poorten, "Learning Catheter-Aorta Interaction Model Using Joint Probability Densities," in *Proceedings of the 3rd Joint Workshop on New Technologies for Computer/Robot Assisted Surgery (CRAS)*, 2013, pp. 158–160.

[4] G. Mclachlan and D. Peel, *Finite Mixture Models*, 1st ed., ser. Wiley Series in Probability and Statistics. Wiley-Interscience, 2000.

Towards learning-based catheter distal section steering

Bingbin Yu, Abraham T. Tibebu, Yohannes Kassahun, Felix Bernhard
University of Bremen
Faculty 3 - Mathematics and Computer Science
Robert-Hooke-Strae 5, D-28359 Bremen, Germany
Email: bingbin.yu@uni-bremen.de

Emmanuel Vander Poorten
University of Leuven
Dept. of mechanical engineering, division PMA
Celestijnenlaan 300B, B-3001 Heverlee, Belgium

I. Abstract

Despite the growing popularity of catheter based therapy in cardiovascular diseases, the operation of steerable catheters is still inaccurate due to their inherent compliance and in case of cable-based steerable catheters friction between cable and catheter sleeve. The performance of most catheter therapies such as cardiac ablation depends on the accuracy of catheter tip navigating and settling on the target position of the heart tissue, which is moving dynamically when the heart is still beating. Since it is a tedious task, in fact any method to improve the catheter tip steering is welcomed.

To improve the positioning accuracy of cable-actuated steerable catheters, this paper proposes the use of joint probability density [1] based catheter modelling and model based catheter steering. The joint probability distribution of the catheter handle displacement, the catheter tip position, the catheter shape and the bending angle is learned. Based on the learned model, a position control of a conventional ablation catheter is developed.

II. Experimental Setup

The experimental setup is shown in Fig.1.

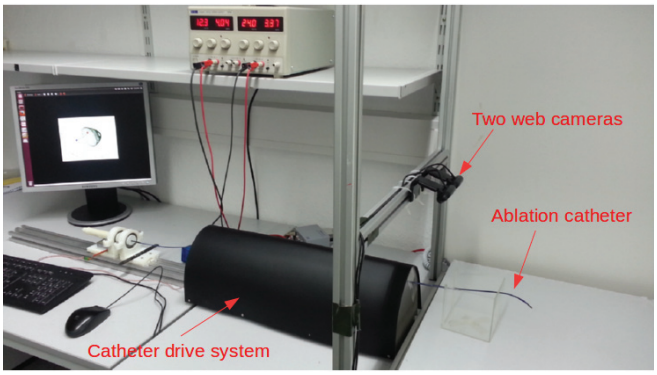

Fig. 1. In the experiment, a RFA ablation catheter (EndoSense SA) is used, which is driven with a tendon mechanism and bends only in one direction. Two web cameras (Logitech C170) are mounted side by side above the testbed at a height of 25 centimeters. A catheter drive system is used for steering the ablation catheter autonomously.

From the two web cameras, the 600×450 resolution images of the catheter are captured, from which the following parameters are extracted: (1) the shape of the catheter, (2) the tip of the catheter, (3) the bending angle of the catheter (4) the rotation angle of the catheter. For the purpose of extracting the parameters listed above, we used an OpenCV implementation programmed in Python [2]. The catheter drive system provides the actions push, pull, bend and rotate on the catheter with a precision of 0.2 micrometer in translational movement and 2.1 degree in rotary movement. The handle of the ablation catheter is mounted on a bending device as Fig.2 shows, which is driven by a step motor and the displacement of the handle corresponds to the bending angle of the catheter distal section.

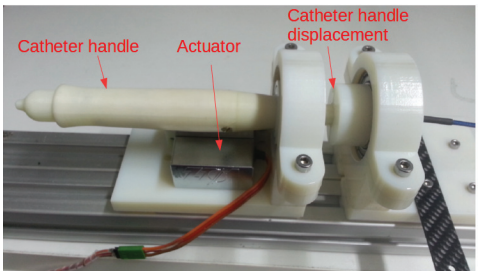

Fig. 2. The catheter bending device. The handle of the ablation catheter is mounted on the two components of the bending device. A step motor is used to increase and decrease the displacement of the catheter handle.

III. Method

Due to the compliance of the catheter material and unknown internal friction and associated internal load, the precise modelling of the tendon-driven catheter is still challenging and is being studied by a number of groups, e.g. [3], [4], [5], [6], [7]. Most of these methods focus on the bending angle of the distal section and require the internal information of the catheter which is difficult to know for a conventional ablation catheter. This paper provides a data driven method for learning the model of the catheter distal section in 3D cartesian space where the internal information of the ablation catheter is not required.

The bending function of the catheter driver and the ablation catheter system is studied through an experiment. By controlling the actuator of the bending device, the displacement

of the handle increases and decreases between 0 mm and 4.7 mm. From the camera images, the tip of the catheter, the bending point and the distal base point of the catheter (Fig.4) are extracted, where the bending point is the transition position between passive catheter body and distal bending segment and the distal base point is a position on the catheter's body at a distance of 1 cm from the bending point. With these three points, the bending angle of the catheter distal section is calculated. Fig.3 shows the bending angles of the catheter with respect to the displacement of the catheter handle. A clear hysteresis-like behaviour can be observed from the figure: The red curves show the bending angles of the catheter when the handle displacement increases. The bending angle starts to rise when the handle displacement increases from 1.5 mm. The blue dash curves show the bending angles of the catheter when the handle displacement decreases. The yellow star is the current bending angle of the catheter which is 30 degrees. When the bending angle decreases from 30 degrees, the catheter bends following the green curves. Due to the internal friction and load of the catheter, the catheter can not straighten itself again once it has been bent. Therefore, the bending range of the catheter in the experiment is from 11 degrees to 50 degrees.

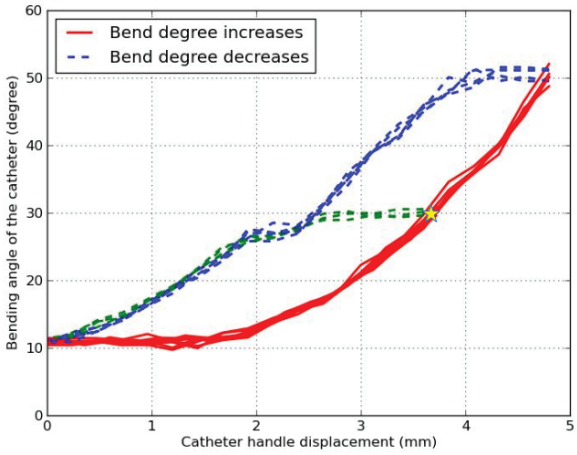

Fig. 3. The hysteresis model of the catheter bending

Since the internal friction of the catheter is difficult to be precisely modelled, a learning method is used to model the behaviour of the catheter distal section. Two joint probability distributions

$$p(\boldsymbol{\theta}_b, \boldsymbol{p}_t, \boldsymbol{\alpha}, \boldsymbol{d}_{push}), p(\boldsymbol{\theta}_b, \boldsymbol{p}_t, \boldsymbol{\alpha}, \boldsymbol{d}_{pull}), \quad (1)$$

are learned from the training data, where $\boldsymbol{\theta}_b$ stands for the bending angle of the catheter, $\boldsymbol{p}_t$ is the 3D position of the catheter tip, a vector of coefficient α is used to represent the shape of the catheter distal section and $\boldsymbol{d}_{push}$ and $\boldsymbol{d}_{pull}$ represent the push and pull distances of the catheter handle. From these two joint probability distributions, the relationship of the push distance, bending angle, catheter tip position and the catheter distal shape can be captured.

Since the catheter can also be rotated by the catheter drive system, the steering actions include catheter bending and rotation. Figure 4 illustrates the rotation and bending actions of a catheter distal section as well as its workspace (bowl shape). The yellow, red and green points represent the catheter tip, bending point and distal base point respectively. The red dash line is the rotation axis of the catheter. According to the rotational symmetry, the shapes of the bended catheter distal section are the same in any rotation angle. Once the catheter distal section is modelled for a given rotation angle, the catheter tip in the other rotation angles can be calculated with a rotation matrix $\boldsymbol{R}$ with respects to the rotation axis (BA). As a result, the available positions of the catheter tip can be calculated as the workspace of the catheter distal section, which is represented as the shaded bowl shape surface in Figure 4.

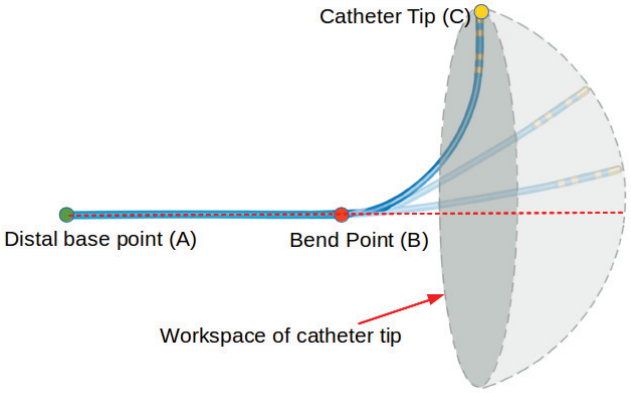

Fig. 4. The catheter steering mechanism and the catheter tip workspace

For steering the catheter, a reference position of the catheter tip is selected on this bowl shape surface workspace. Based on the reference tip position, the expected bending angle can be calculated using

$$\mathbb{E}\left[\boldsymbol{\theta}_b | \boldsymbol{p}_t\right]. \quad (2)$$

If the bending angle of the target tip position $\boldsymbol{\theta}_b$ is larger than the current bending angle, the control action $\boldsymbol{d}_{push}$ can be calculated using

$$\mathbb{E}\left[\boldsymbol{d}_{push} | \boldsymbol{p}_t\right]. \quad (3)$$

Otherwise, the pull action is needed which is given by,

$$\mathbb{E}\left[\boldsymbol{d}_{pull} | \boldsymbol{p}_t\right]. \quad (4)$$

Transforming the detected catheter, reference tip position to a local coordinate system, which the original point of the system is placed at the distal base point of the catheter and the rotation axis BA is aligned with the x axis, and projecting the catheter tip and reference position into Y-Z plane, the rotation angle between the catheter tip and the reference position can be calculated. As a result, the bending action and rotation action are determined and catheter distal section is controlled.

IV. Experimental Results

After training the catheter distal section model in one rotation angle, based on the trained two joint probability distributions (expressions (1)) the expected catheter tip positions are estimated with the bending angles using

$$\mathbb{E}\left[\boldsymbol{p}_t | \boldsymbol{\theta}_b\right]. \quad (5)$$

The bending angle increases in the available range from 11 degrees to 50 degrees in each degree. Therefore, the position of the catheter tip in each bending angle is calculated which is the trajectory of the catheter tip in the rotation angle. By rotating the catheter tip trajectory around the rotation axis BA (Fig. 4) from 0 to 360 degree in every 2 degrees, the workspace of the catheter tip with respect to a bending point are calculated, as the green bowl shape surface represents in Fig. 5. Since the catheter can not straighten itself again once it has been bent, the bottom of the bowl shape area can not be reached by the catheter tip.

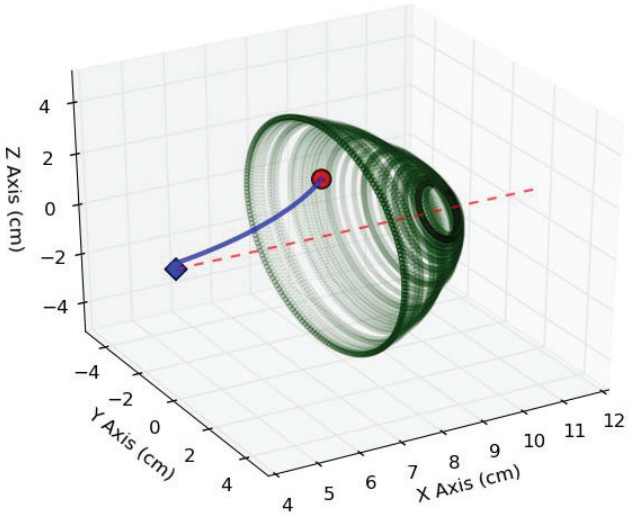

Fig. 5. The catheter tip workspace and the detected catheter distal section

The blue curve in Fig. 5 represents the detected catheter distal section and the red dot is the detected catheter tip. The red dash line which represents the rotation axis BA aligns with the x axis and the blue diamond mark is the bending point of the catheter.

In order to test the trained model and the steering algorithm, a wire is placed nearby the ablation catheter. The crossing point between the wire and catheter tip workspace is detected which is selected as the reference position. According to the expressions (3) and (4), the tip of the catheter is steered to approach to the wire as Fig.6 shows: the Fig.(a),(c) are the detected catheter (blue curve) and wire (yellow curve) before the steering actions. The red dot represents the catheter tip and the red star is the crossing point between the wire and the bowl shape workspace, which is the reference position of the catheter tip. After the steering actions, the catheter tip moves approaching to the reference position as the Fig.(b),(d) shows.

For testing the repeatability and the accuracy of the steering method, 25 different reference positions are selected by placing the wire in random poses nearby the catheter. The catheter is steered from the random starting poses to reach these reference positions.

Figure. 7 shows the positioning error which is the distance

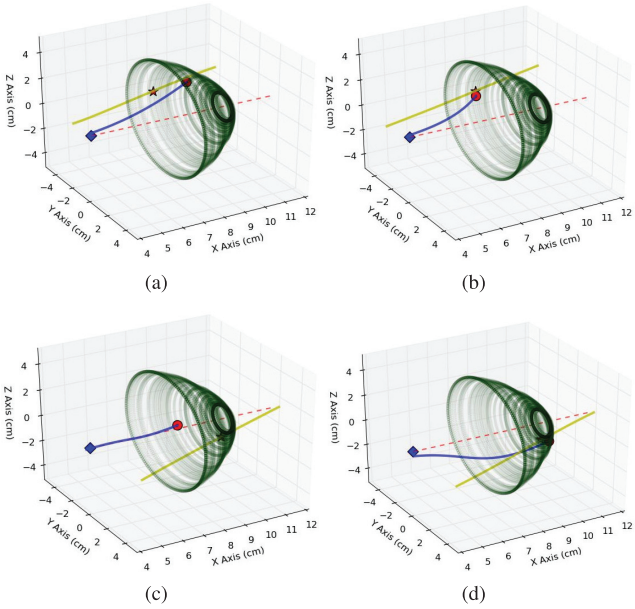

Fig. 6. Catheter distal section before steering (a,c) and after steering (b,d), with different reference positions and starting poses.

measured between the catheter tip and the reference positions. As can be seen from the figure, the tip of the catheter is steered approaching to the reference positions in all of the 25 repetitions of the tests. The average positioning error of the repeatability test is 3.56 mm and standard deviation is 1.48 mm. The error is mainly caused by the 3D image processing and the catheter drive system. Therefore, in the immediate future, the image processing method will need to be enhanced and the hardware of the catheter drive system should be improved. On a longer term, the problematic effects such as the rotational stiffness of the catheter in different insertion length and the possible contact with the environment will need to be investigated.

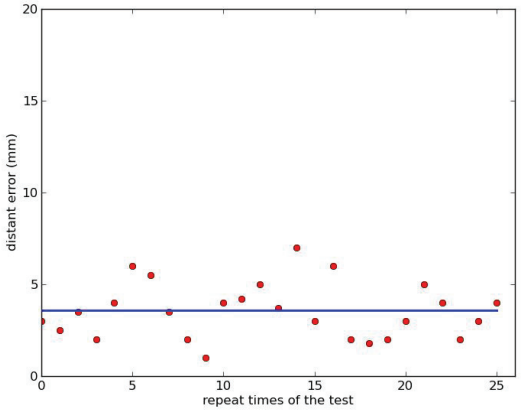

Fig. 7. The results of the repeatability test

References

[1] M. Edgington, Y. Kassahun, and F. Kirchner, "Using joint probability densities for simultaneous learning of forward and inverse models," in *IEEE IROS International Workshop on Evolutionary and Reinforcement Learning for Autonomous Robot Systems*, N. T. Siebel and J. Pauli, Eds., 10 2009, pp. 19–22.

[2] G. Bradski, "The OpenCV Library," *Dr. Dobb's Journal of Software Tools*, 2000.

[3] D. Camarillo, C. Milne, C. Carlson, M. Zinn, and J. Salisbury, "Mechanics modeling of tendon-driven continuum manipulators," *Robotics, IEEE Transactions on*, vol. 24, no. 6, pp. 1262–1273, Dec 2008.

[4] P. E. Dupont, J. Lock, B. Itkowitz, E. Butler, and J. K. Salisbury, "Design and control of concentric-tube robots," *IEEE TRANSACTIONS ON ROBOTICS*, vol. 26, no. 2, 2010.

[5] K. Xu and N. Simaan, "Analytic formulation for kinematics, statics and shape restoration of multi-backbone continuum robots via elliptic integrals," *IEEE TRANSACTIONS ON ROBOTICS*, vol. 2, no. 1, 2011.

[6] M. Khoshnam, A. Yurkewich, and R. V. Patel, "Modeling of a steerable catheter based on beam theory," in *2012 IEEE International Conference on Robotics and Automation(ICRA)*, 5 2012.

[7] ——, "Model-based force control of a steerable ablation catheter with a custom-designed strain sensor," in *2013 IEEE International Conference on Robotics and Automation(ICRA)*, 5 2013.

This workshop was made possible

through the joint efforts of the following supporting

EU funded projects on surgical robotics

and through the support of the Istituto Italiano di Tecnologia

CRAS 2014

4th Joint Workshop on Computer/Robot Assisted Surgery

Genova, Italy October 14–16, 2014

www.cras2014.eu


STIFF
flop


μRALP


eSurge


CASCADE


Active


A.R.A.K.N.E.S.
Array of Robots Augmenting the KINematics of Endoluminal Surgery


i-Sur


MICROVAST


SEVENTH FRAMEWORK
PROGRAMME


iit
ADVR
ISTITUTO ITALIANO DI TECNOLOGIA
ADVANCED ROBOTICS

COMPUTER SCIENCE
UNIVERSITY OF VERONA


KATHOLIEKE UNIVERSITEIT
LEUVEN
MECHANICAL ENGINEERING